Thermodynamics and kinetics of Mg intercalation for multivalent cathode applications

by

Sai Gautam Gopalakrishnan

Submitted to the Department of Materials Science and Engineering
in partial fulfillment of the requirements for the degree of

Doctorate of Philosophy in Materials Science and Engineering

at the

MASSACHUSETTS INSTITUTE OF TECHNOLOGY

June 2017

Author .....
Department of Materials Science and Engineering
April 25, 2017

Certified by .....
Gerbrand Ceder
Professor
Thesis Supervisor

Accepted by .....
Donald R. Sadoway
Chairman, Departmental Committee on Graduate Students

Thermodynamics and kinetics of Mg intercalation for multivalent cathode applications

by

Sai Gautam Gopalakrishnan

Submitted to the Department of Materials Science and Engineering
on April 25, 2017, in partial fulfillment of the
requirements for the degree of
Doctorate of Philosophy in Materials Science and Engineering

Abstract

Energy storage, especially through electrochemical mechanisms such as batteries, is crucial for sustaining the ever-increasing energy needs of the future in a fossil-free manner. While the current industrial workhorse, lithium ion batteries, has shown tremendous improvements in energy and power-densities, via both materials selection and engineering advancements, the lithium ion technology is approaching the fundamental limits of what more can be achieved. Multi-valent (MV) chemistry, that pairs an energy-dense MV metal anode (such as Mg) with a high voltage cathode has the potential to surpass the energy densities achieved by current Li-ion batteries, along with improved safety and lower costs. However, moving into newer chemistries leads to newer challenges, such as developing cathodes that can reversibly intercalate Mg at high voltages, high rates and high capacities, apart from designing electrolytes that remain stable against both the electrodes. In this thesis, I focus on the challenge of MV cathode design and I explore the thermodynamic and kinetic properties of candidate oxide cathode materials for MV batteries, including polymorphs of V_2O_5, spinel-Mn_2O_4 and layered-$Mg_2Mo_3O_8$, using first-principles based methods. The undercurrent of the thesis is to obtain design principles that will aid in both optimization of existing cathodes and in the identification of new candidate materials. Utilizing a diverse set of tools, I benchmark the calculated properties, including average voltage curves, lattice parameters, cation-anion decorations in structures and activation barriers for Mg diffusion, to experimental observations, where possible. Finally, this thesis should serve as a guide for other computational-theorists and experimentalists, in the search for an energy-dense MV cathode that will in turn aid in the realization of a high energy density MV battery.

Thesis Supervisor: Gerbrand Ceder
Title: Professor

Acknowledgments

அகர முதல எழுத்தெல்லாம் ஆதி
பகவன் முதற்றே உலகு

— திருவள்ளுவர்

Similar to the letter 'A' being the first of the alphabets,
the Eternal Truth is the first entity in the world

— Thiruvalluvar (Tamizh poet)

Thanks to Prof. Gerbrand 'Gerd' Ceder, without whom this thesis would not have been possible. I am grateful to Gerd for teaching me invaluable research, communication, and (more importantly) life skills that will undoubtedly help me wherever I get to in life. I have always been inspired by (and tried to imbibe) Gerd's infectious enthusiasm and hunger towards addressing deep and relevant scientific questions. Thanks Gerd for all the good, the bad (and the ugly!), which have played a big part in moulding me to be the person I am today.

I am also thankful to Professors Jeffrey C. Grossman and Antoine Allanore, members of my thesis committee, for their timely guidance and encouragement right from my thesis proposal until my defense. Both of them have been particularly accommodative of my scheduling requests, several of which have been last-minute.

Special thanks to Dr. Pieremanuele 'Piero' Canepa, former post-doc at the Ceder group at MIT and Berkeley. Piero was especially helpful in teaching me the basics of first-principles calculations in my early days at the Ceder group, introducing me to some wonderful plotting tools, and being patient enough while I was teaching him thermodynamics! Being a source of constant encouragement, Piero was (and is) a great friend both inside and outside science, and I have particularly enjoyed the several scientific and philosophical discussions that we have had, especially over some great food. I wish him well for his career in academia and definitely hope to work more with him in the future.

Two members of the Ceder group that I am particularly grateful are Dr. Rahul Malik and Dr. Daniel 'Dan' Hannah, former and current post-docs. Rahul was an invaluable mentor while starting at the Ceder group and introduced me into the world of multivalent battery research. Rahul was a wonderful guide in scientific writing, which have undoubtedly influenced my style of writing papers during my PhD. While Rahul left the Ceder group in Summer 2015, Dan joined the multivalent team in Fall 2015 and has been a good friend and colleague since. Particularly, I would like to thank Dan for being patient through most of my 'useless' ideation sessions, teaching me a ton of python skills and introducing me into the world of matplotlib. I wish good luck to both Rahul and Dan in their respective careers and it will be wonderful to collaborate with them in the future.

I am thankful to all the other members of the Ceder group (at MIT and Berkeley) that I have interacted and worked with during my stay – you have been my family away from home. Special thanks to Dr. William Davidson Richards for the intense 'black-hole' scientific discussions that we have had during my days at MIT – I learned quite a bit from you. I thank Dr. Alexander Urban, Dr. Aziz Abdellahi, Dr. Shou-Hang Bo and Ziqin Rong for being great collaborators and being nice friends outside the group. I am grateful to have had wonderful '13-5025' office-mates in Dr. Nancy Twu and Dr. Shin-Young Kang, who were a source of cheer on several occasions. Special mention to Dr. Valentina Lacivita, Dr. Matteo Bianchini, Dr. Jae-Chul Kim, Dr. Penghao Xiao, Dr. Nongnuch Artrith, Tina Chen, Tan Shi and Yaosen Tian for accommodating me into the UC Berkeley and Lawrence Berkeley Lab (LBL) environs. Prof. Peter Khalifah at Stony Brook University is acknowledged for his useful tips, feedback and scientific discussions during his sabbatical at LBL. The Ceder group secretaries, Kathy E. Simons (MIT) and Alice Mueller (LBL) are thanked for always looking out for me.

It is my privilege to acknowledge the contributions of scientific collaborators outside the Ceder group over the course of my PhD, including Dr. Miao Liu and Prof. Kristin Persson at LBL, Danny Broberg and Prof. Mark Asta at UC Berkeley, Xiaoqi Sun, Dr. Victor Duffort and Prof. Linda Nazar at University of Waterloo, Dr. Ryan

Bayliss and Prof. Jordi Cabana at University of Illinois Chicago, Dr. Baris Key, Dr. Brian Ingram, and Dr. Niya Sa at Argonne National Laboratory.

The life of a PhD student, in general, becomes enjoyable with emotional support from good friends outside the research group, and I feel blessed in this aspect to have met some wonderful people in Cambridge and Berkeley. Ananth Govind Rajan, Srivatsan Rajagopal, Rajesh Sridhar, and Yamini Krishnan formed a great team during the 'Friday hangouts'. I have had plenty of long discussions about life, India, movies, and cricket with Rajan Udwani, Nishant Mundru, Murali Vijayaraghavan, Jaichander Swaminathan, Divya Panchanathan, Rohit Kannan, Ujwal Radhakrishna Bhat, Priyank V. Kumar, Suvinay Subramanian, and Sanket Navale. Some of the nicest people that I have met at Ashdown include Lisa Guay, Chris Foy, Alkiviadis Orfefs Chatzivasileiou, Andrew Rzeznik, Won Kyu Calvin Sun (AHEC 2015-16), my former roommate Jan-Christian Huetter, and the regular attendees at the Cherry Pie Society meetings. I thank the wonderful people at DMSE, including Abigail (and Ross) Regitsky, Olivia Hentz (and Seth Shelley-Abrahamson), Yang Yang, Alex Senko, Arvind Kalidindi, Brendan Smith, Jeremy Poindexter, Astera Tang, Frank McGrogan and Brad Nakanishi for teaching me a bit of materials science and a lot about America! The department admins, Angelita Mireles and Elissa Haverty, deserve a mention for being patient and helping me through the paperwork to move between MIT and Berkeley. It was my pleasure to come across Srivatsav Kunnawalkam, and Dr. Niranjan Srinivas, who were quite helpful during my stay at Berkeley.

A good dose of comedy and music is particularly essential for working and relaxing efficiently. It was sheer coincidence that I got introduced to some of the amazing (political) comedians that exist in America, who have 'made my day' on most occasions, such as John Oliver, Stephen Colbert and the entire cast of Saturday Night Live. I still re-watch the tamizh comedies of Vadivelu and Gounda Mani, absolute colossi in the world of slapstick and satire, respectively. The wonderful world of music created by A.R. Rahman and Ilayaraja has helped me overcome tough situations several times in the past and thoroughly enjoy the high points.

Finally, thank you Amma and Appa for what I am today. You have been the

strongest source of support and have given me immense freedom over the years. With your blessings and support, I will hopefully evolve into an even better person in the years to come. And thanks to Pooja, my sister, for being a source of inspiration and reminding me of my strengths and weaknesses from time to time.

"And miles to go before I sleep, And miles to go before I sleep..."

Sai Gautam Gopalakrishnan
April 25, 2017

Contents

List of Figures

List of Tables

Chapter 1

Introduction

Secondary (i.e. rechargeable) intercalation batteries convert chemical energy into electricity via three main components: the cathode (the intercalation cathode of Figure 1-1) where the working ion is inserted/extracted, an electrolyte transporting working ions between anode and cathode, and the anode. During the battery discharge, working ions are released at the anode and migrate to the cathode through the electrolyte, producing an electrical current in the external circuit to power a load (Figure 1-1). The battery recharges by applying an external electrical potential.

While early battery technology used aqueous electrolytes, Li-technology with non-aqueous electrolytes has now largely outpaced (in terms of market share) all aqueous chemistries except for Pb-acid. After the rapid expansion of Li-ion in the portable electronics industry over the last decade, Li-ion batteries have now made commercial deployment of electric vehicles (EV) an imminent reality. Since 2007, leading manufacturers have achieved $\sim$ 8% annual reduction in pack-level costs, reaching approximately US \$300/kWh in 2014.[156] The source of these cost reductions is primarily attributed to the economies of scale associated with increased production volumes and engineering advances at the cell and pack scale.[156, 49]

The cost of input materials contributes significantly to the overall total, and to continue the path toward cost parity with conventional gasoline powered vehicles, scientists[244] and industrialists[5] alike concede non-incremental improvements in battery technology must be made at the active material level, specifically by develop-

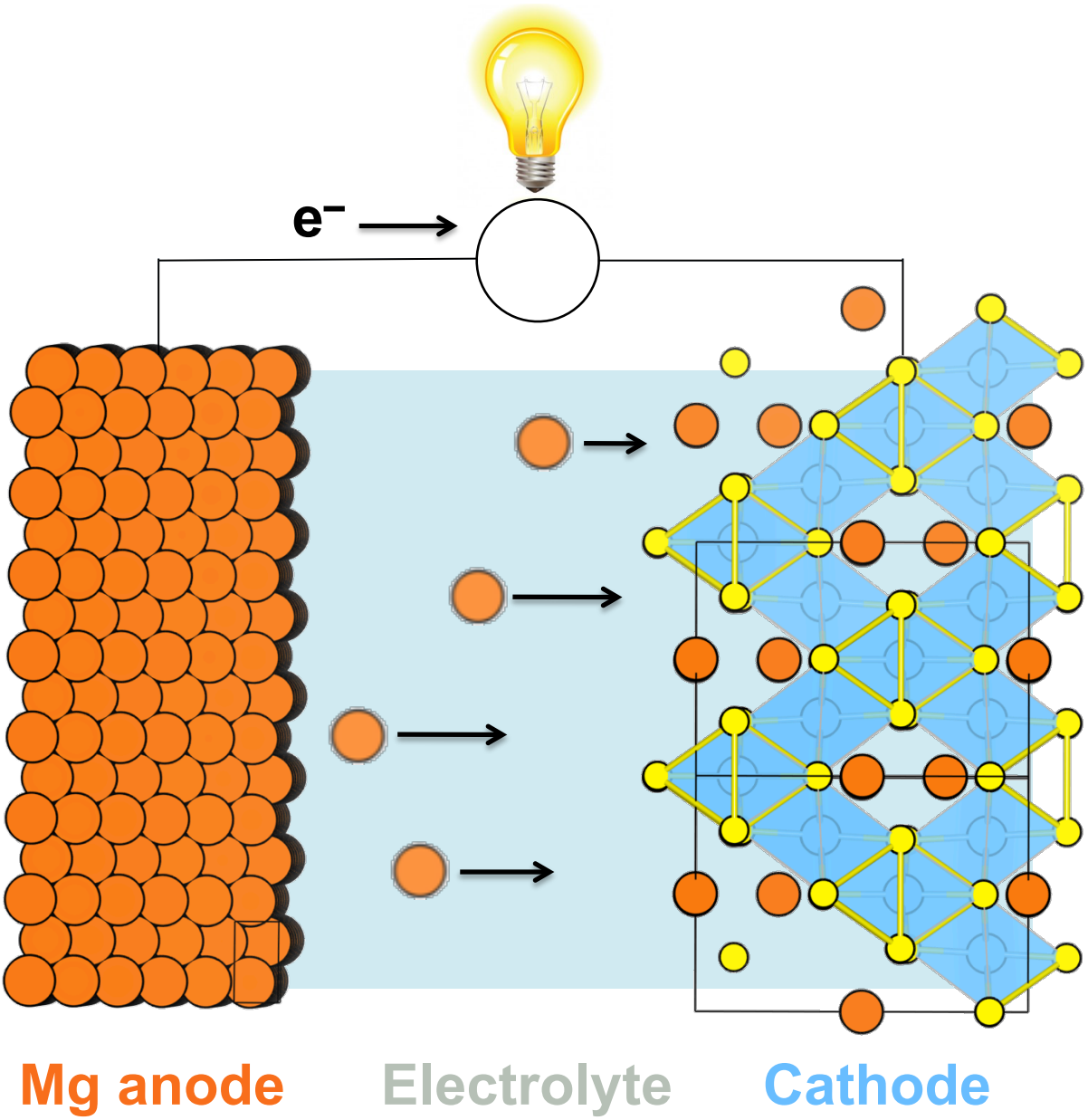

Figure 1-1: (Color online) Representative schematic of a discharging MV battery utilizing a Mg anode, electrolyte, and an intercalation cathode.[32]

ing electrode chemistries that can support both increased gravimetric and volumetric energy densities while maintaining (and improving) the safety, power, lifetime, and cost of state-of-the-art Li-ion batteries. Since advancements at the materials level are approaching a fundamental limit in Li-ion batteries,[219, 244, 69] achieving even higher energy densities has spurred on investigation into the so-called "beyond Li-ion"

technologies, such as Li-O_2 and Li-S.[164, 250, 27, 148, 133]

The most appealing "beyond Li-ion" technology for EVs (and portable electronics) will not only offer a significant energy density improvement and cost reduction, but will also be compatible with existing, highly optimized Li-ion battery architecture (and fabrication) to take advantage of the knowledge accrued over the past twenty years of Li-ion battery manufacturing. From this perspective, intercalation batteries based on new multivalent (MV) chemistries, such as Mg^{2+}, Ca^{2+}, Zn^{2+}, etc., are especially interesting because they have the potential to meet the aforementioned criteria. While current commercial Li-ion batteries operate with a graphitic anode and an intercalation transition-metal oxide cathode separated by a non-aqueous electrolyte, an analogous MV cell can be envisioned with each component now based on a MV chemistry, as shown in Figure 1-1. MV batteries will be able to electrochemically store energy through its three main components: the intercalation cathode where MV ions are inserted/extracted, a metal anode (e.g., Mg) and an electrolyte transporting MV-ions between anode and cathode (Figure 1-1).

1.1 Multivalent anode and electrolytes

A MV chemistry can offer significant improvement in volumetric energy density simply by using a metallic anode (~ 3833 mAh/cm^3 theoretical volumetric energy density for Mg compared to ~ 2046 mAh/cm^3 for Li metal). This is feasible because early evidence indicates that the metallic form of common MV intercalation ions (Mg, Ca) deposits more uniformly than metallic Li during electrochemical cycling.[8, 252, 21, 169] The surface area of lithium metal anodes grows substantially upon cycling, leading to an increase in the surface reactions with the electrolyte. The instability of this surface layer with increased temperature, accelerates thermal runaway, and can even lead to fire.[11, 10, 21, 109, 43] While Li metal anodes are frequently used in lab-made Li-cell prototypes, they so far have been practically unusable in commercial batteries because of lack of cycle life and safety concerns. As a result, current Li-ion batteries operate with lower volumetric energy density graphite anodes (~ 800 mAh/cm^3).

Several attempts at development and commercialization of full electrochemical cells with lithium metal as the anode and a liquid electrolyte have often led to disastrous results.[11, 10, 21, 109, 43]

Although MV cells can potentially achieve high energy densities using metallic anodes,[8, 252, 21, 169] discovering electrolytes capable of reversible MV metal plating/stripping at the anode and supporting reversible intercalation against a high voltage cathode remains a significant and fundamental scientific challenge. The development of versatile MV electrolytes has been curbed by a multitude of factors such as limited chemical and electrochemical compatibility with the electrodes (i.e., narrow electrochemical stability window), lack of reversible MV metal stripping and plating, instability against current collectors, low MV (Mg) mobility leading to the formation of ionic couples (i.e., low MV transference number),[123] and low Coulombic Efficiency (CE).[32, 142] While a detailed analysis of the challenges and accomplishments associated with MV electrolyte development is beyond the scope of this work, several comprehensive reports exist in the literature.[9, 12, 97, 170, 143, 252, 142, 71, 70, 140, 141, 50, 108, 127, 17, 18, 36, 30, 33, 34, 169, 29, 172, 207, 72, 188, 198, 94, 65, 123, 193, 223]

1.2 Multivalent cathode

Significant energy density gains can be realized only if a MV anode can be paired with a MV-insertion cathode material capable of yielding high-capacity at a sufficiently high voltage and with reasonable rate performance.[189, 80, 162, 204, 118] While the literature reports a few working multivalent cathode materials (discussed in the following sections), the MV intercalation host space is relatively unexplored compared to Li-ion,[42] leaving the potential for the discovery of new structure types higher. As a consequence of transferring two (or more) electrons per ion, MV-intercalation can potentially achieve higher capacities than Li-ion cathodes even when occupying a similar number of intercalant sites. Redox reactions permitting, such gains can be combined with the energy density increase associated with the use of a high capacity metal-anode.

This thesis focuses primarily on existing Mg^{2+} intercalation systems widely studied in the literature, alongside examining the possibility of other MV chemistries such as Zn^{2+}, Ca^{2+}, etc., when possible. The increased focus on Mg reflects the volume of burgeoning MV-related research published in the last few years, as presented in Figure 1-2. Also, this thesis will specifically focus on oxide intercalation materials as MV cathode candidates due to their potentially high energy densities (see following sections).

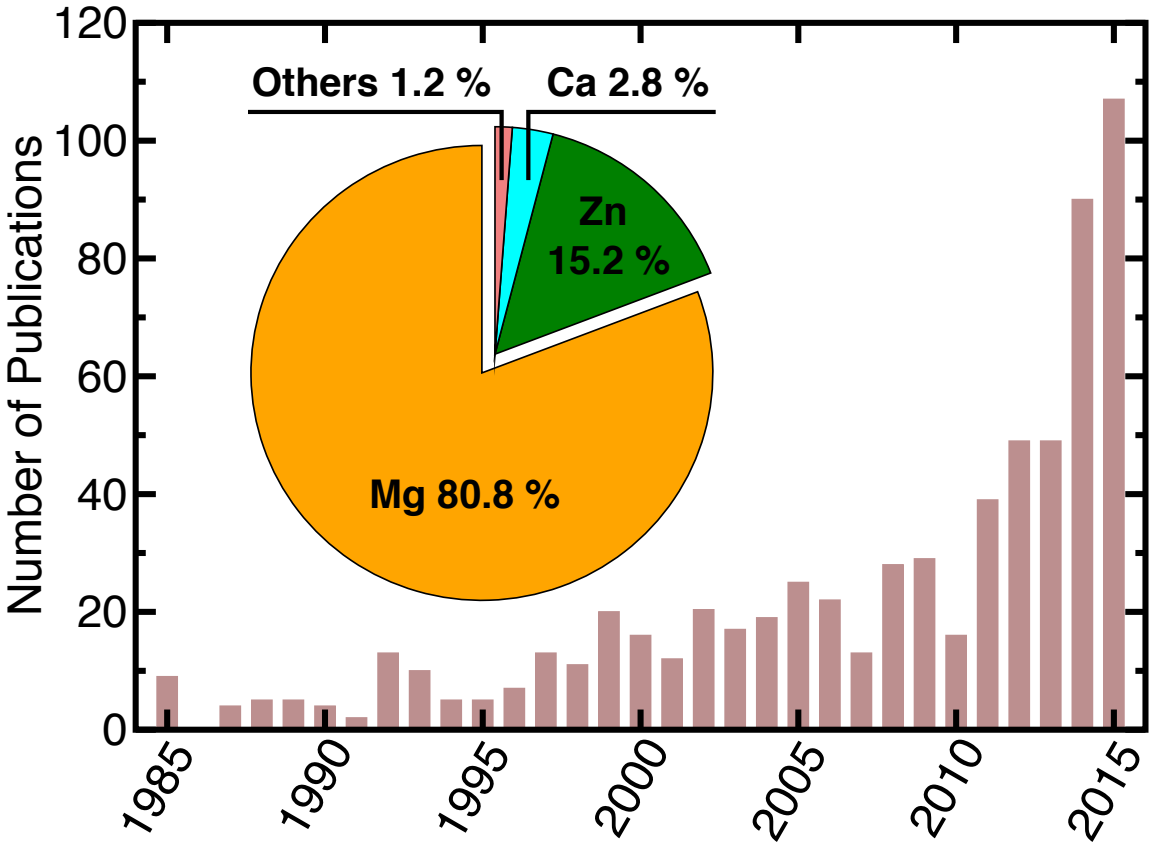

Figure 1-2: (Color online) Number of publications from 1985 until 2015 featuring MV electrochemistry. The pie-chart in the inset shows the partition of MV publications for different reversible chemistries, i.e., Mg, Zn, and Ca. The subset "Others" comprises Al, Sr and Ba electrochemistries. The plotted data is retrieved using Web of Science™ by Thomson Reuters.

1.3 State-of-the-art MV cathodes

Although the concept of a rechargeable magnesium battery was proposed as early as 1990,[68] the first working demonstration of a prototype Mg full cell battery was only achieved in 2000 by Aurbach *et al.*[8] using a magnesium metal anode, an electrolyte based on a solution of Mg organo-halo-aluminate salts in THF, and a Chevrel $Mg_xMo_6S_8$ cathode ($0 < x_{Mg} \leq 2$). With these innovations at the electrolyte and cathode, the authors were able to achieve good kinetics and cycle life (> 2000 cycles) operating at approximately 1.1 V vs. Mg metal and with ~ 70 mAh/g (128.8 mAh/g theoretical capacity),[8] corresponding to ~ 77 Wh/kg and ~ 400 Wh/l energy content at Chevrel's density of ~ 5.2 g/cm^3.[119] This landmark result strengthened the credibility of MV battery technology and also set a definitive benchmark to evaluate novel candidate MV cathode materials.

Unlike today's commercialized Li-ion cathode materials, which are almost entirely structures with close-packed oxygen anion sub-lattices (e.g., layered, spinel, olivine), the Chevrel phase has a unique "cluster" structure as shown in Figure 1-3. The Chevrel structure is comprised of Mo_6T_8 blocks (T = S, Se and Te; gray cubes in Figure 1-3a and b), with 6 Mo forming an octahedron on the faces of the cubes and 8 T anions occupying the corners.[180, 95, 117] The Mo_6S_8 blocks are arranged such that they are separated by three types of "cavities" as illustrated in Figure 1-3b, with each cavity bound by 8 anion atoms forming pseudo-cubes. Type 1 cavities are the farthest away from Mo atoms as they share corners with the Mo_6T_8 cubes, whereas type 2 and type 3 cavities share edges and faces, respectively. Intercalant ions are normally hosted within the cavities of type 1 and 2 since type 3 cavities are destabilized by high electrostatic repulsions with the face-sharing Mo atoms. The specific site position within each cavity varies with the size of the cation species,[115] with the sites for Mg^{2+} shown in the insets of Figure 1-3b and in Figure 1-3c.[180, 117, 115, 89] For example, a ring of six "inner sites" within cavity 1 and two "outer sites" in cavity 2 can be occupied by small ions (such as Li^+, Mg^{2+}, or $Cu^{1+/2+}$), while larger ions (Pb^{2+} or Sn^{2+}) normally occupy the center of each cavity (Figure 1-3b). Considering

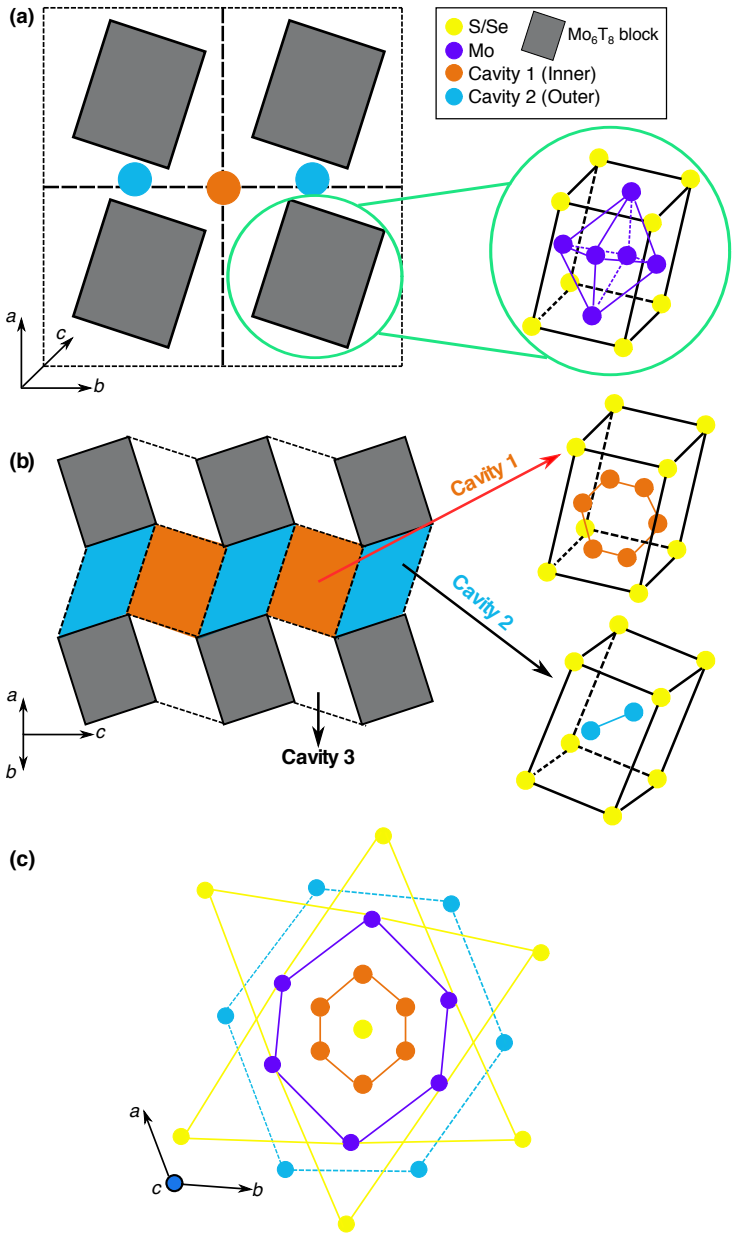

Figure 1-3: (Color online) The crystal structure of the Chevrel host, with the gray rectangles representing Mo_6T_8 blocks (T = S, Se), comprising the Mo_6 octahedra enclosed within a T_8 cube. (a) Displays a projection of the structure on the a–b plane, where orange and blue circles indicate the centers of the cavity sites of type 1 and type 2, respectively, adapted from [174]. (b) Indicates the the 6 "inner" (type 1) and 2 "outer" (type 2) cavity sites.[174] (c) Shows a top view of the structure, highlighting the distorted hexagonal patterns made by the inner and outer cavities.[89, 32]

the topology of Mo_6S_8 blocks, where each block is corner-sharing with 8 cavity cubes of type 1 and edge-sharing with 12 cubes of type 2, there are twelve possible sites (6

inner and 6 outer, as illustrated in Figure 1-3c) between each Mo_6S_8 block where the intercalating ion (such as Li^+, Mg^{2+}) can reside.[89]

Reversible Mg-intercalation in close-packed sulfide frameworks, which has been the subject of extensive experimental[28, 26, 4, 118, 213, 216, 212] and theoretical investigations,[52] has recently been shown in spinel-Ti_2S_4[213] and layered-TiS_2.[212] Sun *et al.*[213] reported highly reversible Mg intercalation in spinel-Ti_2S_4 with an All Phenyl Complex (APC) electrolyte in THF utilizing a coin-cell setup with a Mg counter electrode. A first discharge capacity of $\sim$ 200 mAh/g ($Mg_{0.84}Ti_2S_4$) was obtained at 60 °C with capacity retention for more than 40 cycles. At an average voltage of $\sim$ 1.2 V vs. Mg and at a density of 3.24 g/cm^3 for spinel-Ti_2S_4,[121] a $\sim$ 200 mAh/g capacity corresponds to an energy content of $\sim$ 228 Wh/kg and $\sim$ 731 Wh/l, far above the energy values of the Chevrel. The solid solution character observed in both chemical magnesiation experiments by Bruce *et al.*,[28, 26] and the more recent Galvanostatic Intermittent Titration Technique observations (GITT) by Sun *et al.*[213] fall in excellent agreement with the computed voltage profile of Emly *et al.*[52]

In parallel, reversible intercalation of Mg in the layered-TiS_2 phase, utilizing a similar coin-cell setup used previously for the spinel polymorph,[213] was reported.[212] The initial discharge capacity of $\sim$ 270 mAh/g ($Mg_{0.56}TiS_2$, measured at a rate of C/20) was higher than for the spinel-phase ($\sim$ 200 mAh/g for $Mg_{0.80}Ti_2S_4$)[213] at a similar voltage of $\sim$ 1.2 V. However, successive cycles showed a decreased but constant capacity of $\sim$ 160 mAh/g ($Mg_{0.33}TiS_2$), which varies substantially at different C rates, i.e. $\sim$ 140 mAh/g at C/10 and $\sim$ 90 mAh/g at C/5, respectively, indicating some irreversible capacity in the initial cycles. Given that the densities of spinel and layered-TiS_2 are similar,[121, 44] the energy content of layered-TiS_2, $\sim$ 192 Wh/kg and $\sim$ 623 Wh/l, are comparable to the values of the spinel phase.

Mg intercalation in Chevrel and TiS_2 structures represent state-of-the-art performance in MV batteries, displaying excellent reversibility and intercalation kinetics, but its present form provides energy densities below current Li-ion technology.[32] Subsequently, this work will explore alternative chemistries to the Chevrel-phase and

TiS_2 polymorphs, chiefly oxide host frameworks that can potentially achieve higher voltages and reversible capacity, while maintaining reasonable rate-performance.

1.4 Oxides

One strategy to improve upon the electrochemical performance of chalcogenide MV batteries is to target intercalation materials with higher theoretical voltage and capacity. The possibility of increasing the intercalation voltage by switching the anion species from sulfur to oxygen[13] and increasing the theoretical capacity by considering structures with a higher ratio of intercalant to transition metal makes oxide materials especially appealing as MV cathode materials. Previously, this approach was successfully implemented in the development of Li-ion cathode materials, which began with $LiTiS_2$[241, 243] and lead to today's commercial oxide-based cathode materials, i.e. $LiCoO_2$.[139] To go beyond the performance of Chevrel cathodes, it is not sufficient to only identify candidate MV host systems that possess high theoretical voltage and capacity, but the material must also be synthesizable, allow MV-intercalation at reasonable rates and be stable over many electrochemical cycles. An additional challenge for identifying good MV cathodes comes from the limited stability of MV-ion electrolytes against high-voltage MV cathode materials,[142, 141, 116, 33, 34, 172, 207] which is an ongoing and parallel research challenge that sometimes prevents reliable electrochemical data from being extracted in MV systems. The general considerations and challenges associated with MV intercalation in oxide hosts is discussed below.

1.4.1 Mobility

Based on extensive research on Li^+-ion conductors,[237] which consistently show sulfides to have much better Li^+ mobility than oxides, one would expect Mg^{2+} mobility to decrease similarly when switching from sulfides to oxides. Indeed, the limited mobility of MV ions in oxide host structures is generally considered the chief obstacle in finding an oxide cathode capable of supplanting sulfides.[118, 183] Requirements

for reasonable battery performance allow us to establish minimal values for MV ion mobility. For a given (dis)charge time t the cathode particle size will determine a maximum tolerable barrier (E_m) for MV ion migration, since the diffusion length scales as $\sqrt{Dt}$. Here, the radius of a spherical particle is used as the required diffusion length. We approximate the diffusivity D as $D \approx v \cdot a^2 \cdot \exp(-E_m/kT)$, where v is the atomic jump frequency and a is the atomic jump distance. Assuming (reasonable) values of 10^{12} s^{-1} for v and 3 Å for a, the relationship between E_m and the maximum particle size feasible for MV ion extraction is displayed in Figure 1-4 for several charging rates. In discussing the process of (dis)charge, current is often expressed as a C-rate in order to normalize against the electrode capacity.

The C-rate measures the rate at which the material is discharged relative to its maximum capacity, and 1C indicates a complete discharge of a battery in 1 hour. Therefore C-rate is defined independently of the volumetric capacity (Ah/l) of the cathode under consideration. As such, a material with twice the (volumetric) capacity will require twice as much current at the same C-rate, which directly translates to twice the ionic flux needed at the particle surfaces. Consider Fick's 1^{st} law, $J = -D\frac{dc}{dx}$, where J is the ionic flux (in mol cm^{-2} s^{-1}), D the ionic diffusivity (cm^2 s^{-1}), c the ionic concentration (mol cm^{-3}) and x is distance (cm). A material with twice the volumetric capacity will have twice the concentration of the redox species throughout the material. This in turn doubles the concentration gradient(s) throughout the material which subsequently doubles the ionic flux (and the current), at the same value of ionic diffusivity. As a result, under Fickian diffusion conditions, two materials that have the same ionic migration barrier (E_m) will discharge at the same C-rate irrespective of the volumetric capacity. Therefore, our analysis in Figure 1-4 considers the upper limit of migration barriers at which a steady-state ionic diffusion can occur throughout a cathode particle of a given size, in a specified time interval (as implied by the C-rate), which is independent of volumetric capacity.

For a primary particle size of $\approx$ 100 nm, charge rates of C/3 (as in the USABC for electric vehicles[150]) can be obtained for migration barriers in the $600-750$ meV range and below. Of course, this criterion implies that no other kinetic factors such

as desolvation and charge transfer across the electrolyte/electrode interface, or phase boundary motion in the case of two-phase electrode reactions, are rate-limiting. With these assumptions in place, Figure 1-4 displays the maximum particle size (y-axis) which would permit ion extraction against a particular barrier (x-axis). Curves are shown for multiple charging rates and temperatures. Considering the generally low mobility of MV ions in oxide hosts, the relationship in Figure 1-4 demonstrates the potential importance of nanosizing as a means to achieve viable MV battery cathodes. However, pseudo-capacitive contributions to capacity will naturally be more prominent when high surface-area electrodes are employed, and must be carefully considered when discussing measured values.[90, 56] The advantages and drawbacks of nanostructured electrodes are discussed in more detail later in the review.

1.4.2 Solvent co-intercalation

A commonly adopted strategy to enhance MV ion mobility is by incorporating shielding water molecules in the structure, either by co-intercalation or directly in synthesis. Although the findings of water intercalation aiding Mg insertion in various cathode materials, such as layered MoO_3, *xerogel*-V_2O_5, Birnessite and spinel-MnO_2, are exciting (see respective sections), the observed improvements in capacity and kinetics could indicate the occurrence of proton (or hydronium) intercalation[99] in these cathode materials, highlighting the need for critical interpretation of the experimental results. From the experimental studies discussed in the following sections, it is not clear whether water actively participates in electrochemical reactions —the potential for electrochemical decomposition of water (according to $2H_2O \rightarrow O_2 + 4H^+ + 4e^-$) is only ~ -1.229 V vs. Standard Hydrogen Electrode (SHE). In addition, there has been no clarification with vibrational spectroscopy methods on whether structural water exists in the form of OH^- and H^+ adsorbed on the oxide surfaces, thus creating a source of readily cyclable ions. Proton cycling can also possibly explain the excess capacity reported for organic electrolytes mixed with increasing water concentrations.[153, 146] While thermodynamic models can clarify voltage dependen-

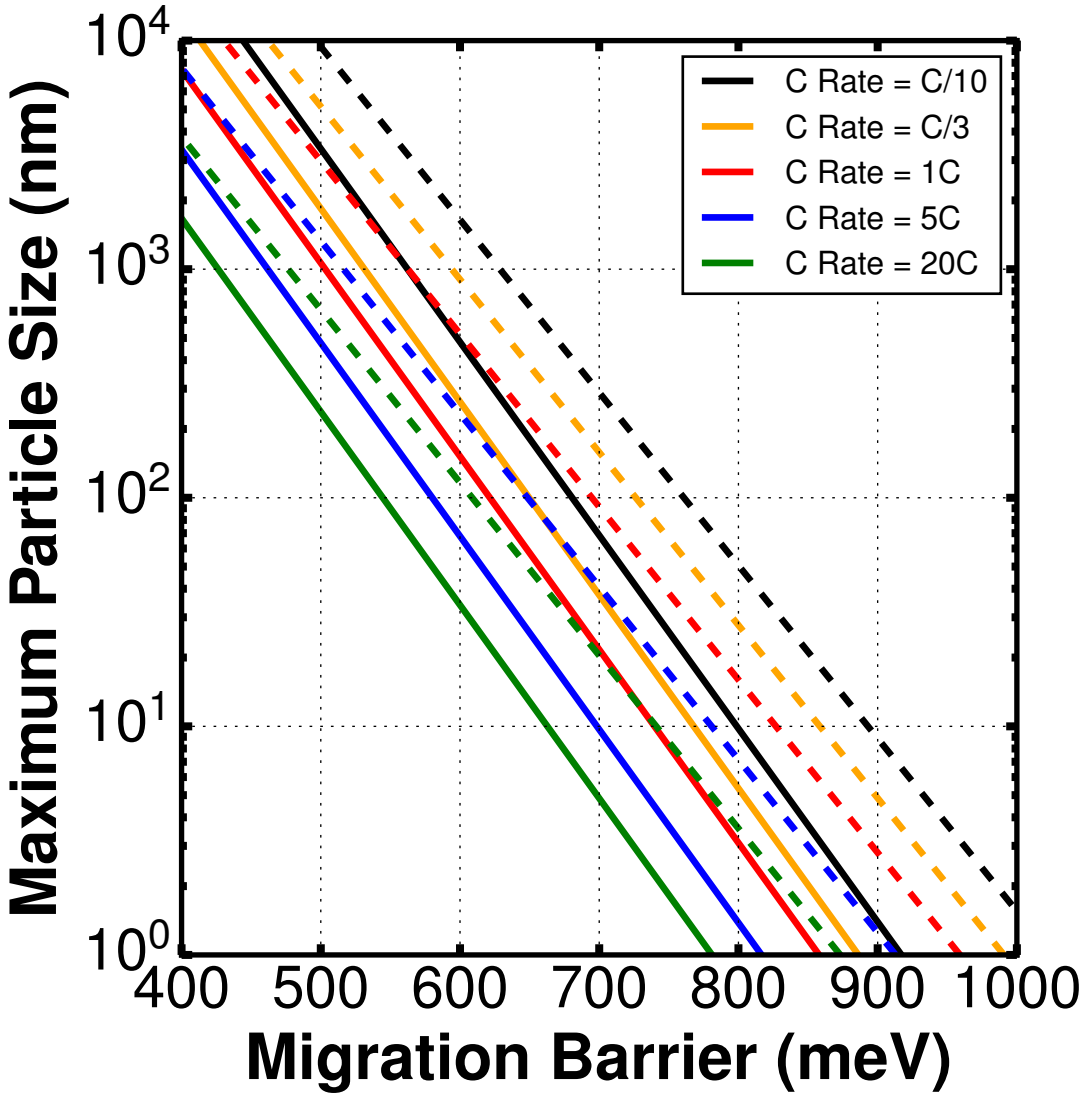

Figure 1-4: Relationship between MV ion migration barrier E_m and the maximum particle size permitting reasonable diffusivity in the context of battery performance. Various charging rates are displayed and color-coded as indicated in the figure legend. Solid lines indicate the relationship between migration barrier and particle size at 298 K, while dashed lines indicate 333 K.

cies and driving forces for water co-intercalation in cathodes, it is challenging for theoretical frameworks to explain observed variabilities in capacities with electrolytic water content. Even if water is not directly involved in any redox reactions, but simply aids Mg intercalation, strategies to avoid water contact with the Mg-metal anode

need to be envisioned before water addition to the system would become practical. If solvent co-intercalation can indeed promote Mg^{2+} mobility, then research should focus on the incorporation of stable solvent in solutions which do not lead to spurious side reactions in the electrochemistry and do not passivate the Mg metal anode.

1.4.3 Conversion reactions

In addition to poor MV-ion mobility, another issue that can afflict oxide intercalation hosts is the tendency to undergo irreversible oxide conversion reactions instead of reversible MV intercalation. The occurrence of undesired conversion reactions as opposed to MV intercalation can be rationalized in terms of competing thermodynamic forces, largely driven by the very low free energy of MgO formation. For example, Figure 1-5 shows the competition between intercalation and conversion reactions for one mole of Mg reacting (i.e. a 2 electron transfer) with a mole of transition metal oxide (TMO_2), where the average voltages are V_{conv} and V_{int} (with respect to Mg metal), respectively.

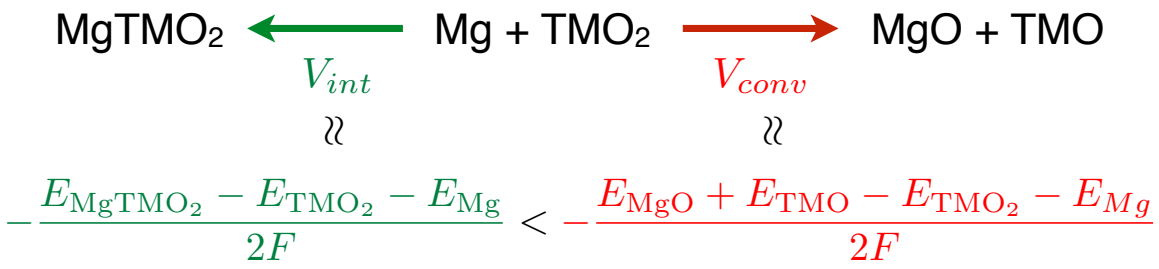

Figure 1-5: Schematic of competing intercalation and conversion reactions for a 2 electron transfer process with Mg. $E_{species}$ is the internal energy of a species from DFT calculations and F the Faraday constant.

$E_{species}$ in Figure 1-5 is the free energy of the species at 298 K, and approximated as the internal energy at 0 K computed by DFT,[13, 259] with F the Faraday constant. If $V_{conv} > V_{int}$, the conversion reaction is thermodynamically favored against the desired MV intercalation, and vice-versa if $V_{int} > V_{conv}$. Generally, MV ions form their respective oxides at a comparable voltage to Li, while intercalating at lower

voltages. For example, Mg and Ca react with O_2 to form MgO at $\sim$ 3.16 V vs. Mg and CaO $\sim$ 3.35 V vs. Ca, respectively, compared to $\sim$ 3.15 V vs. Li for the formation of Li_2O, which are obtained from the experimental free energies tabulated by Kubaschewski and Alcock.[107] Thus, the oxide formation voltage is similar for MgO and Li_2O, even though Li^+ is $\sim$ 0.7 V lower than Mg^{2+} on the SHE scale. This reflects the tremendous thermodynamic stability of MgO compared to the other oxides. The competition with conversion reaction is less of an issue for Ca^{2+}, given that Ca^{2+} is only $\sim$ 0.2 V lower than Li^+ vs. SHE. In TMO_2 cathodes the chemical potential of oxygen is set by the energy difference between the TMO_2 and TMO (reduced) specie, which quantifies the ability of the TMO_2 host to transfer oxygen to the working ion. Thus, MV intercalation reactions must compete against the formation of highly stable oxides.

Figure 1-6 charts the competing nature of conversion (V_{conv}) and intercalation (V_{int}) reactions of several transition metal oxides (MoO_3, V_2O_5, and several layered and spinel TMO_2) for Li^+ and MV ions (Mg^{2+}, Ca^{2+} and Zn^{2+}) obtained by utilizing the lowest DFT energies from the Materials Project database,[88] to construct intercalation voltages and conversion reaction paths.

Trends in Figure 1-6 indicate that while both Li and MV ions are not expected to undergo conversion in most 1 electron reduction processes (i.e. 1 mol of Li or 0.5 mol of MV, left panel), MV conversion is preferred when 2 electrons are transferred per TM (i.e. 1 mol of MV, right panel). This does not necessarily imply that conversion will take place, as many Li^+ intercalation states are metastable, but it does require a reliance on kinetic stabilization. Additionally, the voltage difference between intercalation and conversion reactions ($V_{int}-V_{conv}$, width of green bars in the left panel of Figure 1-6) is nominally higher for Li than for MV ions, making Li-intercalation cathodes very tolerant to degradation due to local polarization, which could potentially drop the actual potential below V_{conv}.

While most MV ions are not expected to undergo conversion reactions in most oxide hosts at low MV content (or $1e^-$ reduction), local accumulation of MV ions can occur during intercalation due to poor MV mobility. A significant increase in local

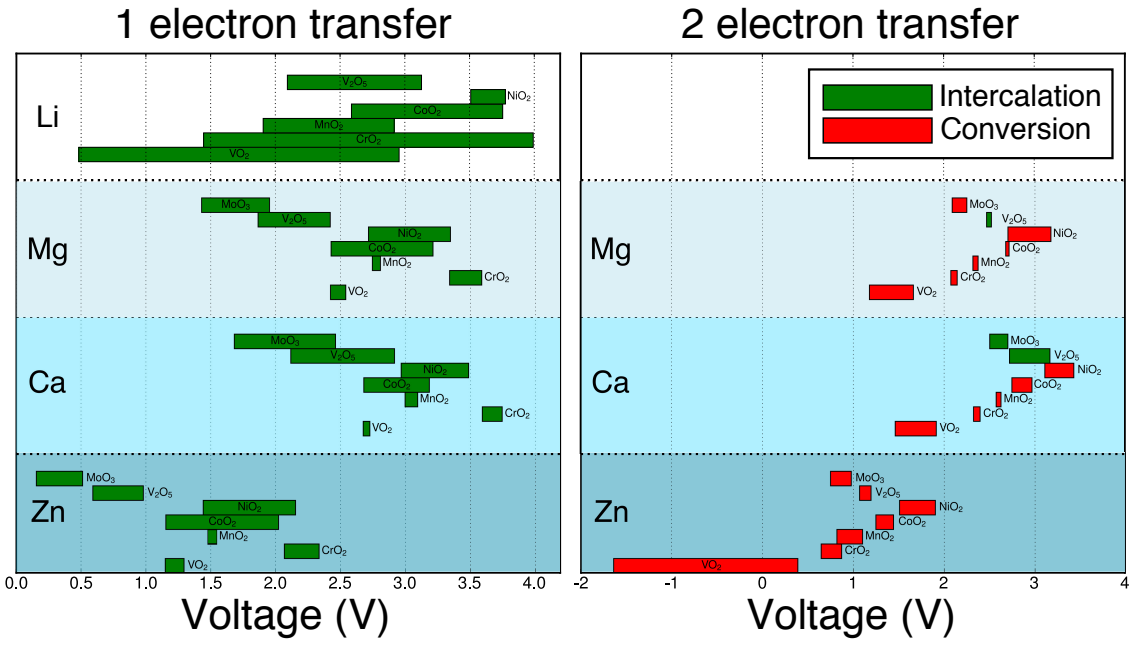

Figure 1-6: Competition between intercalation and oxide conversion reactions for Li, Mg, Ca and Zn, as quantified by V_{int} and V_{conv} of Figure 1-5. For the green bars, the minimum voltage (left of the bar) is V_{conv}, while V_{int} is the maximum (right of the bar). In this condition, intercalation is preferred since $V_{int} > V_{conv}$. Similarly, red bars signify conversion as V_{conv} (maximum of the bar) is greater than V_{int} (minimum). Left and the right panels are for 1 electron (e.g. $TM^{4+} \rightarrow TM^{3+}$) and 2 electron (e.g. $TM^{4+} \rightarrow TM^{2+}$) redox processes, respectively.

concentration of MV ions (and the number of electrons transferred locally) can indeed result in local conversion reactions, given the tendency for most transition metal oxides to convert at high MV content (Figure 1-6, right panel). This analysis points at a key challenge for Mg^{2+} intercalation in oxides. Even though its intercalation kinetics is expected to be much worse than Li^{+}, its tolerant polarization window upon discharge is considerably smaller than for Li^{+} intercalation due to the very negative formation energy of MgO. To compound the problem, MgO is considered to have extremely low mobility for Mg^{2+} ions.[200] While this has never been proven rigorously, the difficulty in operating Mg metal anodes is attributed to the ease by which a blocking MgO layer forms on it in many solvents.[252] While still present, the conversion challenge seems to be less of an issue for Ca^{2+}, particularly in hosts such as V_2O_5 and MoO_3.

Note that for the purpose of plotting Figure 1-6, we considered only the formation of Li_2O_2 in Li-TMO_2 systems and other simple oxide reduction reactions, such as $TMO_2 \rightarrow TMO$, while there could be other competing conversion reactions that could impact the trends in Figure 1-6 (such as the formation of Li_2O in Li-TMO_2 and $MgVO_3$ in Mg-V_2O_5). Since the formation of Li_2O_2 ($\sim$ 3.38 V) occurs at a higher voltage compared to Li_2O ($\sim$ 3.15 V),[107] we adopted Li_2O_2 as the compound of choice for conversion reactions of Li in Figure 1-6, but the qualitative trends should not change if Li_2O is considered as the conversion product. Also, the cathode materials could undergo (ir)reversible phase transformations during intercalation, which could influence the energetics, such as $\alpha \leftrightarrow \delta$ in Li-V_2O_5 and spinel $\rightarrow$ layered or spinel $\rightarrow$ rock-salt in Mg-oxide spinels (see discussion later). These considerations suggest that careful interpretation of the observed electrochemical and structural data is always required, and rigorous analysis of characterization measurements (XRD and other spectroscopic techniques) is a must to check for conversion products.

1.5 Structure of thesis

This thesis consists of 8 chapters, with chapters 3–7 exploring Mg (or MV intercalation) in a given structure. Chapter 2 has a detailed description of the methods used in this work. The polymorphs of V_2O_5, including the Orthorhombic and Xerogel variants are explored over the course of chapters 3–5, with chapter 4 providing a general overview of MV intercalation, including the cases of Ca^{2+}, Zn^{2+} and Al^{3+} intercalation apart from Mg. Chapter 6 details a collaborative experimental-theoretical work into $Mg_2Mo_3O_8$, identified as a potential Mg-cathode based on coordination preferences of Mg. The influence of spinel inversion on Mg mobility in oxide and sulfide spinel structures is analyzed in Chapter 7, where the role of inversion on Mg-electrochemistry is also touched upon. Finally, a few summarizing remarks and important scientific challenges in the short term are outlined in Chapter 8.

Chapter 2

Methods

2.1 Density Functional Theory

Total energy calculations through this thesis are done using Density Functional Theory (DFT) as implemented in the Vienna Ab-Inito Simulation Package (VASP) with the Perdew-Burke-Ernzerhof (PBE) exchange-correlation functional.[102, 105, 104, 165] The Projector Augmented Wave theory[106] together with a well converged energy cutoff of 520 eV is used to describe the wave functions, which are sampled on a well-converged k-point mesh (minimum of 1000 k-points per reciprocal atom). In order to remove the spurious self-interaction of the vanadium, molybdenum, manganese d-electrons, a Hubbard U correction of 3.1, 4.38, 3.9 eV, respectively, is added to the Generalized Gradient Approximation (GGA) Hamiltonian (GGA+U)[6, 259] as fitted by Jain *et al.*[87] All Mg-V_2O_5 structures are fully relaxed within 0.25 meV/f.u, while Mg-Mo_3O_8 structures were relaxed to within 0.01 meV/atom. For 0 K phase diagram calculations of $Mg_xMn_2O_4$ (i.e., the ground state hull of the $Mg_xMn_2O_4$ system), the PBESol exchange-correlation functional[166] is used to improve the description of the energetics.[100] Additionally, calculations of $Mg_xMn_2O_4$ are always initialized with an ideal cubic structure while allowing for potential tetragonal distortions during the geometry relaxation as the spinel can be either cubic ($x_{Mg} \sim 0$) or tetragonal ($x_{Mg} \sim 1$) based on the concentration of Jahn-Teller active Mn^{3+} ions. Since layered materials such as Orthorhombic- and Xerogel-V_2O_5 are bound by van

der Waals interactions that are not well captured by standard DFT,[3, 59] the vdW-DF2+U functional[112, 101] is used to compute the layer spacing values ($b-$axis in Figures 3-1 and 5-1). However, preliminary investigations[35] have shown that GGA+U describes the energetics of redox reactions in layered materials better than vdW-DF2+U.

2.2 Average voltage calculations

Consider an electrochemical reaction, where Mg intercalates into a MO_2 host (M = Transition Metal) and compensating electrons are absorbed into the cathode host from the external circuit.

$$Mg_xMO_2 + \Delta x\ Mg \rightleftharpoons Mg_{x+\Delta x}MO_2 \tag{2.1}$$

Starting from the Nernst equation and using thermodynamic arguments, the voltage for reaction 2.1 can be written as a function of the Mg chemical potential in the cathode (Mg_xMO_2) and the anode (Mg metal), as in Eq. 2.2, with z and F being the number of electrons transferred (2 per Mg) and the Faraday constant, respectively.

$$V(x) = -\frac{\mu^{\mathrm{Mg}}_{\mathrm{Mg}_x\mathrm{MO}_2}(cathode) - \mu^{\mathrm{Mg}}_{\mathrm{Mg\ metal}}(anode)}{zF} \tag{2.2}$$

The average voltage ($\langle V \rangle$) between 2 given compositions of Mg (x_1 and x_2) in MO_2 are obtained by integrating Eq. 2.2. Usually, average voltages are computed across the Mg compositions under consideration, which in most cases is $x_1 = 0$ and $x_2 = 1$. Specifically, at each x_{Mg}, the energy of the ground state configuration of the Mg_xMO_2 system is taken for calculating the voltage, which is nominally obtained from the ground-state hull (or 0 K phase diagram) of the system. Neglecting the entropic ($T\Delta S$) and volumetric ($P\Delta V$) components, the chemical potential (or Gibbs energy per unit Mg composition) can be approximated as the internal energy calculated by Density Functional Theory (DFT) at 0 K, i.e., $G_{\mathrm{Mg}_x\mathrm{MO}_2} \approx E^{DFT}_{\mathrm{Mg}_x\mathrm{MO}_2}$, thus allowing

the average voltage to be computed directly from DFT energies.[13, 259]

$$\langle V \rangle = -\frac{E(\mathrm{Mg}_{x_2}\mathrm{MO}_2) - E(\mathrm{Mg}_{x_1}\mathrm{MO}_2) - (x_2 - x_1)E(\text{Mg metal})}{(x_2 - x_1)zF} \tag{2.3}$$

Eq. 2.3 is applicable for electrochemical systems where the cathode framework (such as V_2O_5, Mo_3O_8, MnO_2, etc.) remains constant as the Mg concentration is changed.

2.2.1 Voltages in co-intercalation systems

To study the thermodynamic effects of a co-intercalating species in a cathode, such as H_2O co-intercalation with Mg in Xerogel-V_2O_5 (Section 5.1), we equilibrate the Mg-Xerogel V_2O_5 system open to varying amounts of H_2O in an electrolyte as governed by the grand-potential,

$$\Phi = G_{\text{Mg-}\mathrm{V_2O_5}} - n_{\mathrm{H_2O}}.\mu_{\mathrm{H_2O}}, \tag{2.4}$$

with $G_{\text{Mg-}\mathrm{V_2O_5}}$, $n_{\mathrm{H_2O}}$ and $\mu_{\mathrm{H_2O}}$ the Gibbs energy of the Mg-Xerogel V_2O_5, the number of moles of water in the Xerogel and the chemical potential of H_2O in the electrolyte, respectively. Grand-potential phase diagrams have been used to study open electrochemical systems before.[161, 34] While we use Density Functional Theory (Section 2.1) calculations to obtain values of $G_{\text{Mg-}\mathrm{V_2O_5}}$ at different Mg concentrations in the Xerogel structure, the procedure used to obtain an accurate reference state for water ($\mu_{\mathrm{H_2O}}$) is detailed in the Appendix (Section 5.7).

In the case of Xerogel-V_2O_5, as Mg is (de)intercalated the cathodic composition changes due to H_2O shuttling along with the Mg^{2+} (see Figure 5-2). In order to account for changes in the Xerogel composition on (de)magnesiation, the grand-potential energies (Φ in Eq. 2.4) must be used in calculating the average voltage, with Eq. 2.3 being re-written as Eq. 2.5.

$$\langle V \rangle = -\frac{\Phi[\mathrm{Mg}_{x_2}(\mathrm{H_2O})_{n_2}\mathrm{V_2O_5}] - \Phi[\mathrm{Mg}_{x_1}(\mathrm{H_2O})_{n_1}\mathrm{V_2O_5}] - (x_2 - x_1)E(\text{Mg metal})}{(x_2 - x_1)zF} \tag{2.5}$$

where, $\Phi[\mathrm{Mg}_{x_2}(\mathrm{H_2O})_{n_2}\mathrm{V_2O_5}] = E[\mathrm{Mg}_{x_2}(\mathrm{H_2O})_{n_2}\mathrm{V_2O_5}] - n_2.\mu_{\mathrm{H_2O}}$, with E calculated using DFT and the value of μ obtained through the procedure described in Sec-

tion 5.7.5.

2.3 Cluster expansion formalism and Monte-Carlo simulations

To obtain a temperature-composition phase diagram (such as the Mg-V_2O_5 system, Figure 3-7), Grand-canonical Monte Carlo (GMC) simulations are performed on a cluster expansion (CE) Hamiltonian. The CE is a parameterization of the total energy with respect to the occupancy of a predefined topology of sites, which in the case of the Mg-V_2O_5 system are the possible Mg insertion sites.[38, 194, 226] In practice the CE is written as a truncated summation of the Effective Cluster Interactions (ECIs) of the pair, triplet, quadruplet and higher order terms as given in Equation 2.6.

$$E(\sigma) = \sum_{\alpha} m_{\alpha} V_{\alpha} \langle \prod_{i \in \beta} \sigma_i \rangle \tag{2.6}$$

where the energy, E of a given configuration of Mg ions σ is obtained as a summation over all symmetrically distinct clusters α. Each term in the sum is a product of the multiplicity m, the effective cluster interaction (ECI) V for a given α, and the occupation variable σ_i averaged over all clusters β that are symmetrically equivalent to α in the primitive cell of the given lattice. In this work, the CE is performed on the Mg sub-lattice and the various configurations correspond to the arrangement of Mg ($\sigma_i = 1$) and Vacancies (Va; $\sigma_i = -1$) on the available Mg sites. The Pymatgen library is used to generate the various Mg-Va arrangements to be calculated with DFT.[160, 74, 75, 76] The CE is built on the DFT formation energy of 97 distinct Mg-Va configurations using the compressive sensing paradigm and optimized through the split-Bregman algorithm.[149, 67] The root mean square error (RMSE) and the weighted cross-validation (WCV) score are used to judge the quality and the predictive ability of the fit, respectively.[234]

The high temperature phase diagram is then obtained with GMC calculations on supercells containing at least 1728 Mg/Va sites (equivalent to a 12×6×6 supercell of

the conventional unit cell) and for a minimum of 100,000 equilibration steps followed by 200,000 sampling steps.[227] Monte Carlo scans are done on a range of chemical potentials at different temperatures, and phase transitions are detected by discontinuities in Mg concentration and energies. In order to remove numerical hysteresis from the Monte Carlo simulations, particularly at low temperatures, free energy integration is performed[79] with the fully magnesiated and fully demagnesiated phases as reference states.

2.4 Activation barrier calculations

The activation barriers for Mg^{2+} diffusion in structures considered in this work are calculated with the Nudged Elastic Band (NEB) method,[78, 202] as implemented in VASP. The barriers are calculated in supercells of V_2O_5, Mo_3O_8 and Mn_2O_4 such that a minimum distance of ~ 8 Å between the elastic bands is ensured to reduce fictitious interactions with periodic images. Notably, migration barriers do not change appreciably ($< 3\%$ deviation) when equivalent calculations are performed in larger supercells (see sample calculations done in spinel-Mn_2O_4, Figure **??**). 7–9 images are introduced between the initial and final end points to capture the saddle point and the diffusion trajectory. The endpoint energies are converged to 0.01 meV/supercell while the forces in the NEB are considered converged within 0.1 eV/Å in V_2O_5 structures (Chapters 3, 4) and 0.05 meV/Å in spinels-Mn_2O_4, In_2S_4 (Chapter 7) and layered-Mo_3O_8 (Chapter 6) . All NEB results are based on the PBE functional, and the Hubbard U correction is avoided in order to limit convergence issues during the calculations.[126] The migration barriers in spinel-$MgIn_2S_4$ (a potential Mg-solid electrolyte[31], see Chapter 7) are calculated with compensating electrons added as a background charge to ensure charge-neutrality of the structure at non-stoichiometric Mg concentrations.

2.5 Percolation theory and Monte-Carlo simulations

While activation barriers for the various cation arrangements, as illustrated for a spinel lattice in Figure 7-2, determine the active Mg^{2+} diffusion hops (or channels) on the atomic scale, the macroscopic migration of Mg^{2+}, which is essential for (dis)charge of cathodes or ionic conduction in solid electrolytes, depends on the existence of a percolating network of active diffusion channels. As the $8a - 16c - 8a$ channels form a percolating network throughout the spinel structure, stoichiometric normal spinels with Mg in $8a$ enable macroscopic migration of Mg^{2+} as long as the $8a - 16c - 8a$ hop is open, i.e., the migration barrier for Hop 1 is below a threshold value. However, inversion leads to mixing of cation occupancies in both the $8a$ and $16d$ sites, potentially causing some $8a-16c-8a$ channels to close (due to higher Mg^{2+} migration barriers along Hop 2) while opening new channels typically closed in a normal spinel (e.g., Hops 3, 4, or 5). Hence, in addition to identifying facile microscopic hops, it is important to consider whether a percolating network of low-barrier diffusion channels exists. Analogous studies have been done on Li^+ percolation in rocksalt lattices.[224]

In percolation theory, the site percolation problem[210, 81, 86, 54] identifies the critical concentration, $x = x_{crit}$, at which an infinite network of contiguous connected sites exists in an infinite lattice of randomly occupied sites. In terms of ionic diffusion, x_{crit} sets the "percolation threshold", above which percolating channels exist in a given structure and macroscopic ion migration is feasible. While percolation thresholds are accessible analytically for 2D lattices,[86] Monte-Carlo (MC) simulations serve to estimate x_{crit} in 3D structures.[225, 128, 224]

The existence of a percolating diffusion network in a structure at a certain x ($> x_{crit}$) does not imply that all ions in the structure can be (reversibly) extracted. Mg sites that are not part of a percolating network will form isolated clusters throughout the structure so that the amount of extractable ions is lower than the total concentration, i.e., $x_{ext} < x$. In electrochemical measurements, x_{ext} directly corresponds to the capacity of a cathode material. Numerically, x_{ext} is also estimated from MC simulations.[224]

In summary, the two central quantities obtained from percolation MC simulations are the Mg concentration beyond which macroscopic migration is feasible (x_{crit}) and the fraction of extractable Mg ions in a percolating structure (x_{ext}). In order to study Mg migration in spinels, we modified the nearest neighbor model (normally considered in site percolation estimations) to include occupancies up to the 3^{rd} nearest neighbor (i.e., corner-sharing sites in Table 7.1). Two Mg sites in a given spinel arrangement are considered connected only if the diffusion channel linking them is open (i.e., the migration barrier is below an upper-limit). Thus, a percolating network of Mg sites is formed solely via open diffusion channels. Whether a channel is considered open will depend on the migration barrier for Mg diffusion through it.

Monte-Carlo simulations are used to estimate the Mg percolation thresholds (x_{crit}) and the fraction of extractable Mg ions (x_{ext}). A 6×6×6 supercell of the primitive spinel structure is used, which corresponds to 1728 anion atoms (Figure 7-12 plots convergence behavior with supercell size). In MC simulations, a network of Mg sites is considered percolating when it spans the periodic boundaries of the simulation cell in one or more directions.[151] Note that in an ideal stoichiometric spinel, the Mg and M (M = Mn, In) sub-lattices comprise all 8*a* and all 16*d* sites, respectively (Table 7.1). Thus, all 8*a* (all 16*d*) sites are labeled as part of the Mg (M) sub-lattice during MC sweeps in a normal spinel. In the case of an inverted stoichiometric spinel, Mg can occupy both 8*a* and 16*d* sites, where the number of 8*a* and 16*d* sites being Mg-occupied is dictated by the degree of inversion. For example, in a conventional stoichiometric spinel cell at $i = 0.25$, six 8*a* and two 16*d* sites will be occupied by Mg. Hence, the Mg sub-lattice in an inverted spinel will comprise those 8*a* and 16*d* sites that are occupied by Mg. As a result, inversion in the spinel is introduced during MC sweeps by labelling a number of random 8*a* and 16*d* sites, corresponding to the degree of inversion, as part of the Mg sub-lattice.

Each MC sweep comprises of the following steps:[151] (*i*) the supercell is initialized with M atoms in both M and Mg sub-lattices, corresponding to a M_3X_4 (X = O, S) stoichiometry, (*ii*) M atoms on the Mg sub-lattice are randomly changed to Mg, (*iii*) after all Mg sub-lattice sites are changed (i.e., a stoichiometry of MgM_2X_4 is

attained), M atoms on the M sub-lattice are randomly flipped to Mg, and (*iv*) the sweep is stopped after all M atoms are flipped to Mg. During an MC sweep, once a Mg atom replacement results in the formation of a percolating network, the current Mg concentration (x_{Mg}) is taken as an estimate of the percolation threshold (x_{crit}), while for $x > x_{crit}$, the fraction of sites within the percolating network, x_{ext}, is stored. The values of x_{crit} and x_{ext} are averaged over 2000 MC sweeps to guarantee well-converged estimates. The effect of vacancies on Mg percolation in the Mn-spinel is captured by initializing the Mg sub-lattice with varying vacancy concentrations, at a given degree of inversion, corresponding to a $Vac_yMn_{3-y}O_4$ stoichiometry ($y \leq 1$). Whenever vacancies are initialized in a supercell, only the Mn atoms are changed to Mg during a MC sweep.

Chapter 3

The intercalation phase diagram of Mg in V_2O_5 from first principles

3.1 Introduction

A multi-valent (MV) battery chemistry, which pairs a non-dendrite forming Mg metal anode with a high voltage ($\sim$ 3 V) intercalation cathode offers a potentially safe and inexpensive high energy density storage system with the potential to outperform current Li-ion technology.[152] A change in chemistry leads to new challenges, however, one being the design of a cathode that can reversibly intercalate Mg at a high enough voltage. Orthorhombic V_2O_5 is one such material that offers exciting prospects of being a reversible intercalating cathode for Mg batteries.[204, 8, 252] The theoretical energy density of a cathode based on Mg intercalation into V_2O_5 is $\sim$ 660 Wh/kg,[88] which approaches the practical energy densities of current commercial Li-ion chemistries ($\sim$ 700 Wh/kg for $LiCoO_2$[243]), but the major benefit of switching to a MV chemistry is the gain in volumetric energy density arising from the usage of a metallic anode ($\sim$ 3833 mAh/cm^3 for Mg[204] compared to $\sim$ 800 mAh/cm^3 for Li insertion into graphite.[88])

The orthorhombic V_2O_5 structure has been well characterized due to its interesting spin ladder characteristics and widely known Li intercalation properties, with a reversible capacity of $\sim$ 130 mAh/g and voltage of $\sim$ 3.3 V vs. Li metal.[15, 53, 136,

103, 242, 61, 2] Consequently, Li intercalation into V_2O_5 has been the subject of several experimental[46, 144, 48, 245, 247] and theoretical[24, 181, 196] studies. Li-V_2O_5 undergoes several first-order phase transformations during intercalation, such as the $\alpha \rightarrow \epsilon$ and $\epsilon \rightarrow \delta$ between $x_{Li} = 0$ and $x_{Li} = 1$, the irreversible $\delta \rightarrow \gamma$ transition at $x_{Li} > 1$, and another irreversible $\gamma \rightarrow \omega$ transition at $x_{Li} > 2$.[46] Several authors have investigated Mg-insertion into V_2O_5[2, 167, 68, 154, 64] and to date, V_2O_5 is one of only three cathode materials to have shown reversible intercalation of Mg, the other two being the chevrel Mo_3S_4[8] and layered MoO_3.[64]

While Li-ion has been investigated extensively for the past $\sim$ 25 years, there are significantly fewer studies, theoretical or otherwise, of Mg intercalation hosts in the literature. Pereira-Ramos *et al.*[167] showed electrochemical intercalation of Mg into V_2O_5 (at 150 °C and 100 μA/cm^2 current density), and Gregory *et al.*[68] have reported chemical insertion of Mg up to $Mg_{0.66}V_2O_5$. Novak *et al.*[153] demonstrated reversible electrochemical insertion of Mg in V_2O_5 at room temperature while also demonstrating superior capacities ($\sim$ 170 mAh/g) using an acetonitrile (AN) electrolyte containing water as opposed to dry AN. Yu *et al.*[254] showed similar improvements in capacity ($\sim$158.6 mAh/g) using a H_2O + Polycarbonate (PC) system compared to dry PC. Electrochemical insertion of Mg into V_2O_5 nanopowders and thin films using activated carbon as the counter electrode was shown by Amatucci *et al.*[2] and Gershinsky *et al.*,[64] respectively, and insertion into V_2O_5 single crystals was reported by Shklover *et al.*[203]

Thus far, all reported experimental attempts have begun in the charged state and succeeded in reversibly inserting only about half a Mg ($x_{Mg} \sim 0.5$) per formula unit of V_2O_5, in contrast to Li-V_2O_5 where up to $x_{Li} \sim 3$ has been inserted per V_2O_5.[46, 167, 254, 203] When the grain size of V_2O_5 is reduced, e.g., nano powders and thin films, insertion levels can reach $x_{Mg} \sim 0.6$.[2, 64] In addition, in cells where a Mg metal anode was used rapid capacity fade was reported upon cycling.[153, 254] Unlike Li intercalation systems, anode passivation by the electrolytes is a major issue for Mg batteries using a Mg metal anode.[254] Out of the two experiments that have not reported significant capacity fade so far,[2, 64] the work done by Gershinsky *et al.*

is particularly useful to benchmark theoretical models as the Mg insertion was done at extremely low rates (0.5 μA/cm^2), and therefore corresponds most to equilibrium conditions.

Previous theoretical studies of the Mg-V_2O_5 system have benchmarked structural parameters, average voltages and the electronic properties of layered V_2O_5 upon Mg insertion.[239, 35, 258] Wang *et al.*[239] showed an increase in the Mg binding energy and Li mobility in single-layered V_2O_5 compared to bulk V_2O_5. Carrasco[35] found that while incorporating van der Waals dispersion corrections in the calculations improved the agreement of the lattice parameters with experiments, it led to an overestimation of the voltage. Zhou *et al.*[258] calculated the band structures, average voltages, Mg migration barriers, and the $\alpha \rightarrow \delta$ phase transformation barrier in Mg-V_2O_5. While reporting higher computed average voltage for Mg-V_2O_5 compared to the Li-V_2O_5 system (in apparent disagreement with experiments[46, 64]), the authors explained the slow diffusion of Mg in V_2O_5 by predicting a facile $\alpha \rightarrow \delta$ transition coupled with an estimated lower Mg mobility in δ than α.[258]

In the present work, we have explored in detail the physics of room temperature Mg intercalation in orthorhombic V_2O_5 using first-principles calculations. Compared to Li, Mg insertion is accompanied by twice the number of electrons, which means that the properties of the Mg intercalation system will be largely dictated by how the additional electron localizes on the nearby V atoms. To study the combined effects not only of inserting a different ion but also a different number of electrons on the equilibrium phase behavior, we calculate the Mg-V_2O_5 intercalation phase diagram using the Cluster expansion-Monte Carlo approach. A similar approach has been previously used to study Li-intercalation systems[39, 260] and can be derived formally through systematic coarse graining of the partition function.[38] Our calculations focus particularly on Mg intercalation into the α and δ polymorphs of V_2O_5, evaluating their respective ground state hulls, subsequent voltage curves and activation barriers for Mg diffusion. We have also constructed the temperature-composition phase diagram for Mg in the δ polymorph. Calculations in this chapter are carried out as described in Sections 2.1, 2.2, 2.3, and 2.4.

3.2 Polymorphs of V_2O_5

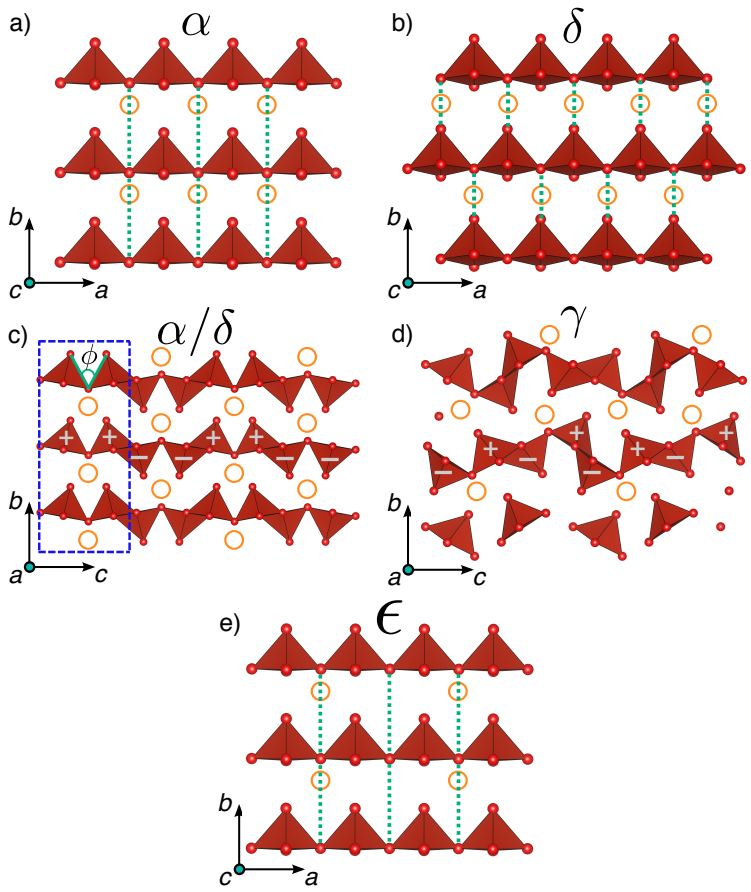

Figure 3-1: (Color online) (a) α and (b) δ polymorphs of orthorhombic V_2O_5 are shown along the c-axis (shown to a depth of $c/2$ for viewing clarity) and along the (c) a-axis, which compared to the (d) γ polymorph has a different orientation of VO_5 pyramids as denoted by '+' and '−' signs along the c-axis. Hollow orange circles correspond to the intercalation sites, the green dotted lines show the differences in layer stacking and the dashed blue rectangle in (c) indicates a distance of $c/2$. (e) illustrates the ϵ phase corresponding to a specific ordering of Mg atoms in α-V_2O_5 at half magnesiation, where alternate intercalant sites are occupied in the a axis as indicated by the orange circles. The schematics here correspond to 'supercells' of the respective polymorph unit cells.

The V_2O_5 structure consists of layers of VO_5 pyramids, each of which have 4 V−O bonds that form the base of the pyramid and one V=O (Vanadyl) bond that forms the apex. Each layer consists of alternate corner and edge sharing pyramids, with an offset in the a-axis between the edge-sharing pyramids. The different poly-

morphs of V_2O_5 observed experimentally are illustrated in Figure 3-1,[46] with the α (space group *Pmmn*), δ (*Cmcm*) and γ (*Pnma*) polymorphs all having orthorhombic symmetry. The notation, specific to this work, is a being the shortest axis of the lattice (3.56 Å for α; 3.69 Å for δ), b being the axis perpendicular to the layers indicative of the layer spacing (4.37 Å; 9.97 Å), and c being the longest axis (11.51 Å; 11.02 Å). Pure V_2O_5 crystallizes in the α phase at 298 K and remains stable at higher temperatures,[46] while the fully magnesiated phase (MgV_2O_5) has been found to form in the structure of the δ polymorph.[23] For simpler visualization, a single slice of the α and δ polymorphs, corresponding to a depth of $c/2$ (illustrated by the dashed blue rectangle in Figure 3-1c) is shown in Figure 3-1a and Figure 3-1b respectively. The α and δ polymorphs are very similar when viewed along the a-axis or the b-c plane (Figure 3-1c).

The main difference between the δ phase and the α phase is a translation of alternating V_2O_5 layers in the a-direction by '$a/2$' which doubles the 'b' lattice parameter (as well as the unit cell) of the δ phase. The Mg sites in both α and δ are situated near the middle of the VO_5 pyramids (along a) and between the 2 layers (along b), as illustrated by the orange circles in Figure 3-1. As a result of shifting of layers between the α and δ phases, the anion coordination environment of the Mg sites also changes. Considering a Mg−O bond length cutoff of 2.5 Å, the Mg in the α phase is 8-fold coordinated (4 nearest neighbor O atoms and 4 next nearest neighbors, 4+4) whereas the Mg in the δ phase is 6-fold coordinated (4+2). In this work, the ϵ phase is a specific ordering of Mg atoms on the α-V_2O_5 host at half magnesiation, as shown in Figure 3-1e. This intercalant ordering is observed in the Li-V_2O_5 system,[46] and has intercalant ions at alternate sites along the a axis, as illustrated by the absence of Mg sites in Figure 3-1e.[181, 40] The VO_5 pyramids in the α and δ phases 'pucker' upon Li intercalation as observed experimentally by Cava *et al.*[37] For the sake of simplicity we define puckering here as the angle 'ϕ', as shown in Figure 3-1c. As the pyramids pucker with intercalation, the angle 'ϕ' decreases.

In the Li-V_2O_5 system, at $x_{Li} > 1$, the host structure undergoes an irreversible phase transformation to form the γ phase, in which the VO_5 pyramids adopt a dif-

ferent orientation compared to α and δ, as seen in Figure 3-1c and 3-1d.[46] In the γ phase, the VO_5 pyramids along the c-direction alternate between up and down (denoted by '+' and '−' in Figure 3-1); whereas, in α and δ, the sequence goes as 'up-up-down-down'. The γ phase has not yet been reported in the Mg-V_2O_5 system and hence will not be further discussed in this chapter.

3.3 Results

3.3.1 Mg-V_2O_5 Ground State Hull

Figure 3-2 shows the ground state hull and average voltage curves as a function of Mg concentration in V_2O_5 as computed by DFT. The solid blue and red lines in Figure 3-2a indicate the ground state hulls of the α and δ polymorphs respectively. All formation energies are referenced to the fully magnesiated and fully demagnesiated end points of the δ-phase. The overall equilibrium behavior of the system is that of phase separation between unintercalated α-V_2O_5 and fully intercalated δ-$Mg_1V_2O_5$ as indicated by the solid maroon line. As can be observed, the α phase is stable compared to the δ phase at low Mg concentrations up to $x_{Mg} \sim 0.35$ where the α and δ hulls intersect, and the δ phase is stable at higher Mg concentrations. In Figure 3-2a, the dash-dotted blue line indicates the end members of the α hull (pure α-V_2O_5 and α-$Mg_1V_2O_5$), and the dashed red line the lowest energy configurations computed at intermediate Mg concentrations for the δ phase.

The α-hull represents the energy trajectory for metastable Mg insertion into α-V_2O_5 (i.e., without transformation of the host to δ), and it displays a convex shape with ground state configurations at Mg concentrations of 0.25 and 0.5. The most stable configuration at $x_{Mg} = 0.5$ in the α hull is the ϵ phase. In contrast, there are no metastable Mg orderings in the δ phase implying that in the δ-phase host the Mg ions will want to phase separate into MgV_2O_5 and V_2O_5 domains. Some Mg configurations when initialized in the α phase relax to the δ phase as indicated by the green diamond points on Figure 3-2a. These structures undergo a shear-like

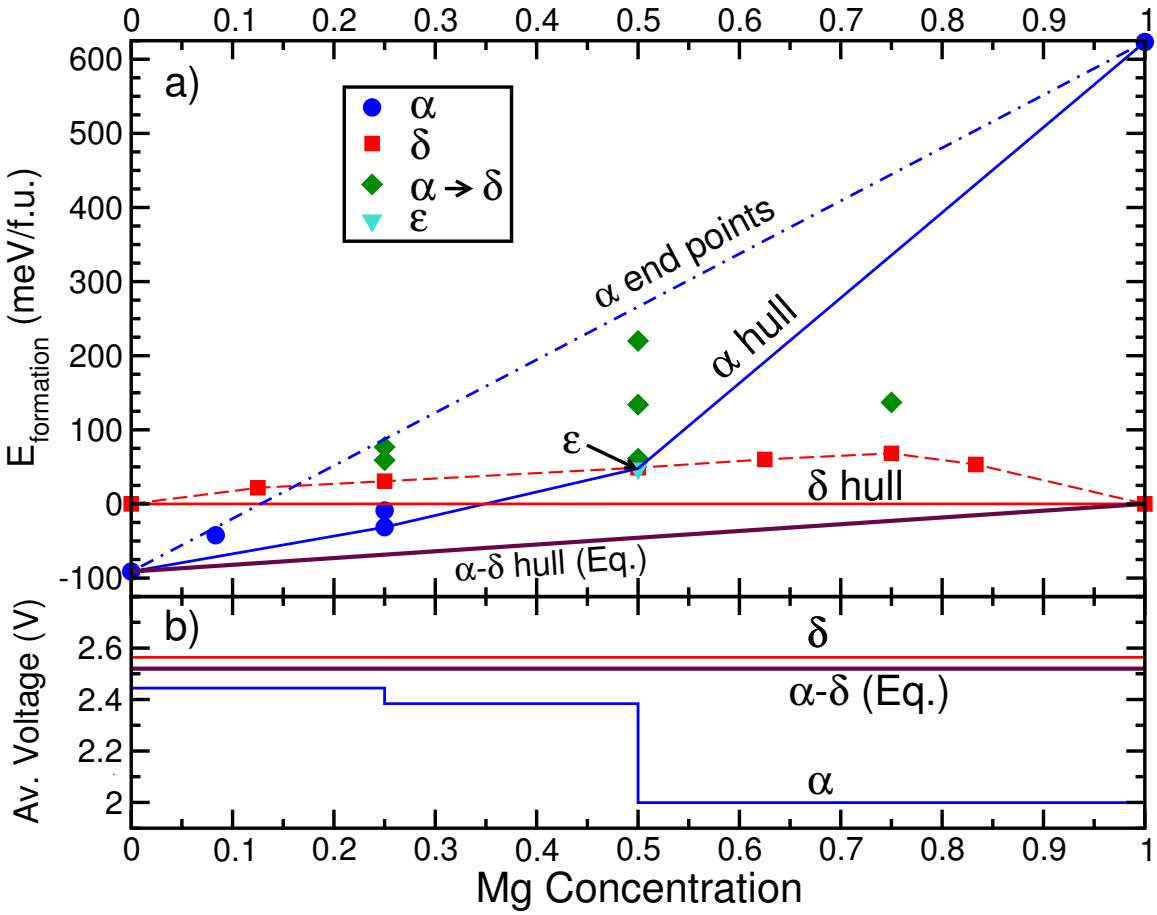

Figure 3-2: (Color online) (a) The ground-state hull of Mg in V_2O_5 considering both α and δ phases. The formation energy per formula unit has been plotted with respect to Mg concentration. (b) The average voltage curves at 0 K for the α and δ phases with respect to pure Mg metal, obtained from the respective hulls are plotted against the Mg concentration.

transformation from α to δ, which involves V_2O_5 layers sliding along the a-direction. This mechanical instability phenomenon has been observed in our calculations both at low Mg concentrations ($x_{Mg} = 0.25$) and at high Mg concentrations ($x_{Mg} = 0.75$), but never at very low Mg concentrations ($x_{Mg} = 0.08$).

The Mg insertion voltage will depend on which of the possible stable or metastable paths the system follows and the voltage for several possible scenarios is shown in Figure 3-2b. The equilibrium voltage curve is a single plateau at 2.52 V vs. Mg metal, consistent with phase separating behavior between α-V_2O_5 and δ-$Mg_1V_2O_5$. The voltage for the metastable insertion in the α host averages $\sim$ 2.27 V vs. Mg

metal for $0 < x_{Mg} < 1$ and exhibits a steep potential drop of ~ 400 mV at $x_{Mg} = 0.5$, corresponding to the ϵ ordering. Metastable Mg insertion in δ occurs on a single plateau at 2.56 V vs. Mg metal, consistent with phase separation between δ-$Mg_0V_2O_5$ and fully intercalated δ-$Mg_1V_2O_5$. The average voltage of the α phase best agrees with the experimental average voltage of ~ 2.3 V.[2, 64]

3.3.2 Puckering and Layer spacing

The VO_5 pyramids in both α and δ-V_2O_5 pucker upon Mg intercalation, quantified by the angle ϕ shown in Figure 3-1c. We find that ϕ decreases (corresponding to increased puckering) with increasing Mg concentration, resulting in the formation of ripples in the layers. Current calculations show a decrease from $\phi \sim 76^\circ$ at $x_{Mg} = 0$ (which corresponds to flat layers) to $\phi \sim 56^\circ$ at $x_{Mg} = 1$ in the α phase and a decrease from $\phi \sim 68^\circ$ at $x_{Mg} = 0$ to $\phi \sim 54^\circ$ at $x_{Mg} = 1$ in δ-V_2O_5.

Figure 3-3 shows the variation of the V_2O_5 layer spacing (seen in Figure 3-1a and Figure 3-1b) as a function of Mg concentration in both the α (blue) and the δ (red) phases. In other layered materials, van der Waals interactions are known to cause layer binding in the deintercalated limit,[3] which is not well described by standard DFT calculations.[59, 186] Therefore, in order to obtain a better estimate of the layer spacing values, additional calculations are performed using the vdW-DF2 functional,[112, 101] which includes the van der Waals interactions in addition to the Hubbard $+U$ Hamiltonian (for removing self-interaction errors).

The layer spacing values in Figure 3-3 are taken from the relaxed ground states for α and δ in Figure 3-2a. The blue circles and red squares are obtained from PBE ($+U$) calculations, while the blue and red triangles are calculated with vdW-DF2 ($+U$). The experimental values listed (green diamonds) correspond to pure α-V_2O_5,[53] $Mg_{0.2}V_2O_5$ reported by Pereira-Ramos *et al.*[167] and pure δ-$Mg_1V_2O_5$.[137] As expected, the PBE and vdW-DF2 layer spacing values differ at complete demagnesiation (~ 0.3 Å) but remain similar at all other Mg concentrations, where the layer spacing is determined by the electrostatics and short range repulsion.

With increasing Mg concentration, the layer spacing increases significantly for

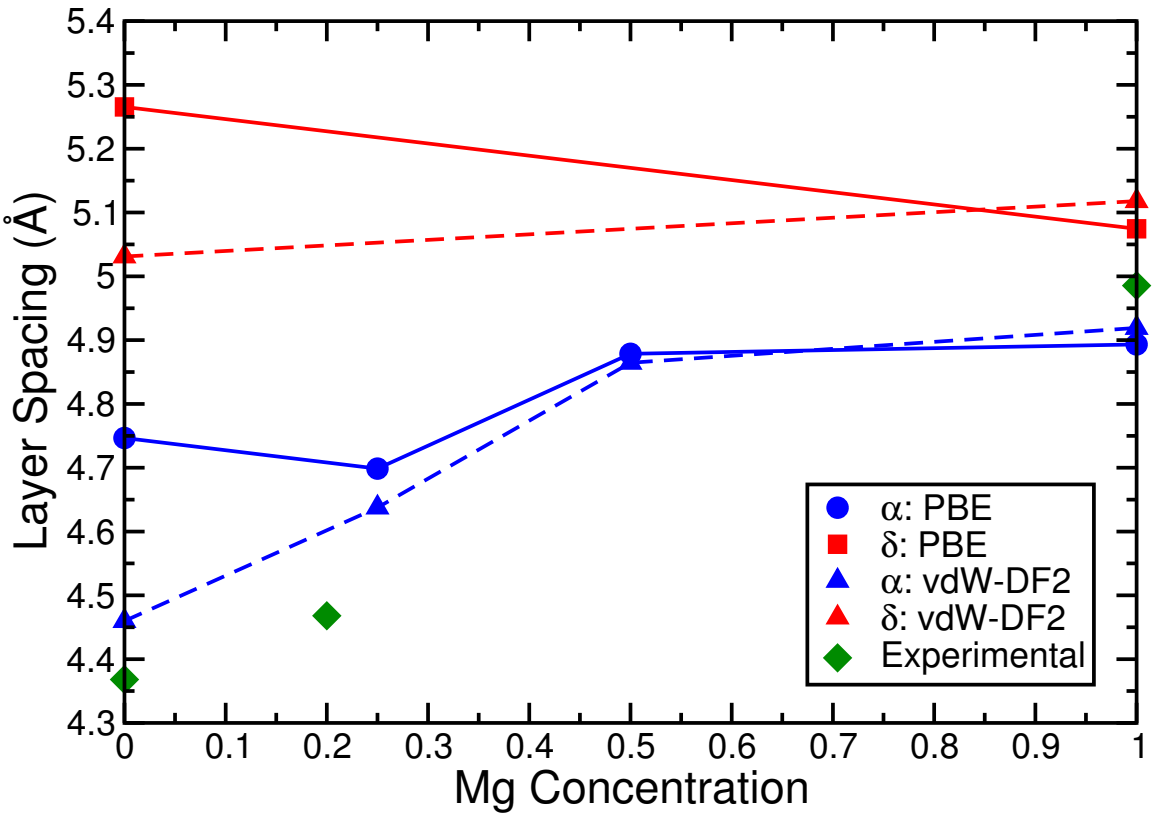

Figure 3-3: (Color online) Variation of layer spacing with Mg concentration in both α and δ phases. The experimental data points correspond to the pure α-V_2O_5, intercalated $Mg_{0.2}V_2O_5$ and pure δ-$Mg_1V_2O_5$.

α-V_2O_5 ($\sim$ 9% increase from $x_{Mg} = 0$ to $x_{Mg} = 0.5$ while using vdW-DF2) but remains fairly constant in δ-V_2O_5 ($\sim$ 2% increase from $x_{Mg} = 0$ to $x_{Mg} = 1$). However, the layer spacing in the δ phase remains higher than in the α phase across all Mg concentrations. Also, the layer spacing seen in the α phase (with vdW-DF2) benchmarks better with experimental layer spacing values at low Mg concentrations (up to $x_{Mg} = 0.2$) compared to the δ phase. Though including the van der Waals corrections in DFT leads to better agreement with the experimental V_2O_5 layer spacing, the Mg insertion voltage is overestimated[35] (by 18% as compared to 6% with PBE+U), showing that PBE+U describes the energetics more accurately than vdW-DF2. If the $Mg_xV_2O_5$ hull (Figure 3-2a) were to be calculated with vdW-DF2, we speculate that the energies of the demagnesiated structures will shift to higher values than PBE+U, since van der Waals corrections tend to penalize under-binded (demagnesiated) struc-

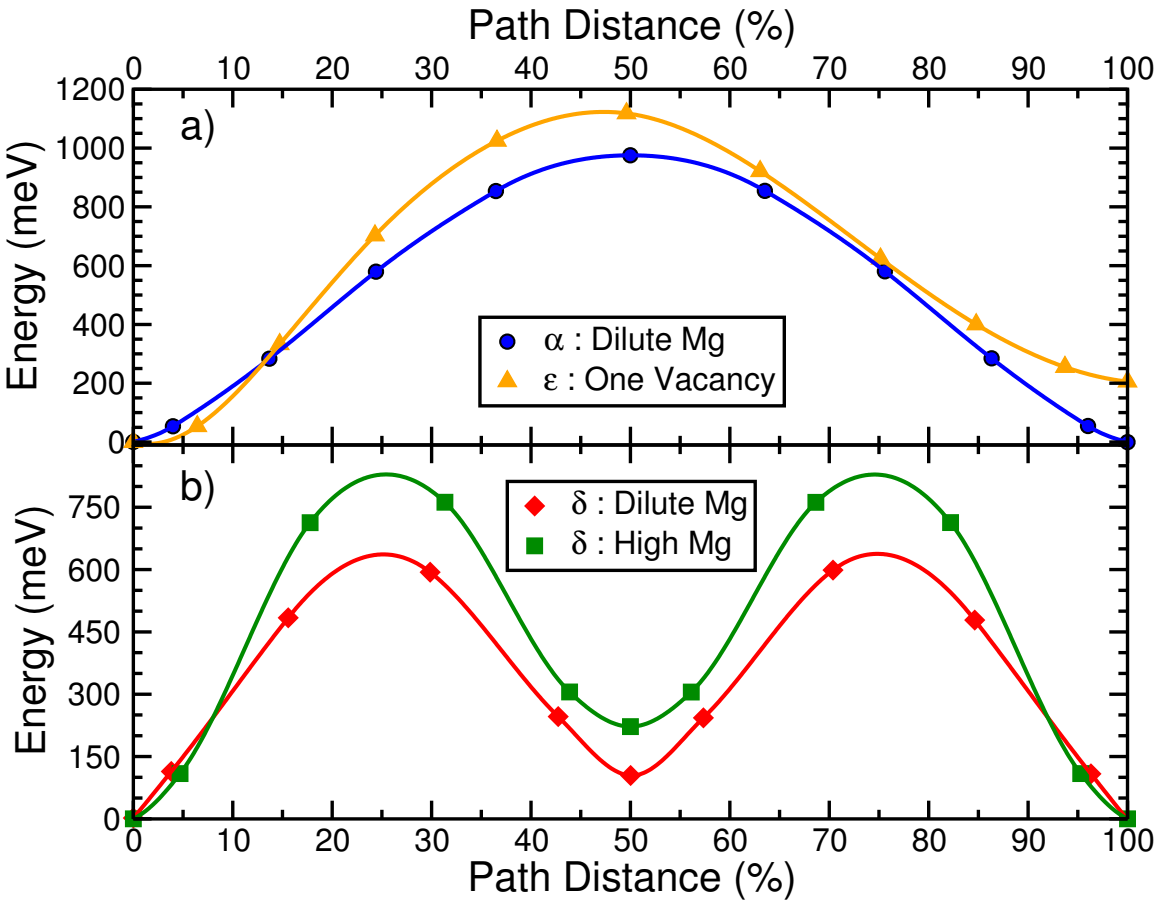

Figure 3-4: (Color online) (a) Activation barriers for Mg diffusion in select limiting cases in α-V_2O_5 and (b) for Mg diffusion in δ-V_2O_5 calculated through the NEB method.

tures.

3.3.3 Mg diffusion barriers in V_2O_5

To gain insight into the migration behavior of Mg in α and δ polymorphs, the calculated activation barriers using the NEB method are plotted in Figure 3-4. The migration energy is plotted along the diffusion path with the energies of the end points referenced to zero and the total path distance normalized to 100%. The diffusion paths in both α and δ polymorphs correspond to the shortest Mg hop along the a-direction as in Figure 3-1a and 3-1b respectively and perpendicular to the b-c plane in Figure 3-1c. The energy difference between the site with the highest energy

along the path (the activated state) and the end points is the migration barrier. A simple random walk model for diffusion would predict that an increase in the activation barrier of ~ 60 meV would cause a drop in diffusivity by one order of magnitude at 298 K.

Specifically, we have performed four sets of calculations: dilute Mg concentration ($x_{Mg} = 0.08$) in the α phase (blue dots on Figure 3-4a), high Mg concentration ($x_{Mg} = 0.44$) in the α phase (orange triangles), dilute Mg concentration ($x_{Mg} = 0.08$) in the δ phase (red diamonds on Figure 3-4b) and high Mg concentrations ($x_{Mg} = 0.92$) in the δ phase (green squares). Due to the mechanical instability of the α phase at high Mg concentrations, we performed NEB calculations in the ϵ phase. Because the ϵ phase has a specific Mg ordering, migration to an equivalent site requires two symmetrically equivalent hops. The path in the orange triangles of Figure 3-4a therefore only shows one half of the total path.

The data in Figure 3-4 illustrates that the barriers in the δ phase ($\sim 600 - 760$ meV) are consistently much lower than in the α-phase ($\sim 975 - 1120$ meV), with the respective migration energies adopting “valley" and “plateau" shapes. Upon addition of Mg the migration barriers in α and δ both increase. The differences in the magnitude of the migration barriers and the shape of the migration energies between the α and δ can be explained by considering the changes in the coordination environment of Mg along the diffusion path. For example, in the α phase, Mg migrates between adjacent 8-fold coordinated sites through a shared 3-fold coordinated site (activated state), a net 8→3→8 coordination change, while in the δ phase Mg migrates between adjacent 6-fold coordinated sites through two 3-fold coordinated sites separated by a metastable 5-fold coordinated “valley", a net 6→3→5→3→6 coordination change. Hence, the lower barriers of the δ phase compared to the α phase are likely due to the smaller coordination changes and the higher layer spacing in δ than α as seen in Figure 3-3. The indication of superior diffusivity of Mg in δ-V_2O_5 motivates investigating the intercalation properties of Mg in the δ phase further.

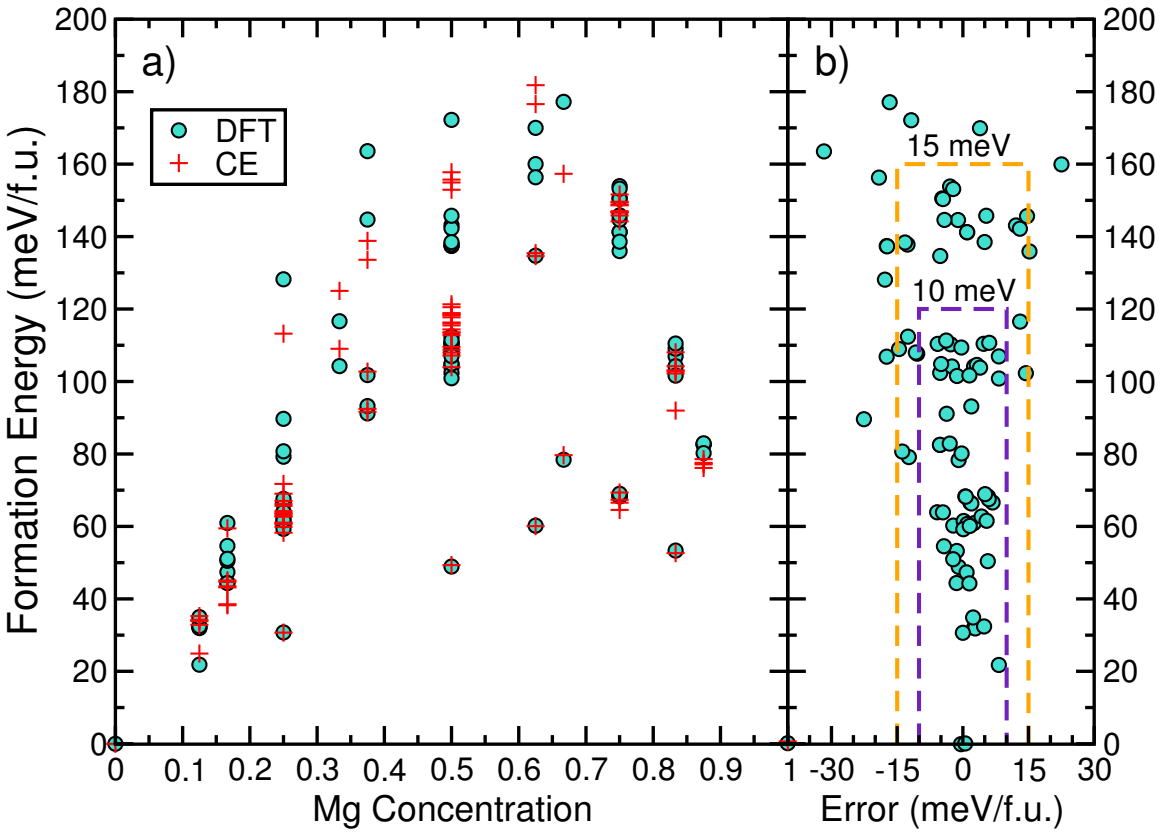

Figure 3-5: (Color online) (a) DFT and Cluster expansion predicted formation energies are plotted on the vertical scale with respect to different Mg concentrations on the horizontal scale. (b) The staircase plot indicates the errors in energies encountered for structures using the cluster expansion (horizontal scale) with respect to their respective distances from the hull (vertical scale).

3.3.4 Cluster expansion on Mg in δ-V_2O_5 and temperature-composition phase diagram

Consistent with the data in Figure 3-2a all Mg-Va arrangements have higher energy than the linear combination of δ-V_2O_5 and δ-MgV_2O_5, supporting phase separation on the δ lattice as illustrated in Figure 3-5a, where the zero on the energy scale is referenced to the DFT calculated end members of the δ phase. A total of 97 Mg-Va configurations, across Mg concentrations are used to construct the CE, which encompasses 13 clusters with a RMSE of $\sim$ 9 meV/f.u. The CEs Weighted Cross Validation (WCV) score of $\sim$ 12.25 meV/f.u. indicates a very good match with the current

input set and good predictive capability. In Figure 3-5b the staircase plot displays the error in predicting the formation energies of different Mg-Va configurations by the CE against their respective DFT formation energies. A good CE will have lower errors for configurations that are closer to the hull, i.e. shorter absolute distance from the ground state hull, and higher errors for configurations that are further away from the hull. The current CE displays errors below 10 meV/f.u. for most structures whose formation energies are smaller than 120 meV/f.u. Also, it can be seen in Figure 3-5b that the structures with the highest errors in the formation energy prediction normally have formation energies greater than 125 meV/f.u.

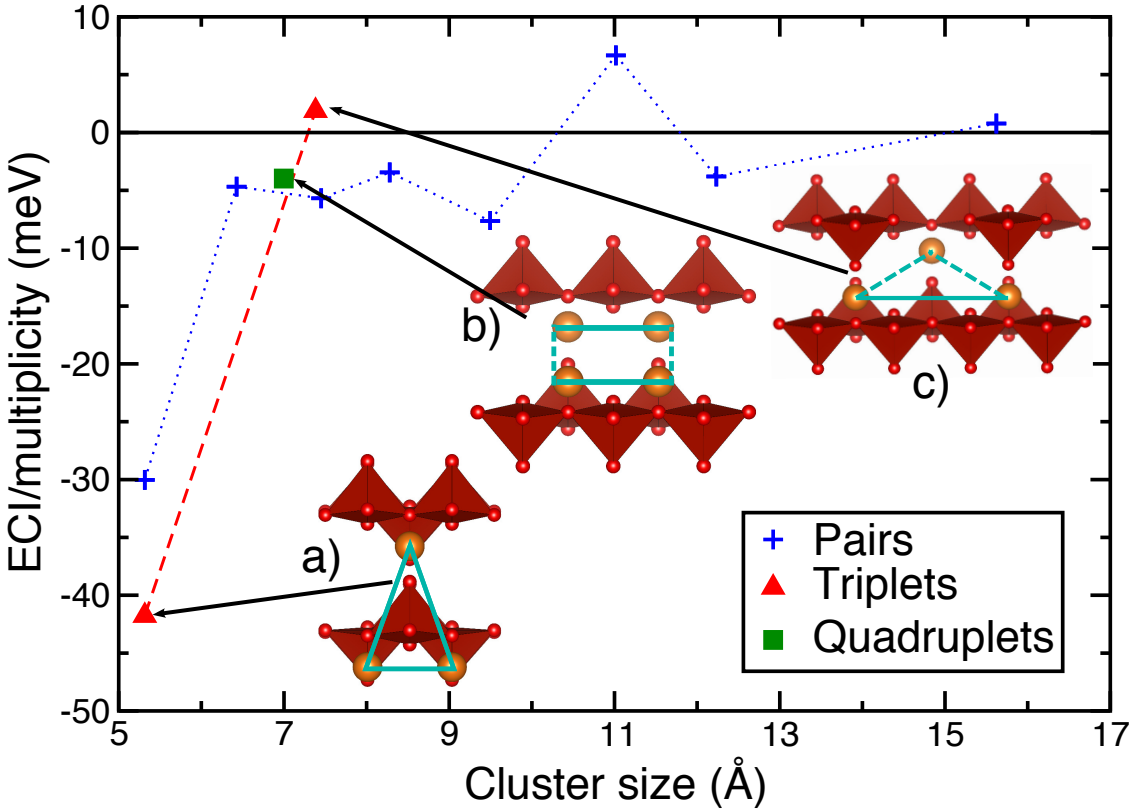

Figure 3-6: (Color online) ECI of the clusters vs. their respective cluster size are plotted. The insets (a) and (c) display the triplet terms and inset (b) shows the quadruplet term with the solid blue lines indicating in-plane interactions and the dotted blue lines indicating out-of-plane interactions. All insets are displayed on the *a*-*b* plane.

The ECIs for the clusters in the CE, normalized by their multiplicity and plotted

against their respective cluster sizes, are displayed in Figure 3-6. The size of a given cluster is indicated by its longest dimension; for example, in a triplet the cluster size is given by its longest pair. Negative pair terms indicate 'attraction' (i.e. Mg-Mg and Va-Va pairs are favored) and positive pair terms indicate 'repulsion' (i.e. Mg-Va pairs are favored). The figures inside the graph show the triplets and the quadruplet used in the current CE with the solid lines indicating interactions in the a-b plane and dotted lines indicating interactions out of plane (b is the direction perpendicular to the V_2O_5 layers). The orange circles indicate Mg atoms. The data in Figure 3-6 illustrates that the most dominant (highest absolute ECI value) cluster of the CE is a triplet where Mg ions are along the a-b plane (as shown in Figure 3-1b). The most dominant pair term is attractive and is the longest pair of the most dominant triplet. The negative sign of the dominant triplet and the dominant pair terms implies that there are 2 possible configurations containing Mg which are stabilized: *i*) all three sites are occupied by Mg, and *ii*) only one of the three sites is occupied by Mg, consistent with the sign convention adopted in the CE ($\sigma_i = 1$ for occupied Mg site and $\sigma_i = -1$ for a vacancy).

The temperature-concentration phase diagram for Mg intercalation into δ-V_2O_5 is displayed in Figure 3-7. The black line traces the phase boundary between the single and two phase regions, obtained from Monte Carlo simulations with the numerical hysteresis removed by free energy integration. Consistent with the δ hull in Figure 3-2a, the Mg-V_2O_5 is a phase separating system at room temperature with extremely low solubilities at either ends ($< 1\%$). Note that only the solid δ-phase is considered in this phase diagram. In reality, the high temperature part of the phase diagram would probably form a eutectic since pure V_2O_5 melts at ~ 954 K.[77]

3.4 Discussion

In this work, we have performed a first-principles investigation of Mg intercalation into orthorhombic V_2O_5. Specifically, we investigated the α and δ polymorphs using DFT calculations, evaluating their respective ground state hulls, subsequent volt-

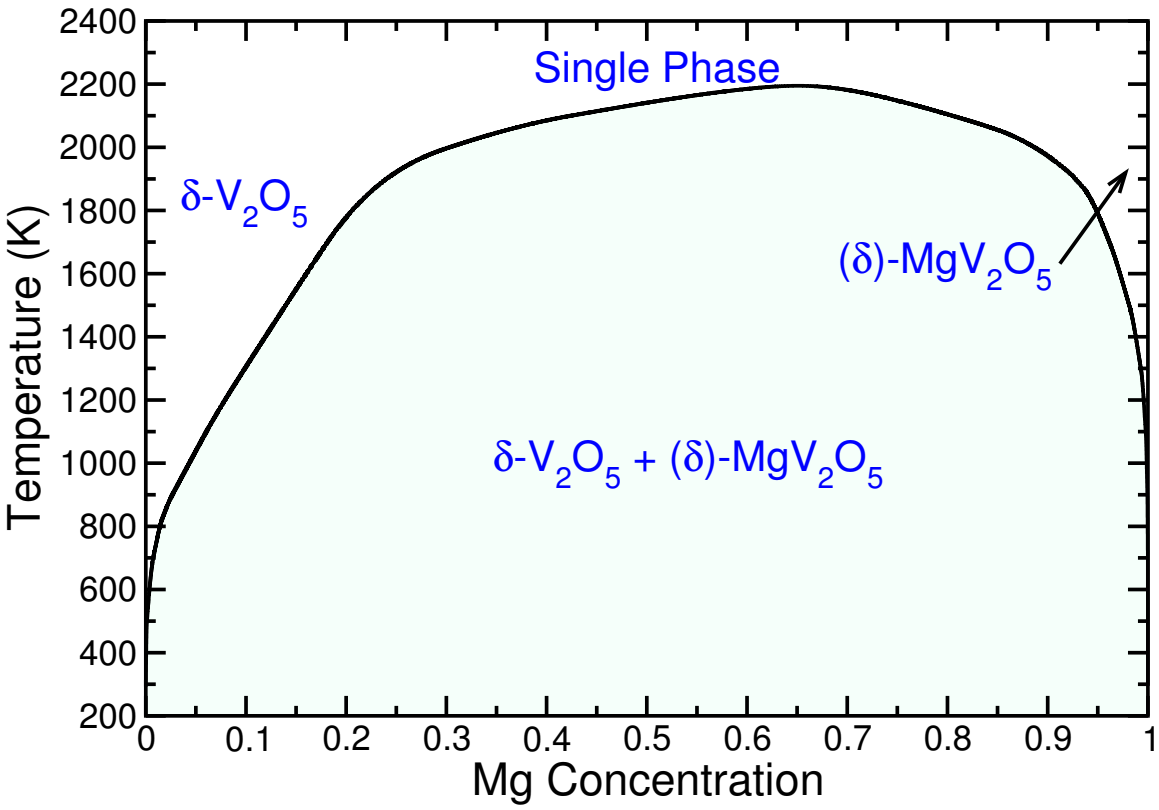

Figure 3-7: (Color online) Mg-V_2O_5 intercalation phase diagram for the δ phase. The black line indicates the phase boundary between the single and two phase regions obtained from Monte Carlo simulations of the CE.

age curves, and their Mg migration barriers. For the δ polymorph, we constructed the composition-temperature phase diagram using the CE and GMC approach. The theoretical data we have collected sheds light not only on the existing experiments intercalating Mg into V_2O_5, but also provides a practical strategy to improve performance.

From a thorough comparison of the experimental data available in the literature to the calculations performed in this work, we conclude that by synthesizing V_2O_5 and intercalating Mg (i.e. beginning in the charged state), the structure remains in the α phase. For example, in the experimental voltage curves[2, 167, 64, 153, 254] the characteristic plateau followed by a drop at $x_{Mg} \sim 0.5$ compares well with the computed voltage curve for the α phase (Figure 3-2b) which shows a similar voltage drop corresponding to the ϵ ordering while δ-V_2O_5 would show no such drop. In X-ray

diffraction (XRD) data in the literature on magnesiated V_2O_5, no additional peaks which would indicate the formation of the δ phase have been observed.[167, 64, 155] Also, the observed increase in the layer spacing[64] is consistent with the computed predictions of layer expansion in the α phase until $x_{Mg} = 0.5$ (Figure 3-3) rather than the δ phase which has a minimal increase in layer spacing from $x_{Mg} = 0$ to $x_{Mg} = 1$. The migration barriers for Mg in the α phase are high ($\sim$ 975 meV as seen in Figure 3-4a), and indeed, reversible Mg insertion can be reliably achieved only when the diffusion length is greatly reduced (i.e. in thin films and nano-powders) and at very low rates (i.e. ~ 0.5 μA/cm^2 by Gershinsky *et al.*[64]). Magnesiation past the ϵ-phase ($x_{Mg} \sim 0.5$) is expected to be difficult as the potential drops thereby reducing the driving force for Mg insertion, and the Mg migration barrier increases with Mg concentration in α (Figure 3-4a). While the driving force to transform from $\alpha \rightarrow \delta$ is small up to $x_{Mg} \sim 0.5$ (as in Figure 3-2a), it steeply increases thereafter, leading us to speculate that further magnesiation would lead to the formation of a fully magnesiated δ-MgV_2O_5 on the surface.

Our thinking on the magnesiation process of V_2O_5 is summarized in Figure 3-8. The ground state hull in Figure 3-2a, suggests that under equilibrium conditions the Mg insertion mechanism is through a two-phase reaction, by nucleation and growth of magnesiated δ phase from supersaturated α, rather than through the metastable formation of the ϵ phase. These two reaction pathways (cycling between 0 and 50% state of charge) are illustrated schematically in Figure 3-8, with the orange squares representing Mg atoms. If nucleation and growth of the fully magnesiated δ phase (i.e. $x_{Mg} = 1$) were to occur, there would be no inherent upper limit to magnesium insertion up to $x_{Mg} \sim 1$. However, the metastable insertion path of Mg in the α phase, which once fully converted to ϵ phase remains at $x_{Mg} \sim 0.5$, is more consistent with experiments. The reason the system follows the metastable insertion path through α is that the equilibrium path (α-V_2O_5 to δ-MgV_2O_5), requires structural rearrangement of the host structure through the translation of V_2O_5 layers, which may kinetically be difficult once some Mg is inserted and more strongly bonds the layers. Also, a nucleation-growth process involves high interfacial energies and may lead to low

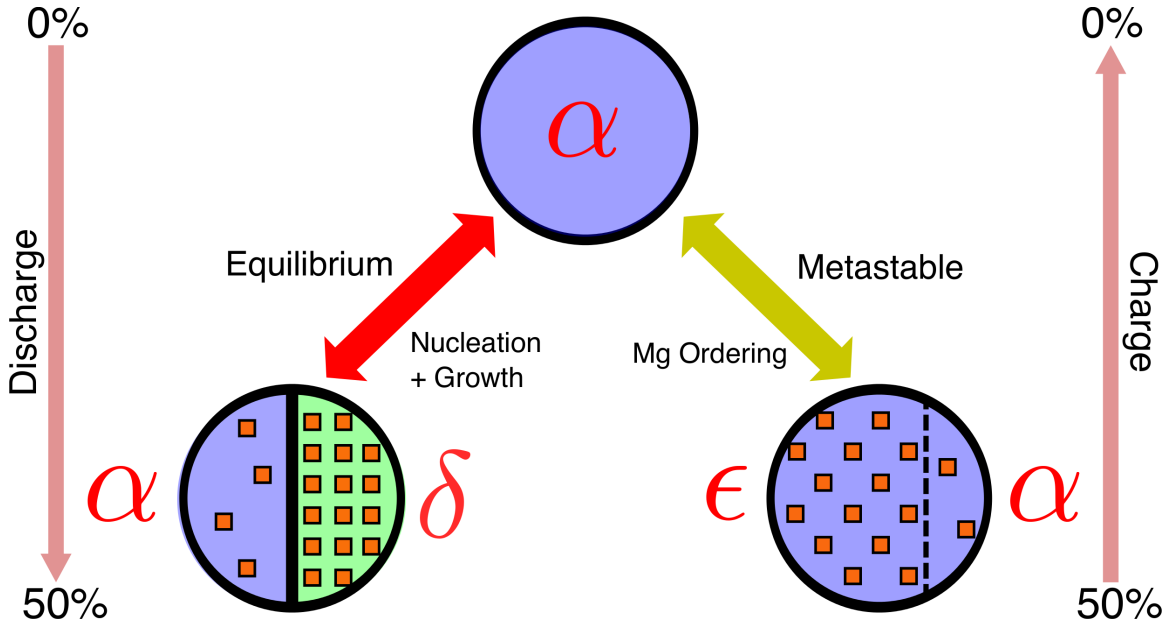

Figure 3-8: (Color online) Possible intercalation pathways for Mg in V_2O_5 up to $x_{Mg} = 0.5$. The left half corresponds to the equilibrium case where the δ phase nucleates and grows in a supersaturated α phase, with a well-defined interface between the two phases and the right half corresponds to the Mg atoms ordering into the metastable ϵ phase and the lack of a well defined interface in this case since ϵ and α have the same V_2O_5 layer stacking.

rates. A similar metastable solid solution transformation has been predicted and documented for other thermodynamic phase separating systems.[131, 92, 62]

While our calculations, supported by experimental data, suggest that the host V_2O_5 structure remains in the α phase upon Mg intercalation, they also suggest an approach to substantially improve the electrochemical properties by cycling Mg beginning in the δ phase. Mg in δ-V_2O_5 not only possesses a higher average voltage compared to α ($\sim$ 120 mV higher as seen in Figure 3-2b), but also a significantly better mobility ($\sim 600 - 760$ meV compared to $\sim 975 - 1120$ meV) which accounts for approximately 5 orders of magnitude improvement in the diffusivity at room temperature (Figure 3-4). Prior computations have reported higher migration barriers in the δ phase compared to the α phase in the charged limit, in contrast to our calculations in Figure 3-4,[258] which we attribute to the authors allowing only Mg and nearby oxygen ions to relax in their NEB calculations. In order to cycle Mg in the δ

phase, V_2O_5 must be prepared in the fully discharged state (δ-$Mg_1V_2O_5$), where the δ phase is thermodynamically stable. Fortunately, the synthesis of δ-MgV_2O_5 is well established in the literature.[137]

Since at intermediate Mg concentrations the equilibrium state is a coexistence between the demagnesiated α-phase and the fully magnesiated δ-phase, the δ phase must remain metastable over a wide Mg concentration range to ensure higher capacities. If the δ-phase is not metastable, transformation to the α-phase will take place. We speculate that the possibility of δ phase metastability is likely, given that nucleation and growth of the α phase requires restructuring of the host lattice, and the absence of mechanically unstable Mg configurations (even at $x_{Mg} = 0$) in δ (Figure 3-2a) in our calculations. Also, an applied (over)underpotential is required to access a metastable (de)insertion path, which can be quantified by the difference between the metastable and equilibrium voltage curves in Figure 3-2b. For example, to avoid the equilibrium path, an applied underpotential of ~ 800 mV is required to insert Mg and retain the α-V_2O_5 structure, but only ~ 400 mV is required to remove Mg and retain the δ-MgV_2O_5 structure, which supports the possibility of a metastable δ phase.

Assuming the δ-MgV_2O_5 phase remains metastable, the temperature-composition phase diagram computed for Mg in δ-V_2O_5 using the CE (Figure 3-7) indicates a phase separating behavior with negligible solubility at both end members at room temperature. By investigating the dominant interactions (ECIs) that contribute to the CE, we gain some insight into the possible intercalation mechanism. The dominant Mg-Va interactions, specifically the triplet and the nearest interlayer pair as seen in Figure 3-6, are entirely contained in the a-b plane, which indicates that the δ-V_2O_5 host lattice will contain fully magnesiated and fully demagnesiated domains separated by an interface along an a-b plane. Hence, Mg insertion into the 3D δ-V_2O_5 structure can be effectively described by considering the interactions in each 2D a-b plane.

Figure 3-9 illustrates the interplay between these dominant pair and triplet terms which results in the specific sequence of Mg-Va configurations in terms of their relative stability. The orange circles indicate Mg atoms, the hollow circles the vacancies, and

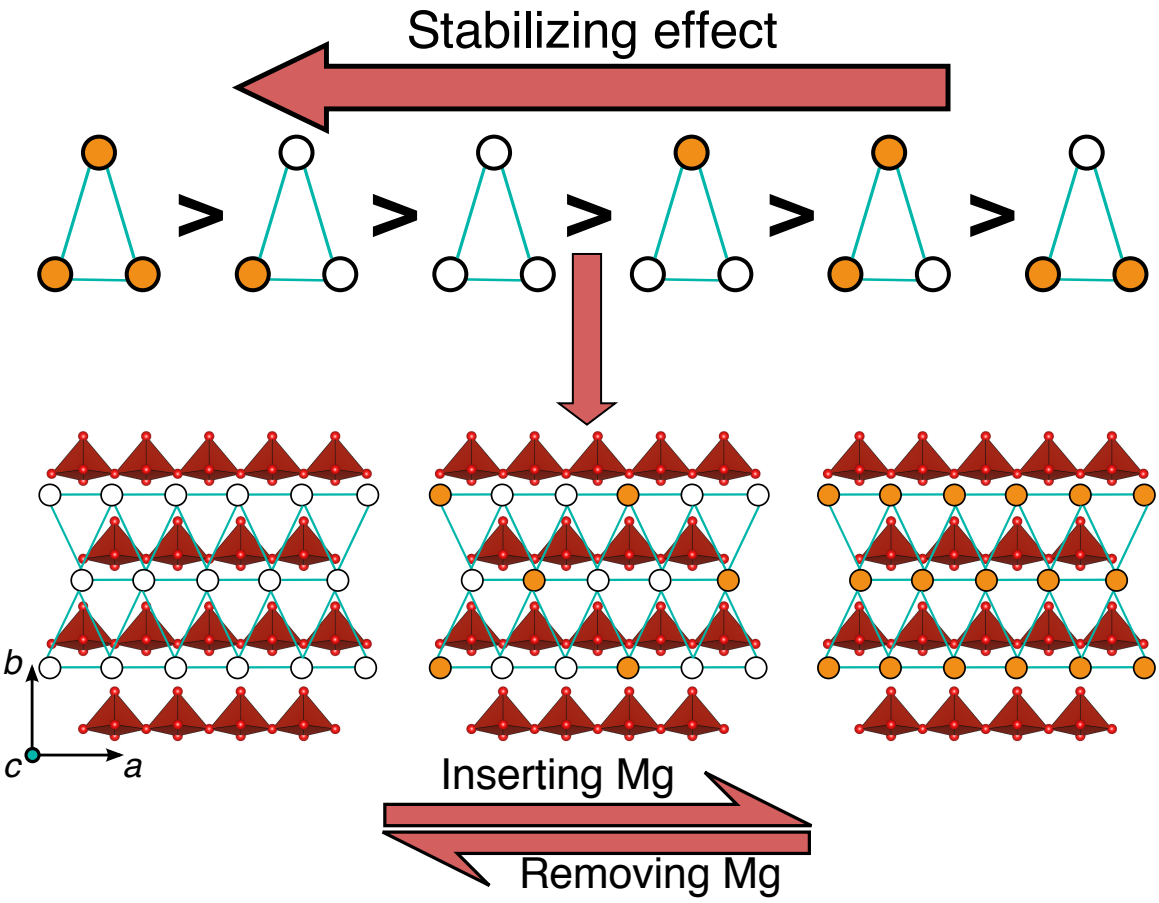

Figure 3-9: (Color online) Interplay between the dominant pair and triplet terms of the CE stabilizing different Mg-Va arrangements.

all insets are viewed in the a-b plane. Given the sign convention used in the CE ($\sigma_i = 1$ for Mg and $\sigma_i = -1$ for Va) and the negative sign of the dominant pair and triplet, the formation of Mg-Mg and Va-Va pairs are favored while triplets containing one or three Mg atoms are favored. Thus, a fully occupied triplet is most stable due to favorable contributions from both the triplet (~ -40 meV) and the two longest pair terms (~ -60 meV in total) resulting in a net stabilization of ~ -100 meV, while the triplet with two Mg atoms forming the shortest pair and a vacancy at the apex is least stable due to unfavorable contributions from both the pairs and the triplet resulting in a destabilizing contribution of $\sim +100$ meV.

The bottom half of Figure 3-9 illustrates a sample sequence in which Mg atoms fill up sites on a given a-b plane. The fully magnesiated structure (right inset) is

highly stabilized due to the presence of fully filled triplets (~ -100 meV/triplet) while the fully demagnesiated structure (right inset) is stabilized to a lesser extent (~ -20 meV/triplet). At an intermediate composition, the Mg atoms will arrange themselves in such a way that the number of fully filled and one-third filled triplets (~ -40 meV/triplet, depicted in the centre inset) is maximized. Since one-third filled triplets stabilize a structure more than triplets containing two Mg atoms, non-phase separated configurations at low Mg concentrations ($x_{Mg} < 0.33$) will be more stabilized than those at high Mg concentrations ($x_{Mg} > 0.66$), as indicated by the higher solubilities at lower Mg concentrations in the phase diagram shown in Figure 3-7 at high temperatures.

Since the occurrence of fully magnesiated and demagnesiated *a*-*b* planes is highly stabilized, the intercalation of Mg in the 3D δ-V_2O_5 structure will then progress via propagation of fully magnesiated *a*-*b* planes along the *c*-axis. With additional applied overpotential, not only can the δ phase be retained, but also a non-equilibrium solid solution intercalation pathway in δ can be thermodynamically accessible, leading to further improved kinetics.[131] An estimate for the additional overpotential required can be computed by considering the lowest energy structure at $x_{Mg} = 0.83$ in Figure 3-5a, whose formation energy is 53 meV/Mg, resulting in an approximate additional overpotential requirement of ~ 320 mV. Therefore, the net overpotential required to access a solid-solution transformation path entirely in the δ phase upon charge is ~ 720 mV, which is comparable to the underpotential applied (~ 800 mV) to remain in the metastable α phase upon discharge. Hence, we suggest that the electrochemical performance of Mg in V_2O_5 can be improved by beginning cycling in the discharged state, δ-MgV_2O_5, with the prospect of improved voltage, capacity, and kinetics.

3.5 Conclusions

In this work, we have used first-principles calculations to perform an in-depth investigation of Mg intercalation in the orthorhombic α and δ polymorphs of V_2O_5 to evaluate their suitability as high energy density cathode materials for Mg-ion

batteries. Specifically, we computed the ground state hulls and the activation energies for Mg migration in both polymorphs. For the δ polymorph we calculated the temperature-composition phase diagram. The equilibrium state of $Mg_xV_2O_5$ ($0 < x_{Mg} < 1$) is determined to be a two-phase coexistence between the fully magnesiated δ-MgV_2O_5 and fully demagnesiated α-V_2O_5 phases. NEB calculations indicate that room-temperature Mg migration is several orders of magnitude faster in the δ phase ($E_m \sim 600 - 760$ meV) than in the α phase ($E_m \sim 975 - 1120$ meV).

By comparing the calculated voltage curves and changes in the layer spacing with intercalation with available experimental data on Mg insertion in V_2O_5, we conclude that the α phase likely remains metastable when Mg is initially inserted into fully demagnesiated α-V_2O_5. Although the computed α phase migration barriers indicate poor Mg mobility, consistent with reversible Mg intercalation being achievable exclusively at very low rates and in small particles, α-V_2O_5 is still one of only three known cathode materials where reversible cycling of Mg is possible at all (along with chevrel Mo_6S_8 and layered MoO_3).

Therefore, our finding that the δ-V_2O_5 polymorph displays vastly superior Mg mobility as well as a modest increase in voltage compared to the α phase is especially promising, assuming that the δ-V_2O_5 host structure can remain stable or metastable across a wide Mg concentration range. Fortunately, the δ polymorph is thermodynamically stable in the fully discharged state and its synthesis procedure well known.

From our first-principles calculations of the formation energies of several Mg orderings in the δ-V_2O_5 host structure and the resulting computed temperature-composition phase diagram, we have also gained insight into the possible mechanism of Mg intercalation within the δ host structure. At room temperature, Mg displays strong phase-separating behavior with negligible solid-solution in the end-member phases and favors the formation of either completely full or empty a-b planes, which are perpendicular to the layers formed by the connecting VO_5 pyramids, suggesting an intercalation mechanism based on nucleation and growth through the propagation of an a-b interface along the c-axis.

Chapter 4

First-Principles Evaluation of Multi-valent cation insertion into Orthorhombic V_2O_5

4.1 Introduction

A promising and realistic strategy to improve the energy density beyond the capability of current Li-ion battery technology is to transition to a battery architecture based on shuttling multi-valent (MV) ions (e.g. Mg^{2+} or Ca^{2+}) between an intercalation cathode host and MV metal anode.[152, 11] Specifically, improvement in the volumetric energy density arises from the combination of using a multi-valent metal as the anode as opposed to an insertion structure (e.g. $\sim$ 3833 mAh/cm^3 volumetric capacity for Mg metal compared to $\sim$ 800 mAh/cm^3 for graphite), and storing more charge per ion in the cathode.[204, 252]

One of the major bottlenecks preventing the development of MV battery technology, however, is the poor electrochemical performance of potential MV cathode materials, thought to originate predominantly from poor MV ion mobility in the intercalation host structure.[252, 64, 2] Moreover, the simultaneous challenge of developing functioning MV anodes and electrolytes compatible with candidate cathode

materials has limited the ability to experimentally isolate and evaluate cathode electrochemical performance,[142] and as such there is a general dearth of reliable data on MV ion intercalation in the literature to date to guide the ongoing search for new MV cathode materials with improved performance.

Nevertheless, reversible electrochemical Mg^{2+} intercalation has been successfully demonstrated in a handful of cathode hosts, namely Chevrel Mo_6S_8 ($\sim$ 135 mAh/g capacity at $\sim 1.0 - 1.3$ V vs. Mg metal),[11] as well as layered V_2O_5 ($\sim$ 150 mAh/g at $\sim 2.3 - 2.6$ V)[64, 2] and MoO_3 ($\sim$ 220 mAh/g at $\sim 1.7 - 2.8$ V).[64] The orthorhombic V_2O_5 structure is especially interesting because it has also demonstrated the ability to reversibly intercalate Ca^{2+} and Y^{3+} in addition to Mg^{2+} ions.[2] First-principles calculations (described in detail in Sections 2.1, 2.2, and 2.4) have proven to be an accurate and effective method to systematically assess the electrochemical properties of Li-ion batteries,[91, 228, 135] and have also been used to study the process of ion intercalation in layered materials, such as graphite[253] and V_2O_5.[190, 239, 258, 35] In this work, we have performed a systematic first principles study of MV ion intercalation in the orthorhombic $\alpha-$ and $\delta-V_2O_5$ polymorphs by evaluating the structural change, voltage, thermodynamic stability, and intercalant mobility for Li^+, Mg^{2+}, Zn^{2+}, Ca^{2+}, and Al^{3+} insertion and comparing to data in the literature when available.

4.2 Structure

The crystal structure and intercalation sites of the $\alpha-$ and $\delta-V_2O_5$ polymorphs[46, 137, 53, 15] are shown in Fig. 4-1. Perpendicular to the b-axis (i.e. in the $a-c$ plane), the orthorhombic V_2O_5 structure consists of layers of alternating corner− and edge−sharing VO_5 pyramids (shown in red), each consisting of 4 V−O bonds that form the base and one short V=O bond that forms the apex. The intercalation sites (yellow spheres) are situated in between the layers, and assuming no limitation in the number of redox centers, the theoretical gravimetric capacities for AV_2O_5 where A = Li, Mg, Zn, Ca and Al are 142, 260, 217, 242 and 385 mAh/g, respectively.

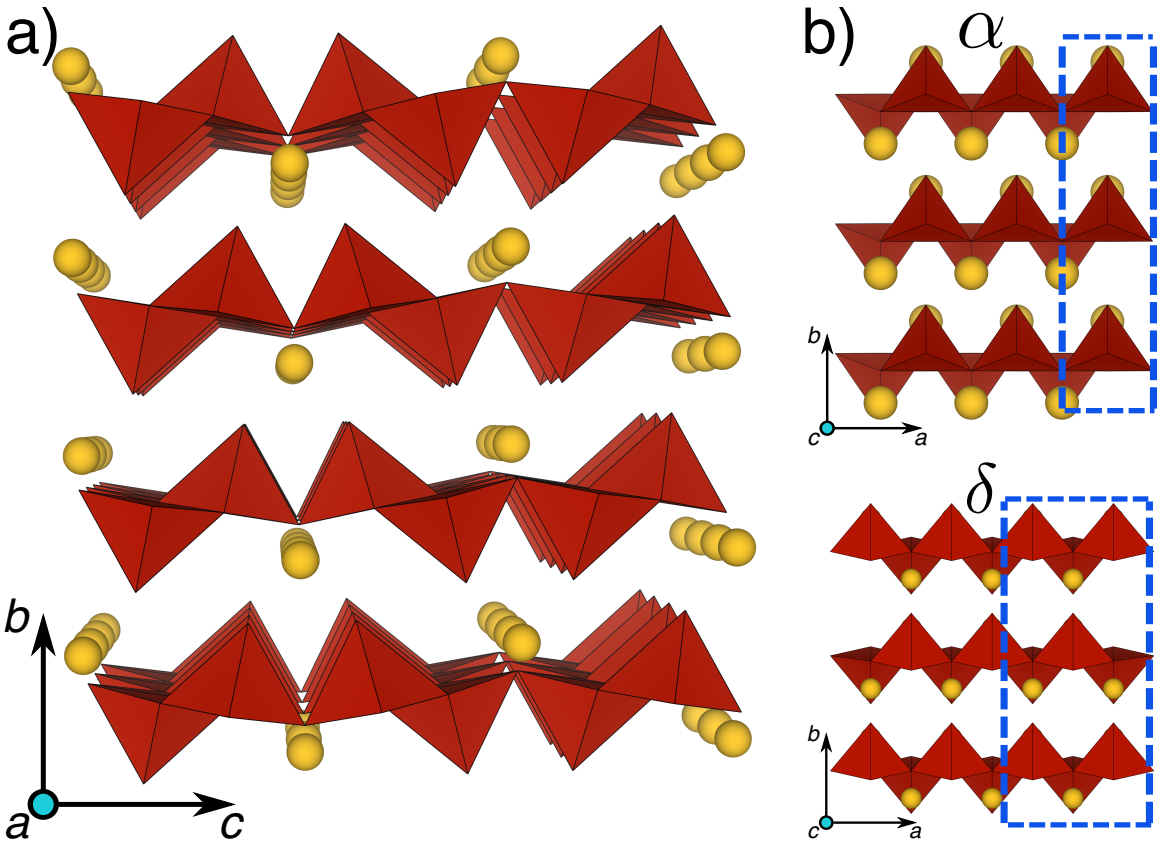

Figure 4-1: a) The V_2O_5 structure of both the α and δ polymorphs on the $b-c$ plane with the yellow spheres indicating the intercalant sites while b) shows the α and δ polymorphs on the $a-b$ plane. As indicated by the dashed blue regions, both the polymorphs differ by a change in the stacking of the V_2O_5 layers.

Structurally, the main difference between the α and δ polymorphs is a shift in the layer stacking, indicated by the dashed blue lines in Fig. 4-1b, with alternate V_2O_5 layers displaced in the a-direction by half a lattice spacing, accompanied by a change in the interlayer distance and the anion coordination environment of the intercalation sites.[46] While 8 oxygen atoms coordinate the intercalant ion in α (for Mg, there are two Mg$-$O bonds with length $\sim$ 2.11 Å, two with $\sim$ 2.39 Å, and four with $\sim$ 2.46 Å, respectively), "4+2" oxygen atoms coordinate the intercalant in δ (for Mg, there are four Mg-O bonds with length $\sim$ 2.05 $-$ 2.07 Å, and two with $\sim$ 2.33 Å).

4.3 Results and Discussion

In Fig. 4-2a, the interlayer spacings in the α and δ polymorphs (filled and hollow bars, respectively) are shown for empty V_2O_5 and intercalated AV_2O_5, where A = Li, Mg, Zn, Ca, and Al. To better capture the increased effect of van der Waals effects in the deintercalated limit, the interlayer spacings for empty V_2O_5 (4.46 Å for α; 5.03 Å for δ) are calculated using the vdW-DF2 functional[112, 101] rather than standard DFT as the latter significantly overestimates this spacing (4.75 Å for α; 5.27 Å for δ) compared to experiment (4.37 Å for α).[190, 35, 53] As detailed in the appendix, Al^{3+} intercalation in the $\alpha-V_2O_5$ structure is found to be mechanically unstable and relaxes to the δ polymorph in our calculations, and we therefore remove it from further consideration in this study.

At the same intercalant composition, the δ structures consistently have larger layer spacings than α, $\sim 3-5$ % larger for Li, Mg, and Zn and $\sim 10-12$ % for Ca and empty V_2O_5. With the exception of Ca intercalation, which increases the layer spacing by more than 10 % in both polymorphs, the change in the layer spacing is much smaller in δ than α, less than 2 % for Li^+, Mg^{2+}, Zn^{2+}, and Al^{3+} intercalation in $\delta-V_2O_5$ compared to $\sim 9-14$ % for Li^+, Mg^{2+}, Zn^{2+}, and Ca^{2+} in $\alpha-V_2O_5$. The behavior for Ca^{2+} is consistent with intercalation in the spinel system,[126] where the volume change is also much larger than for Li^+, Mg^{2+}, Zn^{2+}, and Al^{3+} intercalation, and in general may be attributed to the larger ionic radius of Ca^{2+} in comparison to the other ions.[201] Al^{3+} intercalation in $\delta-V_2O_5$, in contrast to the other ions considered, is accompanied by a contraction of the layers, which is consistent with its small ionic radius and higher positive charge density that strengthens the attraction with nearby oxygen ions.

The average voltages of the compounds computed using the method of Aydinol *et al.*[13] are plotted in Fig. 4-2b and are referenced to the potential of the bulk metal of the corresponding intercalating ion (i.e., Li metal for Li^+ intercalation, etc.). The average voltages computed for Li, Mg, and Ca intercalation compare very well to available experimental data: $\sim 3.2-3.4$ V for Li measured by Delmas *et al.*,[46]

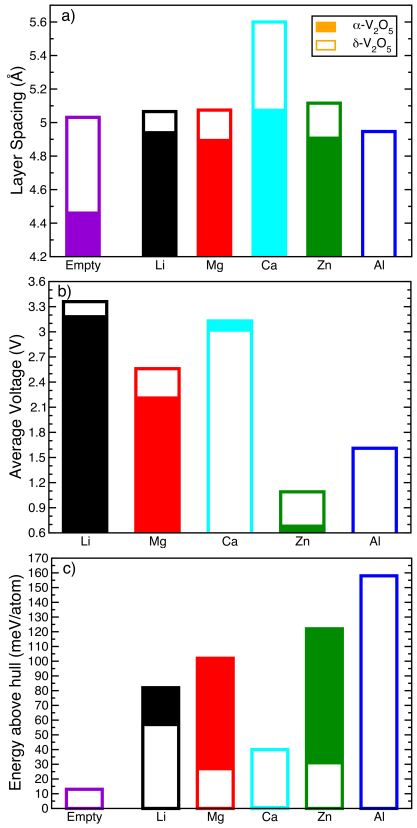

Figure 4-2: a) Plots the layer spacing values for the empty and intercalated versions of AV_2O_5 (A = Li, Mg, Ca, Zn and Al) for both the α and δ polymorphs. b) Displays the calculated average voltage values for the intercalation of the different ions and c) shows the energy above hull, which quantifies the stability of a structure, for the empty and intercalated versions of α and δ. The filled regions in all the graphs correspond to the α structure while the hollow regions correspond to the δ structure. Note that the energy above hull for $\alpha-CaV_2O_5$ is 0 meV/atom, implying that it is a ground state configuration in the Ca-V-O system.

$\sim$ 2.2 $-$ 2.4 V for Mg measured by Gershinsky *et al.*,[64] and $\sim$ 2.4 $-$ 3.1 V for Ca measured by Amatucci *et al.*[2] In general, the Li polymorphs have the highest voltage, followed by Ca, Mg, Al, and Zn, which reflects both the same order and approximately the same potential difference indicated by the electrochemical series (-3.04 V vs. SHE for Li, -2.86 V for Ca, -2.37 V for Mg, -1.66 V for Al, and -0.76 V for Zn). In comparison, the voltage difference between the V_2O_5 polymorphs is much smaller for a given intercalation chemistry. For Li, Mg, and Zn the insertion voltage is higher in δ (3.36 V, 2.56 V, and 1.09 V, respectively) than in α (3.18 V,

2.21 V, and 0.68 V), unlike for Ca where α is higher (3.13 V for α; 3.02 V for δ).

Fig. 4-2c displays the energy above the convex ground state energy hull (E^hull) of the deintercalated and intercalated V_2O_5 polymorphs with respect to the intercalant-V-O ternary phase diagram. The ternary ground state hulls were determined from the available calculated compounds in the Materials Project database.[88] A predicted thermodynamically stable structure will have a E^hull value of 0 meV/atom while higher (more positive) E^hull values indicate greater instability, which may be reflected in experimental difficulties in synthesis or decomposition during battery operation. Note that the E^hull values calculated here reflect the ground state (i.e. 0 K), and entropy contributions, which scale with k_BT, can stabilize certain structures at higher temperatures.

In the deintercalated limit, V_2O_5 is thermodynamically stable in the α phase, but δ is only $\sim$ 13 meV/atom higher in energy, indicating the possibility of metastability at room temperature. For Li intercalation, the α and δ structures are 82 meV/atom and 57 meV/atom more unstable than the ground state orthorhombic $\gamma-LiV_2O_5$ structure, which has a different orientation of the VO_5 pyramids[46] along the c-direction shown in Fig 4-1a, but the δ structure can remain metastable and has shown to be reversibly cycled electrochemically.[46] $\delta-MgV_2O_5$, which has been synthesized experimentally,[137] is only $\sim$ 27 meV/atom more unstable (compared to $\sim$ 102 meV/atom for α) than the thermodynamic ground state, a two-phase equilibrium consisting of $MgVO_3$ and VO_2. Similarly δ-ZnV_2O_5 is only $\sim$ 31 meV/atom more unstable than the ground state (ZnO and VO_2), indicating that a metastable synthesis comparable to the Mg system may be possible. As Al intercalated α-V_2O_5 displays mechanical instability in our calculations, when relaxed its energy is not defined, but the Al intercalated δ-phase is $\sim$ 158 meV/atom unstable compared to the ground state ternary equilibrium of Al_2O_3, VO_2 and V_3O_5. With the exception of $\alpha-CaV_2O_5$, which is the ground state in the intercalated Ca-V_2O_5 system, the δ structures tend to be more stable than α in the discharged state (by 25 meV/atom for Li; 75 meV/ atom for Mg; and 91 meV/atom for Zn), and accordingly the insertion voltages for δ are higher than α for Li, Mg, and Zn insertion but lower for Ca

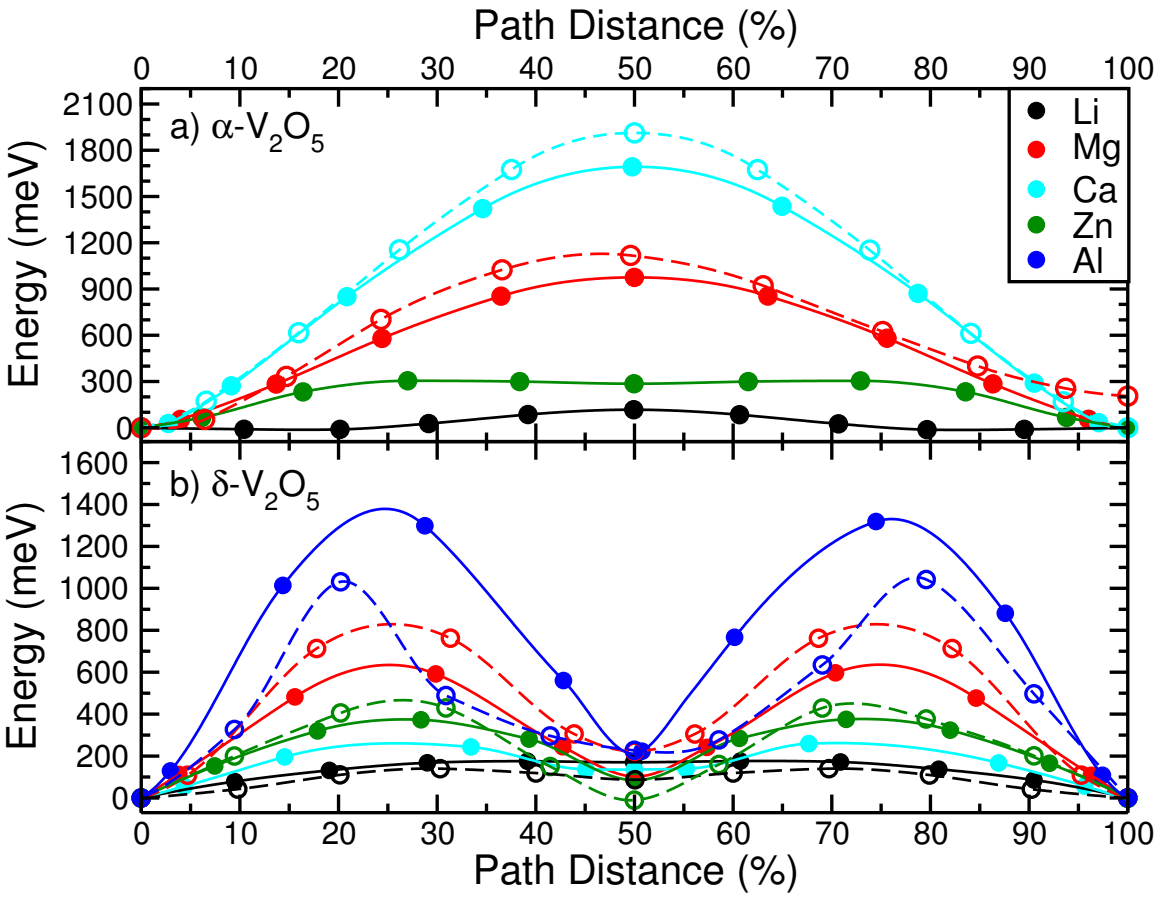

Figure 4-3: The activation barriers for the diffusion of the different intercalating ions in the α and δ polymorphs are plotted in a) and b) respectively. The solid lines correspond to the empty lattice limit (charged state) while the hollow lines correspond to the full lattice limit (discharged state).

insertion, as observed in Fig 4-2b. Given that the intercalant sites in α and δ are coordinated by 8 and "4+2" oxygen atoms respectively, the stability of the discharged δ-V_2O_5 structures for Li, Mg and Zn, and α-V_2O_5 for Ca align well with the preferred coordination environment of the respective ions, as tabulated by Brown.[25] Hence for intercalant ions that prefer a lower coordination number (i.e., coordinated by a maximum of 6 neighboring atoms), an $\alpha \rightarrow \delta$ transition upon insertion in V_2O_5 is likely.

Fig. 4-3 displays the migration energies for intercalant diffusion along the a-direction in the α (Fig. 4-3a) and δ (Fig. 4-3b) polymorphs plotted against the normalized path distance calculated with the Nudged Elastic Band method.[202] The solid

lines correspond to migration energies obtained in the empty lattice limit (charged state), and the dashed lines correspond to the fully intercalated limit (discharged state). As elaborated upon in the appendix, converging the migration energies in structures that exhibit a high degree of thermodynamic instability may not be possible, as was the case for Li, Mg, and Zn in the intercalated $\alpha-V_2O_5$ structure, and for Ca in the intercalated $\delta-V_2O_5$ structure. In lieu of determining the Mg migration barrier in the fully discharged $\alpha-V_2O_5$ structure, we have computed the energy for Mg migration in a half intercalated structure with a specific ordering of Mg ions, referred to as the "ϵ" phase, which has also been observed in the Li-V_2O_5 system.[46]

In Fig 4-3, the maximum energy difference encountered along the diffusion path defines the migration barrier (E_m), which provides an approximate estimate of the ionic diffusivity. As a guide, at room temperature, $E_m \sim 525$ meV corresponds to a diffusivity of $\sim 10^{-12}$ cm^2s^{-1}, and a 60 meV increase (decrease) in the migration energy corresponds to an order of magnitude decrease (increase) in diffusivity. Due to stronger interactions between a multivalent intercalant and the surrounding anion environment, the migration barriers within the same host structure, for example Al^{3+}, are generally higher than the divalent ion barriers (Mg^{2+}, Zn^{2+}, Ca^{2+}), which are generally higher than the barriers for Li^+. For the divalent intercalants, the trend in the migration barriers is Ca^{2+} ($\sim$ 1700$-$1900 meV) $>$ Mg^{2+} ($\sim$ 975$-$1100 meV) $>$ Zn^{2+} ($\sim$ 305 meV) in the α-phase, but Mg^{2+} ($\sim$ 600$-$800 meV) $>$ Zn^{2+} ($\sim$ 375$-$425 meV) $>$ Ca^{2+} ($\sim$ 200 meV) in the δ phase. The energy above the hull (Fig 4-2c) ranked from the lowest to highest reflects this same trend, with $Ca^{2+} > Mg^{2+} > Zn^{2+}$ in α and $Mg^{2+} > Zn^{2+} > Ca^{2+}$ for δ, and highlights the positive correlation between high intercalant mobility and low thermodynamic stability. For both V_2O_5 polymorphs considered, the change in the migration barrier from the deintercalated to intercalated limit for the same diffusing species is much smaller than the variation across intercalating ions.

Although the α and δ polymorphs of V_2O_5 are structurally very similar as earlier discussed, the anion coordination environment and therefore diffusion topology of the migrating intercalant vary significantly, which accounts for the different shape of the migration energies seen in Fig 4-3a and Fig 4-3b. In the α phase, the stable

insertion site is coordinated by 8 oxygen anions which is connected to the adjacent insertion site along the a-axis by a 3-coordinated shared face. The shape of the migration energies shown in Fig. 4-3a, therefore, reflect the change in coordination of 8→3→8 encountered by the diffusing species with the migration barrier corresponding to passing through the shared face. For the δ phase, the stable insertion site adopts a "4+2" coordination and shares a corner with the adjacent insertion site along the a-axis. To migrate to this site, the intercalant passes through a 3-coordinated face shared with an intermediate 5-coordinated (pyramidal) site, and finally performs a symmetric hop to the next insertion site. The change in the anion coordination along the diffusion path is then "4+2"→3→5→3→"4+2", where occupation of the intermediate pyramidal site corresponds to a local minimum in the migration energy, as is reflected in Fig 4-3b. Overall, the migration barriers are also lower in the δ phase compared to α (significantly lower for some cases), which we attribute in large part to the smaller coordination change during the migration process encountered in δ. Also, the change in the relative order of the migration barriers of divalent ions between α (Ca > Mg, Zn) and δ (Mg, Zn > Ca) can be explained by the correlation between the "preferred" coordination environments of the respective ions and the available anion coordination environments around the intercalation sites.[183] In a given structure, migration barriers are higher for an ion whose preferred coordination aligns with that of the coordination environment available for the intercalant site compared to an ion whose preferred coordination is different from that present in the structure. For example, Ca is in its preferred 8-coordinated site in α and hence has higher barriers than Mg and Zn, which are not in their respectively preferred 6 and 4 coordinated sites. Whereas in δ, Ca is present in an unfavored "4+2" coordinated site and hence has lower barriers than either of Mg or Zn, which are closer to their preferred coordination environments. Our results thus lend support to the hypothesis that coordination of the intercalation site is a good screening criterion for identifying fast multi-valent cation diffusers.

4.4 Conclusions

An ideal MV cathode intercalation host must possess several properties−high capacity, high insertion voltage, and MV ion mobility, while simultaneously minimal structural change and thermodynamic instability. From the systematic first-principles study performed in this work, we are able to evaluate all of the candidate materials across each of these criteria. On the basis of ion mobility, Al^{3+} intercalation appears unfeasible at room temperature in V_2O_5 due to its prohibitively high migration barriers, and although Zn^{2+} intercalation is determined to be facile in both polymorphs and relatively stable in the δ phase, the insertion voltage is low. Mobility of Mg^{2+} and Ca^{2+} is determined to be poor in the α phase, but intercalation of these ions in the δ phase appear most promising, with sufficiently high voltage (3.02 V for Ca, and 2.56 V for Mg) and mobility ($E_m \sim 200$ meV for Ca and $\sim 600-800$ meV for Mg) albeit with moderate thermodynamic instability (27 meV/atom for Mg and 40 meV/atom for Ca above the ground state hull in the discharged state).

4.5 Appendix

4.5.1 Layer-spacing calculations

The V_2O_5 layers in the fully deintercalated α and δ polymorphs are bound by van der Waals interactions, which are not well described by standard DFT.[3, 59, 186] Hence, in order to obtain a better estimate of the spacing between the layers in α and δ-V_2O_5, we used the vdW-DF2 ($+U$) functional[112, 101] to describe the van der Waals forces instead of the PBE ($+U$) functional. Though including the van der Waals interactions in DFT gives better agreement with experimental layer spacing values, it leads to higher errors in the calculated average voltages as pointed out by Carrasco.[35]

4.5.2 Mechanical Instability

In a few thermodynamically unstable structures (see Figure 4-2c), such as Li, Mg and Zn (in the intercalated α-V_2O_5), Al (in both intercalated and deintercalated α) and Ca (in the intercalated δ-V_2O_5) the energies of the initial and final states for the NEB could not be converged. At first glance, all these structures undergo a shear-like transformation (mechanical instability), which involves the sliding of alternating V_2O_5 layers along the a-direction, leading to an artificial change in the layer stacking from α to δ (and vice-versa in the case of Ca in δ-V_2O_5).

4.5.3 Mg migration barrier in the "ϵ" phase

In order to estimate the change in the migration barriers with increasing Mg concentration, we performed NEB calculations on a specific Mg ordering at half Mg insertion in α-V_2O_5, referred to as the "ϵ" phase. Consisting of alternate Mg sites occupied in the a direction, the ϵ phase has also been observed in the Li-V_2O_5 system.[46] The NEB calculations on the ϵ phase require a vacancy in the supercell, and two symmetrically equivalent hops to account for the specific Mg ordering of this phase. The migration energies displayed in Figure 4-3a (dashed red lines) correspond to half of the total path, explaining the difference in energies between the NEB endpoints.

Chapter 5

Role of structural H_2O in intercalation electrodes: the case of Mg in nano-crystalline Xerogel-V_2O_5

5.1 Introduction

Several cathode materials that have shown appreciable electrochemical performance in Li- and Na-ion batteries are influenced by the presence of H_2O in either the cathode structure or the electrolyte. A few examples of these include the MnO_2 polymorphs –distorted-spinel Mn_2O_4,[120] Hollandite,[185] and Birnessite,[147, 146] Tavorite-$FeSO_4F$,[257, 222] Prussian-blue analogues,[248, 124] 2D Nb/V carbides,[145] and Xerogel-V_2O_5.[251, 206, 238, 256, 218] While it is speculated that structural H_2O increases the mobility of the intercalating redox-active cation by solvation,[153, 116] a key challenge has been to establish whether the structural H_2O stays in the electrode or perhaps shuttles with the cation during electrochemical cycling. More generally, the co-intercalation of solvent molecules in layered materials has recently been a focus of great research activity; for example, the thermodynamically prohibited intercalation of Na^+ in graphitic anode electrodes is made possible by solvent co-intercalation,[98] while the spinel $\rightarrow$ layered phase transition in MnO_2 electrodes is facilitated by water

intercalation.[99]

Determining how the presence or co-intercalation of water in an electrode influences the intercalation of cations may help to explain contrasting phenomena such as high capacities in a few intercalation systems[154, 146, 98, 214] and rapid capacity fade in a few others,[175, 7, 99] when water is present. In this study, we investigate the role that H_2O plays in the intercalation of Mg^{2+} in nanocrystalline Xerogel-V_2O_5. Using first-principles calculations (described in Sections 2.1,2.2 and 2.2.1), we demonstrate that water co-intercalation with Mg^{2+} is different in wet and dry electrolytes and generally increases the Mg insertion voltage.

While replacing Li^+ with a multi-valent ion, such as Mg^{2+} coupled with a Mg metal anode, is viewed as a potential way to achieve higher energy densities than current Li-ion batteries,[152, 126, 183] obtaining cathode materials that can reversibly intercalate Mg^{2+} at high voltage and with substantial capacity remains a pressing challenge.[204, 252, 116] As a known Li-intercalation host,[46] and being one of the few cathode materials that has shown reversible electrochemical Mg^{2+} intercalation,[190, 191, 2, 153, 64, 11, 98, 146] V_2O_5 is a key component in the design of future multivalent cathodes. Although orthorhombic-V_2O_5 possesses multiple polymorphs,[46] the nanocrystalline bilayered form of Xerogel-V_2O_5 is expected to have good Mg mobility owing to electrostatic shielding of the divalent Mg^{2+} by the water contained in the structure.[153, 116]

Electrochemical experiments intercalating Mg^{2+} in the Xerogel have reported varying voltages and capacities when employing organic[82, 83, 217, 113] and aqueous[211, 230] electrolytes, respectively. Imamura *et al.*[82, 83] showed Mg insertion in Xerogel-V_2O_5 using acetonitrile (AN) at voltages and capacities higher than that observed with the orthorhombic form [2, 64] with cyclic performance up to $\sim$ 40 cycles at a current density of $\sim$ 17 mA/g. Tepavcevic *et al.*[217] explored a full-cell arrangement consisting of a Sn anode, $Mg(ClO_4)_2$ dissolved in an AN electrolyte and a magnesiated Xerogel cathode and showed reversible Mg intercalation limited by anode capacity. Lee *et al.*[113] compared the electrochemical performance of AN and an ethylene carbonate: dimethyl carbonate (EC:DMC) mixture as solvents for Mg in-

sertion and reported improved kinetics with AN than EC:DMC. Stojković *et al.*[211] demonstrated reversible Mg intercalation in aqueous electrolytes with a capacity of $\sim$ 107 mAh/g at a higher initial voltage (voltage peaks at $\sim$ 3.02 V and 2.42 V) compared to the experiments with organic electrolytes.[82, 217] Recently, Vujković *et al.*[230] reported high capacity retention ($\sim$ 30 cycles) for Mg^{2+} cycling in Xerogel under aqueous electrolytes in comparison to Li^+, Na^+ or K^+.

So far, there have been no theoretical studies undertaken on the Mg-Xerogel V_2O_5 system to reveal the role of water co-intercalation under different solvent conditions. In the present work, we describe the Xerogel-V_2O_5 structure, the phase diagram at 0 K, and voltages as a function of both Mg and H_2O content in the structure. We investigate whether the structural H_2O in the Xerogel shuttles with the Mg^{2+} ion during cycling at various electrolytic conditions and Mg concentrations in the structure. Finally, we have explored the importance of electrochemical systems with solvent co-intercalation into electrodes, leading to solvent-based voltages that can impact the design of future electrolyte-electrode systems.

5.2 Structure

As the Mg- and H-positions in the Mg-intercalated Xerogel structure are not known experimentally, we have combined relevant experimental information with DFT calculations to obtain for the first time an atomic-level structural description of this system. While Petkov *et al.*[168] resolved the Xerogel-V_2O_5 structure by employing pair distribution functions from X-ray diffraction measurements, the positions of the intercalant atom were not reported. Oka *et al.*[158] described the Mg sites in σ-V_2O_5, which has a bilayered arrangement but is different from the Xerogel-V_2O_5 structure. In order to describe not only the Mg (intercalant) positions in the Xerogel structure but also the positions of the water molecules, comprising the oxygen (O^w) and the hydrogen atoms, we choose the Ni-intercalated bilayered V_2O_5 structure as a template (see Figure 5-1).[157] As Ni and Mg have similar octahedral coordination preference,[25] the initial positions of the Mg atoms are obtained from the known

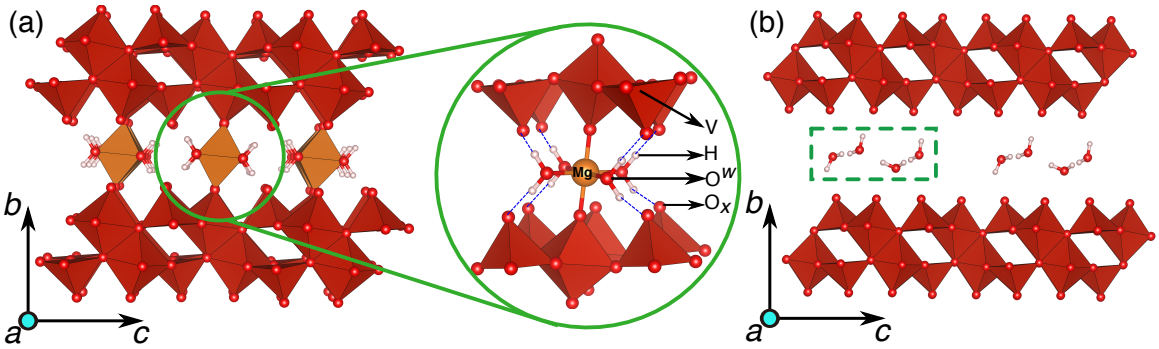

Figure 5-1: Structures of the fully magnesiated ($x_{Mg} = 0.5$) and the fully demagnesiated Xerogel, with 1 H_2O per formula unit of V_2O_5 are displayed in (a) and (b) respectively. The coordination of each Mg by 4 O^w can be observed in the enlarged image in the green circle, with the dashed blue lines indicating hydrogen-bonding between the water molecules and the lattice oxygen. The atomic species in the Xerogel structure are labelled in the enlarged image with O^w and O_x indicating the water and lattice oxygen, respectively.

Ni-positions in the bilayered structure.[157] In this structure, Ni (Mg) is coordinated by 2 oxygen atoms from the VO_5 pyramids and 4 O^w atoms as shown in Figure 5-1. The H-positions for the intercalated water in the Xerogel are initialized using a 3-step strategy by placing H-atoms $\sim$ 1 Å away from the O^w as explained in the Appendix (Section 5.7.4) and then relaxing these structures with DFT.

Figure 5-1a and b display the fully relaxed structures of the fully magnesiated and demagnesiated Xerogel respectively, containing 1 H_2O per formula unit of V_2O_5 (i.e., $n_{H_2O} = 1$) on the $b-c$ plane. Two individual V_2O_5 layers (red polyhedra in Figure 5-1) are bound by long interlayer V$-$O bonds ($\sim$ 2.66 Å) in the fully demagnesiated structure that lead to the formation of a single 'bilayer' of V_2O_5, giving rise to the term "bilayered" V_2O_5. While each V_2O_5 bilayer is composed of both VO_5 square pyramids and VO_6 octahedra, the intercalant atoms and the H_2O molecules are found in the space between two bilayers. In this work the $a-$, $b-$, and $c-$axes indicate the shortest axis, the inter-bilayer spacing direction, and the longest axis, respectively.

The orange octahedra in Figure 5-1a correspond to Mg atoms (at the center) coordinated by 6 oxygen atoms. As illustrated in the enlarged version of the Mg coordination environment (green circles, Figure 5-1a), each Mg is bonded to 4 O^w

atoms and 2 O atoms of the VO_x polyhedra (referred to as 'lattice' oxygen). While H atoms (in white) are bound to O^w, the dashed blue lines in Figure 5-1a indicate hydrogen-bonding between the water molecules and the lattice oxygen. The influence of H_2O molecules on the electronic structure and density of states in the Mg-Xerogel system is examined in Section 5.7.8 of the Appendix.

On Mg removal, hydrogen-bonding becomes more prominent amongst the H_2O molecules than with the lattice oxygen, as deduced by the shorter O–H bonding distances ($\sim 1.6 - 1.8$ Å) between H and next-nearest O^w atoms compared to hydrogen and lattice oxygen ($\sim 2.2 - 2.6$ Å), leading to the formation of stable hydrogen-bonded arrangements in the $a-$ and $c-$ directions (dashed green square in Figure 5-1b). The Xerogel structure in our work is limited to 2 fully occupied Mg sites for every 8 vanadium sites, hence the maximum Mg content in the structure is $x_{Mg} = 0.5$ per formula unit of V_2O_5, hereafter referred to as the "fully magnesiated" state. Based on our observations in the Ni-based Xerogel structure, we assumed a maximum of 4 H_2O molecules for 8 vanadium sites, and $n_{H_2O} = 1$ (per V_2O_5 formula unit) is denoted as the "fully hydrated" state.

The inter-bilayer spacing for the fully magnesiated phase (at $n_{H_2O} = 1$) using GGA+U is $\sim$ 10.18 Å, which agrees well with $\sim$ 10.22 Å predicted by the vdW-DF2+U functional, and is similar to the experimental value of $\sim$ 10.36 Å reported for the Ni-intercalated phase.[157] The Mg and H_2O positions calculated by GGA+U and vdW-DF2+U are similar, suggesting that the Mg-O electrostatic interactions dominate the geometry of the bilayer once Mg is inserted. For the fully demagnesiated phase (at $n_{H_2O} = 1$), the inter-bilayer spacing computed by GGA+U ($\sim$ 12.76 Å) differs significantly from the vdW-DF2+U value ($\sim$ 11.28 Å) and the experimental value of $\sim$ 11.52 Å.[168] Although GGA+U overestimates the layer spacing for the fully demagnesiated Xerogel structure (at $n_{H_2O} = 1$, as in Figure 5-1b), the hydrogen-bonded arrangement of H_2O molecules is similar to that found with the vdW-DF2+U functional.

5.3 Equilibration of the water content

Obtaining the equilibrium water content in the Xerogel requires one to know the free energy of the cathode as a function of the water content in the electrolyte, after which a minimization of the grand potential at the μ_{H_2O} of the electrolyte gives the equilibrium amount of H_2O in the cathode. We calculated the free energies of various Xerogel structures, enumerated in supercell volumes twice that of the conventional cell. We assessed the stability of the enumerated structures at $x_{Mg} = 0, 0.25$ and 0.5, containing various amounts of co-intercalated H_2O ($n_{H_2O} = 0, 0.5$ and 1), and for several water-concentration regimes in the electrolyte (see Figure 5-5 in the Appendix).

The stable Mg-Xerogel V_2O_5 phases, obtained by minimizing the grand-potential at 0 K, are plotted in Figure 5-2 as a function of a_{H_2O} and the Mg chemical potential (μ_{Mg}) with pictorial descriptions provided in Figure 5-6 in the Appendix. A high Mg chemical potential, such as $\mu_{Mg} = 0$ (see Section 5.7.6, Appendix), refers to a highly magnesiated Xerogel configuration ($x_{Mg} = 0.5$), while decreasing the chemical potential represents a more oxidizing environment that leads to demagnesiation ($x_{Mg} \sim 0$). To explore the effect of changing electrolytic conditions on the electrochemical properties of Xerogel-V_2O_5, we consider three different regimes (separated by dashed lines in Figure 5-2): *i*) *wet* or aqueous electrolyte, where the water activity, a_{H_2O}, is set to ~ 1, *ii*) *dry* with $10^{-2} < a_{H_2O} < 10^{-6}$, and *iii*) *superdry* with $a_{H_2O} < 10^{-7}$. An activity $a_{H_2O} = 10^{-4}$ would correspond to ≈ 10 ppm by weight of water under the ideal solution approximation in solvents such as glymes[173, 215]. Each colored region in Figure 5-2 corresponds to a single stable phase, whose composition is indicated with a $Mg_x(H_2O)_nV_2O_5$ notation. While the lines separating the single phase regions indicate the co-existence of two phases, the triple points correspond to a three phase co-existence.

For a wet electrolyte ($a_{H_2O} \sim 1$), the ground state structures as a function of μ_{Mg} consist of the fully magnesiated − fully hydrated structure ($x_{Mg} = 0.5$, $n_{H_2O} = 1$ per V_2O_5, blue region in Figure 5-2), the 'half' magnesiated − half hydrated structure

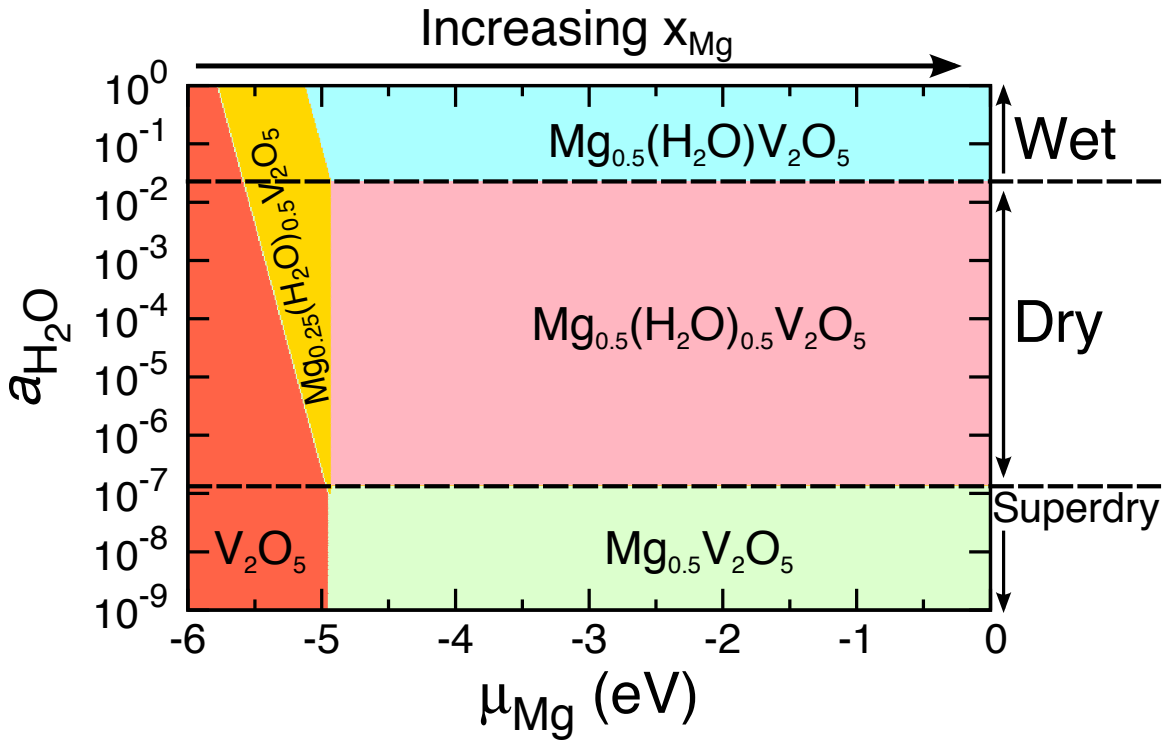

Figure 5-2: The Grand-potential phase diagram at 0 K of Mg-Xerogel V_2O_5 as a function of various electrolytic conditions and Mg chemical potentials is shown. Each colored region represents a single phase with the indicated Mg and water content. The dashed lines display different electrolytic regimes, with $\mu_{Mg} = 0$ corresponding to full magnesiation.

($x_{Mg} = 0.25$, $n_{H_2O} = 0.5$, yellow region), and the fully demagnesiated − dehydrated structure ($x_{Mg} = 0$, $n_{H_2O} = 0$, red region). Hence, under these electrolyte conditions, each Mg^{2+} intercalates with two H_2O molecules and a decrease in Mg content also corresponds to a decrease of water intercalated. Thus, when an aqueous electrolyte is used, there is a thermodynamic driving force for the water content to change with the Mg content.

When Mg^{2+} intercalation occurs from a dry electrolyte ($10^{-2} < a_{H_2O} < 10^{-6}$), the ground state phases are: $x_{Mg} = 0.5$, $n_{H_2O} = 0.5$ (fully magnesiated − half hydrated, pink region in Figure 5-2), $x_{Mg} = 0.25$, $n_{H_2O} = 0.5$ (half magnesiated − half hydrated, yellow), and $x_{Mg} = 0$, $n_{H_2O} = 0$ (fully demagnesiated − dehydrated, red). The results demonstrate that in a dry electrolyte, H_2O co-intercalates with Mg for $x_{Mg} < 0.25$, whereas the water content remains unchanged as more Mg is inserted.

For a superdry electrolyte ($a_{H_2O} < 10^{-7}$) the stable phases consist of fully dehydrated structures, both at $x_{Mg} = 0.5$ (fully magnesiated, green region in Figure 5-2) and $x_{Mg} = 0$ (fully demagnesiated, red). The absence of ground state configurations at intermediate Mg compositions (Figure 5-5c in the Appendix) in a superdry electrolyte indicates a phase separating behavior into Mg-rich and Mg-poor domains. Since the superdry ground states are fully dehydrated, there is a high driving force for all the water in the Xerogel to leave the structure. Interestingly, the activity of H_2O in the electrolyte not only influences the level of co-intercalation but also controls the nature of the Mg intercalation. Without water Mg-intercalation occurs as a 2-phase reaction between $x_{Mg} = 0$ and $x_{Mg} = 0.5$, whereas water in the electrolyte stabilizes intermediate Mg states.

The ground state structure of V_2O_5, across the range of μ_{Mg} and a_{H_2O} considered is the orthorhombic α-V_2O_5, [46, 190] which is consistent with experimental evidence of an irreversible transformation of the Xerogel to α-V_2O_5 at high temperatures,[114] suggesting the metastable nature of the Xerogel. In fact, the α polymorph is lower in energy at $x_{Mg} = 0$ and 0.5 compared to the dehydrated Xerogel phases (red and green regions in Figure 5-2) by $\sim$ 360 meV/f.u. and $\sim$ 200 meV/f.u., respectively.

Combining the results of Figure 5-2, we find that under wet conditions Mg^{2+} ions shuttle along with H_2O molecules across Mg concentrations, whereas under dry conditions H_2O co-intercalation only occurs between $0 \leq x_{Mg} \leq 0.25$. Hence, water will not shuttle with Mg under dry conditions and high Mg concentrations ($0.25 \leq x_{Mg} \leq 0.5$) in the Xerogel. In a superdry electrolyte, there is no H_2O within the Xerogel structure. Although we have discussed the general phenomenon of Mg-H_2O co-intercalation[146, 153] for the case of Xerogel-V_2O_5, similar models are readily applicable to study solvent co-intercalation in other layered electrode materials.[98]

5.4 Effect of water on the Mg insertion voltage

In regimes where H_2O shuttles with the Mg, the activity of water affects the cell voltage, as illustrated by the average voltage curves computed for Mg insertion into

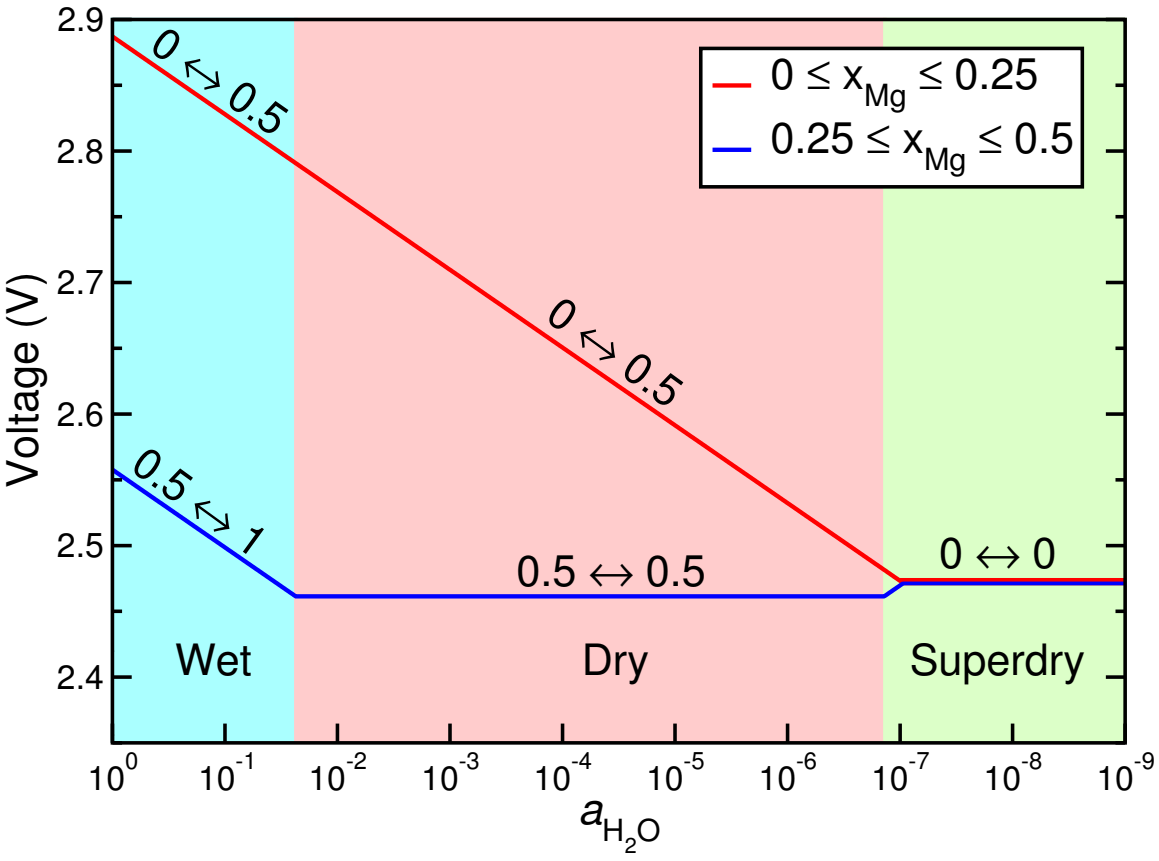

Figure 5-3: Average Mg insertion voltage for low (red line) and high (blue) Mg concentrations as a function of the electrolyte water content (a_{H_2O}). Equations on the curves indicate the change in H_2O content in the Xerogel as Mg is inserted in each electrolytic regime.

Xerogel-V_2O_5 in Figure 5-3. The voltages as a function of a_{H_2O}, under the wet (cyan background), dry (pink), and superdry (green) regimes, are obtained from the phase diagram of Figure 5-2, using the procedure detailed in Section 2.2.1.[13] The red and blue lines indicate the voltages for Mg insertion between concentration ranges of $0 \leq x_{Mg} \leq 0.25$ and $0.25 \leq x_{Mg} \leq 0.5$ respectively. Thus, at a given a_{H_2O}, the values on the red and blue curves indicate the average voltage that will be observed between $0 \leq x_{Mg} \leq 0.25$ and $0.25 \leq x_{Mg} \leq 0.5$. The equations on the voltage curves indicate changes in the structural H_2O content of the Xerogel, as Mg is inserted. For example, "$0.5 \leftrightarrow 1$" on the blue line for $a_{H_2O} \sim 10^{-1}$ (wet electrolyte) indicates a variation in n_{H_2O} from 0.5 to 1 as x_{Mg} increases from 0.25 to 0.5. The slope changes of the voltage

curves, particularly the ones at high Mg concentration (blue line), indicate the critical water content in the electrolyte at which the H_2O co-intercalation behavior changes. The merging of the red and blue curves in the superdry region in Figure 5-3 reflects that only a single voltage plateau for $0 \leq x_{Mg} \leq 0.5$ is found. The interpretation of the kink on the blue voltage curve observed in the superdry region is given in the Appendix.

Although Mg intercalation experiments in Xerogel-V_2O_5 are normally performed on structures with higher H_2O and Mg content than considered in our structural model,[114, 82, 83, 217] the calculated voltage curves in Figure 5-3 qualitatively agree with the experimental voltage features for Mg insertion in wet,[211] and dry electrolytes.[82] The calculated voltage for the superdry electrolyte (~ 2.47 V, $a_{H_2O} \sim 10^{-8}$), where the H_2O exits the Xerogel during Mg cycling, is higher but comparable to α-V_2O_5 at low Mg concentrations (~ 2.44 V). [190] Importantly, the increase in voltages with increase in a_{H_2O}, as predicted by theory (Figure 5-3), is in good agreement with experimental observations of higher initial voltages in aqueous (voltage peak at ~ 3.02 V) compared to dry (peak at ~ 2.88 V) electrolytes and α-$Mg_xV_2O_5$ (~ 2.35 V, no water).[64, 211, 82]

5.5 Discussion

In this work, we have used first-principles methods based on DFT (Section 2.1) to investigate Mg intercalation into Xerogel-V_2O_5. Specifically, we have clarified the structure of the Xerogel, evaluated the phase diagrams for Mg intercalation under different electrolytic conditions (wet, dry and superdry), and calculated the average voltages for each case. The data presented in this work not only sheds light on existing experiments in the Mg-Xerogel system, with possible Mg-H_2O co-intercalation, but also provides a working model for studying solvent co-intercalation properties in layered materials for batteries and other applications.

Figure 5-4 displays a phase diagram of the Xerogel V_2O_5 − Magnesiated Xerogel V_2O_5 − H_2O ternary system, summarizing the results of Figure 5-2. The base of the

triangle (Figure 5-4) corresponds to Mg intercalation in the Xerogel-V_2O_5 structure in the absence of H_2O, or the superdry electrolyte, as indicated by the green arrow. The colored solid lines on the phase diagram represent the trajectories of stable phases that will form upon magnesiation of the Xerogel-V_2O_5 structure under different electrolyte conditions. While the solid blue and red lines correspond to the wet and the dry electrolytes respectively, the purple line indicates the commonality of the stable phases between wet and dry electrolytes at low Mg concentrations. The blue and red circles are the stable states at full magnesiation in a wet and dry electrolyte, respectively. The purple circle indicates the half magnesiated − half hydrated ground state common to both the wet and dry electrolytes.

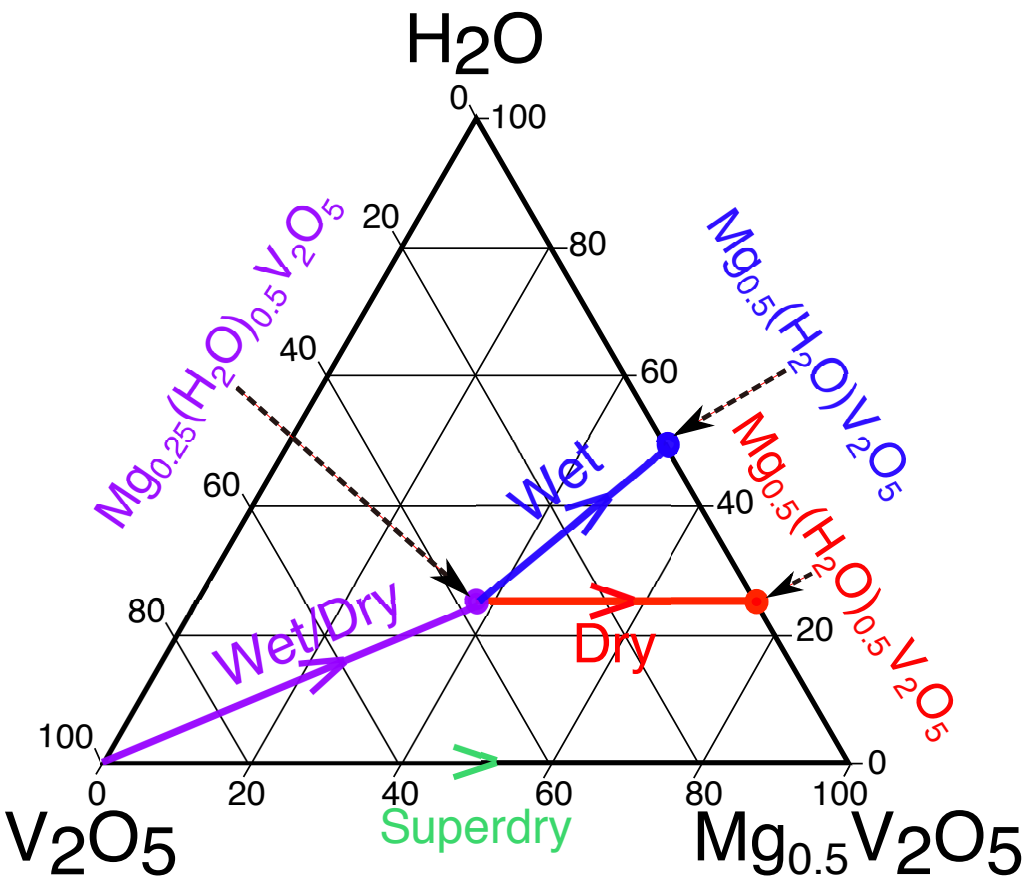

Figure 5-4: Ternary phase diagram of the Mg-(Xerogel)V_2O_5-H_2O system, which summarizes the possible equilibrium phases under different electrolyte conditions. The "Wet/Dry" trajectory indicates that the equilibrium states are similar for both wet and dry electrolytes in that Mg concentration range. The green arrow shows the stable phases in a superdry electrolyte.

While initial Mg intercalation up to $x_{Mg} = 0.25$ pulls H_2O into the structure for both wet and dry electrolytes, further co-intercalation of water with Mg depends more sensitively on the water content of the electrolyte. Interestingly, the presence of water in the electrolyte changes the phase behavior of the Mg-Xerogel system from that of a two phase reaction at a single voltage (superdry) to one with a capacity over a range of voltages (wet and dry).

In conventional secondary batteries, where the solvent or electrolyte do not co-intercalate with the redox-active cation, the voltage depends on the chemical potential difference of the cation species between the cathode and the anode.[13, 39] However, our study suggests that the measured voltages are subjected to change if the co-intercalation of the solvent/electrolyte with the redox ion occurs, leading to a co-dependence on the solvent/electrolyte chemical potential. As illustrated by Figure 5-3, the Mg insertion voltage in the Xerogel is calculated to be ~ 150 mV higher in a wet electrolyte than in a dry electrolyte ($a_{H_2O} \sim 10^{-4}$), in good agreement with reported higher voltages in aqueous compared to organic (dry) electrolytes.[82, 217, 211, 230] Electrolyte/solvent-dependent voltages give rise to important design consequences in a battery system, since the voltage generated can be calibrated based on both the solvent polarity (polar/apolar) and the quantity (wet/dry) of the intercalating solvent species. Further analysis on the variability of voltages based on solvents is relevant not only in the design of improved electrolytes but also in selecting possible electrolyte-additive combinations that can ultimately improve the energy density of an electrochemical system.

H_2O co-intercalation in Xerogel-V_2O_5 has three important technological consequences: *i*) higher Mg insertion voltages, *ii*) change in phase behavior from a two phase regime (superdry) to one with intermediate stable Mg concentrations (wet, dry) and *iii*) higher kinetic rate of Mg insertion originating from the electrostatic shielding effect of the coordinating water molecules in the cathode.[116, 153] Nevertheless, in the case of Mg-ion batteries, where the Mg metal anode is crucial to achieve energy densities higher than current Li-ion technology,[152] the presence of H_2O in the electrolyte or coordinated with the Mg^{2+} ions could cause passivation at

the Mg anode.[142, 66, 204] While there exist solvents that successfully solvate Mg^{2+} and do not cause passivation of the Mg metal (e.g., ethers like tetrahydrofuran and glymes[252]), it is crucial to understand their fate as a co-intercalant together with the Mg in the bilayered-V_2O_5 structure, and their impact on the Mg insertion voltage and mobility. More generally, investigations of solvent co-intercalation properties in other layered materials will be useful and important in designing the next generation of rechargeable Li, Na and multi-valent batteries.

5.6 Conclusion

In this work, we have integrated experimental information with first-principles computations to resolve the nano-crystalline Mg-Xerogel V_2O_5 structure and observed Mg being coordinated by 2 lattice oxygen and 4 oxygen from co-intercalated H_2O. Using grand-potential phase diagrams, we found that water co-intercalation with Mg^{2+} depends on the water activity in the electrolyte, ranging from full co-intercalation in wet to none in superdry conditions. Also, we have established the significant impact of water (or solvent) co-intercalation on the voltages and voltage profiles obtained.

5.7 Appendix

5.7.1 Grand-potential phase diagrams

Each graph in Figure 5-5 plots the relative stability of the Xerogel structures as function of Mg composition, with green triangles, red diamonds and blue dots representing structures with $n_{H_2O} = 0,\ 0.5,$ and 1, respectively. The formation energy is plotted with respect to the lowest energy states at $x_{Mg} = 0$ and $x_{Mg} = 0.5$ so that the relative stability of the states at $x_{Mg} = 0.25$ can be assessed. Finally, the dashed purple lines indicate the stable phases at 0 K under the given electrolyte conditions.

For a wet electrolyte ($a_{H_2O} \sim 1$), the ground state structures in Figure 5-5a consist of the fully magnesiated − fully hydrated structure (x_{Mg} =0.5, $n_{H_2O} = 1$ per V_2O_5), the 'half' magnesiated − half hydrated structure (x_{Mg} =0.25, $n_{H_2O} = 0.5$), and the

fully demagnesiated − dehydrated structure (x_{Mg} =0, $n_{H_2O} = 0$). When a dry electrolyte is employed (Figure 5-5b), set by $a_{H_2O} \sim 10^{-4}$, the ground state phases are: x_{Mg} =0.5, $n_{H_2O} = 0.5$ (fully magnesiated − half hydrated), x_{Mg} =0.25, $n_{H_2O} = 0.5$ (half magnesiated − half hydrated), and x_{Mg} =0, $n_{H_2O} = 0$ (fully demagnesiated − dehydrated). Figure 5-5c displays the stability values for a superdry electrolyte ($a_{H_2O} \sim 10^{-8}$) consisting of the fully dehydrated structures, both at $x_{Mg} = 0.5$ (fully magnesiated) and $x_{Mg} = 0$ (fully demagnesiated).

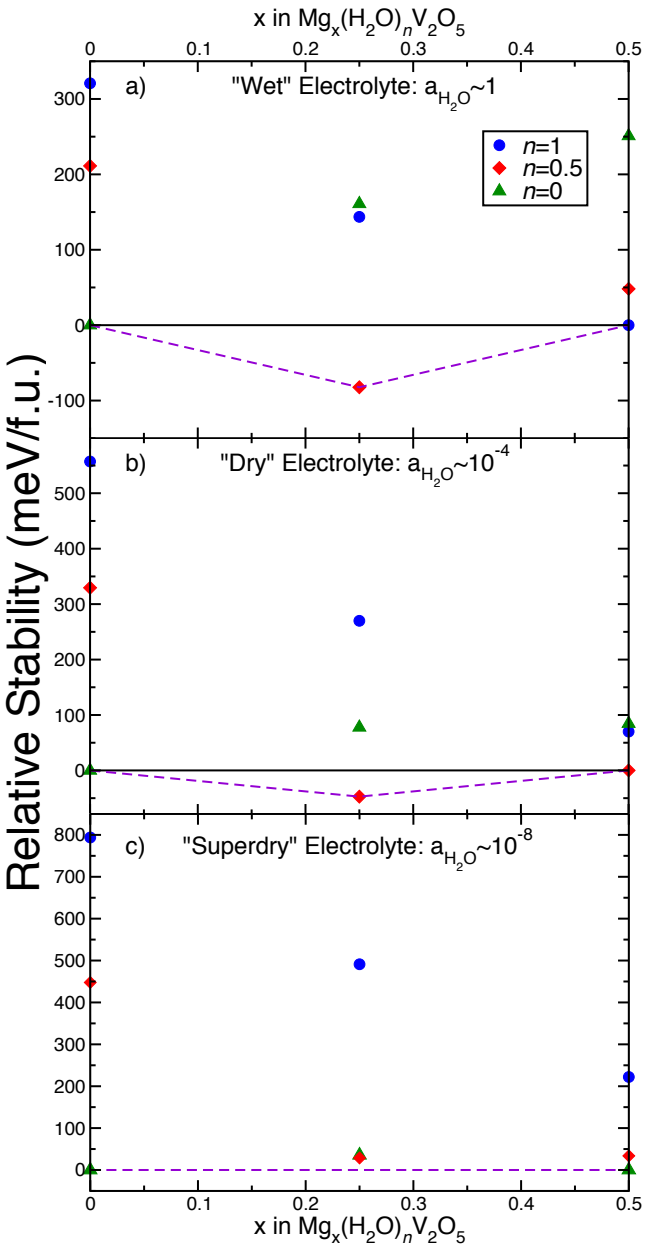

Figure 5-5: The Grand-potential phase diagram at 0 K of the Mg-Xerogel V_2O_5 system in a (a) wet, (b) dry, and (c) superdry electrolytes. Blue dots, red diamonds and green triangles respectively indicate structures with n_{H_2O} = 1, 0.5, and 0 at different x_{Mg}.

5.7.2 Structures and lattice parameters of ground states

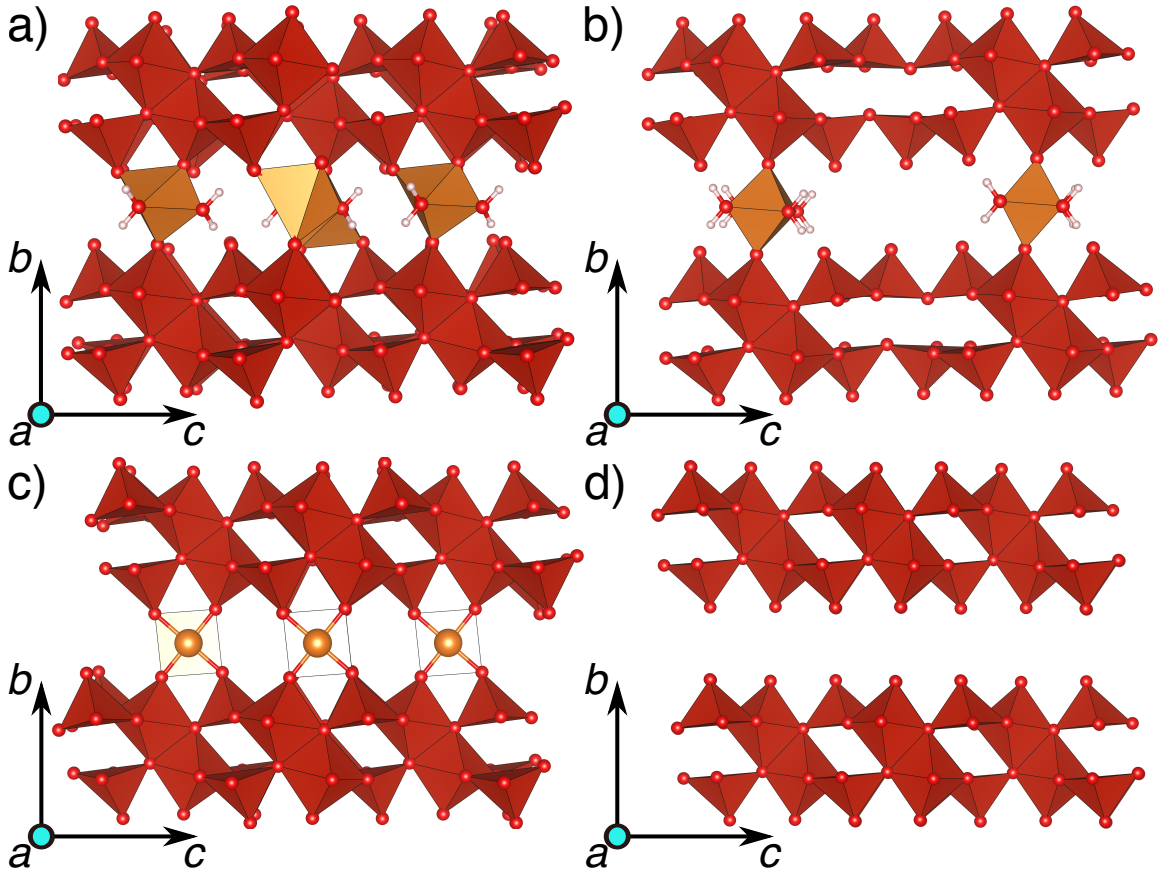

Figure 5-6: The ground state configurations at different Mg and H_2O contents within the Xerogel structure are displayed. Sub-panels (a), (b), (c), and (d) indicate the stable states at (x_{Mg} = 0.5, n_{H_2O}=0.5), (x_{Mg} = 0.25, n_{H_2O}=0.5), (x_{Mg} = 0.5, n_{H_2O}=0), and (x_{Mg} = 0, n_{H_2O}=0), respectively. The notation used for the crystallographic axes is the same as that used in Figure 5-1, while the orange and red polyhedra correspond to the Mg and V atoms (at the center) coordinated by oxygen atoms.

Figure 5-6 shows the structures of the ground state configurations at different Mg and H_2O concentrations, as described in Figure 5-2 and Figure 5-5, including the fully magnesiated − half hydrated (x_{Mg} = 0.5, n_{H_2O}=0.5; Figure 5-6a), the half magnesiated − half hydrated (x_{Mg} = 0.25, n_{H_2O}=0.5; Figure 5-6b), the fully magnesiated − dehydrated (x_{Mg} = 0.5, n_{H_2O}=0; Figure 5-6c) and the fully demagnesiated − de-

hydrated states (x_{Mg} = 0, n_{H_2O}=0.5; Figure 5-6d). Mg can be found in a 5- and 4-coordinated environment in Figure 5-6a and c respectively, with the ground state configuration in Figure 5-6a being in a $2\times1\times1$ supercell configuration. The bilayered-V_2O_5 framework is retained while calculating the fully dehydrated configurations of Figure 5-6c and d. The lattice parameters of all ground state configurations (including those displayed in Figure 5-1), resulting from GGA ($+U$) and vdW-DF2 ($+U$) calculations are given in Table 5.1. The atomic coordinates of all ground states have been indicated in Section 5.7.9.

Phase	Functional	Lattice parameters					
		a	b	c	α	β	γ
		Å			°		
$Mg_{0.5}(H_2O)V_2O_5$	GGA	3.73	10.18	11.86	94.60	90.06	89.86
	vdW-DF2	3.72	10.22	12.19	93.69	89.91	90.19
$Mg_{0.5}(H_2O)_{0.5}V_2O_5$	GGA	7.6	9.64	11.70	90.09	90.01	90.03
	vdW-DF2	7.66	9.76	11.85	90.12	90.01	90.00
$Mg_{0.25}(H_2O)_{0.5}V_2O_5$	GGA	3.70	10.30	11.70	93.16	90.00	90.00
	vdW-DF2	3.71	10.79	11.97	94.46	90.00	90.00
$Mg_{0.5}V_2O_5$	GGA	3.80	9.30	11.66	81.06	90.00	90.00
	vdW-DF2	3.84	9.42	11.81	81.25	90.00	90.00
V_2O_5	GGA	3.66	10.01	11.74	95.52	90.00	90.00
	vdW-DF2	3.69	9.30	11.90	95.85	90.00	90.00
$(H_2O)V_2O_5$	GGA	3.69	12.76	11.69	96.73	90.00	87.30
	vdW-DF2	3.69	11.28	11.91	94.37	90.06	91.21

Table 5.1: The lattice parameters of all ground state configurations of the Mg-Xerogel V_2O_5 system. The Hubbard $+U$ correction was added to both GGA and vdW-DF2 calculations with the cell symmetry broken.

5.7.3 Feature on the voltage profile

The kink in the blue voltage curve of Figure 5-3, at $a_{H_2O} \sim 10^{-7}$, together with the red curve, indicates a scenario where the ground state hull is comprised of the $x_{Mg} = 0$, $n_{H_2O} = 0$ (fully demagnesiated − dehydrated), $x_{Mg} = 0.25$, $n_{H_2O} = 0.5$ (half magnesiated − half hydrated), and $x_{Mg} = 0.5$, $n_{H_2O} = 0$ (fully magnesiated − dehydrated) states, implying that Mg co-intercalates with H_2O into the empty Xerogel up to $x_{Mg} = 0.25$ beyond which the H_2O exits the structure upon more Mg insertion.

5.7.4 Strategy for resolving H-positions

We use a 3-step strategy to resolve the H-positions in both Mg-intercalated and empty Xerogel structures. Firstly, we obtain Voronoi positions ~ 1 Å away from the O^w atoms (see Figure 5-1), since the O−H bonds in water are ~ 1 Å long.[240, 221] Secondly, we order the H-sites obtained from the Voronoi positions,[159] based on Ewald summation energies[60, 55] to minimize electrostatic repulsion between the H-atoms by assigning formal charges of $+2$, $+5$, -2 and $+1$ to Mg, V, O, and H atoms, respectively. In order to ensure a diverse set of H-positions to initialize our first-principles calculations, we also assign sets of unphysical charges to the Mg, V, and O atoms, such as Mg^{2-}, V^{5-}, and O^{2+}. Each permutation of the charges assigned to the Mg, V and O atoms give rise to $\sim 40 - 50$ distinct H-orderings. The pymatgen library [160] is used to obtain both the Voronoi positions and enumerate the H-orderings. Finally, each structure stemming from the ordering procedure is subjected to a two-step structure relaxation calculation. In the first step the H-atoms are allowed to rotate about the O^w atoms while the positions of all other atoms in the structure are fixed. In the second step we perform the full structure relaxation allowing all ions in the structure to relax. The fully relaxed H-ordering with the lowest energy among those calculated is considered to be the 'ground state' configuration for the given Mg and H_2O content in the Xerogel (and plotted in Figure 5-5). The above procedure is then repeated for other Mg and H_2O concentrations in the Xerogel structure.

5.7.5 Obtaining $\mu_{\mathbf{H_2O}}$ for calculating the Grand-potential

In order to calculate the Grand-potential, Φ, described in Section 2.2.1, reliable first-principles values for the chemical potential of H_2O, μ_{H_2O}, need to be obtained. With $\mu^0_{H_2O}$, a_{H_2O}, R and T defined as the chemical potential of H_2O in its standard state, activity of H_2O in the electrolyte (external to the Xerogel cathode), universal gas constant and temperature, respectively. μ_{H_2O} can be expanded as,

$$\mu_{H_2O} = \mu^0_{H_2O} - RT \ln a_{H_2O} \tag{5.1}$$

By assigning various values to a_{H_2O}, different electrolyte conditions can be simulated, such as the wet ($a_{H_2O} \sim 1$), dry ($a_{H_2O} \sim 10^{-4}$), and superdry ($a_{H_2O} \sim 10^{-8}$) electrolytes. Hence, to obtain reliable values of μ_{H_2O}, an accurate value of $\mu^0_{H_2O}$ needs to be calculated.

To obtain a reliable value of $\mu^0_{H_2O}$ from DFT, we consider two approaches in this work, namely using the "Ice" and "Vapor" references. In the case of the "Ice" reference, $\mu^0_{H_2O}$ is obtained by adding to the DFT energy of ice (E_{Ice}) the experimental enthalpy of melting of ice ($\Delta H^{melting}_{\text{Ice}}$, at 298 K) and the entropy of liquid H_2O at 298 K (S_{Water}).

$$\mu^0_{H_2O} = E_{\text{Ice}}(calc.) + \Delta H^{melting}_{\text{Ice}}(exp.) - T.S_{\text{Water}}(exp.) \tag{5.2}$$

The ice-XI structure reported by Leadbetter *et al.*[110] is used for calculating the DFT ice energy in Eq. 5.2, with a k-point mesh of 6×4×4. Similarly, for the "Vapor" reference, $\mu^0_{H_2O}$ is given by starting from the DFT total energy of water vapor (E_{Vapor}), which is obtained by calculating the energy of a single molecule of H_2O in a 15×15×15 Å^3 box, and subtracting the experimental enthalpy of evaporation of water ($\Delta H^{evaporation}_{\text{Water}}$, at 298 K) and S_{Water} at 298 K. Both the Ice and the Vapor calculations were done with the Generalized Gradient Approximation as elaborated in the Section 2.1.

$$\mu^0_{H_2O} = E_{\text{Vapor}}(calc.) - \Delta H^{evaporation}_{\text{Water}}(exp.) - T.S_{\text{Water}}(exp.) \tag{5.3}$$

Using both the Ice and the Vapor references, the formation energies of a few alkali and alkaline earth hydroxides (from their corresponding oxides) are calculated from DFT and compared with the experimental enthalpies of formation (ΔH_{r}) in order to determine which of the two reference states describes a realistic value for $\mu^0_{\mathrm{H_2O}}$. For example, consider the reaction $\mathrm{MgO} + \mathrm{H_2O} \rightarrow \mathrm{Mg(OH)_2}$. The experimental enthalpy of formation of $\mathrm{Mg(OH)_2}$ from MgO can be computed as,

$$\Delta H_{\mathrm{r,Mg(OH)_2}} = H^0_{\mathrm{Mg(OH)_2}} - H^0_{\mathrm{MgO}} - H^0_{\mathrm{H_2O}} \tag{5.4}$$

where H^0 of a species is the standard enthalpy of formation of that species at 298 K, obtained from the Kubaschewski[107] and Wagman[232] tables. Similarly, the enthalpy of formation of $\mathrm{Mg(OH)_2}$ from MgO can be calculated from the DFT total energies as in Eq. 5.5, while disregarding the negligible volumetric (PV), the zero point energy and the temperature contributions to the enthalpy at 298 K. The $E_{\mathrm{H_2O}}$ in Eq. 5.5 will either correspond to the Ice reference ($E_{\mathrm{Ice}} + \Delta H^{melting}_{\mathrm{Ice}}$, Eq. 5.2) or the Vapor reference ($E_{\mathrm{Vapor}} - \Delta H^{evaporation}_{\mathrm{Water}}$, Eq. 5.3). Thus, the Ice- or Vapor-based $\Delta H_{\mathrm{r,Mg(OH)_2}}$ that benchmarks best with the experimental $\Delta H_{\mathrm{r,Mg(OH)_2}}$ will be used further in our grand-potential phase diagram calculations.

$$\Delta H_{\mathrm{r,Mg(OH)_2}} = E_{\mathrm{Mg(OH)_2}} - E_{\mathrm{MgO}} - E_{\mathrm{H_2O}} \tag{5.5}$$

In order to benchmark a wide range of experimental and calculated ΔH_r, we considered a set of alkali and alkaline earth hydroxides and oxides that satisfied few conditions:

- The valence state of the metal or oxygen should not change during hydroxide formation from the oxide. For example, NaOH formation from a conventional $\mathrm{Na_2O}$ will be considered instead of a $\mathrm{Na_2O_2}$ peroxide.

- The existence of reliable experimental structures for both oxides and hydroxides with known positions of all atoms in the structure, including the H-atoms. The Inorganic Crystal Structure Database[1] database was used for the structure

search.

Benchmarking $\mu^0_{\mathbf{H_2O}}$

Figure 5-7 displays the benchmarking of the DFT and experimental formation enthalpies of a few alkali (Li, Na) and alkaline earth (Be, Mg, Ca, Sr and Ba) hydroxides from the corresponding oxides. The black dots indicate the experimental values obtained from the literature,[107, 232] while the theoretical calculations using the Ice and Vapor references are marked by the blue stars and the red diamonds respectively. The absolute distances between the black dot and the DFT points denote the errors encountered in predicting the experimental enthalpy values. The text annotations in the graph correspond to the respective systems for which the experimental and computed values are displayed. For example, the notation $CaO/Ca(OH)_2$ is equivalent to the reaction $CaO + H_2O \rightarrow Ca(OH)_2$.

While the Vapor-referenced calculations predict the experimental formation enthalpies of the hydroxide from the oxide with an average error of $\sim 16\%$, the Ice-referenced calculations predict the same enthalpies with almost twice the error ($\sim 32\%$). Also, the Vapor-referenced calculations have lower errors consistently than the Ice-referenced calculations for all the oxide/hydroxide systems considered. Thus, it can be concluded that the Vapor-referenced calculations capture the energetics of H_2O better than the Ice-referenced calculations, specifically for obtaining a reliable $\mu^0_{H_2O}$. The results described in Section 5.3 are based on the Vapor-referenced calculations.

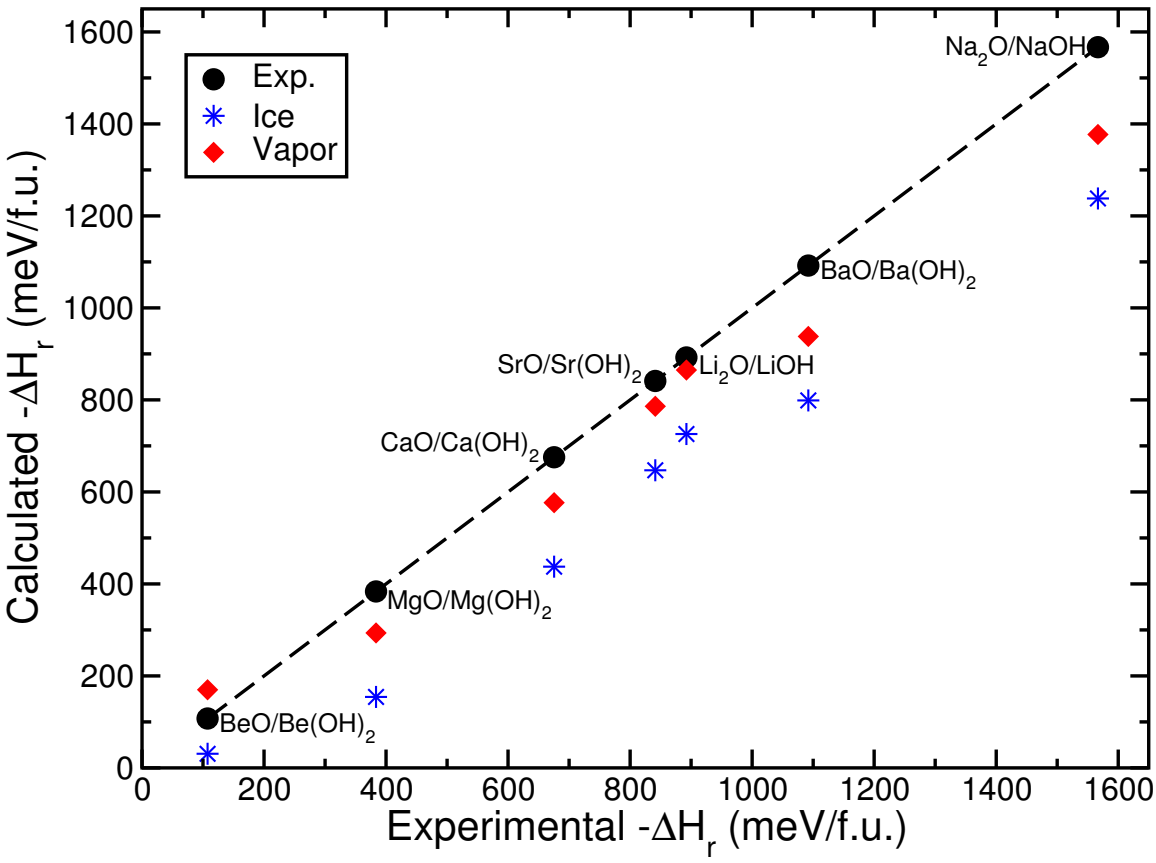

Figure 5-7: Benchmarking the DFT "Ice"- and "Vapor"-referenced formation enthalpies of alkali and alkaline earth hydroxides from their corresponding oxides, with respect to the analogous experimental values.

5.7.6 Obtaining μ_{Mg}

Similar to $\mu_{\mathrm{H_2O}}$, the chemical potential of Mg (μ_{Mg}^{ref}) can be referenced to the Mg chemical potential in its standard state (μ_{Mg}^{0}).

$$\mu_{\mathrm{Mg}}^{ref} = \mu_{\mathrm{Mg}}^{0} + \Delta\mu_{\mathrm{Mg}} \tag{5.6}$$

μ^0_{Mg} is obtained from DFT calculations of pure Mg metal, in its Hexagonal Close-packed form, and by neglecting the entropic and volumetric contributions.

$$\mu^0_{\mathrm{Mg}} \approx E^{DFT}_{\mathrm{Mg}} \tag{5.7}$$

The Mg chemical potential scale is then re-normalized, such that $\mu_{\mathrm{Mg}} = 0$ corresponds to the DFT-computed value of μ^0_{Mg}, and the grand-potential energies (Φ) are adjusted (as in Eq. 5.9) to reflect this normalization.

$$\mu_{\mathrm{Mg}} = \mu^{ref}_{\mathrm{Mg}} - \mu^0_{\mathrm{Mg}} \equiv \Delta\mu_{\mathrm{Mg}} \tag{5.8}$$

$$\Phi'[\mathrm{Mg}_x(\mathrm{H_2O})_n\mathrm{V_2O_5}] = \Phi[\mathrm{Mg}_x(\mathrm{H_2O})_n\mathrm{V_2O_5}] - x \cdot \mu^0_{\mathrm{Mg}} \tag{5.9}$$

The normalized Φ' thus obtained is minimized as a function of both $a_{\mathrm{H_2O}}$ and the shift in the Mg chemical potential (μ_{Mg}) as in Eq. 5.10. The phases that have the lowest Φ' are subsequently plotted in Figure 5-2.

$$\min_{\Phi'}\{\Phi'[\mathrm{Mg}_x(\mathrm{H_2O})_n\mathrm{V_2O_5}] - x \cdot \mu_{\mathrm{Mg}} - n \cdot (\mu^0_{\mathrm{H_2O}} - RT \ln a_{\mathrm{H_2O}})\};\ \forall\ \mu_{\mathrm{Mg}} \leq 0, a_{\mathrm{H_2O}} \leq 1 \tag{5.10}$$

Note that with Eq. 5.8 as the definition of the Mg chemical potential, μ_{Mg} is related to the voltage as ($\langle V \rangle \approx \frac{\mu_{\mathrm{Mg}}}{2}$).

5.7.7 k-point convergence

Figure 5-8 displays the energy per atom as a function of the k-point grid density for the Mg-Xerogel V_2O_5 system, indicating rapid convergence of the energy with increase in k-points. A fully magnesiated − hydrated ($\mathrm{x_{Mg}} = 0.5$, $n_{\mathrm{H_2O}} = 1$) unit cell, as illustrated in Figure 5-1a with lattice parameters provided in Table 5.1, was used for performing the convergence study. As indicated by the text in Figure 5-8, a k-point density of ~ 1000 per atom corresponds to a mesh of $6 \times 2 \times 2$, with energy per atom converged to within < 0.1 meV/atom compared to a denser k-point meshes. Hence, a $6 \times 2 \times 2$ mesh was used in all our energy calculations.

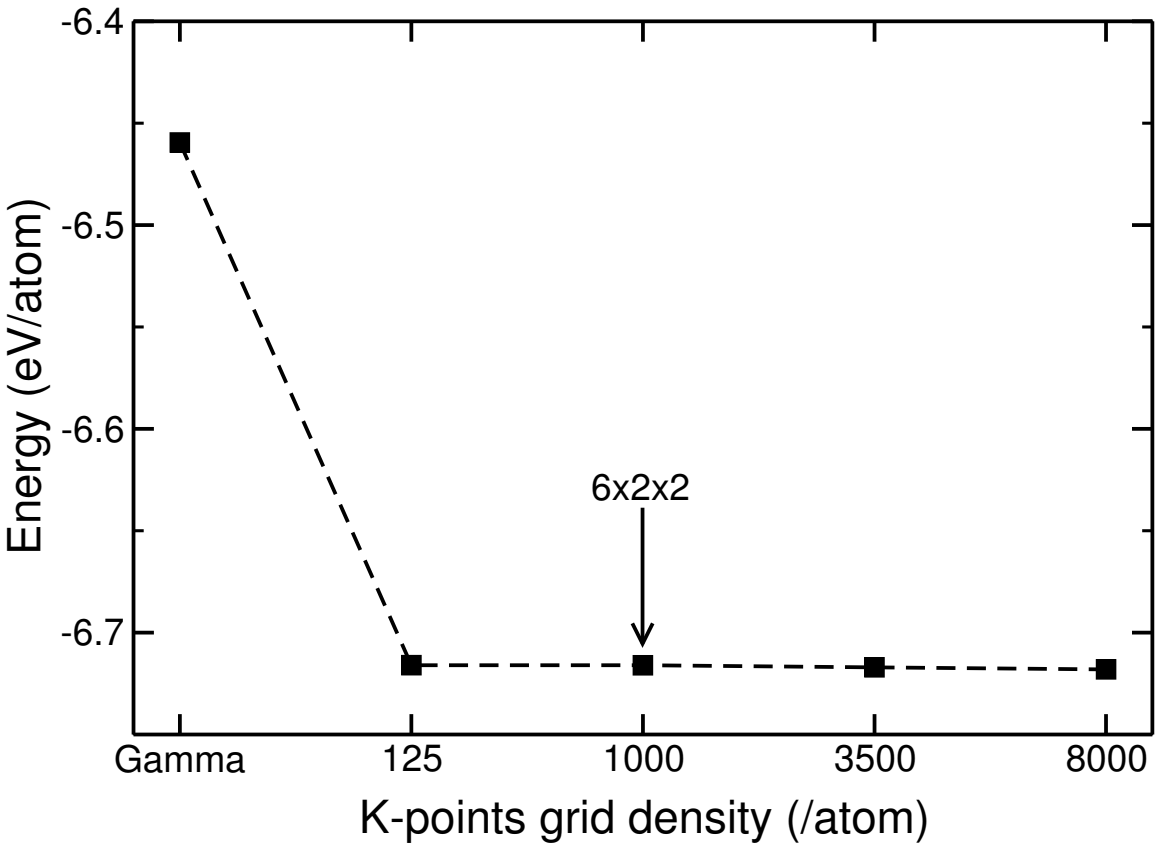

Figure 5-8: Convergence of energy per atom with respect to k-point grid size for the calculations done on the Mg-Xerogel system.

5.7.8 Impact of H_2O on the electronic structure of Mg-V_2O_5

The presence of excess electrons from H_2O partially shielding the divalent Mg^{2+} ion can be observed from the difference in charge densities between hydrated and dehydrated structures of a fully magnesiated xerogel-V_2O_5 ($x_{Mg} = 0.5$) in Figure 5-9. To this end, we analyze variations of the electronic charge density and the density of states (DOS) when Mg intercalates with and without water in the xerogel Mg-V_2O_5 system.

In order to perform a valid comparison of charge densities (and the DOS), the ground state configuration at $x_{Mg} = 0.5$, $n_{H_2O} = 1$ (Figure 5-1a) is chosen and electronic relaxation is done with and without water molecules. The blue regions indicate

zones of excess electrons in the hydrated structure as compared to the dehydrated version, with the iso-surface displayed in Figure 5-9 being ~ 0.0133 electrons. The presence of H_2O thus significantly alters the electronic structure of the Mg-Xerogel V_2O_5 system, influencing both the ground state configurations observed and the Mg-intercalation kinetics.

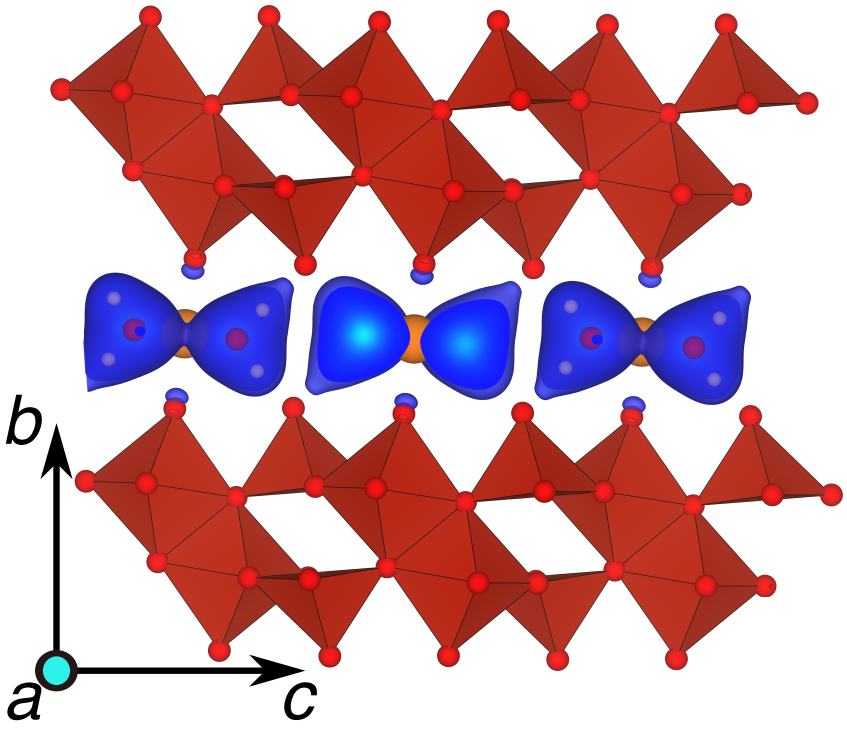

Figure 5-9: The red polyhedra contain the V atoms at the center and the orange spheres indicate Mg atoms in Mg-Xerogel V_2O_5. The difference between the electronic charge densities of the fully magnesiated, fully hydrated structure ($x_{Mg} = 0.5$, $n_{H_2O} = 1$) and the fully magnesiated, dehydrated structure ($x_{Mg} = 0.5$, $n_{H_2O} = 0$) is displayed. The ground state configuration of Figure 5-1a is chosen for comparing the charge densities. The blue regions show the excess of electrons in the hydrated structure in comparison to the dehydrated version.

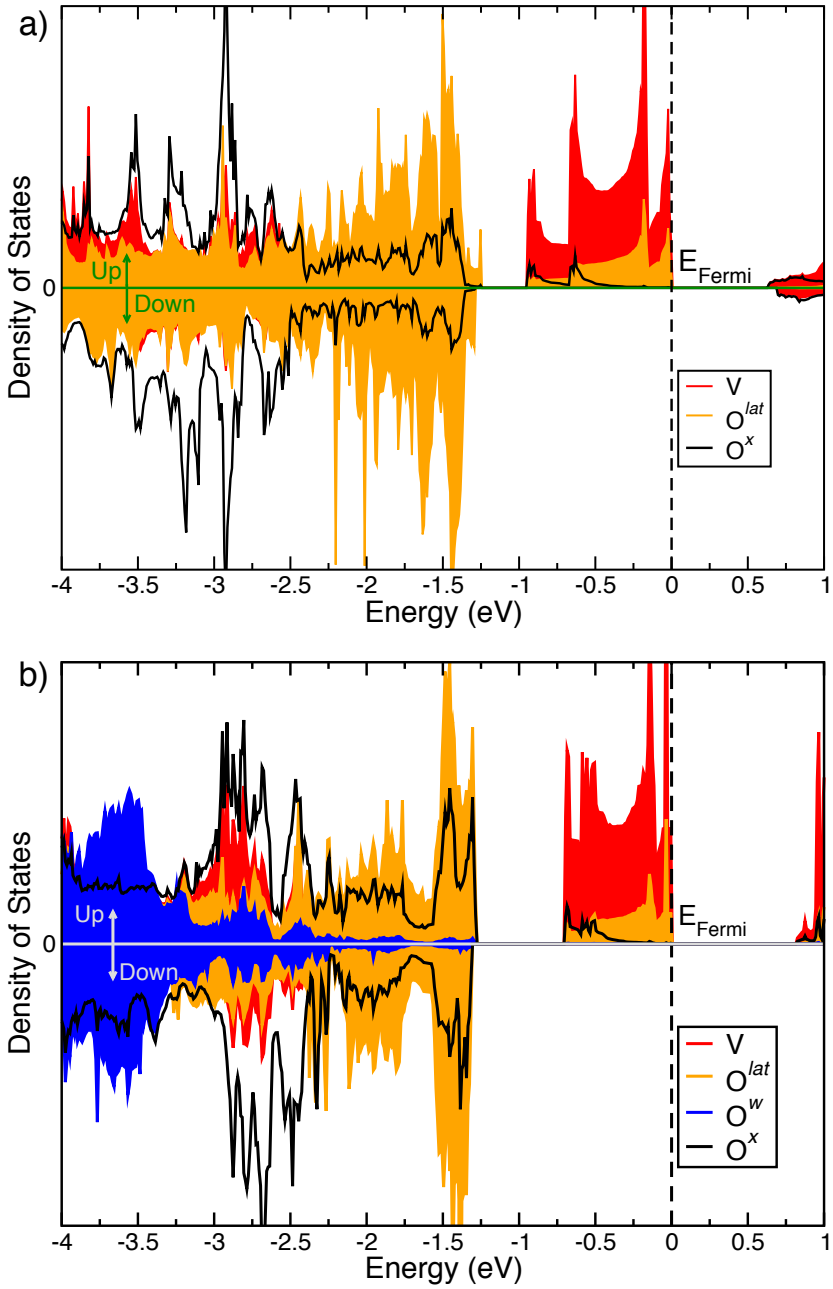

Figure 5-10: Projected Density of States on vanadium (V, red), lattice oxygen away from Mg (O^{lat}, orange), lattice oxygen bonded to the Mg (O^{x}, black) and the oxygen of the water molecules (O^{w}, blue) in the a) dehydrated ($x_{Mg} = 0.5$, $n_{H_2O} = 0$) and b) fully hydrated ($x_{Mg} = 0.5$, $n_{H_2O} = 1$) Mg-Xerogel V_2O_5 are displayed. The Fermi energy, indicated by dashed lines is arbitrarily set at the top of the valence band. Positive and negative DOS indicate spin-up and spin-down electrons, respectively.

The projected DOS of the dehydrated ($x_{Mg} = 0.5$, $n_{H_2O} = 0$) and fully hydrated ($x_{Mg} = 0.5$, $n_{H_2O} = 1$) Mg-Xerogel V_2O_5 are compared in Figure 5-10. From the DOS an increase of the band-gap from the dehydrated ($\sim$ 0.6 eV, Figure 5-10a) to hydrated ($\sim$ 0.8 eV, Figure 5-10b) Mg-Xerogel structure is observed, indicating the importance of nano-crystallinity in ensuring reasonable electrical conductivity of the cathode.

In the DOS of Figure 5-10a and b, the valence band is dominated by localized V (*3d*) spin-up orbitals, a sign that the electrons have been transferred from Mg to V during the intercalation. Close to the Fermi energy, the V (*3d*) states are slightly hybridized with the O (*2p*) of the V_2O_5 bilayers. However, most of the O (*2p*) are found at lower energies and are well separated from the valence band (V (*3d*)), with an increase in separation on hydration. The O (*2p*) orbitals from the water molecules (O^w in Figure 5-10b) are found at lower energies (between -4.0 and -3.0 eV) and hybridize with V (*3p*) orbitals, screening the Mg. Finally, the Mg levels, which are not shown for simplicity in Figure 5-10b, overlap with O^w states attesting the stabilizing coordination effect exerted by H_2O molecules on the intercalated Mg ions.

5.7.9 Atomic coordinates of ground states

All atomic positions are given in fractional coordinates defined by the lattice parameters given for each structure.

$Mg_{0.5}(H_2O)V_2O_5$

GGA

a 3.73 b 10.18 c 11.86
α 94.60 β 90.06 γ 89.86

```
O  0.012741 0.685121 0.772431
O  0.996311 0.691940 0.032341
O  0.005753 0.916003 0.909949
O  0.500740 0.881778 0.105826
O  0.507347 0.882021 0.736529
O  0.506992 0.684734 0.272438
O  0.504150 0.692174 0.532540
O  0.502892 0.915983 0.409790
O  0.005794 0.881941 0.605782
O  0.002163 0.881533 0.236513
O  0.003770 0.315284 0.227768
O  0.000847 0.307941 0.967704
```

O 0.001214 0.084065 0.090391
O 0.504260 0.118147 0.894441
O 0.501295 0.118477 0.263664
O 0.505284 0.314924 0.727794
O 0.496361 0.308144 0.467798
O 0.504048 0.084055 0.590242
O 0.000777 0.118266 0.394366
O 0.004914 0.118057 0.763686
O 0.980774 0.509829 0.388255
O 0.002314 0.490694 0.612062
O 0.478350 0.490240 0.112034
O 0.497419 0.509440 0.888185
H 0.957836 0.590161 0.348090
H 0.985121 0.433442 0.328167
H 0.999495 0.409953 0.652031
H 0.003234 0.566975 0.672361
H 0.458546 0.409822 0.152177
H 0.483315 0.566576 0.172157
H 0.482770 0.590129 0.848280
H 0.498729 0.433171 0.827902
V 0.008563 0.847983 0.766599
V 0.000919 0.856790 0.064621
V 0.502736 0.847673 0.266588
V 0.505559 0.857079 0.564624
V 0.001274 0.152356 0.233599
V 0.003845 0.143029 0.935581
V 0.505188 0.152073 0.733610
V 0.500746 0.143277 0.435551
Mg 0.488434 0.500215 0.500143
Mg 0.983866 0.499907 0.000156

vdW-DF2

a 3.72 b 10.22 c 12.19
α 93.69 β 89.91 γ 90.19

O 0.985590 0.687118 0.767826
O 0.003369 0.690150 0.035154
O 0.002620 0.909338 0.919301
O 0.503622 0.876048 0.093399
O 0.496784 0.900056 0.726562
O 0.511624 0.687080 0.267712
O 0.492339 0.690060 0.535127
O 0.497624 0.909245 0.419292
O 0.996329 0.876029 0.593378
O 0.003345 0.900057 0.226580
O 0.999094 0.312634 0.231720
O 0.008138 0.309638 0.964306
O 0.003699 0.090491 0.080425
O 0.504850 0.123628 0.906342
O 0.499736 0.099706 0.273162
O 0.515909 0.312656 0.731734
O 0.494389 0.309718 0.464442
O 0.498892 0.090515 0.580447
O 0.997808 0.123691 0.406389
O 0.004466 0.099693 0.773130
O 0.974060 0.512746 0.387550
O 0.985072 0.487196 0.610682
O 0.502309 0.487284 0.110671
O 0.517725 0.512627 0.887803
H 0.949708 0.591914 0.346092
H 0.979333 0.436849 0.330406
H 0.961980 0.407761 0.651867
H 0.986901 0.562935 0.667905
H 0.501127 0.407643 0.151958
H 0.503372 0.563056 0.167932
H 0.540363 0.591848 0.846264

H 0.515140 0.436615 0.830729
V 0.995922 0.852257 0.758923
V 0.003683 0.856082 0.054840
V 0.503195 0.852203 0.258929
V 0.495908 0.856023 0.554842
V 0.000216 0.147583 0.240799
V 0.005312 0.143649 0.944856
V 0.505357 0.147541 0.740802
V 0.497214 0.143746 0.444904
Mg 0.470949 0.500035 0.498874
Mg 0.014872 0.500070 0.998956

$Mg_{0.5}(H_2O)_{0.5}V_2O_5$

GGA

a 7.6 b 9.64 c 11.70
α 90.09 β 90.01 γ 90.03

O 0.018723 0.660442 0.801248
O 0.503369 0.674096 0.788641
O 0.502941 0.664674 0.058163
O 0.969969 0.689129 0.040815
O 0.008511 0.917888 0.909033
O 0.503137 0.911736 0.917501
O 0.242517 0.863398 0.112448
O 0.739369 0.881544 0.112763
O 0.256291 0.878434 0.743234
O 0.761000 0.863491 0.746959
O 0.231455 0.660276 0.301275
O 0.744994 0.673714 0.288714
O 0.278733 0.689638 0.540783
O 0.746211 0.664570 0.558194
O 0.240961 0.918159 0.408835
O 0.746336 0.911650 0.417446
O 0.006646 0.863617 0.612453
O 0.509978 0.881630 0.612688
O 0.993022 0.877452 0.243309
O 0.488365 0.863642 0.246922
O 0.973212 0.332049 0.209940
O 0.504986 0.335601 0.194503
O 0.000509 0.337457 0.942298
O 0.529790 0.309247 0.958492
O 0.996674 0.090521 0.082346
O 0.490246 0.080493 0.088904
O 0.256263 0.132039 0.887953
O 0.761536 0.122963 0.883375
O 0.240352 0.143033 0.251554
O 0.741219 0.120452 0.255069
O 0.276704 0.331699 0.710039
O 0.745291 0.335469 0.694649
O 0.249426 0.337591 0.442267
O 0.720593 0.309173 0.458611
O 0.253008 0.090630 0.582214
O 0.759481 0.080455 0.588877
O 0.993649 0.132042 0.387817
O 0.488324 0.123130 0.383328
O 0.009496 0.142630 0.751657
O 0.508629 0.120188 0.755101
O 0.939279 0.506173 0.392091
O 0.050977 0.490895 0.614560
O 0.199243 0.490921 0.114494
O 0.310305 0.505709 0.892037
H 0.865518 0.581007 0.352669
H 0.936054 0.428195 0.336070

H 0.130533 0.417589 0.649138
H 0.048340 0.565394 0.674053
H 0.119251 0.417830 0.149062
H 0.202596 0.565213 0.174149
H 0.383770 0.580620 0.852418
H 0.313242 0.427597 0.836121
V 0.009965 0.833402 0.776062
V 0.510216 0.843186 0.774743
V 0.989406 0.858967 0.073029
V 0.495052 0.839236 0.076889
V 0.239503 0.833244 0.276044
V 0.739063 0.842832 0.274780
V 0.259717 0.859492 0.572951
V 0.754159 0.839163 0.576905
V 0.987696 0.160759 0.224337
V 0.492120 0.166225 0.221608
V 0.004756 0.162952 0.921775
V 0.510663 0.139796 0.925840
V 0.262123 0.160385 0.724411
V 0.757830 0.166048 0.721638
V 0.245162 0.163088 0.421655
V 0.739313 0.139759 0.425795
Mg 0.189197 0.537391 0.448453
Mg 0.798486 0.462826 0.555600
Mg 0.451434 0.462743 0.055380
Mg 0.060563 0.537390 0.948429

vdW-DF2

a 7.66 b 9.76 c 11.85
α 90.12 β 90.01 γ 90.00

O 0.014473 0.657972 0.802591
O 0.510909 0.671329 0.788718
O 0.505969 0.663692 0.056456
O 0.968034 0.686047 0.041656
O 0.009176 0.916524 0.908590
O 0.503317 0.911704 0.917080
O 0.242412 0.860984 0.112216
O 0.738870 0.881482 0.113447
O 0.256603 0.872175 0.743826
O 0.761899 0.863384 0.746409
O 0.235408 0.658075 0.302608
O 0.738163 0.671472 0.288658
O 0.280993 0.686222 0.541692
O 0.743439 0.663609 0.556157
O 0.240501 0.916617 0.408607
O 0.746262 0.911614 0.417148
O 0.006929 0.861167 0.612273
O 0.510521 0.881401 0.613525
O 0.992871 0.872106 0.243802
O 0.487554 0.863855 0.246371
O 0.967967 0.333478 0.207158
O 0.508372 0.338487 0.195730
O 0.997231 0.338774 0.944937
O 0.531142 0.311986 0.958274
O 0.996860 0.089668 0.083147
O 0.489158 0.082754 0.089522
O 0.256092 0.134679 0.887719
O 0.761634 0.123074 0.883119
O 0.240138 0.148047 0.251955
O 0.741028 0.121672 0.255390
O 0.281584 0.333849 0.707176
O 0.741091 0.338753 0.695524
O 0.252222 0.338907 0.444913
O 0.718958 0.311914 0.458035
O 0.252607 0.089852 0.583205

O 0.760118 0.082726 0.589576
O 0.993581 0.134495 0.387777
O 0.487975 0.123083 0.383323
O 0.009414 0.148284 0.751860
O 0.508513 0.122208 0.755373
O 0.943190 0.506410 0.391926
O 0.045455 0.490378 0.613594
O 0.204164 0.490397 0.113687
O 0.306332 0.506231 0.892179
H 0.871224 0.579828 0.354743
H 0.936496 0.429911 0.336922
H 0.123204 0.417963 0.645926
H 0.044693 0.562794 0.672655
H 0.126710 0.417904 0.146126
H 0.205137 0.562899 0.172679
H 0.377937 0.579796 0.854922
H 0.313094 0.429828 0.837080
V 0.009855 0.830783 0.776979
V 0.511743 0.840259 0.775788
V 0.988789 0.856050 0.073238
V 0.495275 0.837935 0.075948
V 0.239734 0.830888 0.276983
V 0.737731 0.840407 0.275769
V 0.260535 0.856221 0.573283
V 0.754106 0.837792 0.575973
V 0.986211 0.163371 0.223164
V 0.492178 0.168727 0.221463
V 0.004428 0.164828 0.922514
V 0.510721 0.142307 0.926335
V 0.263278 0.163724 0.723170
V 0.757244 0.169004 0.721365
V 0.245166 0.164923 0.422588
V 0.739006 0.142152 0.426335
Mg 0.194209 0.536696 0.447626
Mg 0.791314 0.463610 0.556721
Mg 0.458309 0.463674 0.056893
Mg 0.055278 0.536561 0.947714

$\mathbf{Mg_{0.25}(H_2O)_{0.5}V_2O_5}$

GGA

a 3.70 b 10.30 c 11.70
α 93.16 β 90.00 γ 90.00

O 0.994055 0.681661 0.770223
O 0.992227 0.686517 0.041114
O 0.992967 0.901997 0.916043
O 0.492124 0.873440 0.098269
O 0.493862 0.878318 0.741277
O 0.489001 0.692938 0.282256
O 0.496694 0.691935 0.534809
O 0.493066 0.917585 0.410826
O 0.994258 0.880439 0.607630
O 0.991866 0.883823 0.231222
O 0.994030 0.318362 0.229775
O 0.992206 0.313498 0.958888
O 0.992961 0.098007 0.083961
O 0.492114 0.126564 0.901731
O 0.493855 0.121689 0.258723
O 0.488950 0.307084 0.717746
O 0.496679 0.308077 0.465193
O 0.493055 0.082423 0.589175
O 0.994254 0.119569 0.392369
O 0.991851 0.116183 0.768778

```
O  0.002581 0.487214 0.613306
O  0.002522 0.512798 0.386689
H  0.013649 0.408032 0.656137
H  0.000400 0.560394 0.673667
H  0.000357 0.439617 0.326333
H  0.013494 0.591973 0.343866
V  0.993986 0.839564 0.767550
V  0.992234 0.841754 0.060351
V  0.491515 0.849228 0.268792
V  0.494342 0.853962 0.565465
V  0.993975 0.160420 0.232452
V  0.992223 0.158238 0.939646
V  0.491495 0.150763 0.731211
V  0.494338 0.146045 0.434534
Mg 0.503726 0.500005 0.500001
```

vdW-DF2

a 3.71 b 10.79 c 11.97
α 94.46 β 90.00 γ 90.00

```
O  0.997991 0.678383 0.773927
O  0.995806 0.682138 0.041376
O  0.996779 0.900083 0.916920
O  0.496063 0.870813 0.098623
O  0.497815 0.875800 0.742287
O  0.494289 0.690090 0.285074
O  0.501527 0.689736 0.535341
O  0.496843 0.916831 0.410702
O  0.998296 0.878715 0.608636
O  0.995934 0.881097 0.231484
O  0.997979 0.321613 0.226060
O  0.995828 0.317854 0.958633
O  0.996775 0.099898 0.083059
O  0.496082 0.129182 0.901387
O  0.497795 0.124196 0.257725
O  0.494286 0.309919 0.714935
O  0.501523 0.310268 0.464666
O  0.496842 0.083166 0.589296
O  0.998288 0.121294 0.391373
O  0.995930 0.118897 0.768523
O  0.009286 0.485251 0.612706
O  0.009278 0.514753 0.387266
H  0.020759 0.405736 0.653895
H  0.007502 0.555484 0.672750
H  0.007502 0.444513 0.327233
H  0.020754 0.594265 0.346065
V  0.997963 0.836462 0.769721
V  0.995792 0.837818 0.059937
V  0.495613 0.846838 0.270429
V  0.498425 0.851811 0.565726
V  0.997928 0.163541 0.230303
V  0.995811 0.162174 0.940087
V  0.495622 0.153168 0.729606
V  0.498422 0.148215 0.434264
Mg 0.511816 0.500010 0.499988
```

$Mg_{0.5}V_2O_5$

GGA

a 3.80 b 9.30 c 11.66
α 81.06 β 90.00 γ 90.00

```
O  0.000000 0.643397 0.852230
O  1.000000 0.665288 0.083636
O  0.000000 0.913845 0.923834
O  0.500000 0.865145 0.135109
O  0.500000 0.851165 0.767794
O  0.500000 0.643380 0.352247
O  0.500000 0.665274 0.583646
O  0.500001 0.913844 0.423826
O  0.000000 0.865153 0.635101
O  0.000000 0.851135 0.267800
O  0.000001 0.356612 0.147751
O  0.999999 0.334724 0.916351
O  0.000000 0.086154 0.076174
O  0.499999 0.134851 0.864902
O  0.500001 0.148864 0.232203
O  0.499998 0.356607 0.647762
O  0.500001 0.334728 0.416366
O  0.500000 0.086152 0.576167
O  0.000001 0.134859 0.364892
O  0.999999 0.148831 0.732208
V  0.000000 0.821104 0.802277
V  0.000000 0.843297 0.098352
V  0.500000 0.821088 0.302285
V  0.500000 0.843313 0.598345
V  0.000001 0.178922 0.197716
V  0.999999 0.156695 0.901656
V  0.499999 0.178874 0.697730
V  0.500000 0.156695 0.401647
Mg 0.500000 0.499993 0.500008
Mg 0.000000 0.500009 0.999985
```

vdW-DF2

a 3.84 b 9.42 c 11.81
α 81.25 β 90.00 γ 90.00

```
O  0.000000 0.641018 0.852240
O  1.000000 0.664284 0.082920
O  0.000000 0.913392 0.923015
O  0.500000 0.865008 0.135207
O  0.500000 0.848335 0.767933
O  0.500000 0.641020 0.352239
O  0.500000 0.664291 0.582919
O  0.500000 0.913394 0.423015
O  0.000000 0.865007 0.635210
O  1.000000 0.848339 0.267932
O  1.000000 0.358983 0.147761
O  0.000000 0.335711 0.917082
O  1.000000 0.086607 0.076987
O  0.500000 0.134991 0.864791
O  0.500000 0.151662 0.232068
O  0.500000 0.358978 0.647762
O  0.499999 0.335716 0.417081
O  0.500000 0.086609 0.576986
O  1.000000 0.134993 0.364793
O  0.000000 0.151663 0.732067
V  0.000000 0.818704 0.802898
V  1.000000 0.842020 0.097858
V  0.500000 0.818704 0.302898
V  0.500000 0.842012 0.597857
V  1.000000 0.181291 0.197104
V  0.000000 0.157986 0.902142
V  0.500000 0.181299 0.697099
V  0.500000 0.157983 0.402142
Mg 0.500000 0.500002 0.499997
Mg 1.000000 0.499998 1.000000
```

V_2O_5

GGA

a 3.66 b 10.01 c 11.74
α 95.52 β 90.00 γ 90.00

O 0.000001 0.670473 0.763010
O 1.000000 0.674681 0.023638
O 1.000000 0.898770 0.911236
O 0.500000 0.865758 0.094277
O 0.500001 0.870801 0.728440
O 0.500005 0.670455 0.263025
O 0.500000 0.674705 0.523660
O 0.500000 0.898766 0.411224
O 1.000000 0.865786 0.594276
O 0.000001 0.870758 0.228435
O 0.999999 0.329548 0.236976
O 0.999999 0.325299 0.976336
O 0.000000 0.101241 0.088776
O 0.499999 0.134214 0.905724
O 0.500000 0.129249 0.271566
O 0.499998 0.329520 0.736989
O 0.499999 0.325316 0.476366
O 0.500000 0.101226 0.588764
O 0.000001 0.134244 0.405723
O 0.999999 0.129196 0.771561
V 1.000000 0.829570 0.760735
V 0.000000 0.833971 0.052166
V 0.500001 0.829532 0.260733
V 0.499999 0.833998 0.552168
V 0.000000 0.170476 0.239268
V 1.000000 0.165997 0.947830
V 0.499998 0.170427 0.739265
V 0.500001 0.166022 0.447833

vdW-DF2

a 3.69 b 9.30 c 11.90
α 95.85 β 90.00 γ 90.00

O 0.999999 0.638846 0.762683
O 0.999998 0.646554 0.020166
O 1.000000 0.890648 0.910330
O 0.499999 0.853980 0.093800
O 0.500000 0.857784 0.728221
O 0.499999 0.638839 0.262682
O 0.499999 0.646554 0.520159
O 0.500000 0.890650 0.410331
O 1.000000 0.853978 0.593800
O 0.999999 0.857788 0.228222
O 0.000001 0.361152 0.237321
O 0.000001 0.353443 0.979842
O 0.000000 0.109352 0.089671
O 0.500001 0.146022 0.906201
O 0.500000 0.142213 0.271778
O 0.500001 0.361161 0.737315
O 0.500001 0.353439 0.479831
O 0.500000 0.109349 0.589668
O 0.000001 0.146016 0.406198
O 0.000001 0.142214 0.771780
V 1.000000 0.812361 0.760578
V 0.999999 0.819929 0.050340
V 0.499999 0.812360 0.260579
V 0.499999 0.819931 0.550340
V 0.000001 0.187658 0.239422

```
V 0.000000 0.180075 0.949661
V 0.500001 0.187628 0.739423
V 0.500001 0.180074 0.449660
```

$(H_2O)V_2O_5$

GGA

a 3.69 b 12.76 c 11.69
α 96.73 β 90.00 γ 87.30

```
O 0.009797 0.260547 0.241356
O 0.008987 0.257638 0.984181
O 0.036721 0.079652 0.090250
O 0.532557 0.107765 0.909180
O 0.533658 0.103184 0.272420
O 0.508475 0.261529 0.744906
O 0.508968 0.258083 0.478582
O 0.536864 0.081602 0.590319
O 0.032950 0.107157 0.407083
O 0.033223 0.103940 0.774440
O 0.092875 0.742053 0.755014
O 0.089037 0.744360 0.015786
O 0.062138 0.921049 0.907999
O 0.565481 0.894276 0.089884
O 0.566638 0.899559 0.725285
O 0.590146 0.741842 0.257383
O 0.593590 0.746359 0.516473
O 0.561977 0.922197 0.408504
O 0.067213 0.896728 0.590172
O 0.064944 0.898440 0.225283
O 0.938131 0.526170 0.409455
O 0.992064 0.429610 0.614666
O 0.461151 0.488863 0.247661
O 0.473544 0.506010 0.762279
H 0.745885 0.505394 0.349883
H 0.879355 0.600350 0.435758
H 0.781428 0.460138 0.663887
H 0.970158 0.459658 0.540744
H 0.431098 0.419899 0.204788
H 0.247443 0.502932 0.300604
H 0.275460 0.478624 0.708513
H 0.412135 0.580716 0.782872
V 0.028595 0.135001 0.242080
V 0.028583 0.132478 0.950440
V 0.528006 0.136677 0.742943
V 0.528735 0.132820 0.449921
V 0.071676 0.867829 0.756138
V 0.069323 0.869590 0.048540
V 0.569972 0.866815 0.255802
V 0.571199 0.872507 0.548528
```

vdW-DF2

a 3.69 b 11.28 c 11.91
α 94.37 β 90.06 γ 91.21

```
O 0.012689 0.296545 0.223760
O 0.015759 0.290131 0.963308
O 0.004596 0.090632 0.081978
O 0.507202 0.116921 0.898656
O 0.504587 0.116749 0.263977
O 0.525424 0.290447 0.727072
O 0.517718 0.294014 0.467973
```

```
O 0.504504 0.089659 0.579755
O 0.005868 0.121864 0.398199
O 0.007576 0.109599 0.763279
O 0.974437 0.705125 0.760126
O 0.977286 0.704064 0.023846
O 0.992493 0.907183 0.907888
O 0.490477 0.877415 0.090489
O 0.490733 0.886719 0.724869
O 0.483799 0.700736 0.260168
O 0.483035 0.705875 0.525380
O 0.492636 0.906159 0.405796
O 0.990883 0.879459 0.589638
O 0.991706 0.882445 0.224656
O 0.989996 0.530889 0.387412
O 0.130163 0.479850 0.621701
O 0.423683 0.482167 0.097812
O 0.451619 0.532257 0.862832
H 0.732571 0.517185 0.371174
H 0.011397 0.527705 0.469361
H 0.190828 0.517741 0.696257
H 0.341714 0.432329 0.601699
H 0.197092 0.439785 0.112329
H 0.438019 0.546724 0.157162
H 0.703964 0.514270 0.845757
H 0.426728 0.519955 0.943545
V 0.006031 0.153735 0.229921
V 0.008435 0.146662 0.940223
V 0.511250 0.147471 0.729940
V 0.508090 0.150879 0.440655
V 0.987462 0.848020 0.757902
V 0.988005 0.847303 0.047790
V 0.490010 0.844318 0.257984
V 0.489557 0.848998 0.547738
```

Chapter 6

Impact of intermediate sites on bulk diffusion barriers: Mg intercalation in $Mg_2Mo_3O_8$

6.1 Introduction

Rechargeable Mg batteries have received interest as an energy storage system that potentially offers high energy density. The major advantage relies on the benefits of Mg metal as the negative electrode, which, in addition to being inexpensive, abundant and safe in handling and storage, also provides high volumetric capacity (3833 mAh cm^{-3}) and can be free of dendrite growth when operating in an electrochemical cell.[141, 252, 142] However, the development of corresponding positive electrode materials has been slow.[252] Since the discovery of the first seminal functional Mg insertion positive electrode – the Chevrel phase (CP, Mo_6S_8),[8] only recently have two other structures been shown to be suitable for Mg (de)intercalation in a full cell arrangement with a Mg anode, namely the spinel and layered titanium sulfide.[214, 212] The above materials take the advantage of a "soft" anionic framework that interacts weakly with the Mg^{2+} and assist its mobility. On the contrary, sluggish multivalent ion mobility is generally observed in oxide lattices. Nev-

ertheless, oxides are still of great interest due to their potentially higher operating voltage.[2, 115, 183, 190, 22, 64, 191, 192, 126]

Levi *et al.* have speculated that the presence of Mo_6 clusters in the CP structure is one of the key factors for facile Mg^{2+} mobility by promoting charge redistribution.[115] The possibility that a similar principle may apply to oxides guided us to $Mg_2Mo_3O_8$ (Figure 6-1a), which has Mo_3 clusters in the Mo_3O_8 layers (Figure 6-1b).[134, 41] In this structure, Mg occupies both octahedral and tetrahedral sites between the layers. While octahedral Mg share both edges and corners with MoO_6 octahedra (Figure 6-1a), tetrahedral Mg share corners with MoO_6 and MgO_6 octahedra. Since Mg is also present in a "non-preferred" tetrahedral coordination (Figure 6-1a),[25] a Mg diffusion pathway with lower migration barriers is expected than when Mg is exclusively found in its preferred octahedral coordination,[183] such as in conventional layered oxides. In the case of layered oxides, the Mg diffusion pathways contain an intermediate tetrahedral site presumably with high energy relative to the stable octahedral site, leading to poor Mg mobility.[183]

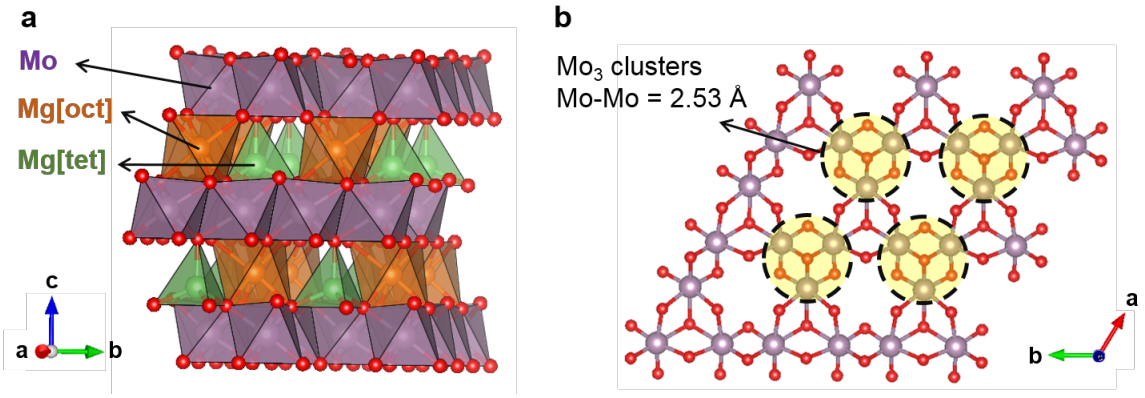

Figure 6-1: (a) Crystal structure of $Mg_2Mo_3O_8$. (b) MoO_6 octahedra layer showing Mo_3 clusters.

We note that the Li analogue ($Li_4Mo_3O_8$) has previously been examined in a Li cell, offering 218 mAh g^{-1} initial specific capacity.[19] Other materials with similar structures containing Mo_3 clusters, such as $LiMoO_2$ and Li_2MoO_3, also function well as Li-ion positive electrodes.[19, 20, 129] On the other hand, only limited work has

been done for Mg intercalation in Mo-oxides,[64, 84, 93] motivating us to examine the Mg^{2+} diffusion properties in $Mg_2Mo_3O_8$ and its potential to be a positive electrode material for Mg batteries.

6.2 Chemical and Electrochemical demagnesiation

$Mg_2Mo_3O_8$ was obtained by solid-state synthesis (see Appendix, Section 6.6) and provided particles a few micrometers in size (Figure 6-2a). Its X-ray diffraction (XRD) pattern was indexed in the $P6_3mc$ space group characteristic of this material (Figure 6-2b). In order to study the possibility of Mg removal from such a structure, chemical demagnesiation was carried out using NO_2BF_4, a commonly used oxidizing agent for chemical delithiation.[246] $Mg_2Mo_3O_8$ and NO_2BF_4 were reacted in a 1:4 ratio, which would allow complete Mg de-intercalation if each NO_2BF_4 sustained a one electron reduction as anticipated. Energy dispersive X-ray spectroscopy (EDX) reveals that the majority of the Mg was removed from the structure (Table 6.1). The particles become smaller after demagnesiation (Figure 6-2c), suggesting some changes in the material. Despite these differences, the XRD results indicate no shift of the peaks (Figure 6-2d). The atomic positions obtained by Rietveld refinement[179] are almost the same as the pristine (Table 6.3 in Section 6.6), suggesting that a two-phase reaction takes place, with the demagnesiated phase being amorphous. During this process, Mg is presumably first removed from the outer shell, leading to the destabilization of the parent lattice and eventual amorphization. The amount of amorphous phase in the demagnesiated product is estimated to be around 87 wt% using Si as an external standard method (Figure 6-2d, see Section 6.6 for details), giving an overall composition of $Mg_{0.24}Mo_3O_8$, which is similar to the cationic ratio determined by EDX (Table 6.1) and indicates complete demagnesiation of the amorphous component. The $\sim$ 13 wt% unreacted $Mg_2Mo_3O_8$ results from the reduced oxidizing strength of NO_2BF_4 exhibited near the end of the reaction due to low oxidizer concentration, or other side reactions. Partial demagnesiation from $Mg_2Mo_3O_8$ was not achieved when the ratio of oxidizing agent was reduced ($Mg_2Mo_3O_8$:NO_2BF_4 = 1:2), as indicated by

the preservation of the initial phase obtained by XRD refinement (Figure S1a and Table 6.5). Together with the decrease of overall Mg concentration (Mg/Mo ratio of $\sim 0.53(4)/3$ by EDX) and the co-existence of different morphologies (Figure S1b), the XRD data suggests that part of $Mg_2Mo_3O_8$ undergoes complete demagnesiation and becomes amorphous with some fraction of material not participating in the reaction.

Table 6.1: EDX results of $Mg_2Mo_3O_8$ before and after chemical demagnesiation.

Sample	Pristine	Demagnesiated
Mg/Mo	1.59(4)/3	0.13(6)/3

Since the degree of chemical oxidation was hard to control, we attempted to evaluate stepwise demagnesiation behavior by an electrochemical method. As it has been suggested that the Mg desolvation process depends on the solvent,[33, 34] and this is critical for the electrochemical mechanism at the positive electrode,[236, 214] $Mg_2Mo_3O_8$ was examined in both non-aqueous (all phenyl complex – APC[12]) and aqueous ($Mg(ClO_4)_2$ in water) systems. A demagnesiation voltage similar to the delithiation of $Li_4Mo_3O_8$ (average of $\sim$ 2.4 V vs. Mg),[19] or at $\sim$ 2.6 V as predicted by first principles calculations (Figure 6-8, see Section 6.6 for details) could be expected. Both electrolytes offer a stable voltage window for this range; however, no electrochemical activity was observed in either system (Figure 6-6). Such results potentially indicate the existence of a high Mg^{2+} diffusion barrier in the structure, hence kinetics being the main limitation. Chemical oxidation, on the other hand, might involve a mechanism other than simple cation diffusion, such as a partial dissolution/re-precipitation process. This helps in lowering the kinetic barrier and establishes successful Mg removal.

In order to understand the amorphization upon chemical demagnesiation and rationalize the lack of electrochemical activity in $Mg_2Mo_3O_8$, we carried out first principles calculations to determine the energy above hull (E^{hull}) indicating the stability of the structure, and the activation barriers for Mg diffusion within the structure (methodological details of the calculations are provided in Sections 2.1, 2.2, and 2.4).

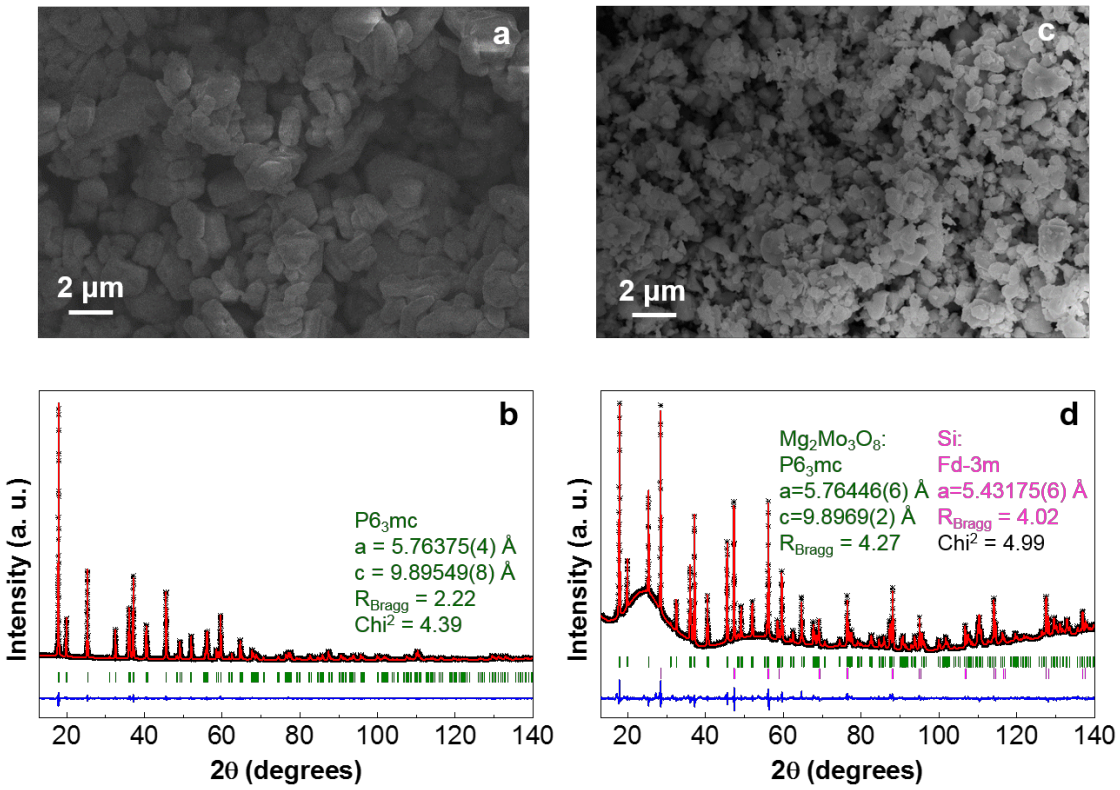

Figure 6-2: (a) SEM image and (b) Rietveld refinement fit of pristine $Mg_2Mo_3O_8$ (Bragg-Brentano geometry). (c) SEM image of the demagnesiated sample. (d) Rietveld refinement of the demagnesiated sample with external silicon standard added to evaluate the percentage of amorphous phase. The mixture was sealed in X-ray capillary under Ar and was measured in Debye-Scherrer geometry. Black crosses – experimental data, red lines – fitted data, blue line – difference map between observed and calculated data, green ticks – the $P6_3mc$ phase of $Mg_2Mo_3O_8$, pink ticks – the $Fd\bar{3}m$ phase of Si.

6.3 Thermodynamics of Mg (de)intercalation

The energy above the convex ground state hull (E^{hull}) of the $Mg_xMo_3O_8$ structure, calculated with respect to the stable compounds in the Mg-Mo-O ternary phase diagram, can be used to evaluate the thermodynamic stability of the structure on demagnesiation.[191, 126] Typically, a thermodynamically stable structure will have an E^{hull} of 0 meV/atom, while more positive E^{hull} values indicate greater driving force to form other phases, which may be reflected as difficulty in synthesizing a compound, or as decomposition during (de)intercalation. Also, E^{hull} values are evaluated

at 0 K and entropic contributions can stabilize a structure at higher temperatures. The values listed in Table 6.2 have been determined from the available compounds in the Materials Project database.[88] The trends in Table 6.2 indicate an increasing E^{hull} with increasing Mg removal from the $Mg_2Mo_3O_8$ structure, corresponding to an increase in the thermodynamic driving force for decomposition. The E^{hull} values at lower Mg concentrations are very high – consistent with the experimentally observed amorphization during chemical Mg extraction from $Mg_2Mo_3O_8$ (Figure 6-2) and the naturally amorphous occurrence of Mo_3O_8.[229, 209]

6.4 Mg mobility in $Mg_2Mo_3O_8$

To evaluate Mg mobility in the $Mg_2Mo_3O_8$ structure, the possible Mg diffusion hops within the structure were determined. Being a layered structure, $Mg_2Mo_3O_8$ can be visualized on a 2D-plane, as shown in Figure 6-3, with octahedral Mo, tetrahedral Mg and octahedral Mg indicated by purple, green and orange triangles, respectively. The four possible Mg→Mg hops that can occur in the structure are illustrated by the black circle and arrows in Figure 6-3. Three hops (black arrows) occur in the same Mg-plane and the fourth hop (black circle) moves Mg across a Mo-plane. The shortest hops (type 1 and 2) span $\sim$ 3.38 Å and $\sim$ 4.33 Å, respectively, and involve Mg migration from a tetrahedral site to an octahedral site (or vice-versa), while hops 3 and 4 are $\sim$ 5.76 Å in distance and involve Mg jumps between similarly coordinated sites (oct → oct or tet → tet). Although hops 3 and 4 are direct between octahedral or tetrahedral Mg sites, they are likely to be constituted by two consecutive hops of type

Table 6.2: The E^{hull} values (in meV/atom) and the corresponding decomposition products are listed as a function of Mg content in the Mo_3O_8 structure, as obtained from the Materials Project database. The comments column indicates available experimental observations.

Composition	E^{hull}	Decomposition products	Comments
$Mg_2Mo_3O_8$	51	MoO_2 + MgO	Chemically synthesizable
$MgMo_3O_8$	180	MoO_2 + $MgMoO_4$	–
Mo_3O_8	330	MoO_2 + Mo_8O_{23}	Naturally amorphous[229, 209]

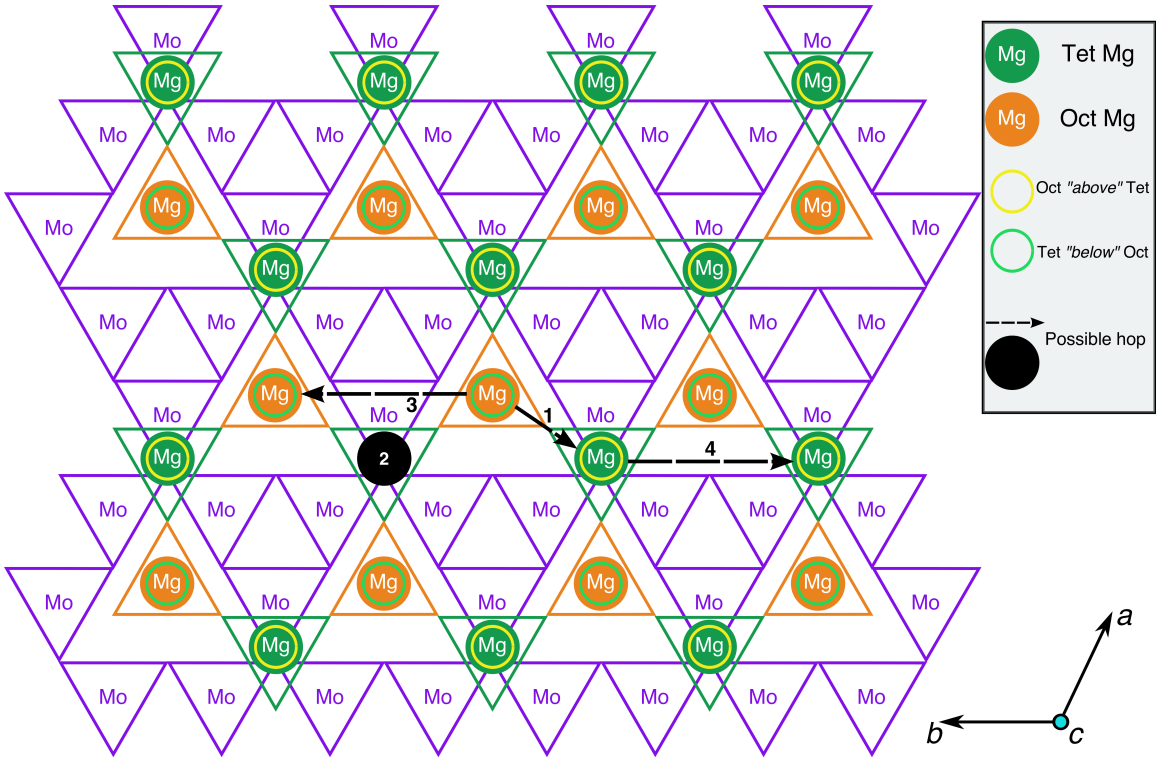

Figure 6-3: A 2D-view of the $Mg_2Mo_3O_8$ structure perpendicular to the layer spacing direction (c-axis) is shown. Purple, green and orange triangles indicate MoO_6 octahedra, Mg tetrahedra and Mg octahedra, respectively. The yellow and green circles correspond to octahedral and tetrahedral Mg atoms across a Mo-plane. The black circles and arrows indicate possible Mg→Mg hops within the structure.

1 (i.e. an oct → tet hop followed by a tet → oct hop and vice-versa). Alternate routes for hops 3 and 4 are not possible due to intermediate Mg tetrahedral sites, which will face-share with MoO_6 octahedra and experience strong electrostatic repulsions as a result. Hence, hops 1 and 2 are the relevant Mg migration pathways that need to be considered in calculations.

Figure 6-4a displays the calculated Mg migration barriers (at $x_{Mg} \sim 2$ with dilute vacancy limit) along the hop 1 (black) and 2 (red) pathways, with the respective hop distances normalized on the x-axis. Both hops begin at a tetrahedral Mg and terminate at an octahedral Mg, explaining the difference in energy between the end points ($\sim$ 250 meV). Notably, Mg mobility along both hops 1 and 2 is expected to be poor, given the large migration barriers ($\sim$ 1200 meV and $\sim$ 2000 meV for

hops 1 and 2, respectively), compared to the 525 – 650 meV required for bulk Mg mobility at reasonable rates.[183] The high migration barriers also explain the lack of electrochemical activity observed. Nevertheless, if any Mg migration is observed in the structure, the Mg^{2+} ions are likely to diffuse along the in-plane hop 1 pathway.

While the high barrier for hop 2 is due to the strong electrostatic repulsion Mg experiences from Mo atoms as it passes through a triangular face of oxygen atoms across the Mo_3O_8 layer, a closer look into hop 1 is required to understand the large barriers. Visualization of the Mg migration along hop 1 is given in Figure 6-4b, with intermediate sites and their respective energies (in Figure 6-4a) indicated by the numbered circles. Sites 1, 2 and 3 respectively correspond to the O–Mg–O "dumbbell" configuration,[183] the intermediate metastable tetrahedral site (yellow) and the triangular face between the intermediate tetrahedral and stable octahedral sites. While site 3 (triangular face, Figure 6-4b) has an energy of $\sim$ 685 meV with respect to the tetrahedral site (similar to $\sim$ 600 – 800 meV observed in oxide spinels[126]), the magnitude of the barrier is determined by site 1, where Mg is situated along an O–O bond (edge of the stable tetrahedron), in a dumbbell configuration. Previous evaluations of Mg migration through an O–O dumbbell hop for layered NiO_2 have reported high barriers ($\sim$ 1400 meV),[183] similar to the value reported in this work.

6.5 Discussion and Conclusions

Although the O–Mg–O dumbbell hops are precluded from occurring in usual cathode materials[183, 190] due to the presence of alternate low-energy pathways, no such possibility exists for Mg migration in the $Mg_2Mo_3O_8$ structure. For example, an alternate pathway for hop 1 that avoids the O–Mg–O dumbbell is shown in Figure 6-4c. The intermediate octahedral (dark blue) and tetrahedral (yellow) sites in Figure 6-4c share a triangular face with the stable tetrahedral (green) and octahedral (orange) sites, respectively. Additionally, each intermediate site also shares a triangular face with a MoO_6 octahedron (blue polyhedron, Figure 6-4c). While an intermediate Mg octahedron that face-shares with a higher valent transition metal octahedron

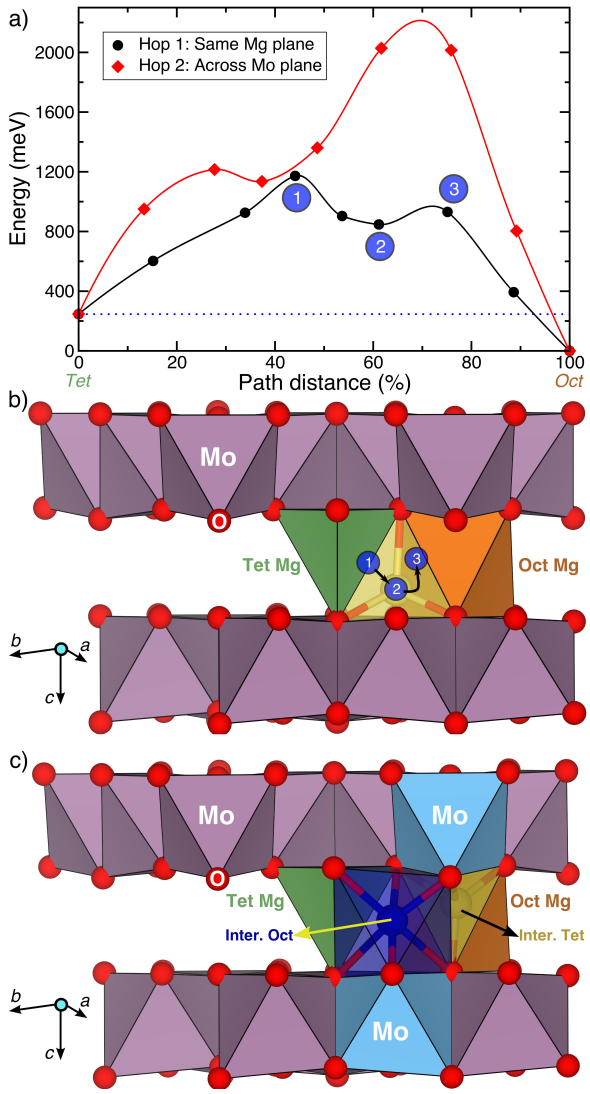

Figure 6-4: (a) The activation barrier for Mg diffusion along hops 1 and 2 in the $Mg_2Mo_3O_8$ structure, with the normalized path distance on the x-axis. (b) A closer view of hop 1, where the numbered circles correspond to various intermediate sites along the hop as labeled in (a). The intermediate tetrahedral site, which is edge-sharing with the stable tetrahedral site (green), is indicated in yellow. (c) An alternate pathway for hop 1 that involves intermediate octahedral (dark blue) and tetrahedral (yellow) sites, which are face-sharing with the stable tetrahedral (green) and octahedral (orange) sites, respectively. The intermediate sites in (c) also share a face with the MoO_6 octahedra (blue).

need not preclude Mg migration, the intermediate tetrahedral site (yellow site, Figure 6-4c) will experience much stronger electrostatic repulsion from the face-sharing MoO_6 octahedron, subsequently increasing its energy and preventing any potential

Mg migration. Indeed, Mg migration calculations initializing hop 1 as displayed in Figure 6-4c relax to a path similar to the O–Mg–O hop (Figure 6-4b) with a similar barrier ($\sim$ 1150 meV, Figure 6-9). Notably, scenarios involving a Mg^{2+} ion diffusing through an intermediate (tetrahedral) site that face-shares with a transition metal polyhedron lead to high migration barriers in oxides (e.g., high Mg barriers in layered NiO_2[183]), while analogous trends have been observed for Li-diffusion in disordered rock-salt structures.[224] Thus, the high Mg migration barrier in $Mg_2Mo_3O_8$ can be attributed to the intermediate O–Mg–O dumbbell configuration, which occurs in the absence of alternate low energy pathways. This indicates the importance of intermediate sites along a diffusion path, determined by the specific topology of cation sites in an anion lattice, in addition to the occurrence of the mobile cation with a non-preferred coordination and a preferentially coordinated metastable site.[183]

One of the challenges towards the development of high energy density secondary Mg batteries is the design of an ideal positive electrode, which can reversibly intercalate Mg at a high voltage with high capacities at reasonable rates. The $Mg_2Mo_3O_8$ structure used in this study was primarily motivated by the presence of Mo_3 clusters (similar to the Mo_6 clusters in the Chevrel-positive electrodes) and the occurrence of Mg in a non-preferred tetrahedral coordination (satisfying one of the design rules known in literature[183]). While Mg could be chemically extracted from the structure, albeit with significant amorphization, no electrochemical activity was observed. Further analysis using first-principles calculations revealed high E^{hull} values (structural instability) at low Mg content and high Mg migration barriers (poor bulk Mg mobility in the structure), explaining the aforementioned experimental observations. The high activation barrier for Mg diffusion in $Mg_2Mo_3O_8$ arises from the O–Mg–O dumbbell hop, reflecting the impact of intermediate sites along a diffusion pathway besides cation coordination preferences. Thus, in searches of high Mg-mobility oxide positive electrodes, a careful analysis of the diffusion pathway and the topology of cation sites is advantageous - such as identifying low-energy intermediate sites - in addition to the requirement of Mg being found in a non-preferred coordination environment.[183] Such understanding of Mg diffusion pathways will help to find

suitable positive electrodes for multivalent batteries.

6.6 Appendix

6.6.1 Experimental Methods

Synthesis and characterization

$Mg_2Mo_3O_8$ was synthesized by heating a 1:1 mixture of MgO and MoO_2 at 1000 °C for 12 hours under Ar flow. The small amount of MgO impurity was washed away with 1M HCl. X-ray diffraction (XRD) was carried out on the PANalytical Empyrean using Cu Kα radiation with Bragg-Brentano geometry. De-magnesiation was carried out by stirring the pristine material in 0.2 M NO_2BF_4 (Sigma-Aldrich, 95%) in acetonitrile (Caledon, 99.9%, dried over 3 Å molecular sieves) at 1:4 molar ratio for 1 day in an Ar-filled glovebox (O_2 and H_2O level below 5 ppm). The product was filtered and washed with acetonitrile. The fraction of crystalline phase in the demagnesiated material was estimated by the external standard method. Typically, the demagnesiated product was ground with silicon (325 mesh, Sigma-Aldrich, 99%) in 9:1 weight ratio in Ar-filled glovebox and sealed in 0.3 mm glass capillary. XRD was carried out with the Debye-Scherrer geometry. Rietveld refinements[179] were performed with FullProf suite.[182] Refining Mg occupancies did result in any change from the pristine composition so they were fixed at 1. The refined $Mg_2Mo_3O_8$:Si weight ratio was 0.54:0.46 (Table **??**), resulting in 13 wt% of crystalline phase in the demagnesiated sample. The morphologies and elemental ratios of the materials were studied with a Zeiss field emission scanning electron microscope (SEM) equipped with an energy dispersive X-ray spectroscopy (EDX) detector.

Electrochemistry

For non-aqueous tests, positive electrodes were prepared by mixing the pristine material with super P and polyvinylidene fluoride (PVDF, Sigma-Aldrich, average Mw 534,000) at 8:1:1 weight ratio in N-methyl-2-pyrrolidone (NMP, Sigma-Aldrich, 99.5%)

and casting on Mo foil. APC electrolyte was synthesized with previous reported procedure.[138] Magnesium metal was polished with carbide paper (Mastercraft ®, 180 grit SiC), cleaned with Kimwipe and served as the counter and reference electrode. The 2325 coin cells with the positive electrode side protected by Mo foil were assembled in an Ar-filled glovebox. In aqueous system, slurry with the same recipe was used and casted on Ti foil. The electrode was assembled in the T-shape Swagelok three-electrode cell with Pt gauze (Sigma-Aldrich, 99.9%) counter, Ag/AgCl reference electrode, and 0.5 M $Mg(ClO_4)_2$ in deionized water electrolyte. Galvanostatic tests were carried out on the Bio-logic VMP3 cycler.

6.6.2 Computational Methods

Voltage calculations

In order to compute the average voltage for Mg intercalation between the ranges of $1 \leq x_{Mg} \leq 2$ and $0 \leq x_{Mg} \leq 1$ in $Mg_xMo_3O_8$, the stable Mg-vacancy ordering at $x_{Mg} = 1$ needs to be determined. To do so, we considered four Mg-vacancy orderings, as displayed in Figure 6-7, enumerated in a conventional Mo_3O_8 cell, which consists of 16 oxygen atoms. Based on the calculated energies, the Mg-vacancy ordering where Mg solely occupies octahedral sites (Figure 6-7a) was found to be the most stable.

Once the stable Mg-ordering at $x_{Mg} = 1$ was determined, average voltages were calculated using the well known methodology of Aydinol *et al.*[13] Calculated average voltages are displayed in Figure 6-8, while there is good agreement between the open-circuit voltage observed in experiments ($\sim$ 2.5 V) and the theoretical voltage calculated for $1 \leq x_{Mg} \leq 2$ ($\sim$ 2.6 V, red curve in Figure 6-8).

6.6.3 Tables and Figures

Table 6.3: Refined parameters for pristine $Mg_2Mo_3O_8$ (space group = $P6_3mc$, a = 5.76375(4) Å, c = 9.89549(8) Å, $\chi^2 = 4.39$, Bragg R-factor = 2.22)

Atom	Wyck.	x	y	z	Occ.	B_{iso} (Å^2)
Mo	6c	0.14639(4)	0.85361(4)	0.250(5)	1	0.050(4)
Mg1	2b	0.33333	0.66667	0.948(5)	1	0.43(4)
Mg2	2b	0.33333	0.66667	0.513(5)	1	0.43(4)
O1	2a	0	0	0.397(5)	1	0.13(3)
O2	2b	0.33333	0.66667	0.142(5)	1	0.13(3)
O3	6c	0.4881(4)	0.5119(4)	0.371(5)	1	0.13(3)
O4	6c	0.1682(6)	0.8318(6)	0.632(5)	1	0.13(3)

Table 6.4: Refined parameters for a mixture of 90 wt% fully demagnesiated $Mg_2Mo_3O_8$ and 10 wt% silicon standard ($\chi^2 = 4.99$). For $Mg_2Mo_3O_8$: S.G. = $P6_3mc$, a = 5.76446(6) Å, c = 9.8969(2) Å, 54.0(6) wt%, Bragg R-factor = 4.27. For Silicon: S.G. = Fd-3m, a = 5.43175(6) Å, 46.0(6) wt%, Bragg R-factor = 4.02.

Atom	Wyck.	x	y	z	Occ.	B_{iso} (Å^2)
			$Mg_2Mo_3O_8$			
Mo	6c	0.14632(8)	0.85368(8)	0.250(6)	1	0.071(6)
Mg1	2b	0.33333	0.66667	0.949(6)	1	0.50(6)
Mg2	2b	0.33333	0.66667	0.513(6)	1	0.50(6)
O1	2a	0	0	0.397(6)	1	0.21(4)
O2	2b	0.33333	0.66667	0.143(6)	1	0.21(4)
O3	6c	0.4880(9)	0.51204(9)	0.371(6)	1	0.21(4)
O4	6c	0.172(1)	0.828(1)	0.632(6)	1	0.21(4)
			Silicon			
Si	8a	0.875	0.875	0.875	1	0.527(6)

Table 6.5: Refined parameters for partially demagnesiated $Mg_2Mo_3O_8$ (space group = $P6_3mc$, a = 5.76384(9) Å, c = 9.8960(2) Å, $\chi^2 = 4.82$, Bragg R-factor = 3.65)

Atom	Wyck.	x	y	z	Occ.	B_{iso} (Å^2)
Mo	6c	0.14626(5)	0.85374(5)	0.250(8)	1	0.059(4)
Mg1	2b	0.33333	0.66667	0.950(8)	1	0.42(4)
Mg2	2b	0.33333	0.66667	0.512(8)	1	0.42(4)
O1	2a	0	0	0.397(5)	1	0.27(3)
O2	2b	0.33333	0.66667	0.146(8)	1	0.27(3)
O3	6c	0.4886(6)	0.5114(6)	0.369(8)	1	0.27(3)
O4	6c	0.1747(8)	0.8253(8)	0.633(8)	1	0.27(3)

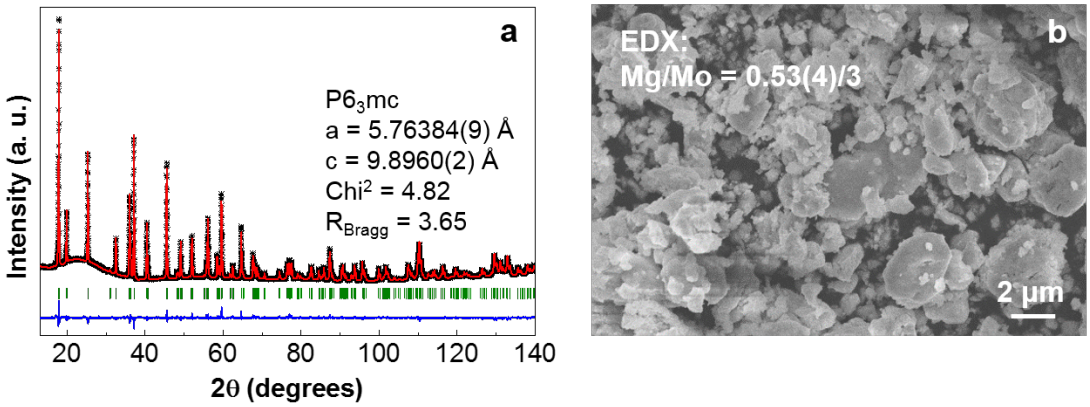

Figure 6-5: (a) Rietveld refinement fit of partially demagnesiated $Mg_2Mo_3O_8$ ($Mg_2Mo_3O_8$:NO_2BF_4 = 1.2). Black crosses — experimental data, red lines – fitted data, blue line – difference map between observed and calculated data, green ticks – the $P6_3mc$ phase. (b) SEM image and EDX result.

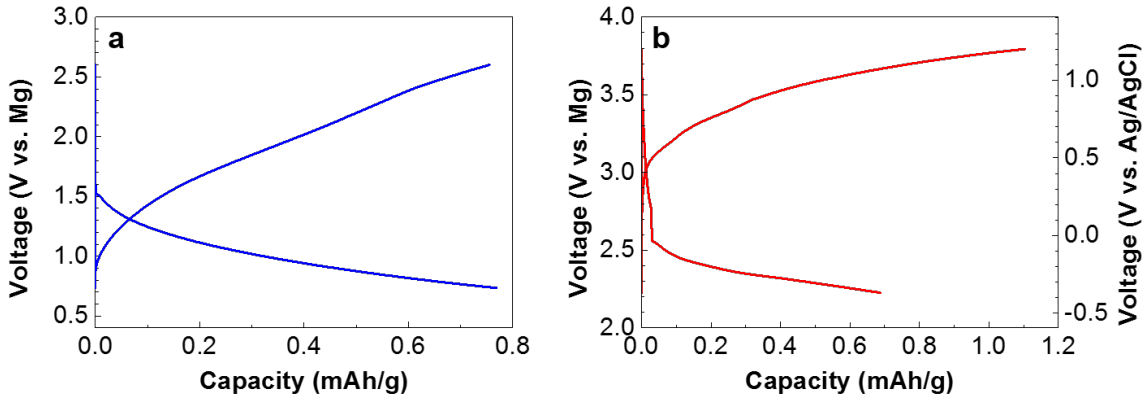

Figure 6-6: Electrochemistry of $Mg_2Mo_3O_8$ tested in (a) 0.4M APC and (b) 0.5M $Mg(ClO_4)_2$ in water at C/20 (1Mg/$Mg_2Mo_3O_8$ in 20 hours) rate and room temperature, showing no activity.

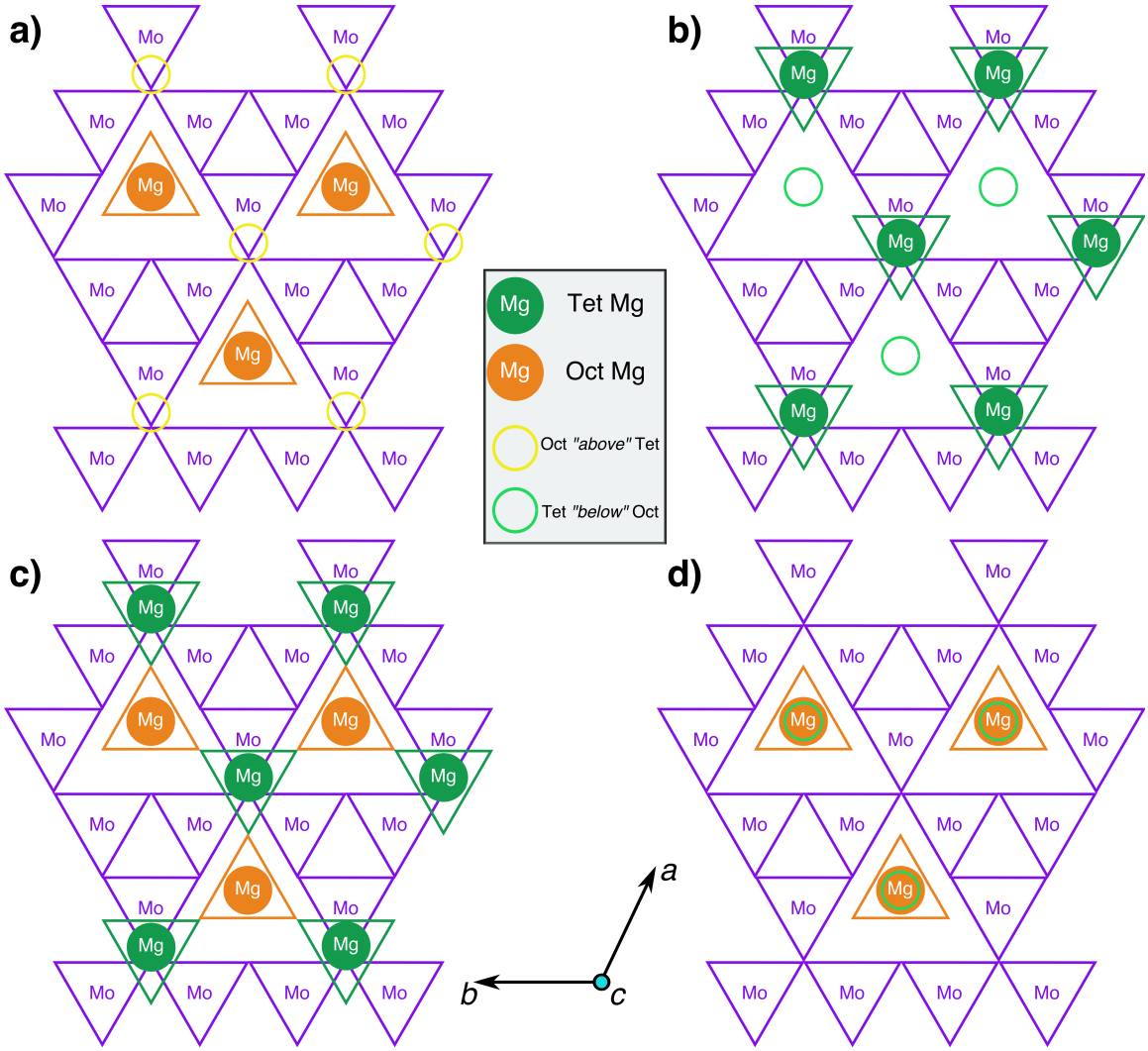

Figure 6-7: 2D view of the Mg-vacancy ordering enumerated for evaluating the stable Mg configuration at $x_{Mg} = 1$. While (a) and (b) have Mg occupancy solely of octahedral (orange, yellow circles) and tetrahedral (green circles) sites, (c) and (d) correspond to an equal Mg distribution among tetrahedral and octahedral sites. All the configurations are viewed along the layer spacing direction (c-axis).

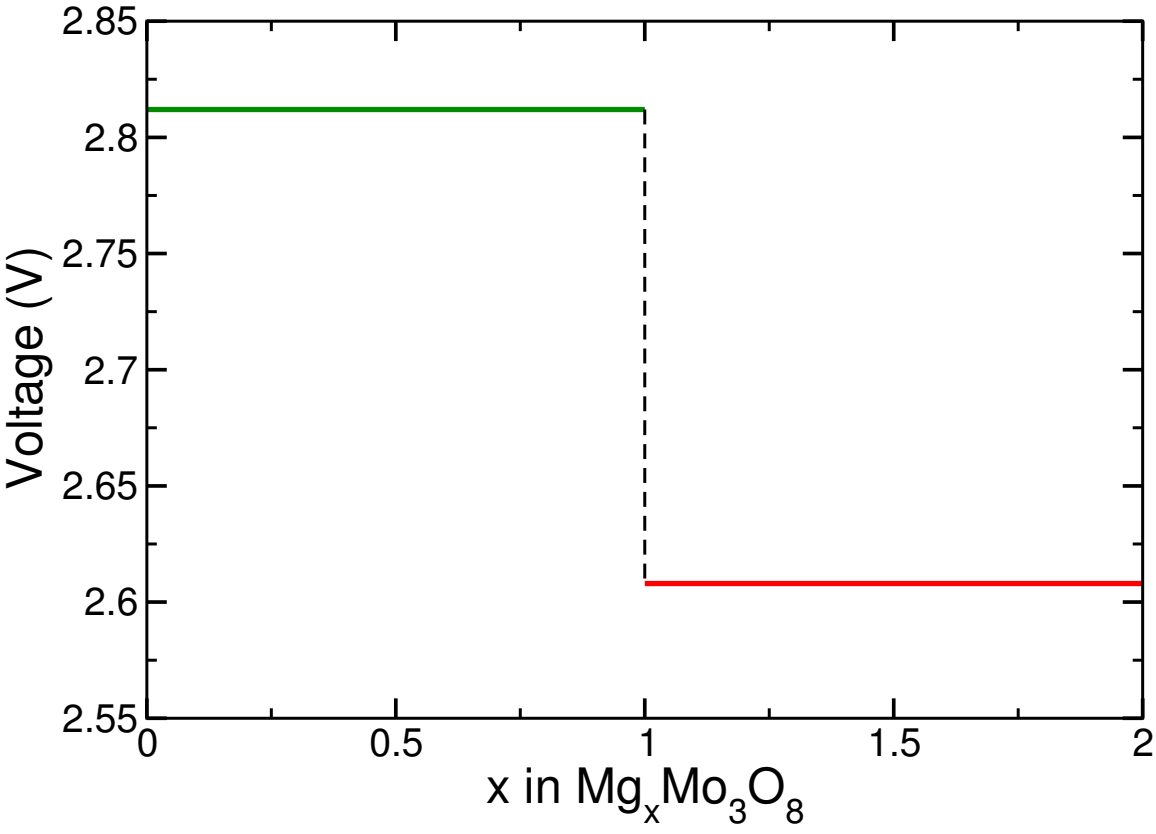

Figure 6-8: Average voltage for Mg intercalation, as calculated for the $1 \leq x_{Mg} \leq 2$ (red) and $0 \leq x_{Mg} \leq 1$ (green) concentration ranges.

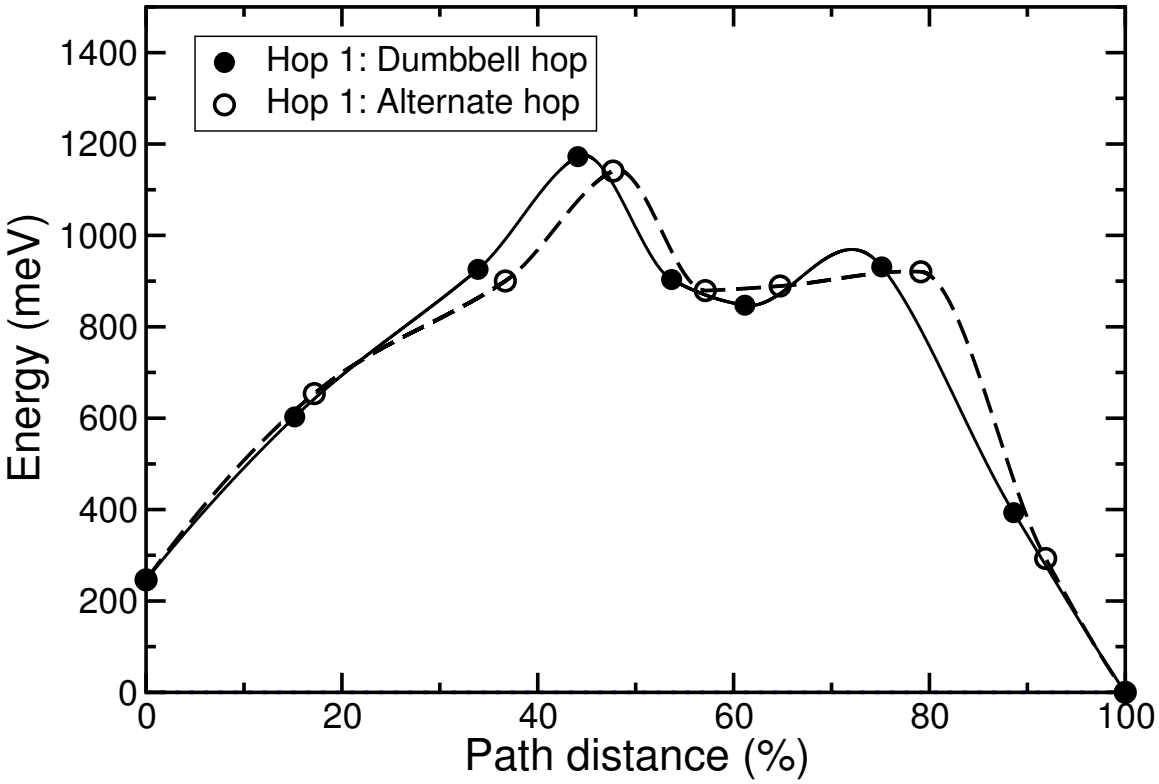

Figure 6-9: The migration barriers for Hop 1 along the O–Mg–O dumbbell path (solid line, identical to Figure 6-4a) and the barrier for the alternate hop as illustrated in Figure 6-4c (dashed lines). Although the alternate pathway for hop 1 was initialized with intermediate tetrahedral and octahedral sites, the NEB calculations converged to a pathway similar to the O–Mg–O dumbbell path, with a similar magnitude.

Chapter 7

Influence of inversion on Mg mobility and electrochemistry in spinels

7.1 Introduction

Multivalent (MV) batteries, such as those based on Mg^{2+},[8, 32] can potentially achieve high volumetric energy density via facile non-dendritic stripping/deposition on an energy-dense metal anode.[252, 21, 141] However, the development of viable MV technology is hindered by poor Mg diffusivity in oxide cathodes as well as poor Coulombic efficiencies in liquid electrolytes.[32, 141, 34, 33]

One pathway to improve Mg migration in solids is to utilize host structures in which the Mg sites are generally destabilized by a unfavorable local coordination environment.[183, 25, 191] Spinels with composition AM_2X_4 (A = Mg, M = metal cations, X = O or S) are appealing structures in this regard because of their tetrahedrally-coordinated Mg sites, rather than the preferred octahedral coordination of Mg. Theoretical calculations indeed predict reasonable Mg^{2+} migration barriers ($\sim 550 - 750$ meV) in both oxide and sulfide spinels.[126, 125] Note that oxide spinels have long been used as cathodes and anodes in commercial Li-ion batteries.[243, 220, 231, 176, 226, 58, 5]

Spinel-Mn_2O_4 is a particularly promising energy-dense MV cathode, as it is one of the few oxides[64, 190, 192, 187, 217, 155] to have shown electrochemically reversible

Mg^{2+} intercalation.[96, 57] However, the cyclable Mg content, i.e., the observed capacity, seems to depend strongly on the synthesis conditions.[96, 57, 99] Several studies on the $MgMn_2O_4$ structure[85, 130, 184, 132, 171] have indicated that the spinel is prone to *inversion*, i.e., Mg/Mn antisite disorder (see Section 7.2), where the *degree of inversion* can range from 20%[130] to 60%.[85] It has further been argued that the propensity of Mn^{3+} to disproportionate into Mn^{2+} and Mn^{4+} promotes spinel inversion and phase transformations.[176, 177] Since inversion directly affects the local cation arrangement, it may significantly impact the Mg^{2+} ionic mobility.[111, 224] For the rational design of improved Mg battery cathodes it is, therefore, crucial to understand how inversion in oxide spinels affects Mg^{2+} migration.

Inversion is not a phenomenon unique to oxides, and other chalcogenide spinels, such as sulfides, which are also important cathode materials in MV technology,[125] are also known to exhibit inversion.[199, 31] A recent combined theoretical and experimental study has identified ternary sulfide and selenide spinels as promising Mg-ion conductors with potential applications as solid electrolytes in MV batteries.[31] Solid electrolytes combine the advantage of improved safety with a high Mg transference number. Three promising compounds were reported, namely, $MgSc_2Se_4$, $MgSc_2S_4$, and $MgIn_2S_4$.[31] $MgIn_2S_4$ spinel had previously been reported,[73, 233] and the available literature as well as our own synthesis attempts (Figure 7-7 in Appendix) indicate that the compound is prone to inversion, where the degree of inversion can be as high as $\sim$ 85% (Table 7.5 in Appendix).

In the present work, motivated by the importance of the spinel structure for MV battery technology, we explore the influence of spinel inversion on Mg mobility in ternary oxides and sulfides, with $MgMn_2O_4$ and $MgIn_2S_4$ being the prototype for each class of spinels. We consider all possible local cation environments that arise due to inversion and present the activation barriers for Mg diffusion in each scenario, determined using first-principles calculations. While solid electrolytes generally require high ionic conductivities, as indicated by low migration barriers ($\sim$ 400 – 500 meV) observed in solid Li-conductors,[14] cathodes can operate under lower ionic mobilities ($\sim$ 750 meV, see Section 7.3.1).[32] Hence, we use an upper limit of 500 meV

and 750 meV on the migration barriers in solid electrolytes (such as $MgIn_2S_4$), and cathodes ($MgMn_2O_4$), respectively, to distinguish open and closed diffusion pathways. Our results indicate that inversion, in both solid electrolytes and cathodes, can simultaneously cause a decrease in activation barriers across certain diffusion trajectories while increasing the barriers across others, leading to a complex interplay of opening and closing of specific Mg diffusion pathways. To quantify the impact of these variations in the microscopic activation barriers on macroscopic Mg migration, we estimate the critical Mg concentrations (percolation thresholds) required to facilitate Mg^{2+} migration through the structure at different degrees of inversion. We estimate that the stoichiometric $MgMn_2O_4$ (upper limit of 750 meV) and $MgIn_2S_4$ (500 meV) spinels remain percolating up to $\sim$ 59% and 44% inversion, respectively. Finally, we discuss the impact of spinel inversion on Mg-electrochemistry in an Mn_2O_4 cathode by evaluating the 0 K phase diagram, average voltages and the accessible Mg capacity at various degrees of inversion.

While previous studies have analyzed the impact of inversion on structural, thermal, electronic, and magnetic properties,[235, 45, 197, 195, 130] the effect on Mg mobility in spinels has not yet been investigated. Understanding the influence of inversion on ion mobility will provide guidelines to tune the synthesis and electrochemical conditions of both cathodes and solid electrolytes, not only in MV systems but also in existing Li-ion architectures.[249] Finally, our results emphasize the importance of the topology of cation sites in setting the diffusion behavior within a general anion framework.[63]

7.2 Structure

A spinel configuration is a specific ordering of cation sites (A and M in AM_2X_4) in a face-centered cubic (FCC) packing of anion sites (X), as shown in Figure 7-1. In a “normal" spinel, half of the octahedral (*oct*) sites, i.e., 16*d*, are occupied by M atoms (Mn/In, blue octahedra in Figure 7-1), while 1/8 of the tetrahedral (*tet*) sites (8*a*) are occupied by A (Mg, orange tetrahedra) cations.

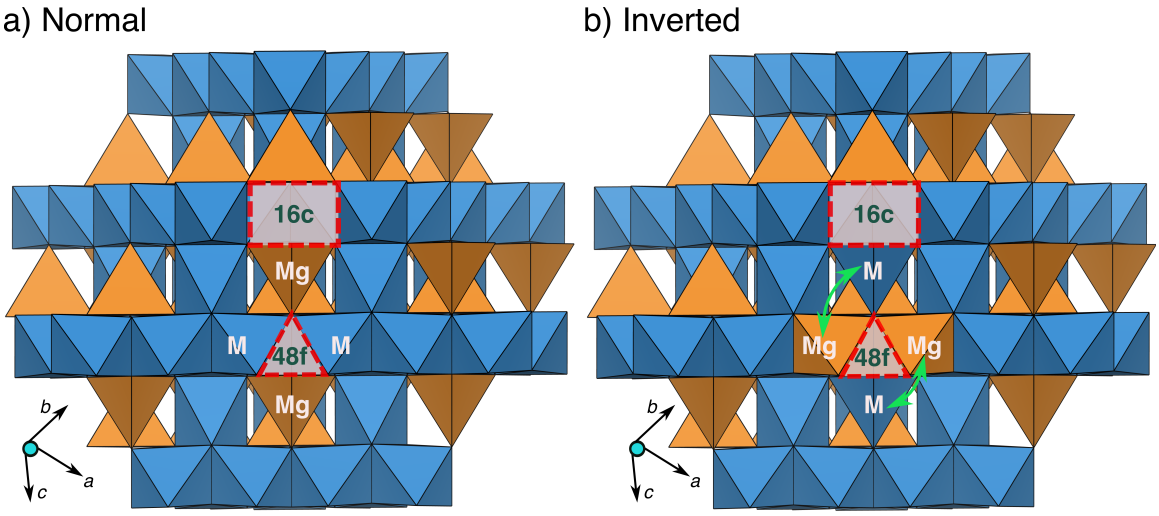

Figure 7-1: Schematic of a normal (a) and an inverted (b) spinel MgM_2X_4 (M = Mn, In and X = O, S). The blue and orange polyhedra correspond to the M ($16d, oct$) and Mg ($8a, tet$). The dashed rectangle indicates the vacant $16c, oct$ site and the dashed triangle the vacant $48f$ *tet* site. In (b), green arrows display the exchange of Mg and M sites, leading to inversion in the spinel.

Each polyhedron in the spinel structure shares faces, edges and corners, as summarized in Table 7.1. For example, the $8a$ sites that are occupied by A are face-sharing with vacant (Vac) $16c$ *oct* sites (dashed red square in Figure 7-1a), edge-sharing with vacant $48f$ *tet* (dashed red triangle) and corner-sharing with vacant *tet* ($48f, 8b$) and M-containing $16d$ *oct* sites.[205] Face-sharing polyhedra have the lowest cation–cation distance, indicating the highest level of electrostatic repulsion, followed by edge-sharing and subsequently corner-sharing polyhedra.[163] Indeed, the $16c, 48f$ and $8b$ sites are vacant in spinel lattices ($8b$ not shown in Figure 7-1) since they face-share with occupied $8a$ or $16d$ sites.

Inversion in a spinel structure refers to the collection of anti-site defects in the $8a$ (A) and $16d$ (M) sub-lattices, as shown in Figure 7-1b. The degree of inversion, i, is defined as the fraction of $8a$ sites occupied by M cations, with a value of 0 (or 0%) and 1 (100%) indicating a normal and a fully inverted spinel, respectively. Thus, cations A and M are exchanged in inverted spinels (green arrows in Figure 7-1b), leading to a stoichiometry of $A_{1-i}M_i[A_{i/2}M_{1-(i/2)}]_2X_4$, compared to AM_2X_4 in normal spinels.

Table 7.1: Notations used in the AM_2X_4 structure of Figure 7-1. Vac indicates vacancy. No. sites is normalized against the conventional (cubic) cell of a normal spinel with 32 anions.

Site	Coordination	Ion in normal spinel	Sharing neighbors			No. sites
			Face	Edge	Corner	
$8a$	*tet*	A (Mg^{2+})	$16c$	$48f$	$48f, 16d, 8b$	8
$16d$	*oct*	M ($Mn^{3+,4+}/In^{3+}$)	$8b, 48f$	$16c, 16d$	$8a, 48f$	16
$16c$	*oct*	Vac	$8a, 48f$	$16d, 16c$	$8b, 48f$	16
$48f$	*tet*	Vac	$16d, 16c$	$8a, 8b, 48f$	$8a, 16c, 16d$	48
$8b$	*tet*	Vac	$16d$	$48f$	$48f, 16c, 8a$	8

7.2.1 Possible Mg-hops

Figure 7-2 and Table 7.2 summarize the possible local cation arrangements in a spinel structure that can originate from inversion. The orange, blue, and green polyhedra in Figure 7-2 correspond to Mg, M, and mixed (Mg/M) occupation, respectively, with the arrows in each panel indicating the Mg diffusion trajectory. The dashed rectangles and triangles signify vacancies. Grey polyhedra correspond to $8a$ sites that are either cation occupied or vacant. While Figure 7-2a indicates the diffusion trajectory in a normal spinel, panels b, c, d, and e depict the possible Mg-hops that can occur in an inverted spinel. The sub-panels in Figure 7-2b correspond to slices along perpendicular directions, i.e., the $8a$ sites in the left sub-panel of Figure 7-2b are perpendicular to the plane of the paper in the right sub-panel.

In a normal spinel, the rate determining hop for Mg diffusion occurs between adjacent $8a$ *tet* sites face-sharing with a $16c$ octahedron, as shown in Figure 7-2a. Hence, the diffusion topology is $tet-oct-tet$, and referred to as "Hop 1" in our work. The intermediate $16c$ site in Hop 1 shares edges with six $16d$ *oct* sites ("ring" sites) that are occupied by M cations (2 out of 6 ring sites are shown in Figure 7-2a). It was recently proposed[126, 183, 125] that the diffusion barrier in normal spinels, both oxides and sulfides, is predominantly set by the size of the shared triangular face (not shown in Figure 7-2a) between the $8a$ *tet* and $16c$ *oct* sites.

Along the $tet-oct-tet$ diffusion pathway in inverted spinels (referred to as "Hop 2") the $16d$ ring sites can be occupied by both M and Mg cations, as indicated by

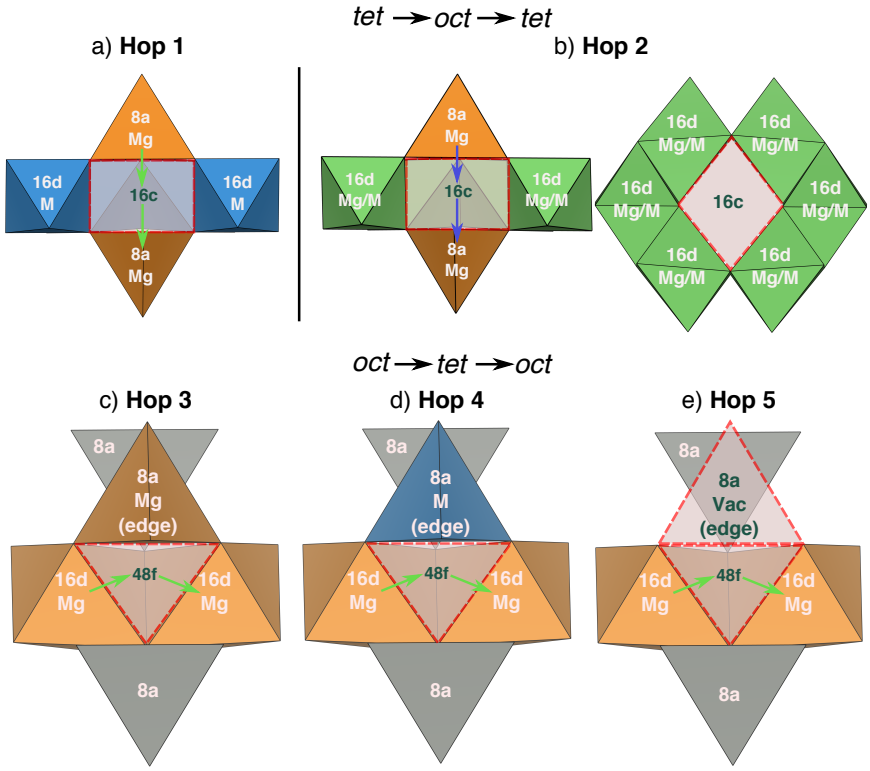

Figure 7-2: Local cation environments and various Mg hops considered in an inverted spinel structure. Hops 1 (a) and 2 (b) occur with a *tet* → *oct* → *tet* topology, while hops 3 (c) and 4 (d) occur along an *oct* → *tet* → *oct* pathway. Blue and orange polyhedra correspond to Mg and M (M = Mn, In), while green polyhedra indicate mixed M/Mg occupancy. In the case of Hops 3, 4, and 5 the 8*a* sites corner-sharing with the intermediate 48*f* site are shown as grey polyhedra. The notation "edge" in panels (c), (d) and (e) corresponds to the 8*a* site that edge-shares with the 48*f*. Vac indicates vacancy.

the six green polyhedra in the right sub-panel of Figure 7-2b. To evaluate Mg^{2+} migration along Hop 2, we considered from 1 ring site occupied by Mg all the way to all 6 ring sites being occupied by Mg. Since each ring site occupancy (e.g., 2/6 or 3/6 Mg) corresponds to a large number of possible cation decorations on the ring sites, we used the decoration that had the lowest electrostatic energy, as obtained by minimizing the Ewald energy[55] using classical charges in the spinel framework.

As inversion leads to Mg^{2+} occupancy of 16*d* sites, Mg-hopping across 16*d* sites must also be considered. A $16d-16d$ hop can occur through two possible tetrahedral intermediate sites, the 8*b* and 48*f*. The 8*b* sites typically share all their triangular faces with occupied 16*d* sites and are therefore not open to Mg^{2+} diffusion due to

high electrostatic repulsion, as shown by previous studies.[63, 183, 224] However, the $48f$ sites share 2 triangular faces with vacant $16c$ sites, enabling them to act as viable intermediate sites for Mg^{2+} hopping. As such, we only consider the $16d - 16d$ hop via the $48f$ as intermediate site, leading to a $16d - 48f - 16d$ topology (Figures 7-2c, d, and e). The $48f$ shares one of its edges with an $8a$ *tet* site (Table 7.1), where the "edge-$8a$" can be occupied by Mg^{2+} ("Hop 3", Figure 7-2c), $M^{3+/4+}$ ("Hop 4", Figure 7-2d) or a vacancy ("Hop 5", Figure 7-2c). Additionally, across Hops 3, 4, and 5, we consider two scenarios where the $8a$ sites that share a corner with the $48f$ ("corner-$8a$", grey polyhedra in Figure 7-2) are either occupied by cations or left vacant.

Table 7.2: Summary of all hops considered for evaluating Mg^{2+} mobility in inverted spinels, where M = Mn, In and Vac = Vacancy. The neighbor column indicates the site that edge-shares with the intermediate site in the corresponding hop. The last column signifies the (maximum) number of configurations, along each diffusion trajectory, for which migration barriers have been calculated in this work. For example along Hop 3, the corner-$8a$ sites being cation-occupied and vacant are the two configurations considered.

Hop	Topology	Intermediate site neighbor(s)	# configurations
1	$8a - 16c - 8a$ ($tet - oct - tet$)	$16d$ (oct, M)	1
2	$8a - 16c - 8a$ ($tet - oct - tet$)	$16d$ (oct, Mg/M)	6
3	$16d - 48f - 16d$ ($oct - tet - oct$)	$8a$ (tet, Mg)	2
4	$16d - 48f - 16d$ ($oct - tet - oct$)	$8a$ (tet, M)	2
5	$16d - 48f - 16d$ ($oct - tet - oct$)	$8a$ (tet, Vac)	2

7.3 Results

7.3.1 $MgMn_2O_4$

Figure 7-3 plots the ranges of Mg^{2+} migration barriers in $Mg_xMn_2O_4$ (y-axis) for all hops of Figure 7-2 and Table 7.2, while the raw data is included in Figure 7-9 of the Appendix. The migration barriers are calculated with respect to the absolute energies of the end points, nominally identical for a given Mg^{2+} hop. However, there are a few cases where the end point energies are different, since the local symmetry of the cation

decoration is broken differently across the end points (e.g., 3/6 hop in Figure 7-9b). In such cases, the barrier is reported with respect to the end point with the lowest energy. The dotted black line in Figure 7-3 is the upper-limit of the Mg migration barrier, as required for reasonable battery performance,[32] and is used to determine the percolation thresholds (see Section 7.3.3). For a $Mg_xMn_2O_4$ cathode particle of size $\sim$ 100 nm being (dis)charged at a C/3 rate at 60°C, the migration barrier upper-limit is $\sim$ 750 meV (the upper-limit decreases to $\sim$ 660 meV at 298 K).[32] Since full-cell Mg batteries so far have displayed superior performance at $\sim$ 60°C than at 25°C,[8, 213] the value of $\sim$ 750 meV has been used as the cut-off to differentiate "open" and "closed" Mg^{2+} diffusion channels. In terms of notations, the fractions used in Hop 2 (e.g., 1/6, 2/6, etc., yellow rectangle in Figure 7-3) correspond to the fraction of 16*d* ring sites (Figure 7-2b) that are occupied by Mg^{2+}. The terms "8a empty" and "8a full" along Hops 3, 4, and 5 in Figure 7-3 indicate that the corner-8*a* sites (Figures 7-2c, d, and e) are vacant and occupied by cations, respectively. x_{Mg} in Figure 7-3 is the Mg concentration in the cell used for the barrier estimation, corresponding to the "dilute Mg" ($x_{Mg} \sim 0$, solid red lines) and "dilute vacancy" ($x_{Mg} \sim 1$, dashed blue lines) limits.

Mg migration barriers along Hop 1 ($tet-oct-tet$, normal spinel) at the dilute Mg and dilute vacancy limits are $\sim$ 717 meV and $\sim$ 475 meV, respectively (red rectangle in Figure 7-3), in good agreement with previous studies.[126, 183] Since the migration barriers at both Mg concentration limits are below $\sim$ 750 meV, Hop 1 is always open for Mg diffusion. Barriers along Hop 2 (yellow rectangle in Figure 7-3) decrease initially with Mg occupation of the 16*d* ring sites ($\sim$ 393 meV at 2/6 vs. 536 meV at 1/6) before increasing beyond 750 meV at 5/6 and 6/6 Mg. The non-monotonic variation of the migration barriers along Hop 2 is due to the gradual destabilization of the 16*c* site. The increasing instability of the 16*c* also changes the migration energy profile (Figure 7-9b) from "valley"-like[183] at 1/6 Mg to "plateau"-like at 5/6 Mg.

In the case of the $oct-tet-oct$ Hops 3 and 4 (green and cyan rectangles in Figure 7-3), which respectively have *tet* Mg and Mn edge-sharing with the intermediate 48*f* site, the barriers vary drastically based on Mg content and occupancy of the corner-

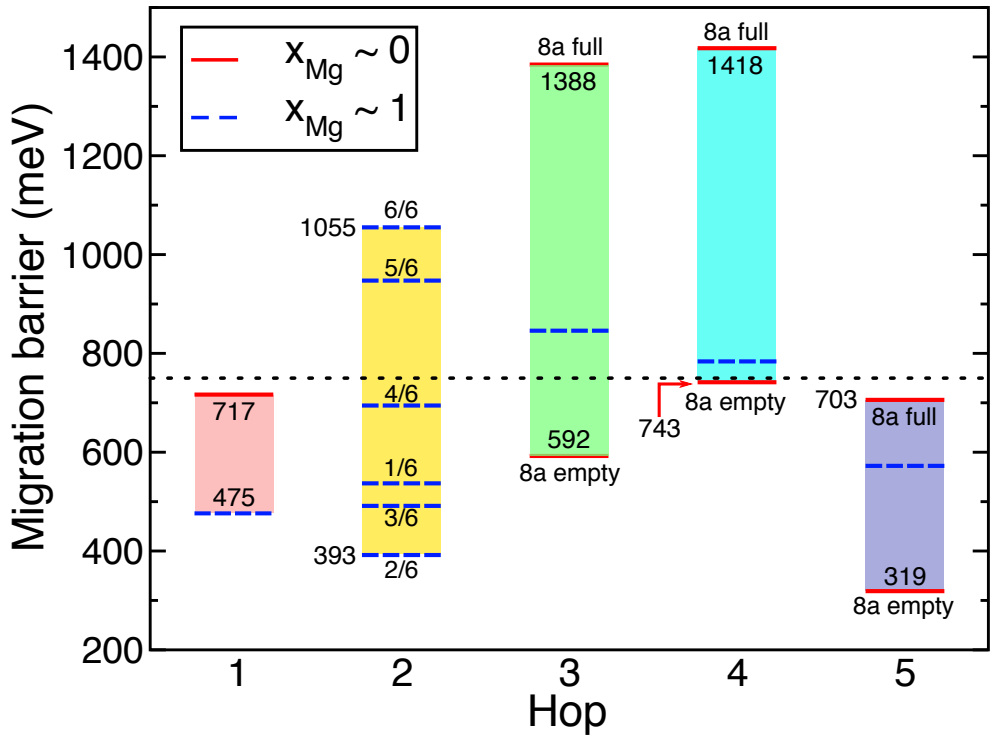

Figure 7-3: Ranges of Mg^{2+} migration barriers along the hops considered in spinel-$Mg_xMn_2O_4$. The dotted black line indicates the upper-limit of migration barriers ($\sim$ 750 meV) used to distinguish open and closed diffusion channels in percolation simulations. Solid red and dashed blue lines correspond to dilute Mg ($x_{Mg} \sim 0$) and dilute vacancy ($x_{Mg} \sim 1$) limits. Fractions along Hop 2 indicate the occupancy of Mg^{2+} in the 16*d* ring sites, while the legend "8*a* full (empty)" corresponds to cation-occupied (vacant) corner-8*a* sites along Hops 3 – 5. The barriers along Hop 1 are calculated at $i \sim 0$, while Hops 3 – 5 have been done at $i \sim 0.25$. Along Hop 2, i varies with Mg occupancy of the ring sites, ranging from $i \sim 0.125$ at 1/6 Mg to $i \sim 0.75$ at 6/6 Mg. The raw data from Nudged Elastic Band calculations are displayed in Figure 7-9 of the Appendix.

8*a* sites. For example, at (*i*) $x_{Mg} \sim 0$ and vacant corner-8*a*, the barrier along Hop 3 ($\sim$ 592 meV) is well below the upper-bound of 750 meV, while the barrier is comparable along Hop 4 ($\sim$ 743 meV). At (*ii*) $x_{Mg} \sim 0$ and cation-occupied corner-8*a*, the barriers along Hops 3 and 4 increase significantly ($\sim$ 1388 meV and $\sim$ 1418 meV) and surpass the upper-limit set for open channels. Eventually, at (*iii*) $x_{Mg} \sim 1$ (cation-occupied corner-8*a*), the barriers decrease to $\sim$ 845 meV and $\sim$ 784 meV along Hops 3 and 4, respectively. Note that the barriers along Hops 3 and 4 in Figure 7-3 are calculated at a degree of inversion, $i \sim 0.25$. At a higher degree of inversion ($i \sim 1$)

and $x_{Mg} \sim 1$ (cation-occupied corner-8a), the barrier is $\sim$ 1039 meV along Hop 4 (Figure 7-11). Hence, from the data of Figure 7-3, Hop 3 is considered closed for Mg diffusion whenever the corner-8a sites are cation-occupied, while Hop 4 is always considered a closed channel.

Mg migration barriers decrease significantly if the edge-8a is vacant (i.e., along Hop 5). For example, the migration barriers along Hop 5 (purple rectangle in Figure 7-3) are well below that of Hops 3 and 4 across the scenarios of (i) low Mg, vacant corner-8a (319 meV for Hop 5 vs. 592 and 743 meV for Hops 3 and 4, respectively), (ii) low Mg, cation-occupied corner-8a (703 meV vs. 1388 and 1418 meV), and (iii) high Mg, cation-occupied corner-8a (570 meV vs. 845 and 784 meV). Hence, Hop 5 is always open for Mg diffusion, since the migration barriers are below the upper limit of 750 meV.

In summary, the $tet - oct - tet$ pathway (Hops 1 and 2) remains open for Mg diffusion in $MgMn_2O_4$ until a high degree of Mg occupation on the 16d ring sites (i.e., $\geq$ 5/6 Mg) is present, which corresponds to high degrees of inversion ($i > 0.625$). The $oct - tet - oct$ pathway is open only when the edge-8a is vacant (Hop 5) or when the corner-8a are vacant with Mg in the edge-8a (Hop 3).

7.3.2 $MgIn_2S_4$

Figure 7-4 plots the Mg^{2+} migration barriers in $MgIn_2S_4$ for the hops of Figure 7-2 (the raw data are shown in Figure 7-10). Since $MgIn_2S_4$ is an ionic conductor, off-stoichiometric Mg concentrations are not of interest. Hence, all hops in Figure 7-4 are evaluated at the dilute vacancy limit ($x_{Mg} \sim 1$, dashed blue lines in Figure 7-4). The fractions used (1/6, 2/6, etc.) in Figure 7-4 are the number of 16d ring sites occupied by Mg^{2+} in Hop 2. Along Hops 3 – 5, we use cation-occupied corner-8a sites (i.e., "8a full" in Figures S4c, d, and e). The upper-limit of the Mg migration barrier for classifying open and closed diffusion channels (as indicated by the dotted black line in Figure 7-4) is set to $\sim$ 500 meV, based on migration barriers of $\sim$ 400 – 500 meV observed in fast Li-ion conductors, such as Garnets and Si-based thio-LISICONs.[14]

In the case of Hop 1, the barrier is $\sim$ 447 meV, well below the upper limit of

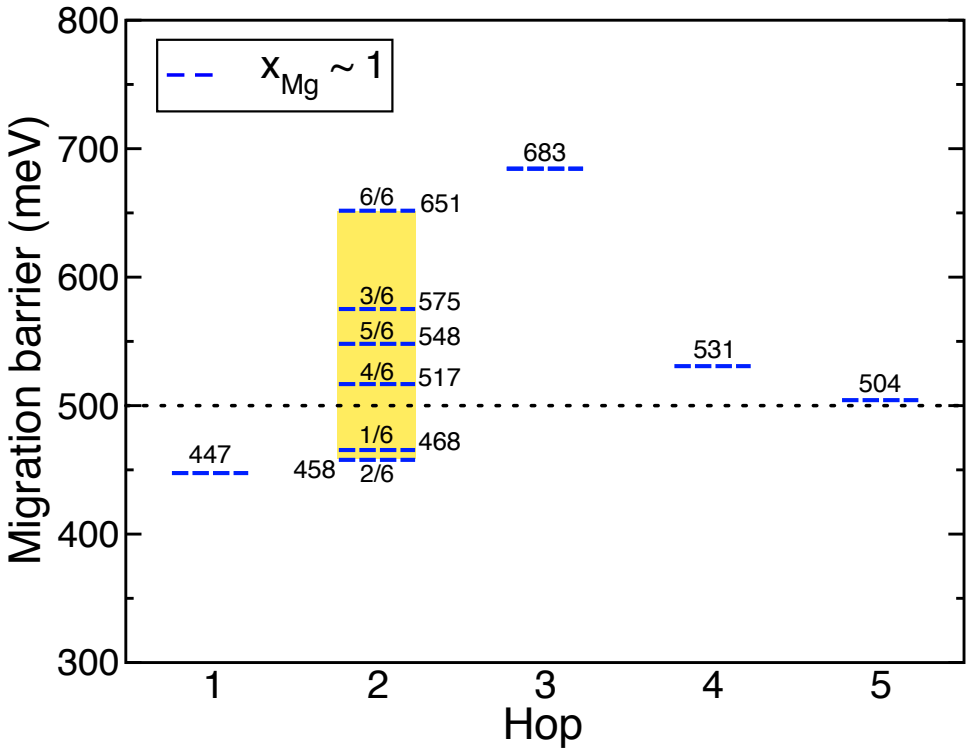

Figure 7-4: Mg^{2+} migration barriers along each possible hop in spinel-$MgIn_2S_4$. The dotted black line indicates the upper-limit of migration barriers ($\sim$ 500 meV) used to distinguish open and closed diffusion channels in percolation simulations. Dashed blue lines indicate the dilute vacancy ($x_{Mg} \sim 1$) limit. Fractions along Hop 2 indicate the occupancy of Mg^{2+} in the 16*d* ring sites, while the corner-8*a* sites are cation-occupied across Hops 3 – 5. The barrier along Hop 1 is calculated at $i \sim 0$, while Hops 3 – 5 have been done at $i \sim 0.25$. Along Hop 2, i varies with Mg occupancy of the ring sites, ranging from $i \sim 0.125$ at 1/6 Mg to $i \sim 0.75$ at 6/6 Mg. The raw data from Nudged Elastic Band calculations are displayed in Figure 7-10.

$\sim$ 500 meV. Mg migration barriers along Hop 2 (yellow rectangle in Figure 7-4) follow trends similar to that of $MgMn_2O_4$ (Figure 7-3). For example, at low Mg occupation of the ring sites (1/6 or 2/6 Mg), the barrier is below the limits for percolating diffusion, before increasing beyond 500 meV at higher Mg content in the ring sites ($>$ 3/6 Mg). Also, the shape of the migration energy curve changes from a "valley" at 1/6 Mg (solid black line in Figure 7-10b) to a "plateau" beyond 2/6 Mg (solid red line in Figure 7-10b), indicating that the 16*c* site becomes progressively unstable with increasing Mg occupation of the ring 16*d*.

Along the $16d - 48f - 16d$ pathways (Hops 3, 4 and 5), the migration barriers are always higher than 500 meV, irrespective of the occupancy of the edge-8*a*. Indeed,

the magnitude of the barriers are $\sim$ 683 meV, $\sim$ 531 meV, and $\sim$ 504 meV for Mg-occupied, In-occupied and vacant edge-8a, respectively, indicating that the $oct-tet-oct$ pathway will not be open for Mg^{2+} diffusion.

7.3.3 Percolation thresholds

Based on the data of Figures 7-3 and 7-4, and the upper limits of Mg migration barriers set for $MgMn_2O_4$ (750 meV) and $MgIn_2S_4$ (500 meV), we compiled a list of conditions that enable the opening of the possible hops in Table 7.3. For example, Hop 1 ($8a-8a$) is open under all x_{Mg} and i for both $Mg_xMn_2O_4$ and $MgIn_2S_4$. Both the oxide and the sulfide spinel exhibit high barriers ($>$ 1 eV) for a $16d-8a$ hop (Figure S8), which would disable any Mg transfer between an octahedral 16d site and an adjacent tetrahedral 8a site. Thus, in our percolation simulations, the $8a-8a$ (Hops 1 and 2) and the $16d-16d$ (Hops 3, 4, and 5) channels remain decoupled, and a percolating network consists solely of either $8a-8a$ or $16d-16d$ channels.

Table 7.3: Summary of rules used during percolation simulations with the conditions for an open channel. The upper limit of migration barriers used to distinguish between open and closed channels is 750 meV and 500 meV for $MgMn_2O_4$ and $MgIn_2S_4$, respectively.

Hop	Topology	Open under condition
	$MgMn_2O_4$ – 750 meV	
1	$8a-16c-8a$	Always open
2	$8a-16c-8a$	Max. 4/6 ring sites with Mg
3	$16d-48f-16d$	Corner 8a vacant
4	$16d-48f-16d$	Always closed
5	$16d-48f-16d$	Always open
	$MgIn_2S_4$ – 500 meV	
1	$8a-16c-8a$	Always open
2	$8a-16c-8a$	Max. 2/6 ring sites with Mg
3	$16d-48f-16d$	Always closed
4	$16d-48f-16d$	Always closed
5	$16d-48f-16d$	Always closed

Figures 7-5a and b plot the critical concentration required to ensure Mg percolation (x_{crit}, solid black lines), at various degrees of inversion (i) in $MgMn_2O_4$ and $MgIn_2S_4$. The dashed yellow lines indicate the stoichiometric spinel (MgM_2X_4). The

blue (red) shaded region corresponds to Mg concentration ranges which do (do not) exhibit percolation. The x-axis in Figure 7-5 begins at a M_3X_4 (i.e., 100% Mg-deficient) configuration and spans Mg concentrations up to $Mg_{1.5}M_{1.5}X_4$ (i.e., 50% Mg-excess). Generally, percolation thresholds in the Mg-deficient domain (i.e., $x_{crit} < 1$) are desired for electrochemical properties, as this implies that the stoichiometric Mg-spinel (MgM_2X_4) should possess percolating networks and facilitate macroscopic Mg transport, resulting in observable capacities (cathodes) and ionic conductivity (solid electrolytes).

Typically during Monte-Carlo simulations, the spinel structure is initialized with a M_3X_4 stoichiometry, and M atoms are randomly flipped to Mg (see Section 2.5), which does not consider diffusion channels with vacant neighbors (e.g., Hop 5 in Figure 7-2e). In stoichiometric ionic conductors, such as $MgIn_2S_4$, the vacancy concentration is low and therefore vacancies are not expected to play a major role in macroscopic Mg transport.[178] However, in the case of cathode spinels ($MgMn_2O_4$), Mg deintercalation from the framework creates vacancies, and vacancies can facilitate the formation of Mg percolating networks by opening certain diffusion channels (e.g., Hop 5 in $MgMn_2O_4$, Figure 7-3). Therefore, the effect of vacancies in creating a percolating Mg network is explored by initializing the Mg sub-lattice with varying vacancy concentrations in $Mg_xMn_{3-x}O_4$ (Figure 7-13). Note that Mg extraction from the cathode corresponds to the creation of Mg-vacancies. Hence, the vacancy concentration in our percolation simulations does not affect the Mg content that can be (de)intercalated in practice, and the x in Figure 7-5a is therefore a *total* Mg concentration that is the sum of Mg and vacant sites in our calculations. To evaluate x_{crit} for a given degree of inversion in Figure 7-5a, we consider the lowest total Mg content at which the cathode spinel starts percolating.

The stoichiometric $MgMn_2O_4$ (or $VacMn_2O_4$) spinel at $i = 0$ (dashed yellow line in Figure 7-5a), permits macroscopic Mg migration, since the percolation threshold ($x_{crit} \sim 0.44$) is in the Mg-deficient domain (i.e., $x_{crit} < 1$), in agreement with previous calculations on spinel-like lattices.[224] Upon inversion, the stoichiometric spinel continues to be percolating up to $i \sim 0.59$. At higher degrees of inversion

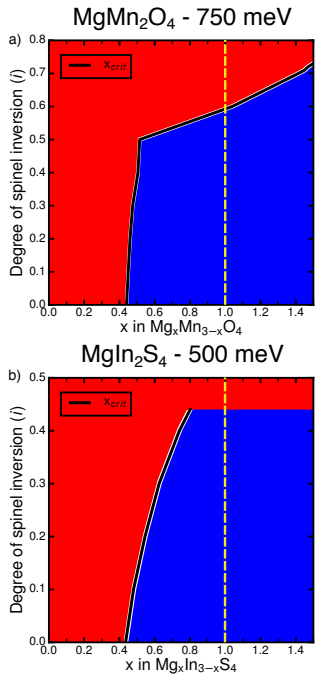

Figure 7-5: The critical concentration for Mg percolation (x_{crit}) in the Mn_2O_4 (a) and In_2S_4 (b) spinels are plotted as thick black lines at different degrees of spinel inversion i. The stoichiometric spinel concentration (MgM_2X_4) is indicated by the dashed yellow lines. Note that the zero on the x-axis corresponds to a stoichiometry of M_3X_4 (M = Mn/In and X = O/S). In the case of $MgMn_2O_4$ (panel a), the x-axis refers to the "total" Mg content in the structure, which includes both Mg and vacancies. The shaded red (blue) region in both panels indicates the Mg concentration range where macroscopic Mg migration is not possible (possible). Thus, the x_{crit} at each i corresponds to the lowest Mg concentration (x) at which percolation becomes feasible.

($0.59 < i < 0.77$), the spinel lattice requires Mg-excess concentrations (i.e., $x > 1$) to facilitate Mg percolation, as illustrated by $x_{crit} \sim 1.05$ (5% Mg-excess) at $i = 0.6$ and ~ 1.42 (42% Mg-excess) at $i = 0.7$. At $i > 0.77$, the oxide spinel does not form a percolating Mg network at any total Mg concentration in the lattice (even up to Mg_3O_4, not shown in Figure 7-5a).

The percolation threshold in $Mg_xIn_{3-x}S_4$ (solid black line in Figure 7-5b) increases continuously with increase in inversion, with $x_{crit} \sim 0.435$, 0.74 at $i = 0$, and 0.4, respectively. Thus, at low i, stoichiometric $MgIn_2S_4$ should exhibit significant ionic conductivity. However, at higher degrees of inversion ($i > 0.44$), the sulfide spinel does not form percolating networks at any Mg-concentration, owing to the absence

of open $16d - 16d$ channels in combination with the $8a - 8a$ channels being closed beyond 2/6 Mg ring site occupancy (Table 7.3). In general, mobility requirements in an ionic conductor are more stringent than in a cathode, leading to a stricter cut-off of 500 meV on migration barriers in $MgIn_2S_4$.[237, 14] Indeed, a sulfide spinel Mg-cathode (such as $Mg_xTi_2S_4$[213]) exhibiting similar activation barriers with inversion as $MgIn_2S_4$ will not suffer from any percolation bottlenecks, since the barriers across all cation arrangements are well below the milder 750 meV cut-off set for cathodes (Figure 7-4).

7.3.4 Impact of inversion on cathode electrochemistry

Under ideal conditions, the structure of an ionic conductor (such as $MgIn_2S_4$) should not undergo significant changes during operation. Thus, the extent of inversion should, in principle, be measured using characterization experiments post-synthesis. However in a cathode material such as $Mg_xMn_2O_4$, which can generate mobile Mn^{2+} ions (Figure S9) through disproportionation of Mn^{3+}, the degree of inversion (i) can change during electrochemical cycling.[176, 177] Consequently, structural changes in a cathode during cycling should manifest themselves as changes in the voltage profile and observed capacity, which can be benchmarked with theoretical predictions.[32, 190] To evaluate the effect of inversion on the voltage profile of $Mg_xMn_2O_4$, we calculated the phase diagram and energy of the intercalation system at 0 K as a function of Mg content under various degrees of inversion.[13, 226, 176, 190]

To evaluate the ground state hull of the $Mg_xMn_2O_4$ system, we enumerated over 400 Mg-vacancy configurations, at different Mg concentrations (x_{Mg} = 0, 0.25, 0.5, 0.75 and 1) and different degrees of inversion (i= 0, 0.25, 0.5, 0.75 and 1). Figure 7-6a displays structures with formation energies (y-axis) below 200 meV/Mn_2O_4 at different Mg concentrations (x-axis), and the formation energies of all the Mg-vacancy configurations considered are plotted in Figure 7-16 of the Appendix. Notably, formation energies in Figure 7-6a have been referenced to the non-inverted ($i = 0$), empty Mn_2O_4 and magnesiated ($MgMn_2O_4$) spinel configurations. For each configuration, the degree of inversion is indicated by the corresponding symbol used, ranging from

$i = 0$ (black circles) to $i = 1$ (red stars).

Overall, the $Mg_xMn_2O_4$ system is phase separating at 0 K across non-inverted ($i = 0$) $MgMn_2O_4$ and Mn_2O_4 domains, since the ground state hull of the system (dashed black line in Figure 7-6a) only exhibits two configurations (i.e., $MgMn_2O_4$ and Mn_2O_4). Some solubility at low Mg content may be possible given the low positive mixing energy at $x_{Mg} = 0.25$ for the non-inverted spinel ($E_{formation} \sim 14$ meV/Mn_2O_4). At higher Mg content, the formation energies are very high for the non-inverted spinel (Figure 7-16), making a solid solution behavior very unlikely. Inversion becomes likely to occur at intermediate Mg compositions, as the low positive formation energies are on the scale of the configurational entropy. For example, $E_{formation} \sim 11$ meV/Mn_2O_4 at $i = 0.25$ and $x_{Mg} = 0.5$ (green square at $x = 0.5$ in Figure 7-6a). Hence, inversion at intermediate states of magnesiation is likely. While Mg by definition has to be mobile in Mn_2O_4 to operate as a cathode, Mn mobility, which is required for spinel inversion to occur, depends strongly on its valence state.[176, 177] Typically, Mn^{3+} can be mobile through a temporary disproportionation mechanism, generating mobile Mn^{2+} (Figure 7-15).[176, 177]

Figure 7-6b plots the average voltages as a function of x_{Mg} at different i by taking the lowest $E_{formation}$ configuration at each i and x_{Mg}.[13] The average voltage for Mg insertion in the non-inverted ($i = 0$) configuration is ~ 2.84 V (dashed black line in Figure 7-6b), in agreement with previous theoretical estimates.[126, 88] Inversion does increase the average insertion voltage (averaged over $x_{Mg} = 0$ to 1) marginally compared to the normal spinel, with specific values of ~ 2.92, 2.99, 2.97 and 2.99 V at $i = 0.25$, 0.5, 0.75 and 1, respectively. Notably, the phase behavior of the $Mg_xMn_2O_4$ system under inversion will be different compared to the normal spinel due to the formation of metastable inverted states at intermediate Mg compositions.

The extractable Mg content (x_{ext}, see Section 2.5), obtained as a function of inversion from our Monte-Carlo simulations, indicates the extractable capacity of a cathode particle, and is shown in Figure 7-6c for stoichiometric $MgMn_2O_4$. The y-axis indicates the % of the cathode's theoretical capacity (~ 270 mAh/g for $MgMn_2O_4$), that can be cycled reversibly. At low degrees of inversion, the extractable capacity

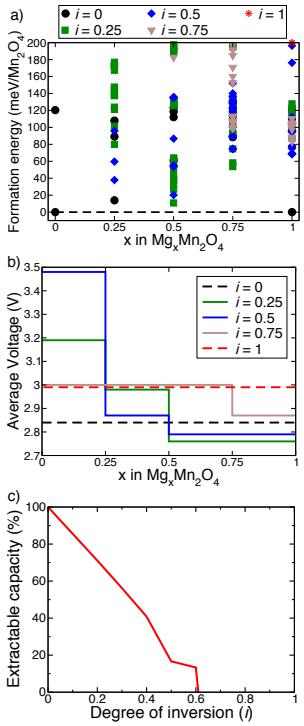

Figure 7-6: (a) Ground state hull (or 0 K phase diagram) of the $Mg_xMn_2O_4$ system, with the zero of the formation energy referenced to the non-inverted (i=0) magnesiated ($MgMn_2O_4$) and empty (Mn_2O_4) spinel configurations. (b) Average voltage curves under i in $Mg_xMn_2O_4$, obtained using the lowest formation energy structures at each i across Mg concentrations. (c) The percentage of the theoretical capacity that can be reversibly extracted is plotted as a function of inversion in stoichiometric $MgMn_2O_4$.

in the stoichiometric spinel decreases roughly linearly with the degree of inversion, reaching $\sim$ 41% ($\sim$ 110 mAh/g) at $i = 0.4$. The extractable Mg content decreases more rapidly from $i = 0.4$ to $i = 0.5$, before stabilizing around $\sim$ 15% ($\sim$ 40 mAh/g) between $i = 0.5$ and 0.6. Eventually, none of the Mg becomes extractable beyond $i =$ 0.61, reflecting the trends in the percolation thresholds ($x_{crit} \sim 0.59$ at stoichiometric $MgMn_2O_4$, Figure 7-5a) at high degrees of inversion. Note that, the overall amount of cyclable Mg from a cathode particle is influenced both by the extractable Mg (shown in Figure 7-6c) and by the phase behavior as a function of x_{Mg}. For example, if the Mg removal occurs via a two-phase reaction (as is the case for the non-inverted spinel), then the presence of a non-percolating layer on the surface may prevent extraction of Mg from the bulk, even if percolation conditions are still favorable in the bulk

material.

7.4 Discussion

In this work, we have used DFT-based NEB calculations to assess the changes in the activation barrier for Mg^{2+} diffusion due to inversion in both oxide ($MgMn_2O_4$) and sulfide ($MgIn_2S_4$) structures. From our results (Figures 7-3 and 7-4), we can conclude that inversion has a significant impact on both oxides and sulfides, by opening and closing specific diffusion trajectories. In order to extrapolate the impact of the various Mg^{2+} diffusion barriers on macroscopic Mg migration, we estimated the percolation thresholds under different degrees of spinel inversion. Furthermore, we analyzed the impact of spinel inversion on cathode properties of $Mg_xMn_2O_4$ by evaluating the average voltages and practical capacities at different degrees of inversion.

7.4.1 Factors influencing barriers in $MgMn_2O_4$

Trends from activation barriers of Figure 7-3 suggest that Mg migration along the $8a-16c-8a$ pathways (Hops 1 and 2) can improve significantly due to Mg occupation of the $16d$ ring sites (up to 4/6 Mg), at low degrees of inversion. Additionally, the $16d-48f-16d$ channels open for Mg migration whenever the edge-$8a$ is vacant. However, high degrees of inversion detrimentally affect Mg^{2+} motion, due to the closing of both $16d-16d$ (corner- and edge-$8a$ become occupied by the metal cation) and $8a-8a$ channels (high migration barriers at high Mg in the ring sites). Although we have specifically considered the case of spinel-$Mg_xMn_2O_4$, similar trends can be expected for other oxide spinels, given the similarity in Mg migration barriers along Hop 1 with different $3d$-metals.[126]

Previous studies have used electrostatic considerations to partially explain trends in Li^+ activation barriers in a Mn_2O_4 spinel.[249] Indeed, the reduction in Mg migration barriers along Hops 1, 3, 4, and 5 (Figure 7-3) with increasing Mg concentration can be attributed to lower electrostatic repulsions at the corresponding intermediate sites caused by the reduction of Mn^{4+} to Mn^{3+}. For example, the barrier reduces

from 717 to 475 meV along Hop 1 and 1388 to 845 meV along Hop 3, as x_{Mg} increases from ~ 0 to ~ 1. However, Mg^{2+} activation barriers generally depend on steric and bonding constraints in addition to electrostatics, which are often difficult to deconvolute over a range of NEB calculations. For example, the Mg^{2+} activation barriers across Hop 2 (yellow bar in Figure 7-3) at low Mg occupation in the ring sites (1/6, 2/6) are lower than Hop 1 (red bar, Figure 7-3), which may be attributed to reduced electrostatic repulsion on the intermediate 16*c* (due to Mg^{2+} replacing higher valent Mn in the ring sites). However, barriers along Hop 2 increase beyond Hop 1 and eventually beyond the limit of ~ 750 meV at higher Mg in the ring sites (5/6, 6/6), despite lower electrostatic repulsion. Thus, the high Mg content in the ring sites decreases the stability of the intermediate 16*c*. One possible reason for the instability of the 16*c* site could arise from charge-deficient oxygen atoms being shared with adjacent, Mg^{2+}-occupied (instead of $Mn^{3+/4+}$) 16*d* sites. Indeed, the instability of the 16*c* (e.g., in the case of 6/6 Mg in Hop 2) is quantified by longer (DFT-based) ~ 2.3 Å Mg–O bonds, compared to ~ 2.08 Å in 16*d* with Mg (along the same hop) and ~ 2.13 Å in rocksalt MgO.[88]

For the $16d-48f-16d$ hops in Figure 7-3 (Hops 3–5), electrostatic effects are more dominant than for the $tet-oct-tet$ hops (Hops 1, 2), primarily due to the intermediate 48*f* edge-sharing with an 8*a*. Indeed, the cation centers in edge-sharing tetrahedra are closer (~ 2.15 Å experimentally between 48*f* and 8*a* in an ideal $LiMn_2O_4$-spinel[16]) compared to edge-sharing octahedra (~ 2.88 Å between 16*c* and 16*d*). Consequently, the Mg barriers are consistently lower with a vacant edge-8*a* (Hop 5, Figure 7-3) compared to Mg/Mn-filled edge-8*a* (Hops 3, 4 in Figure 7-3). Also, Mg^{2+} activation barriers (at $x_{Mg} \sim 0$) increase significantly when the corner-8*a* sites are cation-occupied rather than vacant (Figure 7-3). A closer look at the cation-cation distances across corner-sharing 48*f* and 8*a* (~ 2.88 Å in ideal $LiMn_2O_4$) reveals that the corner-sharing tetrahedra within a spinel framework may experience electrostatic repulsion as high as edge-shared octahedra (i.e., 16*c* and 16*d*). Thus, the combination of cation-cation repulsion arising from both edge- and corner-8*a* sites results in the high barriers along Hops 3 and 4.

7.4.2 Barriers in sulfides vs. oxides

However, the absolute changes in barriers in the sulfide are remarkably lower than the oxide. For example, the absolute difference between the lowest and the highest Mg migration barriers of $MgMn_2O_4$ (at $x_{Mg} \sim 1$) across Hops 1 through 5 is $\sim$ 662 meV (1055 – 393 meV), while this is a much lower $\sim$ 236 meV (683 – 447 meV) for $MgIn_2S_4$. Similarly, the barriers along the $16d - 48f - 16d$ trajectory are far less sensitive to the edge-8a occupancy in the sulfide (504–673 meV) than in the oxide (570–845 meV at $x_{Mg} \sim 1$). Surprisingly, the migration barrier with an edge-8a occupied by Mg^{2+} is higher ($\sim$ 683 meV) than when the edge-8a is occupied by In^{3+} ($\sim$ 531 meV), suggesting that the In–S bonding environment screens the higher In^{3+} charge better than the Mg–S bonds screen Mg^{2+}.

Lower activation barriers for Mg in sulfides have been reported before,[126, 125, 31] which have been assigned to robust electrostatic screening, high polarizability and large volume per anion of S^{2-} compared to O^{2-}.[32, 237] For example, a $Mg_xTi_2S_4$[213] cathode will not suffer from any percolation bottlenecks, if the barriers across all cation arrangements are similar to the calculated values in $MgIn_2S_4$ (i.e., < 750 meV, Figure 7-4). But a more stringent upper-bound of $\sim$ 500 meV on the barrier in a solid-state conductor[237, 14] indicates that inversion can significantly affect a sulfide ionic conductor by closing all $16d - 16d$ channels and several $8a - 8a$ channels with high Mg in the 16d ring (Figure 7-4).

7.4.3 Percolation under inversion

Estimations of percolation thresholds (x_{crit}) in the $Mg_xMn_{3-x}O_4$ system (Figure 7-5a) indicate that spinel inversion should not detrimentally affect macroscopic Mg^{2+} migration across the structure up to a fairly high degree of inversion, $i \sim 0.59$, since x_{crit} remains in the Mg-deficient domain. However, Mg-excess concentrations are required to ensure percolating networks form at $i = 0.6 - 0.7$, while the spinel completely ceases to percolate Mg beyond $i = 0.77$ (Figure 7-5a). Given the preponderance of conversion reactions under Mg-excess concentrations in the oxide spinel, specifi-

cally the decomposition of $Mg_xMn_{3-x}O_4$ ($x > 1$) into MgO and MnO,[32] it is of paramount importance that the chemically synthesizable, stoichiometric $MgMn_2O_4$ remains percolating. Efforts should be made to reduce or precisely control the amount of inversion (i.e., $i < 0.6$), by carefully tuning synthesis temperature and cooling rate[130, 85] during $MgMn_2O_4$ synthesis.

Higher Mg conductivity, as is required for a solid state electrolyte, demands a lower cut-off for the migration barrier along a pathway. In the case of $MgIn_2S_4$, where we used a 500 meV cut-off, MC simulations indicate that the stoichiometric spinel should remain percolating up to $i \sim 0.44$. However, high degrees of inversion ($i \sim 0.85$) can be observed during $MgIn_2S_4$ synthesis (Figure 7-7). As a result, strategies to limit inversion (i.e., $i < 0.44$) in sulfide spinel ionic conductors, such as chemical doping and careful calibration of synthesis conditions, need to be sought.

7.4.4 Voltages and capacities

Inversion can also significantly impact electrochemical properties, such as phase behavior, average voltages and extractable capacities in an oxide-spinel cathode (Figure 7-6). For example, the average voltage for Mg intercalation, across $x_{Mg} = 0-1$ in the Mn_2O_4-spinel, is higher in an inverted spinel compared to a normal spinel (Figure 7-6b). Mg intercalation experiments in spinel-Mn_2O_4 have reported a marginally higher average voltage (~ 2.9 V)[96] than predicted for the normal spinel (~ 2.84 V), with extraction voltages as high as ~ 3.5 V during the charging cycle, which might be an indication of the spinel inverting during electrochemistry. Also, the calculated 0 K phase diagram of the Mg-Mn_2O_4 system (Figure 7-6a) suggests that the tendency to invert is the highest at an intermediate Mg concentration, as indicated by low $E_{formation}$ (< 50 meV/Mn_2O_4) configurations with $i = 0.25$ at $x_{Mg} = 0.5$. Hence, the degree of inversion in the Mn-spinel can indeed change dynamically during electrochemical Mg cycling, especially due to the presence of mobile Mn^{2+} ions (Figure 7-15). Thus, strategies to minimize changes in i, during Mg^{2+} cycling, such as cation-doping of Mn to prevent Mn^{2+} generation, should be employed to ensure reversible Mg (de)intercalation.

Importantly, the extractable Mg content in stoichiometric $MgMn_2O_4$ decreases continuously with inversion, reaching values of $\sim$ 63% (171 mAh/g) and $\sim$ 17% (46 mAh/g) at $i = 0.25$ and 0.5 (Figure 7-6c), respectively. Note that stoichiometric $MgMn_2O_4$ remains percolating to Mg^{2+} migration up to $i \sim 0.59$. The significant decrease in extractable capacity in $MgMn_2O_4$, particularly at low degrees of inversion ($i < 0.4$), can be attributed to the decoupled nature of the $8a - 8a$ and $16d - 16d$ channels (Table 7.3). Thus, the Mg^{2+} present in the $16d$ sites at low i are not a part of the percolating network(s) formed along the $8a - 8a$ channels and remain un-extractable.

7.5 Conclusion

Spinels are promising materials in the development of multivalent battery electrodes and solid electrolytes but are prone to antisite disorder in the form of spinel inversion. With the example of two prototypical oxide and sulfide spinels, $MgMn_2O_4$ (cathode) and $MgIn_2S_4$ (solid electrolyte), we demonstrated that inversion can significantly impact both Mg-ion mobility and electrochemical properties. Using first-principles calculations, we analyzed the migration barrier for Mg^{2+} diffusion in different local cation arrangements, and found that inversion can both open and close select diffusion pathways on the atomic scale. To quantify the influence of local barrier changes on the macroscopic transport of Mg^{2+} ions, we determined the minimal Mg content x in $Mg_xM_{3-x}X_4$ required for percolation. Using a cut-off of 750 meV and 500 meV for cathodes and solid electrolytes, respectively, we found that the stoichiometric $MgMn_2O_4$ and $MgIn_2S_4$ compositions are Mg percolating up to $\sim$ 59% and 44% inversion. Since the degree of inversion in the spinels considered in this work may vary between 20% and 85% depending on the method of preparation,[130, 85, 31] a careful calibration of the synthesis conditions is essential to ensure sufficient Mg transport and to reduce the resultant impedance. In addition, spinel inversion can affect the electrochemical properties of cathode materials by changing the phase behavior, average voltage, and extractable capacities. Specifically, we find that the degree of

inversion can change dynamically during electrochemical Mg cycling, as indicated by the 0 K phase diagram of the $Mg_xMn_2O_4$ system and the activation barriers for Mn^{2+} diffusion. Notably, even low degrees of inversion ($i < 0.4$) can detrimentally reduce the extractable capacity in stoichiometric $MgMn_2O_4$, with an estimated 15% decrease in capacity with every 10% increase in inversion. Thus, spinel inversion can hinder the electrochemical performance of both cathodes and solid electrolytes in MV systems and synthesis efforts must always be made to stabilize the normal spinel structure.

Given that the Mg^{2+} migration barriers over a range of oxide[126] and sulfide spinels[125] show similar trends, we expect similar behavior upon inversion in other spinel materials. Finally, the framework developed in this work, particularly the data reported on percolation thresholds and extractable Mg, is readily transferable to other spinels that have potential applications in Li-ion, Na-ion, Ca/Zn-multivalent and other battery fields.

7.6 Appendix

7.6.1 Structure of inverse-$MgIn_2S_4$

Elemental forms of Mg (Sigma Aldrich $\geq$ 99%), In (Sigma Aldrich, 99.999% trace metal basis) and S (Sigma Aldrich 99.99% trace metal basis) are first weighted with the stoichiometric ratio. Approximately 2 g of the powder mixture was placed into a tungsten carbide ball mill jar, and the mixture was ball milled (SpexSamplePrep 8000M) for 30 minutes. The resulting powder was then pressed into pellets of 6.0 mm in diameter under a pressure of 1.4 metric tons for 1–2 minutes. Typically, less than 3 pellets, each weighted at $\sim$ 0.2 g, were wrapped into a platinum foil (Sigma Aldrich, 99.99% trace metal basis) which was subsequently secured into a stainless-steel tube (Swagelok, 3/8-inch diameter). The tube was later closed with stainless steel caps, to avoid air exposure during the transfer of the tube for synthesis. All the aforementioned steps were performed in an Ar glove box.

The reaction to form the spinel was carried out in a Thermo Scientific Minimite furnace under a continuous flow of Ar gas. To further reduce the level of oxygen and moisture in the Ar gas, an oxygen/moisture trap was attached between the Ar gas cylinder and the quartz tube where the stainless-steel tube was placed. After a quick purge of Ar ($\sim$ 20 min), the temperature was quickly ramped to 800 °C in 1 hour. The temperature was held at 800 °C for 12 hours, before the furnace was slowly cooled down to room temperature over 50 hours. The powder was collected in Ar glove box by cutting the stainless-steel tube.

The structure of $MgIn_2S_4$ was refined using the Rietveld method. The diffraction pattern of $MgIn_2S_4$ can be readily indexed with the spinel lattice (*Fd-3m*, a = b = c = 10.72060 Å). When the site occupancies of Mg, In and S were fixed to 1.0 while allowing other structural parameters to vary, substantial deviation between the simulated and observed patterns was observed, suggesting that the as-prepared $MgIn_2S_4$ is not a normal spinel. Mg and In site inversion was then tested by allowing simultaneous presence of Mg and In on the same site and by constraining each cation site to be fully occupied and the composition to be $MgIn_2S_4$. Excellent agreement between the calculated and

observed data was achieved. THe refinement results show that the 8*a* site is occupied by 15% Mg and 85% In, and the 16*d* site is occupied by 43% Mg and 57% In, corresponding to a degree of inversion, $i = 0.85$. The fitting is presented in Figure 7-7. Structural parameters from the refinement are tabulated in Tables 7.4–7.6.

Table 7.4: Crystallographic data for $MgIn_2S_4$ based on the Rietveld refinement of the synchrotron X-ray data.

Radiation	Synchrotron X-ray (11 BM, APS)
Crystal System	Cubic
Space group	*Fd-3m*:2 (#227)
Lattice parameters	a = b = c = 10.72060(4) Å
Cell volume	1232.13(1) $Å^3$
Density (calculated)	4.12066 g/cm^3
λ	0.414173 Å
R_{wp}	12.955%
R_p	10.286%
χ^2	1.190

Table 7.5: Atomic site information for $MgIn_2S_4$. The thermal parameters (column B_{iso}) should be associated with large errors due to the large absorption of the sample ($\mu R = 4.38$)

Atom	Wyck.	x/a	y/b	z/c	Occ.	B_{iso} ($Å^2$)
S	32*e*	0.24259(1)	0.24259(1)	0.24259(1)	1	1.35(2)
*M*1	16*d*	1/2	1/2	1/2	In = 0.57 Mg = 0.43	6.8(5)
*M*2	8*a*	1/8	1/8	1/8	In = 0.85 Mg = 0.15	1.41(2)

Table 7.6: Selected bond distances (Å) for $MgIn_2S_4$.

*M*1–S (×6)	2.601(1)
*M*2–S (×4)	2.462(2)

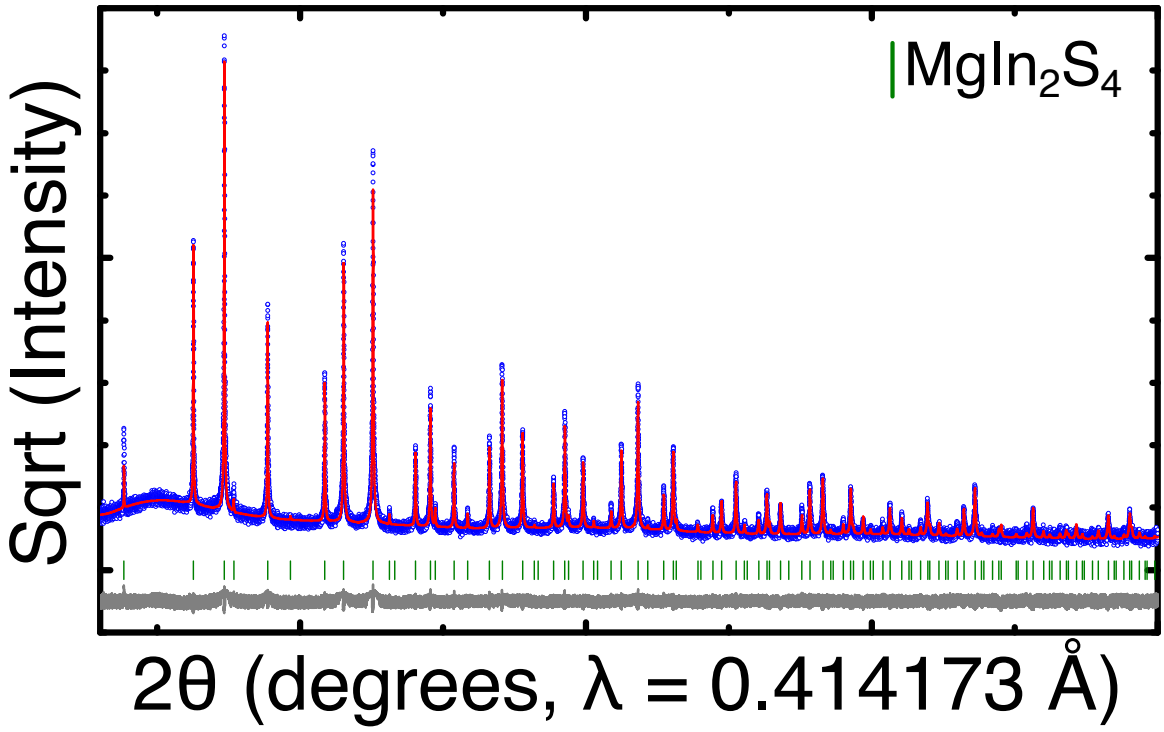

Figure 7-7: Rietveld refinement of the synchrotron XRD pattern for $MgIn_2S_4$. Data was collected at beamline 11 BM of the Advanced Photon Source, Argonne National Laboratory, with a wavelength of 0.414173 Å. The square root of the intensity is plotted on the y-axis. The observed and calculated curves are shown in blue and red, with the difference curve shown in dark grey. Reflections corresponding to $MgIn_2S_4$ are shown as green tick marks.

7.6.2 Convergence of Nudged Elastic Band barriers

Figure 7-8 plots the change in the activation barriers for Mg diffusion, calculated based on Density Functional Theory (DFT)-based Nudged Elastic Band (NEB) calculations, with the size of the spinel cell used. The parameters used in the calculations are as described in the Methods chapter (Section 2.4. The calculations are done along the $16d - 48f - 16d$ ($oct - tet - oct$) trajectory, with the edge-sharing $8a$ site occupied by Mn (Hop 4 in Figure 7-2) in the $Mg_xMn_2O_4$ spinel structure. The corner-sharing $8a$ sites in both calculations are also occupied by cations.

Data from the calculations indicate the Mg^{2+} diffusion barrier, as calculated in a $1\times1\times1$ conventional spinel cell ($\sim$ 1418 meV, solid red line in Figure 7-8) is comparable to a barrier calculated in a larger $2\times1\times1$ cell ($\sim$ 1449 meV, dashed red line,

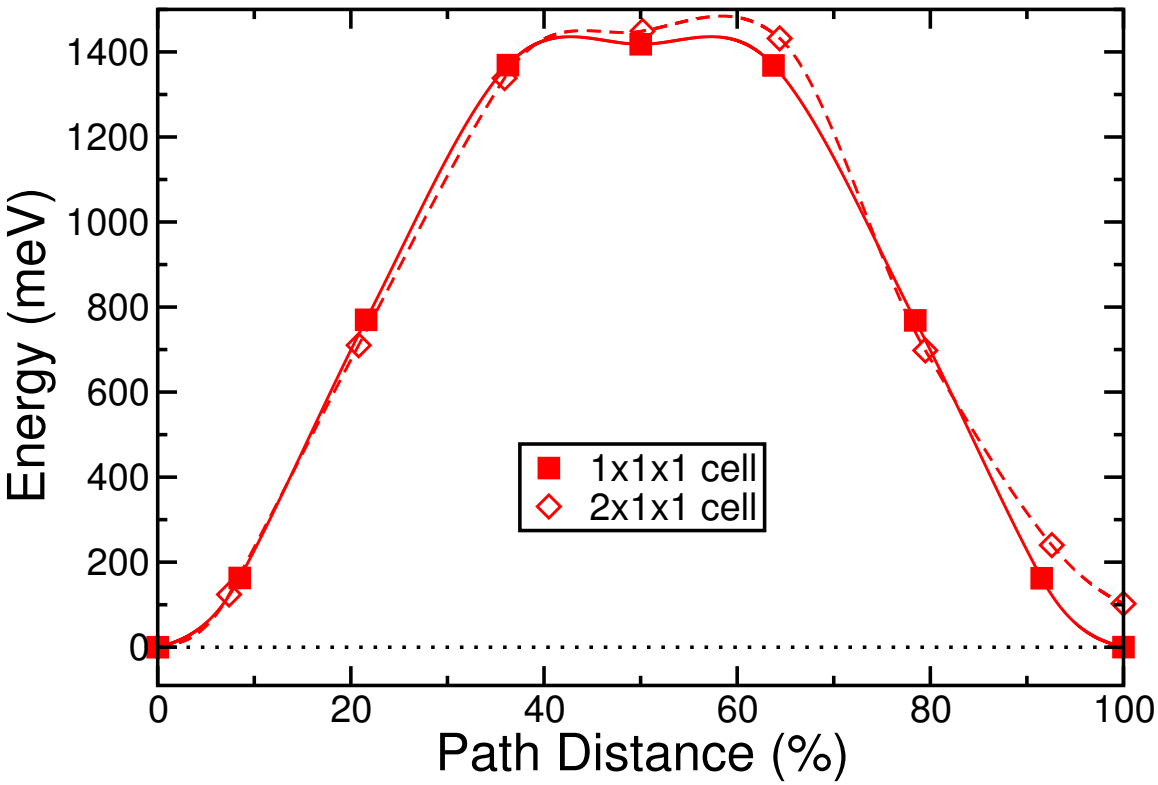

Figure 7-8: Variation of Mg activation barriers with cell size used in the Nudged Elastic Band calculations

$<$ 3% change), demonstrating that NEB calculations in a conventional spinel cell can provide accurate estimations of the barrier. The energy difference across the initial and final states in the 2×1×1 cell ($\sim$ 100 meV) is due to the asymmetry of the cation occupancy in the 16*d* sites across the end points, while the 1×1×1 cell does not display any such asymmetry.

7.6.3 Nudged Elastic Band data for $MgMn_2O_4$

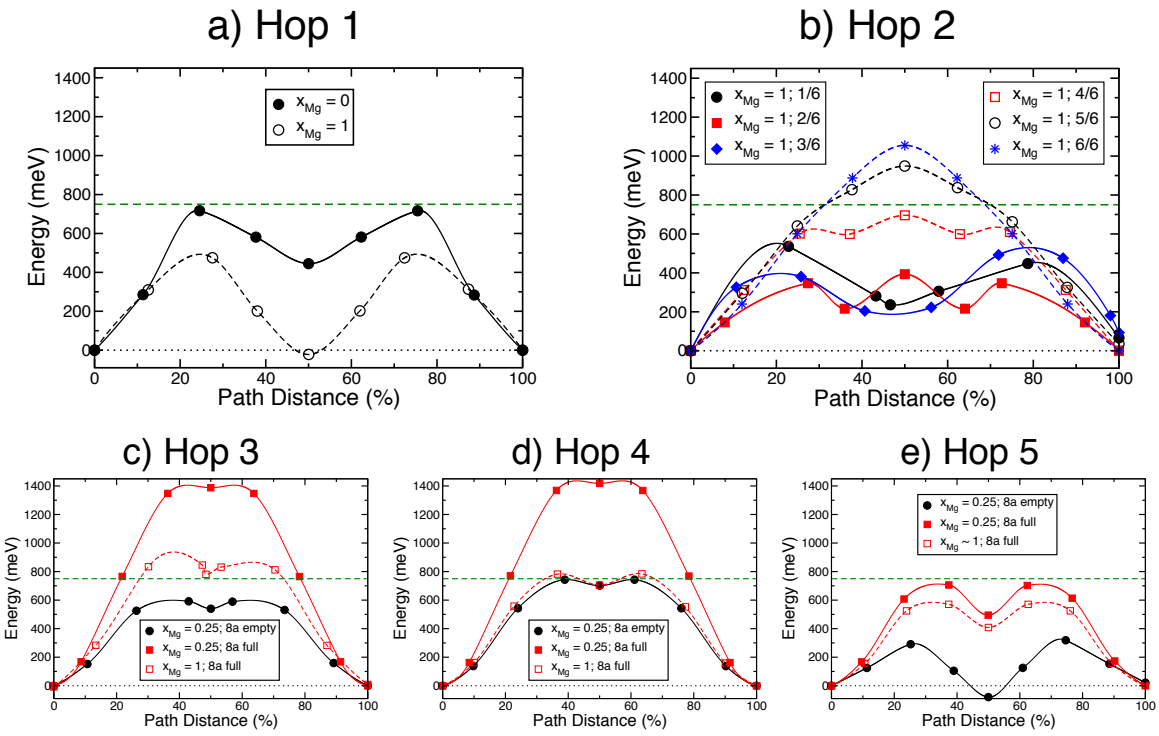

Figure 7-9: Activation barriers for Mg^{2+} diffusion in normal and inverted spinel-Mn_2O_4 under different local environments. The dashed green lines in all panels represent the upper-bound of the migration barrier for a $\sim$ 100 nm ($\sim$ 750 meV) cathode particle being (dis)charged at a C/3 rate. The dotted black lines indicate zero, where zero is referenced to the lowest energy amongst the initial and final end points. The fractions in panel (b) indicate Mg occupancy of the 16*d* "ring" sites (refer Section 7.2.1). The legends "8a full" and "8a empty" in panels (c), (d), and (e) indicate that the 8*a* sites that corner-share with the intermediate 48*f* are cation-occupied and vacant, respectively. x_{Mg} in all panels refers to the Mg concentration at which the corresponding barrier has been calculated. For the specific case of 1/6 Mg ring site occupancy in Hop 2 (solid black line in panel b), we used 5 images across the end points due to convergence issues while using 7 images.

7.6.4 Nudged Elastic Band data for $MgIn_2S_4$

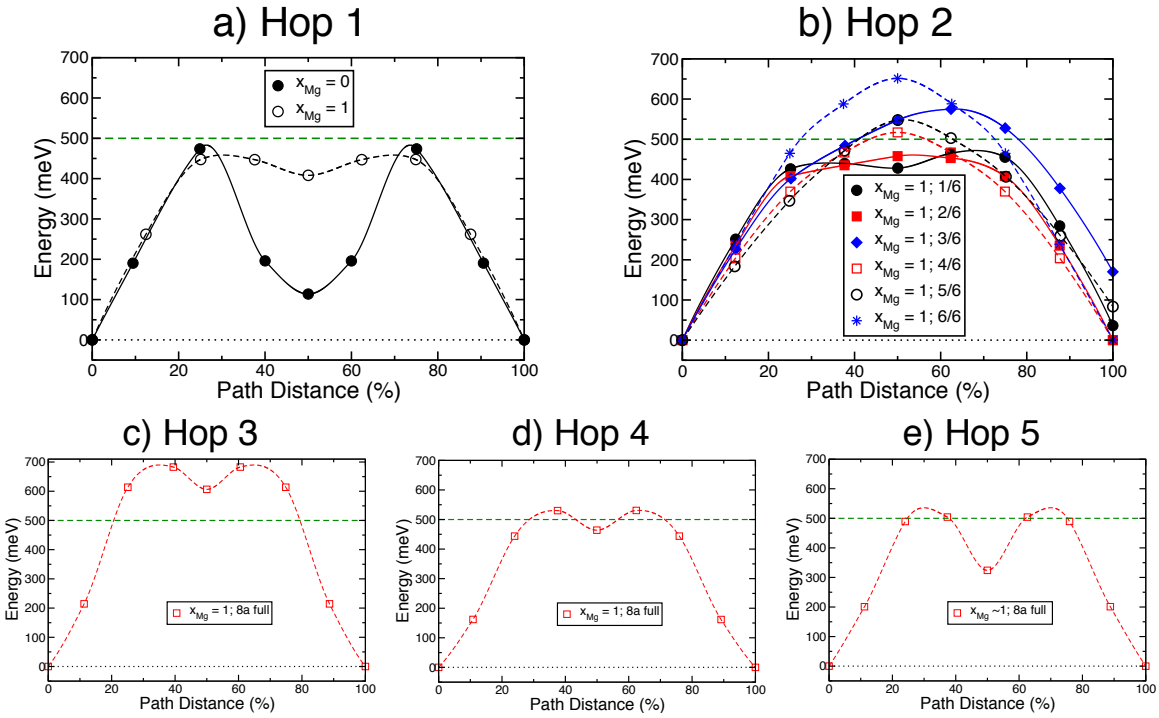

Figure 7-10: Activation barriers for Mg^{2+} diffusion in normal and inverted spinel-In_2S_4 under different local environments. The dashed green lines in all panels represent the upper-bound of the migration barrier for a reasonable solid electrolyte ($\sim$ 500 meV), while the dotted black lines indicate zero. The zero energy in each panel is referenced to the lowest energy amongst the initial and final end points, which should be ideally identical. However, similar to Figure 7-9, there are scenarios with a non-negligible difference between the end point energies, which is due to the symmetry of the cation arrangement being broken differently across the end points. The fractions in panel (b) indicate Mg occupancy of the 16*d* "ring" sites. The legends "8a full" in panels (c), (d), (e) indicates that the 8*a* sites that corner-share with the intermediate 48*f* are cation-occupied. x_{Mg} in all panels refers to the Mg concentration at which the corresponding barrier has been calculated.

7.6.5 Activation barrier along Hop 4 in Mn-spinel

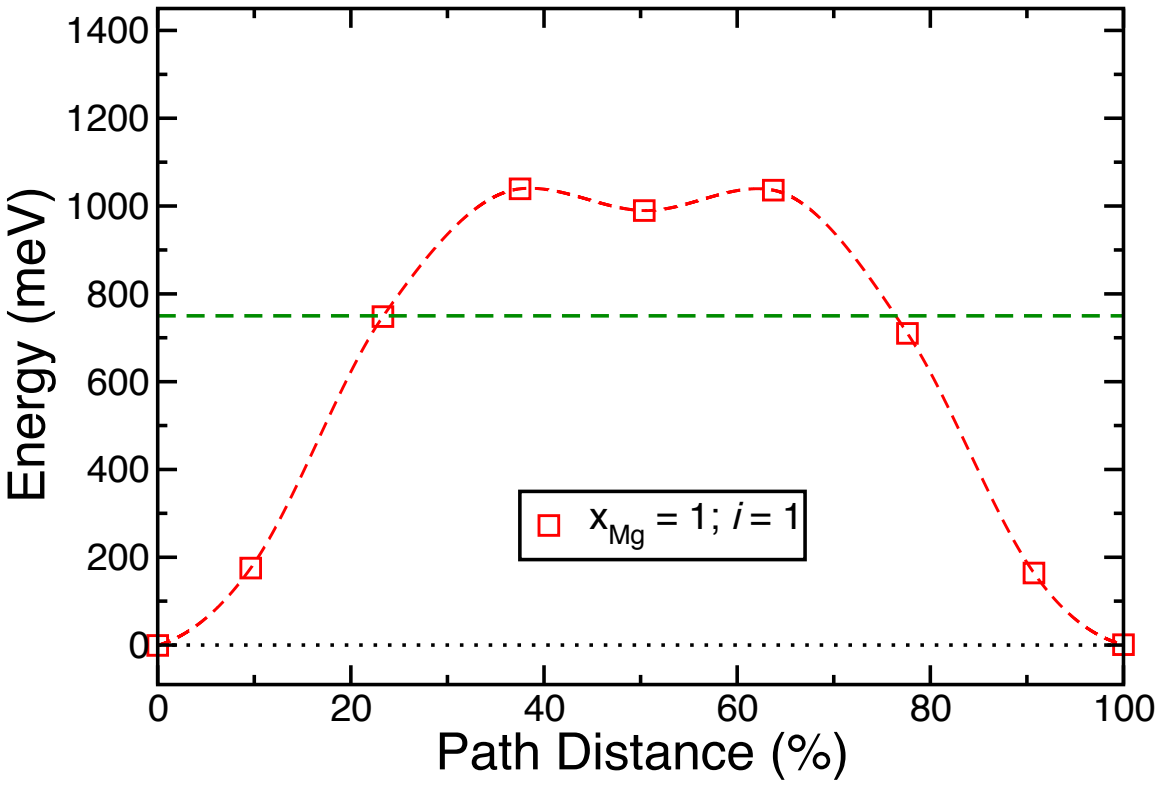

Figure 7-11: Activation barrier for Mg^{2+} diffusion along the Hop 4 trajectory ($16d - 48f - 16d$ with Mn in edge-$8a$, Figure 7-2d) at $x_{Mg} = 1$ and $i \sim 1$ in the $MgMn_2O_4$ spinel structure. The dashed green line (750 meV) indicates the barrier thresholds used in percolation simulations (see Section 7.3.1).

7.6.6 Convergence of Monte-Carlo percolation simulations

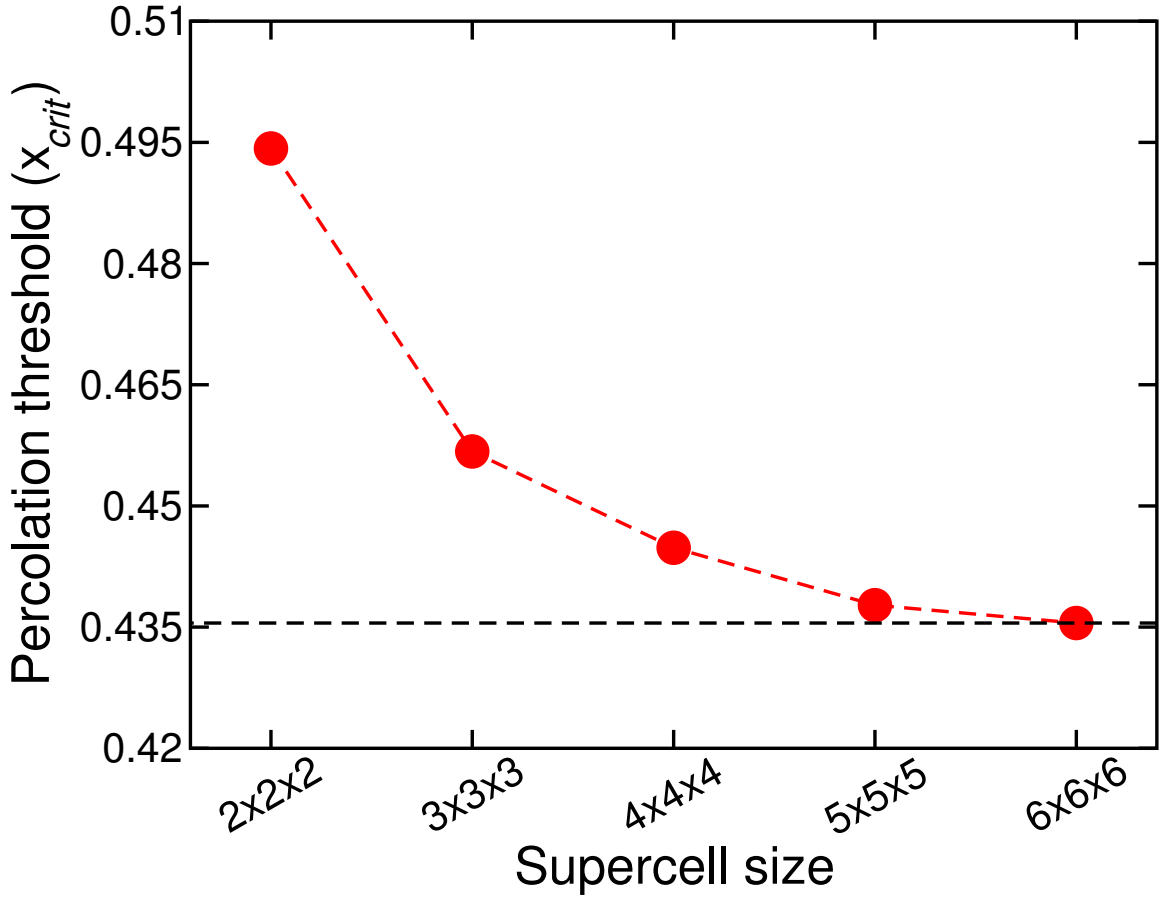

Figure 7-12: The convergence of percolation thresholds (x_{crit}, Section 2.5), with supercell size during Monte-Carlo simulations. The cells are initialized with a M_3X_4 stoichiometry (i.e., no vacancies) and scanned for percolating Mg networks (as detailed in Section 2.5). The supercell size indicated is with respect to the primitive spinel cell, which is equivalent to 8 anion atoms. A 6×6×6 supercell (1728 anions) is used in further x_{crit} estimations, since the difference in thresholds between a 5×5×5 and a 6×6×6 supercell is $< 1\%$.

7.6.7 Varying vacancy concentration in percolation simulations

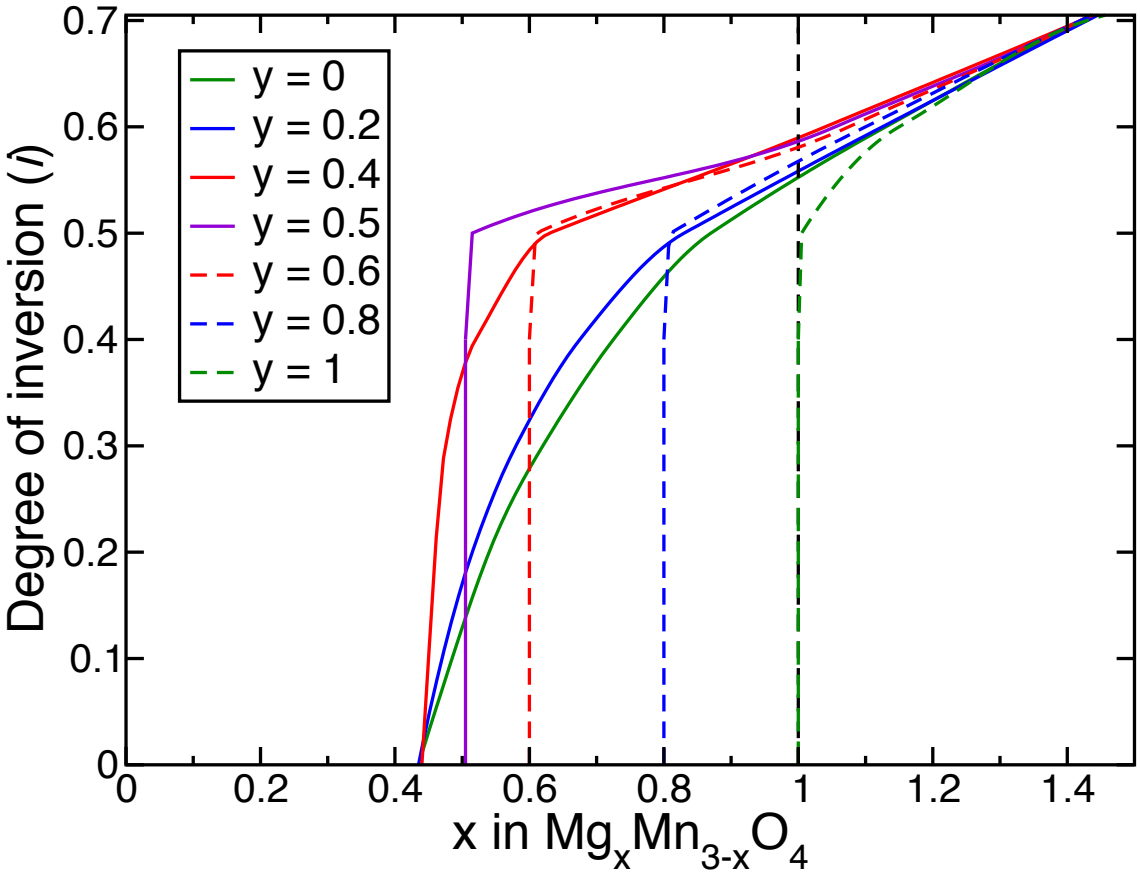

Figure 7-13: Percolation thresholds calculated with different initial vacancy concentrations are plotted for $MgMn_2O_4$. The x-axis corresponds to the total concentration of Mg and vacancies in the supercell. During Monte-Carlo simulations, structures are initialized with different concentrations of vacancies (legends "'y") in the Mg sublattice, leading to initial stoichiometries of $Vac_yMn_{3-y}O_4$, followed by flipping the Mn sites to Mg until the formation of a percolating network (see Section 2.2 and Section 4.3 in the main text). Thus, at a given i, x_{crit} is taken to be the minimum concentration of Mg+vacancies at which a percolating network can form within the supercell.

7.6.8 $16d - 8a$ hops in $MgMn_2O_4$ and $MgIn_2S_4$

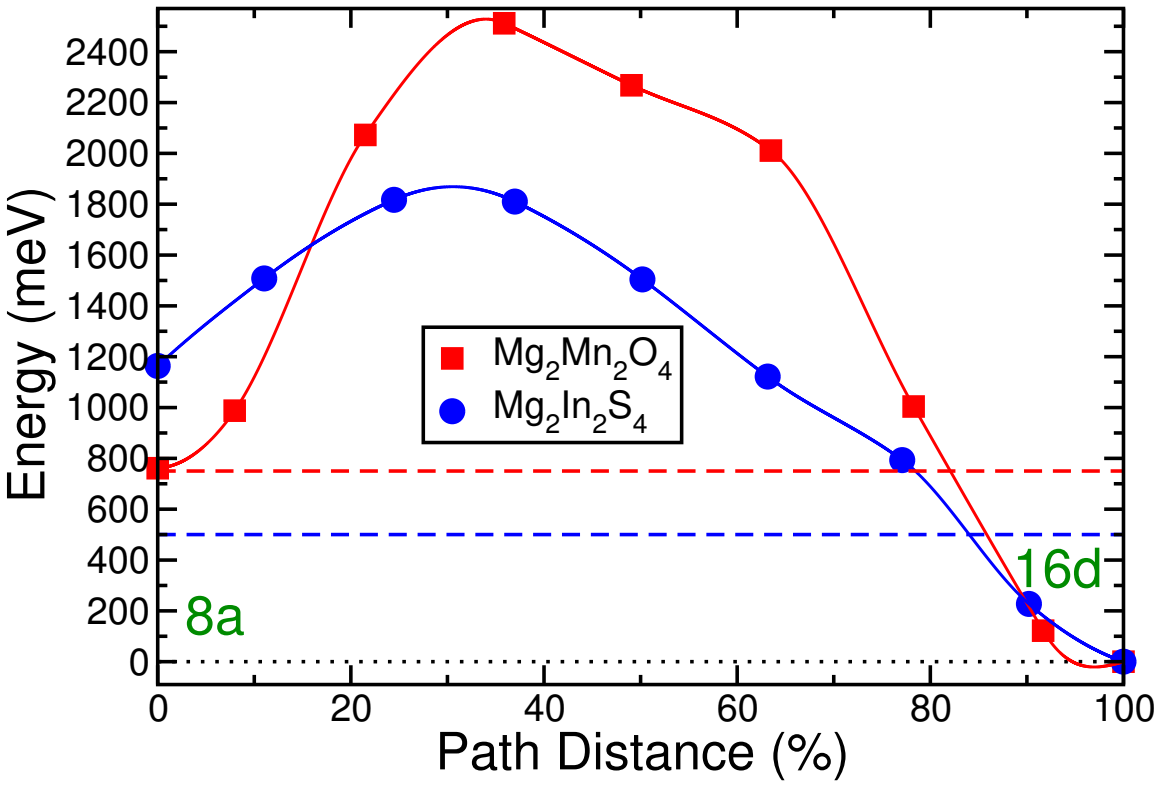

Figure 7-14: Mg^{2+} activation barrier for diffusion from a $8a$ *tet* (0% on the x-axis) to a $16d$ *oct* (100%) site for $Mg_xMn_2O_4$ (at $x_{Mg} \sim 0$, red) and the $MgIn_2S_4$ (at $x_{Mg} \sim 1$, red) spinel structures. The dashed red (750 meV) and blue (500 meV) indicate the barrier thresholds used in percolation simulations for cathode-$Mg_xMn_2O_4$ and ionic conductor-$MgIn_2S_4$, respectively, indicating that the $8a - 16d$ hops will not participate in any percolating Mg^{2+} network in both the oxide and the sulfide spinel. Interestingly, the $8a$ site becomes highly unstable in the presence of a vacant corner-sharing $16d$ site, as demonstrated by the higher energy of the $8a$ compared to $16d$ in both the Mn- and In-spinel. Additionally, the $8a - 16d$ barriers indicate that a given percolating network in the oxide or sulfide spinel will be composed exclusively of either $8a - 8a$ or $16d - 16d$ diffusion channels, and not a mix of both.

7.6.9 Mobility of Mn^{2+} in Mn_2O_4

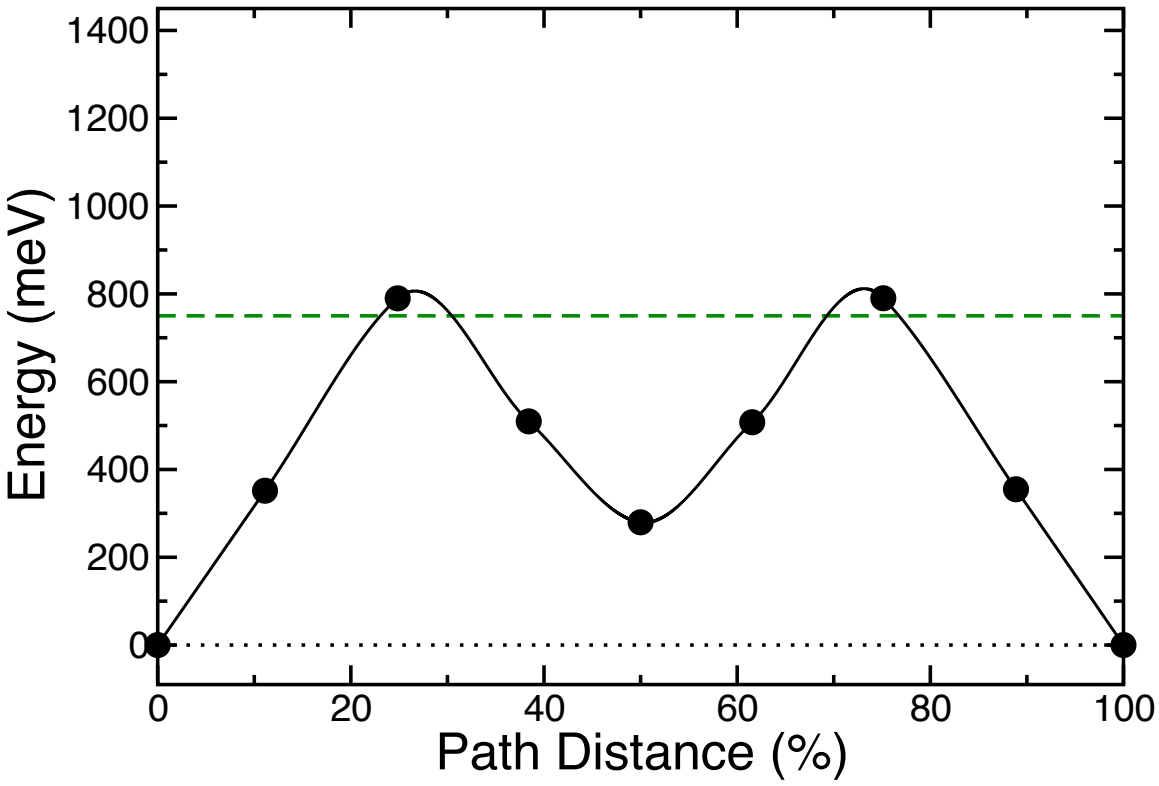

Figure 7-15: Mn^{2+} diffusion barrier along a "Hop 1" pathway ($8a-16d-8a$, Figure 7-2a), with the stoichiometry of the spinel corresponding to $Mn_{\sim 0}Mn_2O_4$. The dashed green line (750 meV) indicates the barrier thresholds used in percolation simulations, suggesting that Mn^{2+} migration along the Hop 1 trajectory might be comparable to Mg^{2+} diffusion along the same pathway ($\sim$ 716 meV barrier for Mg^{2+} along Hop 1 in the dilute Mg limit, Figure 7-3a). Mobile Mn^{2+} ions, generated by the disproportionation Mn^{3+}, can cause a change in the degree of inversion during electrochemical cycling of Mg.

7.6.10 Ground state hull: $Mg_xMn_2O_4$

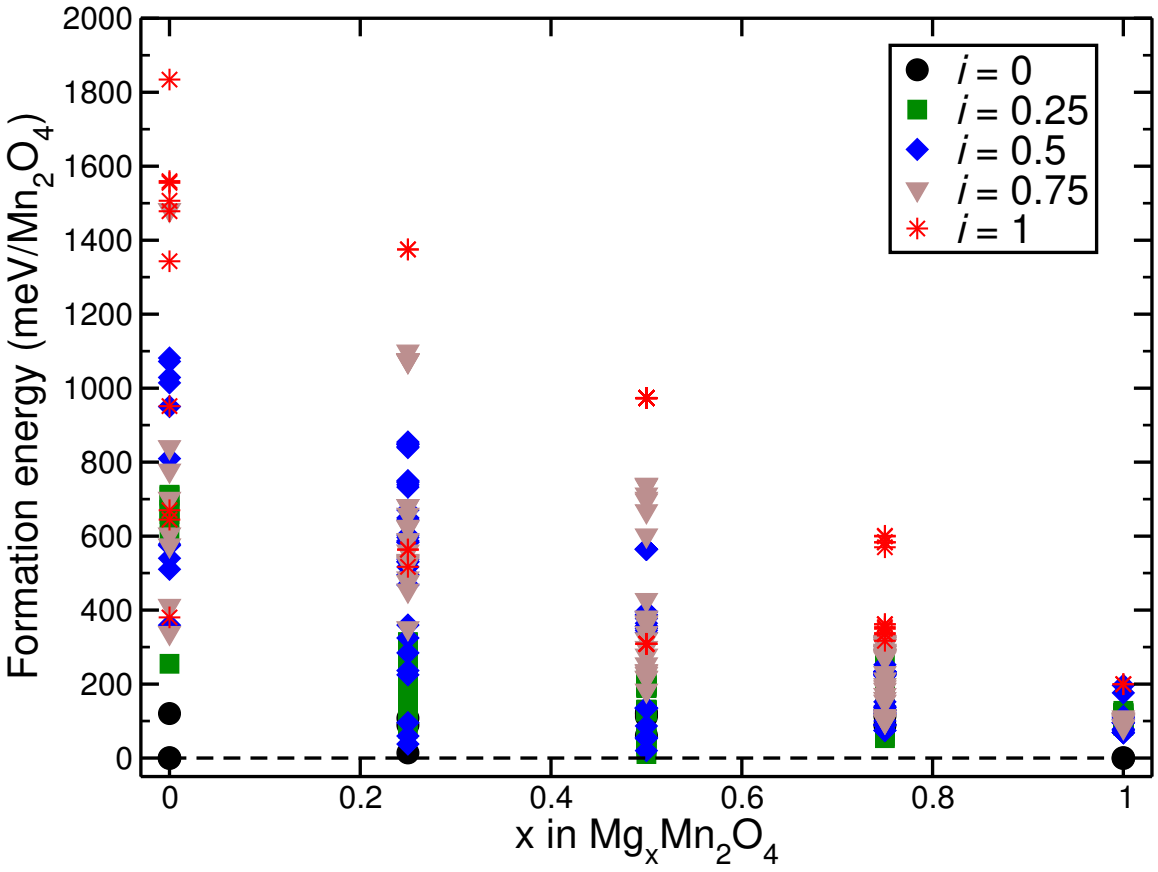

Figure 7-16: Ground state hull, or the 0 K phase diagram of the $Mg_xMn_2O_4$ system, with calculations done at different Mg concentrations (x) and degrees of inversion (i). The zero of the formation energy scale is referenced to the $i = 0$, fully magnesiated ($MgMn_2O_4$) and empty (Mn_2O_4) spinel configurations. The DFT energies of ~ 400 Mg-vacancy orderings within the conventional spinel cell (32 oxygen atoms) are used to construct the hull. The structure-enumeration algorithms,[74, 75, 76] as implemented in the pymatgen library,[160] are used to generate the various Mg-vacancy orderings.

Chapter 8

Conclusions and Future outlook

Multivalent batteries that couple a high voltage cathode with a metal anode, exhibit promise in achieving higher energy densities than current Li-ion technologies, indicating future applications in portable electronics as well as in electric vehicles and the grid. However, there are still many obstacles to be overcome in MV chemistry, such as the lack of compatible electrolytes and poor MV mobility in many compounds. While MV batteries, using the Chevrel-phases as cathodes, demonstrate reversible Mg intercalation with reasonable rate performance, the voltages ($\sim$ 1.1 V) and capacities ($\sim$ 80 mAh/g) obtained are low, resulting in poor energy densities and necessitating the exploration of alternate chemistries for cathode materials.

Cathode improvements over the last 15 years have resulted in significant increases in MV full-cell energy density, with spinel Ti_2S_4[213] doubling the energy density of Chevrel Mo_6S_8. As the state-of-the-art thiospinel MV cathode material falls short of energy density levels needed to compete with present Li-ion technology, there is a demonstrable need for the discovery of high energy-density cathodes. Transition metal oxide hosts have been considered as cathode materials for MV batteries because of their high theoretical voltages and capacities (Section 1.4).[126, 183] Apart from poor MV mobility in the bulk structure,[183, 96, 190, 191] most oxides suffer from possible oxide conversion reactions in the cathode,[122] pseudo-capacitance contributions arising from nano-sized frameworks,[90, 56] and electrolyte incompatibility with high voltage ($\sim$ 3.0 V vs. Mg) cathodes,[255] making it difficult to observe and validate

reversible MV (or Mg) intercalation at reasonable rates. Nevertheless, layered-oxide hosts, such as MoO_3,[208] $Mo_{2.48}VO_{9.93}$,[93] V_2O_5,[64] and MnO_2[146, 214, 96] have received significant experimental and theoretical attention as cathodes for Mg-batteries, and electrochemically reversible Mg intercalation at comparable voltages has already been displayed in these hosts with varied levels of success.

One of the key challenges in the discovery of new MV cathodes is predicting MV mobility in candidate cathode frameworks in a high-throughput fashion. Given the complexity of Nudged Elastic Band calculations, it will be useful to develop descriptors or parameters that can serve as predictors for high MV mobility. In this respect, coordination preference of MV ions was identified as one descriptor that might serve as a screening criterion.[183] However, more robust metrics need to be developed.

Briefly described in Chapter 7, migration barriers generally depend on both electrostatics and MV-bonding constraints, which necessitates careful deconvolution. Electrostatic energetics of the stable and transition states in a given migration pathway can be efficiently computed using classical methods such as Madelung energies and Ewald summations.[55] Hence, the energies of different coordination environments for each MV ion should be accurately computed. For example, the absolute energy of a Mg–O bond in a tetrahedral environment should be calculated as a function of the Mg–O bond length. Eventually, a library of energies in various coordination environments can be established for each MV ion.

Once the electrostatic and bonding energies are available for the stable and transition states in a given framework, the migration barrier, to a first order of approximation, will be given by the sum of the difference in each energy component between the stable and activated states, i.e.,

$$E_m = (E^{\text{activated}}_{\text{electrostatics}} - E^{\text{stable}}_{\text{electrostatics}}) + (E^{\text{activated}}_{\text{bonding}} - E^{\text{stable}}_{\text{bonding}}) \tag{8.1}$$

where each energy term in Eq. 8.1 is calculated according to the "size" of the respective stable and activated states. For example, in the case of an oxide spinel,

the electrostatic and bonding energies should correspond to the size of the triangular activated site (see Section 7.2) and the size of the stable tetrahedral site. The size of the stable and the activated states can be nominally described by the average Mg–O bond length in each polyhedron. Thus, decoupling the electrostatic and bonding energetics during ionic diffusion will aid not only in screening for promising frameworks but also to analyze and calibrate each contribution in candidate structures.

The energetic contributions to the migration barrier that are normally not captured via electrostatic or bonding energetics are the contribution of the transition metal (e.g., the extent of ionic/covalent bonding between the transition metal and the anion, and distortions like Jahn-Teller), and the overall relaxation of the structure (e.g., puckering of layers in V_2O_5 as described in Chapter 3). Although the transition metal contribution to the energy scale of diffusion is intuitively expected to be minimal,[126] it will be good to perform a regression analysis on available migration barriers in different structures to estimate the energetic scale. However, the relaxation of a given structure during ionic motion will be difficult to predict without *apriori* knowledge of soft phonon modes within the material.

Apart from identifying promising new MV cathode candidates, it is equally important to understand the Mg intercalation behavior in existing cathodes that have shown some degree of reversible Mg intercalation, which will in turn aid in both optimizing existing cathodes and identifying new potential cathode materials. Being an in-depth exploration of the thermodynamic and kinetic properties of a few candidate high-energy-density MV cathode materials, including Orthorhombic- and Xerogel-V_2O_5 (Chapters 2–5), $Mg_2Mo_3O_8$ (Chapter 6) and spinel-Mn_2O_4 (Chapter 7), this thesis analyzes and assimilates the Mg-intercalation behavior in several different structures via theoretical methods and hopes will serve as a timely aid in MV cathode design. Additionally, a portion of the thesis also focusses on Mg-diffusion kinetics in spinel-$MgIn_2S_4$ (Chapter 7), which is expected to have high Mg ionic conduction, with potential solid electrolyte applications.

Based on benchmarking theoretical predictions with experimental observations, which are done throughout this work (where possible), this thesis should serve as

a useful guide for the identification of a few practical experimental issues that hinders rigorous characterization of Mg intercalation in oxides. For example, water (or solvent) co-intercalation has often been proposed as a possible solution to improve MV (or Mg^{2+}) mobility in oxide hosts,[153, 154] thus achieving both higher voltages and better mobilities. Despite promising electrochemical performance shown in water co-intercalated hosts such as *xerogel*-V_2O_5[82, 217, 192] and MnO_2 polymorphs (especially Birnessite and Spinel),[146, 214, 96] further investigations are required to clarify possible side reactions (such as proton cycling) that could contribute to the improved performance. Additionally, the presence of water in the electrolyte is detrimental to the usage of a Mg metal anode and may not be viable for practical MV batteries. If solvent co-intercalation is indeed established as the mechanism for improved Mg mobility in oxide hosts, then exploration of other solvents that can reversibly co-intercalate in addition to being compatible with the Mg anode is necessary. A fundamental question that remains to be addressed is whether solvent co-intercalation improves mobility in the bulk and exactly what the mechanism is of such improvement, or whether co-intercalation increases the rate capability by limiting the amount of desolvation that is required upon intercalation. If such solvent co-intercalation enhances Mg mobility in the bulk, it may be possible to pre-intercalate solvent in layered cathode materials.[51]

The field of MV batteries would benefit tremendously from establishing some baseline cathode materials that can be used across laboratories. Even for well-studied materials such as MnO_2, MoO_3 and V_2O_5 electrochemical results vary greatly in the literature and currently no "ground truth" capacity is known for these materials, unlike what is the case for many current Li-ion cathode materials. Additionally, for Mg^{2+} and Ca^{2+}, conversion reactions are competitive with intercalation for many potential cathode materials. In addition, the corrosive nature of some electrolytes can lead to corrosion currents overwhelming the response from the cathode. Hence, at this early stage of the field, when no standard electrolytes and cell designs are available, electrochemical characterization of cathode materials should always be accompanied with structural characterization of the cycled cathode materials to demonstrate that

intercalation is indeed taking place.

Given the complex electrochemistry occurring in MV cells, and the passivation of Mg metal with many electrolytes, alternatives to standard two-electrode full cells should be encouraged. For example, by using hybrid cells with a reference electrode, more electrolyte choices become available to test cathodes, and a more rigorous electrochemical response of the cathode can be obtained. In this regard, the development of good reference electrolytes for MV systems represents a high priority. It is worth nothing that the electrochemistry of several MV cathode materials is often tested at elevated temperatures to facilitate MV ion mobility (see Figure 1-4). Hence, the electrochemical results always necessitate careful interpretation as temperature can promote undesired side reactions (including phase transformations) that contribute to the overall degradation of the cathode.

The result of new investigations should be compared and contrasted to previously published work and to available theory predictions. Often, the results of multiple studies are not consistent with each other, while indications that intercalation is implausible can sometimes be inferred by comparing to *ab initio* predicted properties, in particular for average voltages, diffusion barriers, and changes of lattice parameters with intercalation, which have become quite reliable in *ab initio* methods. While disagreement with such theoretical predictions does not necessarily imply that either theory or experiments is wrong, it usually does indicate that a more complex phenomenon than topotatic intercalation (typically assumed for first principles results) is taking place. Hence, such "disagreements" should be taken as a caution and a starting point for further investigations.

The ability to store electricity in chemical devices represents one of the most successful discoveries of the recent centuries, and the last 30 years have witnessed a swift expansion of this field dominated mainly by Pb-acid, Ni-Metal hydride and now Li-ion batteries. As Li-ion batteries approach their energy density limit, new technologies, such as MV batteries, will be required to meet the rapidly growing demands of grid-scale and portable electrochemical energy storage. Even though MV-ion mobility is on average considerably lower than for mono-valent Li^+ and Na^+

intercalants,[183] the development of a new technology is not controlled by average properties but requires only a few good material families, as evidenced by today's Li-ion technology, which relies almost solely on layered oxides ($O3$–stacking[47]), spinels and the olivine $LiFePO_4$. Fortunately, the vast chemical space of possible MV cathode materials remains largely unexplored,[42] and predictions of high mobility in new material classes such as post-spinels, silicates, and fluoro-polyanions[32] suggest both fast kinetic performance and high energy density, can be simultaneously achieved.

Bibliography

[1] Inorganic Crystal Structure Database (ICSD).

[2] G. G. Amatucci, F. Badway, A. Singhal, B. Beaudoin, G. Skandan, T. Bowmer, I. Plitz, N. Pereira, T. Chapman, and R. Jaworski. Investigation of yttrium and polyvalent ion intercalation into nanocrystalline vanadium oxide. *J. Electrochem. Soc.*, 148(8):A940–A950, 2001.

[3] G. G. Amatucci, J.M. Tarascon, and L.C. Klein. CoO_2, The End Member of the Li_xCoO_2 Solid Solution. *Journal of The Electrochemical Society*, 143(3):1114–1123, 1996.

[4] N. Amir, Y. Vestfrid, O. Chusid, Y. Gofer, and D. Aurbach. Progress in non-aqueous magnesium electrochemistry. *J. Power Sources*, 174(2):1234–1240, dec 2007.

[5] Dave Andre, Sung-Jin Kim, Peter Lamp, Simon Franz Lux, Filippo Maglia, Odysseas Paschos, and Barbara Stiaszny. Future generations of cathode materials: an automotive industry perspective. *J. Mater. Chem. A*, 3(13):6709–6732, 2015.

[6] Vladimir I Anisimov, Jan Zaanen, and Ole K Andersen. Band theory and mott insulators: Hubbard u instead of stoner i. *Phys. Rev. B*, 44(3):943, 1991.

[7] Timothy S. Arthur, Ruigang Zhang, Chen Ling, Per-Anders Glans, Xudong Fan, Jinghua Guo, and Fuminori Mizuno. Understanding the electrochemical mechanism of k-αmno_2 for magnesium battery cathodes. *ACS Appl. Mater. Interfaces*, 6(10):7004–7008, May 2014.

[8] D. Aurbach, Z. Lu, A. Schechter, Y. Gofer, H. Gizbar, R. Turgeman, Y. Cohen, M. Moshkovich, and E. Levi. Prototype systems for rechargeable magnesium batteries. *Nature*, 407(6805):724–727, Oct 2000.

[9] D. Aurbach, G. S. Suresh, E. Levi, A. Mitelman, O. Mizrahi, O. Chusid, and M. Brunelli. Progress in rechargeable magnesium battery technology. *Adv. Mater.*, 19(23):4260–4267, dec 2007.

[10] D. Aurbach, E. Zinigrad, Y. Cohen, and H. Teller. A short review of failure mechanisms of lithium metal and lithiated graphite anodes in liquid electrolyte solutions. *Solid State Ionics*, 148(3-4):405–416, Jun 2002.

[11] Doron Aurbach. Review of selected electrode-solution interactions which determine the performance of li and li ion batteries. *J. Power Sources*, 89(2):206–218, aug 2000.

[12] Doron Aurbach, Haim Gizbar, Alex Schechter, Orit Chusid, Hugo E. Gottlieb, Yossi Gofer, and Israel Goldberg. Electrolyte solutions with a wide electrochemical window for rechargeable magnesium batteries. *J. Electrochem. Soc.*, 149(2):A115–A121, 2002.

[13] M. K. Aydinol, A. F. Kohan, G. Ceder, K. Cho, and J. Joannopoulos. Ab initio study of lithium intercalation in metal oxides and metal dichalcogenides. *Phys. Rev. B*, 56(3):1354–1365, jul 1997.

[14] John Christopher Bachman, Sokseiha Muy, Alexis Grimaud, Hao-Hsun Chang, Nir Pour, Simon F. Lux, Odysseas Paschos, Filippo Maglia, Saskia Lupart, Peter Lamp, Livia Giordano, and Yang Shao-Horn. Inorganic solid-state electrolytes for lithium batteries: Mechanisms and properties governing ion conduction. *Chem. Rev.*, 116(1):140–162, jan 2016.

[15] H. G. Bachmann, F. R . Ahmed, and W. H. Barnes. The crystal structure of vanadium pentoxide. *Zeitschrift für Kristallographie - Crystalline Materials*, 115(1-6):110–131, January 1961.

[16] S BagËĞcı, HM Tütüncü, S Duman, E Bulut, M Özacar, and GP Srivastava. Physical properties of the cubic spinel $limn_2o_4$. *J. Phys. Chem. Solids*, 75(4):463–469, 2014.

[17] Christopher J. Barile, Elizabeth C. Barile, Kevin R. Zavadil, Ralph G. Nuzzo, and Andrew A. Gewirth. Electrolytic conditioning of a magnesium aluminum chloride complex for reversible magnesium deposition. *J. Phys. Chem. C*, 118(48):27623–27630, dec 2014.

[18] Christopher J. Barile, Russell Spatney, Kevin R. Zavadil, and Andrew A. Gewirth. Investigating the reversibility of in situ generated magnesium organohaloaluminates for magnesium deposition and dissolution. *J. Phys. Chem. C*, 118(20):10694–10699, may 2014.

[19] Jeremy Barker, M Yazid Saidi, and Jeffrey L Swoyer. Lithiated molybdenum oxide active materials, June 21 2005. US Patent 6,908,710.

[20] K Ben-Kamel, N Amdouni, H Groult, A Mauger, K Zaghib, and CM Julien. Structural and electrochemical properties of $limoo_2$. *J. Power Sources*, 202:314–321, 2012.

[21] Jürgen O. Besenhard and Martin Winter. Advances in battery technology: Rechargeable magnesium batteries and novel negative-electrode materials for lithium ion batteries. *ChemPhysChem*, 3(2):155–159, Feb 2002.

[22] Shou-Hang Bo, Clare P. Grey, and Peter G. Khalifah. Defect-tolerant diffusion channels for mg^{2+} ions in ribbon-type borates: Structural insights into potential battery cathodes $mgvbo_4$ and $mg_xfe_{2-x}b_2o_5$. *Chem. Mater.*, 27(13):4630–4639, Jul 2015.

[23] Jean-Claude Bouloux, Ivana Milosevic, and Jean Galy. MgV2O5 solid state preparation (French). *Journal of Solid State Chemistry*, 398(16):393–398, 1976.

[24] J S Braithwaite, C. R. A. Catlow, J D Gale, and J H Harding. Lithium Intercalation into Vanadium Pentoxide: a Theoretical Study. *Chemistry of Materials*, 11(8):1990–1998, August 1999.

[25] I.D. Brown. What factors determine cation coordination numbers? *Acta Crystallogr. Sect. B*, 44(6):545–553, dec 1988.

[26] P. Bruce, F. Krok, P. Lighfoot, and J. L. Nowinski. Multivalent cation intercalation. *Solid State Ionics*, 53–56:351–355, Jul 1992.

[27] Peter G. Bruce, Stefan A. Freunberger, Laurence J. Hardwick, and Jean-Marie Tarascon. Li-o_2 and li-s batteries with high energy storage. *Nature Mater.*, 11(1):19–29, dec 2011.

[28] Peter G. Bruce, Franciszek Krok, Jan Nowinski, Vernon C. Gibson, and Kayumars Tavakkoli. Chemical intercalation of magnesium into solid hosts. *J. Mater. Chem.*, 1(4):705–706, 1991.

[29] Claudiu B. Bucur, Thomas Gregory, and John Muldoon. Why grignard's century old nobel prize should spark your curiosity. *Green Energy and Technology*, pages 611–635, 2015.

[30] Claudiu B. Bucur, Thomas Gregory, Allen G. Oliver, and John Muldoon. Confession of a magnesium battery. *J. Phys. Chem. Lett.*, 6(18):3578–3591, Sep 2015.

[31] Pieremanuele Canepa, Shou-Hang Bo, Gopalakrishnan Sai Gautam, Baris Key, William Davidson Richards, Yan Wang, Juchuan Li, and Gerbrand Ceder. High divalent cation mobility in solids. *under review*, 2017.

[32] Pieremanuele Canepa, Gopalakrishnan Sai Gautam, Daniel C. Hannah, Rahul Malik, Miao Liu, Kevin G. Gallagher, Kristin A. Persson, and Gerbrand Ceder. Odyssey of multivalent cathode materials: Open questions and future challenges. *Chem. Rev.*, 2017.

[33] Pieremanuele Canepa, Gopalakrishnan Sai Gautam, Rahul Malik, Saivenkataraman Jayaraman, Ziqin Rong, Kevin R. Zavadil, Kristin Persson, and Gerbrand Ceder. Understanding the initial stages of reversible mg deposition and stripping in inorganic nonaqueous electrolytes. *Chem. Mater.*, 27(9):3317–3325, may 2015.

[34] Pieremanuele Canepa, Saivenkataraman Jayaraman, Lei Cheng, Nav Rajput, William Davidson Richards, Gopalakrishnan Sai Gautam, Larry A Curtiss, Kristin Persson, and Gerbrand Ceder. Elucidating the structure of the magnesium aluminum chloride complex electrolyte for magnesium-ion batteries. *Energy Environ. Sci.*, 8:3718–3730, 2015.

[35] Javier Carrasco. Role of van der waals forces in thermodynamics and kinetics of layered transition metal oxide electrodes: Alkali and alkaline-earth ion insertion into v_2o_5. *J. Phys. Chem. C*, 118(34):19599–19607, Aug 2014.

[36] Tyler J. Carter, Rana Mohtadi, Timothy S. Arthur, Fuminori Mizuno, Ruigang Zhang, Soichi Shirai, and Jeff W. Kampf. Boron clusters as highly stable magnesium-battery electrolytes. *Angew. Chem. Int. Ed.*, 53(12):3173–3177, Feb 2014.

[37] R.J. Cava, A. Santoro, D.W. Murphy, S.M. Zahurak, R.M. Fleming, P. Marsh, and R.S. Roth. The structure of the lithium-inserted metal oxide δliv$_2$o$_5$. *J. Solid State Chem.*, 65(1):63–71, nov 1986.

[38] G. Ceder. A derivation of the Ising model for the computation of phase diagrams. *Computational Materials Science*, 1(2):144–150, March 1993.

[39] Gerbrand Ceder and Anton Van der Ven. Phase diagrams of lithium transition metal oxides: investigations from first principles. *Electrochimica Acta*, 45(1-2):131–150, September 1999.

[40] J.M. Cocciantelli, J.P. Doumerc, M Pouchard, M. Broussely, and J. Labat. Crystal chemistry of electrochemically inserted LixV2O5. *Journal of Power Sources*, 34:103–111, 1991.

[41] F Albert Cotton. Metal atom clusters in oxide systems. *Inorg. Chem.*, 3(9):1217–1220, 1964.

[42] George Crabtree. The joint center for energy storage research: A new paradigm for battery research and development. *AIP Conf. Proc.*, 1652:112–128, 2015.

[43] J. Dahn. Electrically rechargeable metal-air batteries compared to advanced lithium-ion batteries, *San Jose, CA (USA).* `http://www.almaden.ibm.com/institute/2009/resources/2009/presentations/JeffDahn-AlmadenInstitute2009.pdf`, 2009.

[44] J. R. Dahn, W. R. McKinnon, R. R. Haering, W. J. L. Buyers, and B. M. Powell. Structure determination of li_xtis_2 by neutron diffraction. *Can. J. Phys.*, 58(2):207–213, feb 1980.

[45] Debashish Das and Subhradip Ghosh. First-principles investigations into the thermodynamics of cation disorder and its impact on electronic structure and magnetic properties of spinel co $(cr_{1-x}mn_x)_2o_4$. *J. Phys.: Condens. Matter*, 29(5):055805, 2016.

[46] C. Delmas, H. Cognac-Auradou, J.M. Cocciantelli, M Ménétrier, and J.P. Doumerc. The li$_x$v$_2$o$_5$ system: An overview of the structure modifications induced by the lithium intercalation. *Solid State Ionics*, 69(3-4):257–264, Aug 1994.

[47] C. Delmas, C. Fouassier, and P. Hagenmuller. Structural classification and properties of the layered oxides. *Physica B+C*, 99(1-4):81–85, jan 1980.

[48] P G Dickens, S J French, A T Hight, M F Pye, and G J Reynolds. Thermochemistry of the high and ambient temperature lithium vanadium bronze phases LixV2O5. *Solid State Ionics*, 2(1):27–32, February 1981.

[49] Boucar Diouf and Ramchandra Pode. Potential of lithium–ion batteries in renewable energy. *Renew. Ener.*, 76:375–380, Apr 2015.

[50] R.Ẽ. Doe, R. Han, J. Hwang, A.J̃. Gmitter, I. Shterenberg, H.D̃. Yoo, N. Pour, and D. Aurbach. Novel, electrolyte solutions comprising fully inorganic salts with high anodic stability for rechargeable magnesium batteries. *Chem. Commun.*, 50(2):243–245, 2014.

[51] Robert Ellis Doe, Craig Michael Downie, Christopher Fischer, George Hamilton Lane, Dane Morgan, Josh Nevin, Gerbrand Ceder, Kristin Aslaug Persson, and David Eaglesham. Layered materials with improved magnesium intercalation for rechargeable magnesium ion cells, March 11 2013. US Patent App. 13/794,551.

[52] Alexandra Emly and Anton Van der Ven. Mg intercalation in layered and spinel host crystal structures for mg batteries. *Inorg. Chem.*, 54(9):4394–4402, May 2015.

[53] R. Enjalbert and J. Galy. A refinement of the structure of v$_2$o$_5$. *Acta Crystallogr., Sect. C: Cryst. Struct. Commun.*, 42(11):1467–1469, nov 1986.

[54] John W Essam. Percolation theory. *Rep. Prog. Phys.*, 43(7):833, 1980.

[55] Paul P Ewald. Die berechnung optischer und elektrostatischer gitterpotentiale. *Ann. Phys.*, 369(3):253–287, 1921.

[56] Wei-Chuan Fang and Wei-Lee Fang. Fast and reversible surface redox reduction in v$_2$o$_5$ dispersed on cn$_x$ nanotubes. *Chem. Commun.*, pages 5236–5238, 2008.

[57] Z. Feng, X. Chen, L. Qiao, A. L. Lipson, T. T. Fister, L. Zeng, C. Kim, T. Yi, N. Sa, D. L. Proffit, A. K. Burrell, J. Cabana, B. J. Ingram, M. D. Biegalski, M. J. Bedzyk, and P. Fenter. Phase-controlled electrochemical activity of epitaxial mg-spinel thin films. *ACS Appl. Mater. Interfaces*, 7(51):28438–28443, dec 2015.

[58] E Ferg, RJ Gummow, A De Kock, and MM Thackeray. Spinel anodes for lithium-ion batteries. *J. Electrochem. Soc.*, 141(11):L147–L150, 1994.

[59] Roger H. French, V. Adrian Parsegian, Rudolf Podgornik, Rick F. Rajter, Anand Jagota, Jian Luo, Dilip Asthagiri, Manoj K. Chaudhury, Yet-ming Chiang, Steve Granick, Sergei Kalinin, Mehran Kardar, Roland Kjellander, David C. Langreth, Jennifer Lewis, Steve Lustig, David Wesolowski, John S. Wettlaufer, Wai-Yim Ching, Mike Finnis, Frank Houlihan, O. Anatole von Lilienfeld, Carel Jan van Oss, and Thomas Zemb. Long range interactions in nanoscale science. *Reviews of Modern Physics*, 82(2):1887–1944, June 2010.

[60] Daan Frenkel and Berend Smit. Chapter 12 - Long-Range Interactions. In *Understanding Molecular Simulation*, pages xiii–xiv. Elsevier, San Diego, second edition, 2002.

[61] J. Galy and A. Hardy. Structure cristalline du bronze de vanadiumâĂŞlithium LiV2O5. *Acta Crystallographica*, 19(3):432–435, September 1965.

[62] Swapna Ganapathy, Brian D Adams, Georgiana Stenou, Maria S Anastasaki, Kees Goubitz, Xue-Fei Miao, Linda F Nazar, and Marnix Wagemaker. Nature of Li_2O_2 Oxidation in a LiâĂŞO_2 Battery Revealed by Operando X-ray Diffraction. *Journal of the American Chemical Society*, 136:16335–16344, 2014.

[63] G. S. Gautam, X. Sun, V. Duffort, L. F. Nazar, and G Ceder. Impact of intermediate sites on bulk diffusion barriers: Mg intercalation in $mg_2mo_3o_8$. *J. Mater. Chem. A*, 4(45):17643–17648, 2016.

[64] Gregory Gershinsky, Hyun Deog Yoo, Yosef Gofer, and Doron Aurbach. Electrochemical and spectroscopic analysis of mg^{2+} intercalation into thin film electrodes of layered oxides: V_2o_5 and moo_3. *Langmuir*, 29(34):10964–10972, Aug 2013.

[65] Guinevere A. Giffin. Ionic liquid-based electrolytes for "beyond lithium" battery technologies. *J. Mater. Chem. A*, 4(35):13378–13389, 2016.

[66] Y. Gofer, R. Turgeman, H. Cohen, and D. Aurbach. Xps investigation of surface chemistry of magnesium electrodes in contact with organic solutions of organochloroaluminate complex salts. *Langmuir*, 19(6):2344–2348, mar 2003.

[67] Tom Goldstein and Stanley Osher. The Split Bregman Method for L1-Regularized Problems. *SIAM Journal on Imaging Sciences*, 2(2):323–343, January 2009.

[68] Thomas D. Gregory, Ronald J. Hoffman, and Martin Winter. Nonaqueous electrochemistry of magnesium. *J. Electrochem. Soc.*, 137(3):775–780, 1990.

[69] C. P. Grey and J. M. Tarascon. Sustainability and *in situ* monitoring in battery development. *Nat. Mater.*, 16(1):45–56, dec 2016.

[70] Yong-Sheng Guo, Fan Zhang, Jun Yang, and Fei-Fei Wang. Electrochemical performance of novel electrolyte solutions based on organoboron magnesium salts. *Electrochem. Commun.*, 18:24–27, jan 2012.

[71] Yong-Sheng Guo, Fan Zhang, Jun Yang, Fei-Fei Wang, Yanna NuLi, and Hirano Shin-ichi. Boron-based electrolyte solutions with wide electrochemical windows for rechargeable magnesium batteries. *Energy Environ. Sci.*, 5(10):9100–9106, 2012.

[72] Jung Hoon Ha, Brian Adams, Jae-Hyun Cho, Victor Duffort, Jong Hak Kim, Kyung Yoon Chung, Byung Won Cho, Linda F. Nazar, and Si Hyoung Oh. A conditioning-free magnesium chloride complex electrolyte for rechargeable magnesium batteries. *J. Mater. Chem. A*, 4(19):7160–7164, 2016.

[73] Harry Hahn and Wilhelm Klingler. Über die kristallstruktur einiger ternärer sulfide, die sich vom indium (iii)-sulfid ableiten mit 8 abbildungen. *Z. Anorg. Allg. Chem.*, 263(4):177–190, 1950.

[74] Gus Hart and Rodney Forcade. Algorithm for generating derivative structures. *Phys. Rev. B*, 77(22):224115, June 2008.

[75] Gus Hart and Rodney Forcade. Generating derivative structures from multilattices: Algorithm and application to hcp alloys. *Phys. Rev. B*, 80(1):014120, July 2009.

[76] Gus L.W. Hart, Lance J Nelson, and Rodney W Forcade. Generating derivative structures at a fixed concentration. *Comput. Mater. Sci.*, 59:101–107, June 2012.

[77] W. M. Haynes, Thomas J. Bruno, and David R. Lide, editors. *CRC handbook of chemistry and physics*. CRC press Boca Raton, FL, 96 edition, 2016.

[78] Graeme Henkelman and Hannes Jónsson. Improved tangent estimate in the nudged elastic band method for finding minimum energy paths and saddle points. *J. Chem. Phys.*, 113(22):9978–9985, 2000.

[79] Yoyo Hinuma, Ying Meng, and Gerbrand Ceder. Temperature-concentration phase diagram of P2-Na_xCoO_2 from first-principles calculations. *Physical Review B*, 77(22):224111, June 2008.

[80] Matthew M. Huie, David C. Bock, Esther S. Takeuchi, Amy C. Marschilok, and Kenneth J. Takeuchi. Cathode materials for magnesium and magnesium-ion based batteries. *Coordin. Chem. Rev.*, 287:15–27, Mar 2015.

[81] Allen Hunt and Robert Ewing. *Percolation theory for flow in porous media (Lecture Notes in Physics 674)*. Soil Sci Soc America, 2006.

[82] D. Imamura and M. Miyayama. Characterization of magnesium-intercalated v_2o_5/carbon composites. *Solid State Ionics*, 161(1-2):173–180, Jul 2003.

[83] Daichi Imamura, Masaru Miyayama, Mitsuhiro Hibino, and Tetsuichi Kudo. Mg intercalation properties into v_2o_5 gel/carbon composites under high-rate condition. *J. Electrochem. Soc.*, 150(6):A753–A758, 2003.

[84] Jared T. Incorvati, Liwen F. Wan, Baris Key, Dehua Zhou, Chen Liao, Lindsay Fuoco, Michael Holland, Hao Wang, David Prendergast, Kenneth R. Poeppelmeier, and John T. Vaughey. Reversible magnesium intercalation into a layered oxyfluoride cathode. *Chem. Mater.*, 28(1):17–20, jan 2016.

[85] K.S Irani, A.P.B Sinha, and A.B Biswas. Effect of temperature on the structure of manganites. *J. Phys. Chem. Solids*, 23(6):711–727, jun 1962.

[86] Michael B Isichenko. Percolation, statistical topography, and transport in random media. *Rev Mod Phys*, 64(4):961, 1992.

[87] Anubhav Jain, Geoffroy Hautier, Shyue Ping Ong, Charles J Moore, Christopher C Fischer, Kristin A Persson, and Gerbrand Ceder. Formation enthalpies by mixing gga and gga+ u calculations. *Phys. Rev. B*, 84(4):045115, 2011.

[88] Anubhav Jain, Shyue Ping Ong, Geoffroy Hautier, Wei Chen, William Davidson Richards, Stephen Dacek, Shreyas Cholia, Dan Gunter, David Skinner, Gerbrand Ceder, and Kristin A. Persson. The Materials Project: A materials genome approach to accelerating materials innovation. *APL Materials*, 1(1):011002, 2013.

[89] T. Kaewmaraya, M. Ramzan, J.M. Osorio-GuillÃl'n, and R. Ahuja. Electronic structure and ionic diffusion of green battery cathode material: $Mg_2mo_6s_8$. *Solid State Ionics*, 261:17–20, Aug 2014.

[90] Kazuya Kai, Yoji Kobayashi, Yuki Yamada, Kohei Miyazaki, Takeshi Abe, Yoshiharu Uchimoto, and Hiroshi Kageyama. Electrochemical characterization of single-layer mno_2 nanosheets as a high-capacitance pseudocapacitor electrode. *J. Mater. Chem.*, 22(29):14691–14695, 2012.

[91] Kisuk Kang and Gerbrand Ceder. Factors that affect Li mobility in layered lithium transition metal oxides. *Physical Review B*, 74:094105, 2006.

[92] Shinyoung Kang, Yifei Mo, Shyue Ping Ong, and Gerbrand Ceder. A facile mechanism for recharging Li_2O_2 in Li-O_2 batteries. *Chemistry of Materials*, 25:3328–3336, 2013.

[93] Watchareeya Kaveevivitchai and Allan J Jacobson. High capacity rechargeable magnesium-ion batteries based on a microporous molybdenum-vanadium oxide cathode. *Chem. Mater.*, 28(13):4593–4601, jul 2016.

[94] Evan N. Keyzer, Hugh F. J. Glass, Zigeng Liu, Paul M Bayley, Siân E. Dutton, Clare P. Grey, and Dominic S. Wright. Mg $(pf_6)_2$-based electrolyte systems: Understanding electrolyte-electrode interactions for the development of mg-ion batteries. *J. Am. Chem. Soc.*, 138(28):8682–8685, jun 2016.

[95] K. R. Kganyago, P. E. Ngoepe, and C. R. A. Catlow. Voltage profile, structural prediction, and electronic calculations for $mg_xmo_6s_8$. *Phys. Rev. B*, 67(10):104103–1–10, Mar 2003.

[96] Chunjoong Kim, Patrick J. Phillips, Baris Key, Tanghong Yi, Dennis Nordlund, Young-Sang Yu, Ryan D. Bayliss, Sang-Don Han, Meinan He, Zhengcheng Zhang, A. K. Burrell, Rober F. Klie, and J. Cabana. Direct observation of reversible magnesium ion intercalation into a spinel oxide host. *Adv. Mater.*, 27(22):3377–3384, Apr 2015.

[97] H.S̃. Kim, T.S̃. Arthur, G.D̃. Allred, J. Zajicek, J.G̃. Newman, A.Ẽ. Rodnyansky, A.G̃. Oliver, W.C̃. Boggess, and J. Muldoon. Structure and compatibility of a magnesium electrolyte with a sulphur cathode. *Nat. Comm.*, 2:427, aug 2011.

[98] Haegyeom Kim, Jihyun Hong, Gabin Yoon, Hyunchul Kim, Kyu-Young Park, Min-Sik Park, Won-Sub Yoon, and Kisuk Kang. Sodium intercalation chemistry in graphite. *Energy Environ. Sci.*, 8(10):2963–2969, 2015.

[99] Sangryun Kim, Kwan Woo Nam, Soyeon Lee, Woosuk Cho, Joo-Seong Kim, Byung Gon Kim, Yoshifumi Oshima, Ju-Sik Kim, Seok-Gwang Doo, Hyuk Chang, Doron Aurbach, and Jang W. Choi. Direct observation of an anomalous spinel-to-layered phase transition mediated by crystal water intercalation. *Angew. Chem. Int. Ed.*, 54(50):15094–15099, Oct 2015.

[100] Daniil A. Kitchaev, Haowei Peng, Yun Liu, Jianwei Sun, John P. Perdew, and Gerbrand Ceder. Energetics of mno_2 polymorphs in density functional theory. *Phys. Rev. B*, 93(4):045132, jan 2016.

[101] JiÅŹí Klime, David R. Bowler, and Angelos Michaelides. Van der Waals density functionals applied to solids. *Physical Review B - Condensed Matter and Materials Physics*, 83:195131, 2011.

[102] Walter Kohn and Lu Jeu Sham. Self-consistent equations including exchange and correlation effects. *Phys Rev*, 140(4A):A1133, 1965.

[103] M. A. Korotin, V. I. Anisimov, T. Saha-Dasgupta, and I. Dasgupta. Electronic structure and exchange interactions of the ladder vanadates CaV2O5 and MgV2O5 Electronic structure and exchange interactions of the ladder. *J. Phys.: Condens. Matter*, 113:113–124, 2000.

[104] Georg Kresse and Jürgen Furthmüller. Efficient iterative schemes for ab initio total-energy calculations using a plane-wave basis set. *Phys Rev B*, 54(16):11169, 1996.

[105] Georg Kresse and Jürgen Hafner. Ab initio molecular dynamics for liquid metals. *Phys. Rev. B*, 47(1):558, 1993.

[106] Georg Kresse and D Joubert. From ultrasoft pseudopotentials to the projector augmented-wave method. *Phys. Rev. B*, 59(3):1758, 1999.

[107] O Kubaschewski, Elwyn Llewellyn Evans, and C B Alcock. *Metallurgical thermochemistry*. Pergamon Press, Oxford; New York, 1967.

[108] Saul H. Lapidus, Nav Nidhi Rajput, Xiaohui Qu, Karena W. Chapman, Kristin A. Persson, and Peter J. Chupas. Solvation structure and energetics of electrolytes for multivalent energy storage. *Phys. Chem. Chem. Phys.*, 16(40):21941–21945, sep 2014.

[109] Dominique Larcher, Shane Beattie, Mathieu Morcrette, Kristina EdstrÃűm, Jean-Claude Jumas, and Jean-Marie Tarascon. Recent findings and prospects in the field of pure metals as negative electrodes for li-ion batteries. *J. Mater. Chem.*, 17(36):3759–3772, 2007.

[110] A J Leadbetter, R C Ward, J W Clark, P A Tucker, T Matsuo, and H Suga. The equilibrium low-temperature structure of ice. *J. Chem. Phys.*, 82:424 – 428, 1985.

[111] Jinhyuk Lee, Alexander Urban, Xin Li, Dong Su, Geoffroy Hautier, and Gerbrand Ceder. Unlocking the potential of cation-disordered oxides for rechargeable lithium batteries. *Science*, 343(6170):519–522, 2014.

[112] Kyuho Lee, Éamonn D. Murray, Lingzhu Kong, Bengt I. Lundqvist, and David C. Langreth. A Higher-Accuracy van der Waals Density Functional. *Phys. Rev. B*, 82:081101(R), 2010.

[113] S. H. Lee, R. A. DiLeo, A. C. Marschilok, K. J. Takeuchi, and E. S. Takeuchi. Sol gel based synthesis and electrochemistry of magnesium vanadium oxide: A promising cathode material for secondary magnesium ion batteries. *ECS Electrochem. Lett.*, 3(8):A87–A90, Jan 2014.

[114] Jean-Jacques Legendre and Jacques Livage. Vanadium pentoxide gels: I. structural study by electron diffraction. *J. Colloid Interf. Sci.*, 94(1):75–83, Jul 1983.

[115] E. Levi, G. Gershinsky, D. Aurbach, and O. Isnard. Crystallography of chevrel phases, mmo_6t_8 (m = cd, na, mn, and zn, t = s, se) and their cation mobility. *Inorg. Chem.*, 48(18):8751–8758, Sep 2009.

[116] E. Levi, Y Gofer, and D. Aurbach. On the way to rechargeable mg batteries: The challenge of new cathode materials. *Chem. Mater.*, 22(3):860–868, Feb 2010.

[117] E. Levi, E. Lancry, A. Mitelman, D. Aurbach, G. Ceder, D. Morgan, and O. Isnard. Phase diagram of mg insertion into chevrel phases, $mg_xmo_6t_8$ (t = s, se). 1. crystal structure of the sulfides. *Chem. Mater.*, 18(23):5492–5503, Nov 2006.

[118] E. Levi, M. D. Levi, O. Chasid, and D. Aurbach. A review on the problems of the solid state ions diffusion in cathodes for rechargeable mg batteries. *J. Electroceram.*, 22(1–3):13–19, Dec 2007.

[119] E. Levi, A. Mitelman, D. Aurbach, and M. Brunelli. Structural mechanism of the phase transitions in the mg-cu-mo_6s_8 system probed by ex situ synchrotron x-ray diffraction. *Chem. Mater.*, 19(21):5131–5142, Oct 2007.

[120] W. Li, W. R. McKinnon, and J R Dahn. Lithium intercalation from aqueous solutions. *J. Electrochem. Soc.*, 141(9):2310–2316, jan 1994.

[121] P. Lighfoot, F. Krok, J. Nowinski, and P. G Bruce. Structure of the cubic intercalate mg_xtis_2. *J. Mater. Chem.*, 2(1):139–140, 1992.

[122] Chen Ling, Ruigang Zhang, Timothy S. Arthur, and Fuminori Mizuno. How general is the conversion reaction in mg battery cathode: A case study of the magnesiation of α-mno_2. *Chem. Mater.*, 27(16):5799–5807, Aug 2015.

[123] Albert L. Lipson, Sang-Don Han, Baofei Pan, Kimberly A. See, Andrew A. Gewirth, Chen Liao, John T. Vaughey, and Brian J. Ingram. Practical stability limits of magnesium electrolytes. *J. Electrochem. Soc.*, 163(10):A2253–A2257, 2016.

[124] Albert L. Lipson, Baofei Pan, Saul H. Lapidus, Chen Liao, John T. Vaughey, and Brian J. Ingram. Rechargeable ca-ion batteries: A new energy storage system. *Chem. Mater.*, 27(24):8442–8447, Dec 2015.

[125] Miao Liu, Anubhav Jain, Ziqin Rong, Xiaohui Qu, Pieremanuele Canepa, Rahul Malik, Gerbrand Ceder, and Kristin Persson. Evaluation of sulfur spinel compounds for multivalent battery cathode applications. *Energy Environ. Sci.*, 9(10):3201–3209, 2016.

[126] Miao Liu, Ziqin Rong, Rahul Malik, Pieremanuele Canepa, Anubhav Jain, Gerbrand Ceder, and Kristin A. Persson. Spinel compounds as multivalent battery cathodes: a systematic evaluation based on ab initio calculations. *Energy Environ. Sci.*, 8(3):964–974, 2015.

[127] Tianbiao Liu, Yuyan Shao, Guosheng Li, Meng Gu, Jianzhi Hu, Suochang Xu, Zimin Nie, Xilin Chen, Chongmin Wang, and Jun Liu. A facile approach using $mgcl_2$ to formulate high performance mg^{2+} electrolytes for rechargeable mg batteries. *J. Mater. Chem. A*, 2(10):3430–3438, 2014.

[128] Christian D Lorenz and Robert M Ziff. Precise determination of the bond percolation thresholds and finite-size scaling corrections for the sc, fcc, and bcc lattices. *Phys Rev E*, 57(1):230, 1998.

[129] Jun Ma, Yong-Ning Zhou, Yurui Gao, Xiqian Yu, Qingyu Kong, Lin Gu, Zhaoxiang Wang, Xiao-Qing Yang, and Liquan Chen. Feasibility of using li_2moo_3 in constructing li-rich high energy density cathode materials. *Chem. Mater.*, 26(10):3256–3262, 2014.

[130] Lorenzo Malavasi, Paolo Ghigna, Gaetano Chiodelli, Giorgio Maggi, and Giorgio Flor. Structural and transport properties of $mg_{1-x}mn_xmn_2o_{4\pm\delta}$ spinels. *J. Solid State Chem.*, 166(1):171–176, Jun 2002.

[131] Rahul Malik, Fei Zhou, and G. Ceder. Kinetics of non-equilibrium lithium incorporation in $lifepo_4$. *Nat. Mater.*, 10(8):587–590, Jul 2011.

[132] R Mănăilă and P Păuşescu. Structural changes in $mgmn_2o_4$ at high temperatures. *Phys. Stat. Sol.*, 9(2):385–394, 1965.

[133] Arumugam Manthiram, Yongzhu Fu, Sheng-Heng Chung, Chenxi Zu, and Yu-Sheng Su. Rechargeable lithium-sulfur batteries. *Chem. Rev.*, 114(23):11751–11787, dec 2014.

[134] William H McCarroll, Lewis Katz, and Roland Ward. Some ternary oxides of tetravalent molybdenum[1,2]. *J. Am. Chem. Soc.*, 79(20):5410–5414, 1957.

[135] Ying Shirley Meng and M. Elena Arroyo-De Dompablo. Recent advances in first principles computational research of cathode materials for lithium-ion batteries. *Accounts of Chemical Research*, 46(5):1171–1180, 2013.

[136] P Millet, C Satto, J. Bonvoisin, B Normand, K Penc, M. Albrecht, and F. Mila. Magnetic properties of the coupled ladder system MgV2O5. *Physical Review B*, 57(9):5005–5008, March 1998.

[137] Patrice Millet, Christine Satto, Philippe Sciau, and Jean Galy. Mgv_2o_5 and $\delta li_xv_2o_5$: A comparative structural investigation. *J. Solid State Chem.*, 136(1):56–62, 1998.

[138] Oren Mizrahi, Nir Amir, Elad Pollak, Orit Chusid, Vered Marks, Hugo Gottlieb, Liraz Larush, Ella Zinigrad, and Doron Aurbach. Electrolyte solutions with a wide electrochemical window for rechargeable magnesium batteries. *Journal of the Electrochemical Society*, 155(2):A103–A109, 2008.

[139] K. Mizushima, P.C. Jones, P.J. Wiseman, and J.B. Goodenough. Li_xcoo_2 ($0<x\leq1$): A new cathode material for batteries of high energy density. *Solid State Ionics*, 3:171–174, aug 1981.

[140] Rana Mohtadi, Masaki Matsui, Timothy S. Arthur, and Son-Jong Hwang. Magnesium borohydride: From hydrogen storage to magnesium battery. *Angew. Chem. Int. Ed.*, 51(39):9780–9783, Aug 2012.

[141] J. Muldoon, C.B̃. Bucur, and T.D̃. Gregory. Quest for nonaqueous multivalent secondary batteries: Magnesium and beyond. *Chem. Rev.*, 114(23):11683–11720, dec 2014.

[142] John Muldoon, Claudiu B. Bucur, Allen G. Oliver, Tsuyoshi Sugimoto, Masaki Matsui, Hee Soo Kim, Gary D. Allred, Jaroslav Zajicek, and Yukinari Kotani. Electrolyte roadblocks to a magnesium rechargeable battery. *Energy Environ. Sci.*, 5(3):5941–5950, 2012.

[143] John Muldoon, Claudiu B. Bucur, Allen G. Oliver, Jaroslav Zajicek, Gary D. Allred, and William C. Boggess. Corrosion of magnesium electrolytes: chlorides – the culprit. *Energy Environ. Sci.*, 6(2):482–487, 2013.

[144] D. W. Murphy, P A Christian, F. J. DiSalvo, and J. V. Waszczak. Lithium incorporation by vanadium pentoxide. *Inorganic Chemistry*, 18(10):2800–2803, October 1979.

[145] Michael Naguib, Joseph Halim, Jun Lu, Kevin M. Cook, Lars Hultman, Yury Gogotsi, and Michel W. Barsoum. New two-dimensional niobium and vanadium carbides as promising materials for li-ion batteries. *J. Am. Chem. Soc.*, 135(43):15966–15969, oct 2013.

[146] Kwan Woo Nam, Sangryun Kim, Soyeon Lee, Michael Salama, Ivgeni Shterenberg, Yossi Gofer, Joo-Seong Kim, Eunjeong Yang, Chan Sun Park, Ju-Sik Kim, Seok-See Lee, Won-Seok Chang, Seok-Gwang Doo, Yong N. Jo, Yousung Jung, Doron Aurbach, and Jang W. Choi. The high performance of crystal water containing manganese birnessite cathodes for magnesium batteries. *Nano Lett.*, 15(6):4071–4079, Jun 2015.

[147] Kwan Woo Nam, Sangryun Kim, Eunjeong Yang, Yousung Jung, Elena Levi, Doron Aurbach, and Jang Wook Choi. Critical role of crystal water for a layered cathode material in sodium ion batteries. *Chem. Mater.*, 27(10):3721–3725, may 2015.

[148] Linda F. Nazar, Marine Cuisinier, and Quan Pang. Lithium-sulfur batteries. *MRS Bull.*, 39(05):436–442, may 2014.

[149] Lance Nelson, Gus Hart, Fei Zhou, and Vidvuds OzoliÅĘš. Compressive sensing as a paradigm for building physics models. *Physical Review B*, 87(3):035125, January 2013.

[150] Jeremy Neubauer, Ahmad Pesaran, Chulheung Bae, Ron Elder, and Brian Cunningham. Updating United States advanced battery consortium and department of energy battery technology targets for battery electric vehicles. *J. Power Sources*, 271:614–621, Dec 2014.

[151] MEJ Newman and RM Ziff. Efficient monte carlo algorithm and high-precision results for percolation. *Phys. Rev. Lett.*, 85(19):4104, 2000.

[152] Richard Van Noorden. The rechargeable revolution: A better battery. *Nature*, 507(7490):26–28, mar 2014.

[153] Petr Novák and Johann Desilvestro. Electrochemical insertion of magnesium in metal oxides and sulfides from aprotic electrolytes. *J. Electrochem. Soc.*, 140(1):140–144, 1993.

[154] Petr Novák, Roman Imhof, and Otto Haas. Magnesium insertion electrodes for rechargeable nonaqueous batteries – a competitive alternative to lithium? *Electrochim. Acta*, 45(1-2):351–367, Sep 1999.

[155] Petr Novák, Valery Shklover, and Reinhard Nesper. Magnesium insertion in vanadium oxides: A structural study. *Z. Phys. Chem.*, 185(Part_1):51–68, jan 1994.

[156] Björn Nykvist and Måns Nilsson. Rapidly falling costs of battery packs for electric vehicles. *Nat. Clim. Change.*, 5(4):329–332, Mar 2015.

[157] Yoshio Oka, Takeshi Yao, and Naoichi Yamamoto. Crystal structures of hydrated vanadium oxides with δ-type v_2o_5 layers: δ-$m_{0.25}v_2o_5{\cdot}h_2o$, m=ca, ni. *J. Solid State Chem.*, 132(2):323–329, Sep 1997.

[158] Yoshio Oka, Takeshi Yao, and Naoichi Yamamoto. Crystal structures and lattice distortions of σ-type layered vanadium bronzes : σ-$m_{0.25}v_2o_5.h_2o$ (m=mg ,co ,ni). *J. Solid State Chem.*, 144(1):181–187, 1999.

[159] Atsuyuki Okabe, Barry Boots, Kokichi Sugihara, Sung Nok Chiu, and D. G. Kendall. *Spatial Tessellations*. Wiley Series in Probability and Statistics. John Wiley & Sons, Inc., Hoboken, NJ, USA, jul 2000.

[160] Shyue Ping Ong, William Davidson Richards, Anubhav Jain, Geoffroy Hautier, Michael Kocher, Shreyas Cholia, Dan Gunter, Vincent L. Chevrier, Kristin a. Persson, and Gerbrand Ceder. Python Materials Genomics (pymatgen): A robust, open-source python library for materials analysis. *Comput. Mater. Sci.*, 68:314–319, February 2013.

[161] Shyue Ping Ong, Lei Wang, Byoungwoo Kang, and Gerbrand Ceder. $Li-fe-p-o_2$ phase diagram from first principles calculations. *Chem. Mater.*, 20(5):1798–1807, 2008.

[162] Min-Sik Park, Jae-Geun Kim, Young-Jun Kim, Nam-Soon Choi, and Jeom-Soo Kim. Recent advances in rechargeable magnesium battery technology: A review of the field's current status and prospects. *Isr. J. Chem.*, 55(5):570–585, Mar 2015.

[163] Linus Pauling. *The nature of the chemical bond and the structure of molecules and crystals: an introduction to modern structural chemistry*, volume 18. Cornell university press, 1960.

[164] E. Peled, A. Gorenshtein, M. Segal, and Y. Sternberg. Rechargeable lithium-sulfur battery (extended abstract). *J. Power Sources*, 26(3-4):269–271, may 1989.

[165] John P Perdew, Kieron Burke, and Matthias Ernzerhof. Generalized gradient approximation made simple. *Phys Rev Lett*, 77(18):3865, 1996.

[166] John P Perdew, Adrienn Ruzsinszky, Gábor I Csonka, Oleg A Vydrov, Gustavo E Scuseria, Lucian A Constantin, Xiaolan Zhou, and Kieron Burke. Restoring the density-gradient expansion for exchange in solids and surfaces. *Phys. Rev. Lett.*, 100(13):136406, 2008.

[167] J.P. Pereira-Ramos, R. Messina, and J. Perichon. Electrochemical formation of a magnesium vanadium bronze $mg_xv_2o_5$ in sulfone-based electrolytes at 150 °c. *J Electroanal. Chem. Interfacial. Electrochem.*, 218(1-2):241–249, Feb 1987.

[168] Valeri Petkov, Pantelis N. Trikalitis, Emil S. Bozin, Simon J. L. Billinge, Thomas Vogt, and Mercouri G. Kanatzidis. Structure of $v_2o_5{\cdot}nh_2o$ xerogel solved by the atomic pair distribution function technique. *J. Am. Chem. Soc.*, 124(34):10157–10162, Aug 2002.

[169] A. Ponrouch, C. Frontera, F. Bardé, and M. R. Palacín. Towards a calcium-based rechargeable battery. *Nat. Mater.*, 15(2):169âĂŞ–172, Oct 2015.

[170] N. Pour, Y. Gofer, D.T̃. Major, and D. Aurbach. Structural analysis of electrolyte solutions for rechargeable mg batteries by stereoscopic means and dft calculations. *J. Am. Chem. Soc.*, 133(16):6270–6278, apr 2011.

[171] NK Radhakrishnan and AB Biswas. A neutron diffraction study of the cation migration in $mgmn_2o_4$. *Phys. Stat. Sol. (a)*, 37(2):719–722, 1976.

[172] Nav Nidhi Rajput, Xiaohui Qu, Niya Sa, Anthony K. Burrell, and Kristin A. Persson. The coupling between stability and ion pair formation in magnesium electrolytes from first-principles quantum mechanics and classical molecular dynamics. *J. Am. Chem. Soc.*, 137(9):3411–3420, mar 2015.

[173] D. H. S. Ramkumar, A. P. Kudchadker, and D. D. Deshpande. Enthalpies of mixing of tetrahydrofuran + γ-butyrolactone and water + γ-butyrolactone systems at 299.15 k. *J. Chem. Eng. Data*, 30(4):491–492, oct 1985.

[174] C.N.R. Rao and Kanishka Biswas. *Essentials of Inorganic Materials Synthesis*. John Wiley & Sons, Inc., Hoboken, New Jersey, first edition, Feb 2015.

[175] Shahid Rasul, Shinya Suzuki, Shu Yamaguchi, and Masaru Miyayama. High capacity positive electrodes for secondary mg-ion batteries. *Electrochim. Acta*, 82:243–249, Nov 2012.

[176] J. Reed, G. Ceder, and A. Van Der Ven. Layered-to-spinel phase transition in li_xmno_2. *Electrochem. Solid-State Lett.*, 4(6):A78–A81, 2001.

[177] John Reed and Gerbrand Ceder. Role of electronic structure in the susceptibility of metastable transition-metal oxide structures to transformation. *Chem Rev*, 104(10):4513–4534, 2004.

[178] William D Richards, Lincoln J Miara, Yan Wang, Jae Chul Kim, and Gerbrand Ceder. Interface stability in solid-state batteries. *Chem. Mater.*, 28(1):266–273, 2016.

[179] H. M. Rietveld. A profile refinement method for nuclear and magnetic structures. *J Appl Crystallogr*, 2(2):65–71, 1969.

[180] C Roche, R Chevrel, A Jenny, P Pecheur, H Scherrer, and S Scherrer. Crystallography and density of states calculation of $m_x$mo$_6$se$_8$ (m = ti, cr, fe, ni). *Phys. Rev. B*, 60(24):16442–16447, dec 1999.

[181] Xavier Rocquefelte, Florent Boucher, Pascal Gressier, and Guy Ouvrard. First-Principle Study of the Intercalation Process in the $Li_xV_2O_5$ System. *Chemistry of Materials*, 15(9):1812–1819, May 2003.

[182] Juan Rodríguez-Carvajal. Recent advances in magnetic structure determination by neutron powder diffraction. *Physica B: Condensed Matter*, 192(1-2):55–69, 1993.

[183] Ziqin Rong, Rahul Malik, Pieremanuele Canepa, Gopalakrishnan Sai Gautam, Miao Liu, Anubhav Jain, Kristin Persson, and Gerbrand Ceder. Materials design rules for multivalent ion mobility in intercalation structures. *Chem. Mater.*, 27(17):6016–6021, Sep 2015.

[184] M Rosenberg and P Nicolau. Electrical properties and cation migration in mgmn$_2$o$_4$. *Phys. Stat. Sol.*, 6(1):101–110, 1964.

[185] M.H Rossouw, D.C Liles, MM Thackeray, W.I.F David, and S Hull. Alpha manganese dioxide for lithium batteries: A structural and electrochemical study. *Mater. Res. Bull.*, 27(2):221–230, feb 1992.

[186] H. Rydberg, M. Dion, N. Jacobson, E. Schröder, P. Hyldgaard, S. Simak, D. Langreth, and B. Lundqvist. Van der Waals Density Functional for Layered Structures. *Physical Review Letters*, 91(12):126402, September 2003.

[187] Niya Sa, Tiffany L. Kinnibrugh, Hao Wang, Gopalakrishnan Sai Gautam, Karena W. Chapman, John T. Vaughey, Baris Key, Timothy T. Fister, John W. Freeland, Danielle L. Proffit, Peter J. Chupas, Gerbrand Ceder, Javier G. Bareno, Ira D. Bloom, and Anthony K. Burrell. Structural evolution of reversible mg insertion into a bilayer structure of v$_2$o$_5$·nh$_2$o xerogel material. *Chem. Mater.*, 28(9):2962–2969, may 2016.

[188] Niya Sa, Baofei Pan, Anumita Saha-Shah, Aude A. Hubaud, John T. Vaughey, Lane A. Baker, Chen Liao, and Anthony K. Burrell. Role of chloride for a simple, non-grignard mg electrolyte in ether-based solvents. *ACS Appl. Mater. Interfaces*, 8(25):16002–16008, jun 2016.

[189] Partha Saha, Moni Kanchan Datta, Oleg I. Velikokhatnyi, Ayyakkannu Manivannan, David Alman, and Prashant N. Kumta. Rechargeable magnesium battery: Current status and key challenges for the future. *Prog. Mater. Sci.*, 66:1–86, Oct 2014.

[190] Gopalakrishnan Sai Gautam, Pieremanuele Canepa, Aziz Abdellahi, Alexander Urban, Rahul Malik, and Gerbrand Ceder. The intercalation phase diagram of mg in v_2o_5 from first-principles. *Chem. Mater.*, 27(10):3733–3742, May 2015.

[191] Gopalakrishnan Sai Gautam, Pieremanuele Canepa, Rahul Malik, Miao Liu, Kristin Persson, and Gerbrand Ceder. First-principles evaluation of multi-valent cation insertion into orthorhombic v_2o_5. *Chem. Commun.*, 51(71):13619–13622, 2015.

[192] Gopalakrishnan Sai Gautam, Pieremanuele Canepa, William Davidson Richards, Rahul Malik, and Gerbrand Ceder. Role of structural h_2o in intercalation electrodes: the case of mg in nanocrystalline xerogel-v_2o_5. *Nano Lett.*, 16(4):2426–2431, apr 2016.

[193] Michael Salama, Ivgeni Shterenberg, Haim Gizbar, Neta Nitoker Eliaz, Monica Kosa, Keren Keinan-Adamsky, Michal Afri, Linda J.W. Shimon, Hugo E. Gottlieb, Dan Thomas Major, Yosef Gofer, and Doron Aurbach. Unique behavior of dimethoxyethane (dme)/$mg(n(so_2cf_3)_2)_2$ solutions. *J. Phys. Chem. C*, 120(35):19586–19594, aug 2016.

[194] JM Sanchez, F Ducastelle, and D Gratias. Generalized cluster description of multicomponent systems. *Physica A: Statistical Mechanics and its Applications*, 128(1-2):334–350, November 1984.

[195] David Santos-Carballal, Alberto Roldan, Ricardo Grau-Crespo, and Nora H de Leeuw. First-principles study of the inversion thermodynamics and electronic structure of fem_2x_4 (thio) spinels (m= cr, mn, co, ni; x= o, s). *Phys. Rev. B*, 91(19):195106, 2015.

[196] David O Scanlon, Aron Walsh, Benjamin J Morgan, and Graeme W Watson. An ab initio Study of Reduction of V_2O_5 through the Formation of Oxygen Vacancies and Li Intercalation. *The Journal of Physical Chemistry C*, 112(26):9903–9911, July 2008.

[197] Linda Schwarz, Zbigniew Galazka, Thorsten M Gesing, and Detlef Klimm. On the influence of inversion on thermal properties of magnesium gallium spinel. *Cryst. Res. Technol.*, 50(12):961–966, 2015.

[198] Kimberly A. See, Karena W. Chapman, Lingyang Zhu, Kamila M. Wiaderek, Olaf J. Borkiewicz, Christopher J. Barile, Peter J. Chupas, and Andrew A. Gewirth. The interplay of al and mg speciation in advanced mg battery electrolyte solutions. *J. Am. Chem. Soc.*, 138(1):328–337, jan 2016.

[199] Yohanna Seminovski, Pablo Palacios, Perla Wahnón, and Ricardo Grau-Crespo. Band gap control via tuning of inversion degree in $cdin_2s_4$ spinel. *Appl. Phys. Lett.*, 100(10):102112, 2012.

[200] D. R. Sempolinski and W. D. Kingery. Ionic conductivity and magnesium vacancy mobility in magnesium oxide. *J. Am. Ceram. Soc.*, 63(11–12):664–669, November 1980.

[201] R D Shannon and C T Prewitt. Effective ionic radii in oxides and fluorides. *Acta Crystallographica Section B*, 25(5):925–946, May 1969.

[202] Daniel Sheppard, Rye Terrell, and Graeme Henkelman. Optimization methods for finding minimum energy paths. *J. Chem. Phys.*, 128(13):134106, 2008.

[203] V Shklover, T Haibach, F. Ried, R. Nesper, and P. Novák. Crystal Structure of the Product of Mg2+Insertion into V2O5Single Crystals. *Journal of Solid State Chemistry*, 123(2):317–323, May 1996.

[204] I. Shterenberg, M. Salama, Y. Gofer, E. Levi, and D. Aurbach. The challenge of developing rechargeable magnesium batteries. *Mater. Res. Bull.*, 39(05):453–460, may 2014.

[205] Kurt E Sickafus, John M Wills, and Norman W Grimes. Structure of spinel. *J. Am. Ceram. Soc.*, 82(12):3279–3292, 1999.

[206] William H. Smyrl, Stefano Passerini, Marco Giorgetti, Fabrice Coustier, Matthew M. Fay, and Boone B. Owens. Electrochemical and synchrotron xas studies of lithium intercalation into vanadium pentoxide aerogels and nanocomposites. *J. Power Sources*, 97-98:469–472, jul 2001.

[207] Jaehee Song, Emily Sahadeo, Malachi Noked, and Sang Bok Lee. Mapping the challenges of magnesium battery. *J. Phys. Chem. Lett.*, 7(9):1736–1749, apr 2016.

[208] M.E. Spahr, P. Novák, O. Haas, and R. Nesper. Electrochemical insertion of lithium, sodium, and magnesium in molybdenum(vi) oxide. *J. Power Sources*, 54(2):346–351, Apr 1995.

[209] L. W. Staples. Ilsemannite and jordisite. *Am. Mineral.*, 36:609–614, 1951.

[210] Dietrich Stauffer and Ammon Aharony. *Introduction to percolation theory*. CRC press, 1994.

[211] I. Stojković, N. Cvjetićanin, S. Marković, M. Mitrić, and S. Mentus. Electrochemical behaviour of v_2o_5 xerogel and v_2o_5 xerogel/c composite in an aqueous $lino_3$ and $mg(no_3)_2$ solutions. *Acta Phys. Pol. A*, 117(5):837–840, may 2010.

[212] Xiaoqi Sun, Patrick Bonnick, and Linda F. Nazar. Layered tis_2positive electrode for mg batteries. *ACS Energy Lett.*, 1(1):297–301, jul 2016.

[213] Xiaoqi Sun, Victor Duffort, Patrick Bonnick, Ziqin Rong, Miao Liu, Kristin Persson, Gerbrand Ceder, and Linda F. Nazar. A high capacity thiospinel cathode for mg batteries. *Energy Environ. Sci.*, 9(7):2273–2277, 2016.

[214] Xiaoqi Sun, Victor Duffort, B. Layla Mehdi, Nigel D. Browning, and Linda F. Nazar. Investigation of the mechanism of mg insertion in birnessite in nonaqueous and aqueous rechargeable mg-ion batteries. *Chem. Mater.*, 28(2):534–542, Jan 2016.

[215] Shaokun Tang and Hua Zhao. Glymes as versatile solvents for chemical reactions and processes: from the laboratory to industry. *RSC Adv.*, 4:11251 – 11287, 2014.

[216] Zhan-Liang Tao, Li-Na Xu, Xing-Long Gou, Jun Chen, and Hua-Tang Yuan. Tis_2 nanotubes as the cathode materials of mg-ion batteries. *Chem. Commun.*, pages 2080–2081, 2004.

[217] Sanja Tepavcevic, Yuzi Liu, Dehua Zhou, Barry Lai, Jorg Maser, Xiaobing Zuo, Henry Chan, Petr Král, Christopher S. Johnson, Vojislav Stamenkovic, and et al. Nanostructured layered cathode for rechargeable mg-ion batteries. *ACS Nano*, 9(8):8194–8205, Aug 2015.

[218] Sanja Tepavcevic, Hui Xiong, Vojislav R. Stamenkovic, Xiaobing Zuo, Mahalingam Balasubramanian, Vitali B. Prakapenka, Christopher S. Johnson, and Tijana Rajh. Nanostructured bilayered vanadium oxide electrodes for rechargeable sodium-ion batteries. *ACS Nano*, 6(1):530–538, Jan 2012.

[219] M.M̃. Thackeray, C. Wolverton, and E.D̃. Isaacs. Electrical energy storage for transportation-approaching the limits of, and going beyond, lithium-ion batteries. *Energy Environ. Sci.*, 5(7):7854–7863, 2012.

[220] M.M. Thackeray, P.J. Johnson, L.A. de Picciotto, P.G. Bruce, and J.B. Goodenough. Electrochemical extraction of lithium from $limn_2o_4$. *Mater. Res. Bull.*, 19(2):179–187, Feb 1984.

[221] Teodora Todorova, Ari P Seitsonen, Jürg Hutter, I-Feng W Kuo, and Christopher J Mundy. Molecular dynamics simulation of liquid water: Hybrid density functionals. *J. Phys. Chem. B*, 110(8):3685–3691, mar 2006.

[222] Rajesh Tripathi, T. N. Ramesh, Brian L. Ellis, and Linda F. Nazar. Scalable synthesis of tavorite $lifeso_4f$ and $nafeso_4f$ cathode materials. *Angew. Chem.*, 122(46):8920–8924, oct 2010.

[223] Oscar Tutusaus, Rana Mohtadi, Nikhilendra Singh, Timothy S. Arthur, and Fuminori Mizuno. Study of electrochemical phenomena observed at the mg metal/electrolyte interface. *ACS Energy Lett.*, pages 224–229, dec 2016.

[224] Alexander Urban, Jinhyuk Lee, and Gerbrand Ceder. The configurational space of rocksalt-type oxides for high-capacity lithium battery electrodes. *Adv. Energy Mater.*, 4:1400478, 2014.

[225] Steven C Van der Marck. Calculation of percolation thresholds in high dimensions for fcc, bcc and diamond lattices. *Int J Mod Phys C*, 9(04):529–540, 1998.

[226] A Van der Ven, C Marianetti, D Morgan, and G Ceder. Phase transformations and volume changes in spinel $li_xmn_2o_4$. *Solid State Ionics*, 135(1):21–32, 2000.

[227] A. Van der Ven, J.C. Thomas, Qingchuan Xu, and J. Bhattacharya. Linking the electronic structure of solids to their thermodynamic and kinetic properties. *Mathematics and Computers in Simulation*, 80(7):1393–1410, March 2010.

[228] Anton Van Der Ven, Jishnu Bhattacharya, and Anna A. Belak. Understanding Li diffusion in Li-intercalation compounds. *Accounts of Chemical Research*, 46(5):1216–1225, 2013.

[229] PLG Vlek and WL Lindsay. Thermodynamic stability and solubility of molybdenum minerals in soils. *Soil Sci. Soc. Am. J.*, 41(1):42–46, 1977.

[230] M. Vujković, I. Pašti, I.Stojković Simatović, B. Šljukić, M. Milenković, and S. Mentus. The influence of intercalated ions on cyclic stability of v_2o_5/graphite composite in aqueous electrolytic solutions: experimental and theoretical approach. *Electrochim. Acta*, 176:130–140, Sep 2015.

[231] M Wagemaker, A Van Der Ven, D Morgan, G Ceder, FM Mulder, and GJ Kearley. Thermodynamics of spinel li_xtio_2 from first principles. *Chemical Physics*, 317(2):130–136, 2005.

[232] Donald D Wagman, William H Evans, Vivian B Parker, Richard H Schumm, and Iva Halow. The nbs tables of chemical thermodynamic properties. selected values for inorganic and c1 and c2 organic substances in si units. Technical report, DTIC Document, 1982.

[233] Moriaki Wakaki, Osamu Shintani, Tsutomu Ogawa, and Toshihiro Arai. Optical and electrical properties of inverse spinel compound $mgin_2s_4$. *Jpn. J. Appl. Phys.*, 19(3):255–260, 1980.

[234] A. Walle and G Ceder. Automating first-principles phase diagram calculations. *Journal of Phase Equilibria*, 23(4):348–359, August 2002.

[235] Aron Walsh, Su-Huai Wei, Yanfa Yan, MM Al-Jassim, John A Turner, Michael Woodhouse, and BA Parkinson. Structural, magnetic, and electronic properties of the co-fe-al oxide spinel system: Density-functional theory calculations. *Phys. Rev. B*, 76(16):165119, 2007.

[236] Liwen F. Wan, Brian R. Perdue, Christopher A. Apblett, and David Prendergast. Mg desolvation and intercalation mechanism at the mo_6s_8 chevrel phase surface. *Chem. Mater.*, 27(17):5932–5940, Sep 2015.

[237] Yan Wang, William Davidson Richards, Shyue Ping Ong, Lincoln J. Miara, Jae Chul Kim, Yifei Mo, and Gerbrand Ceder. Design principles for solid-state lithium superionic conductors. *Nat. Mater.*, 14(10):1026–1031, aug 2015.

[238] Ying Wang, Katsunori Takahashi, K. H. Lee, and G. Z. Cao. Nanostructured vanadium oxide electrodes for enhanced lithium-ion intercalation. *Adv. Funct. Mater.*, 16(9):1133–1144, jun 2006.

[239] Zhiguo Wang, Qiulei Su, and Huiqiu Deng. Single-layered v_2o_5 a promising cathode material for rechargeable li and mg ion batteries: an ab initio study. *Phys. Chem. Chem. Phys.*, 15(22):8705–8709, 2013.

[240] Ph Wernet. The Structure of the First Coordination Shell in Liquid Water. *Science*, 304(5673):995–999, may 2004.

[241] M. S. Whittingham. Chemistry of intercalation compounds: Metal guests in chalcogenide hosts. *Prog. Solid State Ch.*, 12(1):41–99, jan 1978.

[242] M. Stanley Whittingham. The role of ternary phases in cathode reactions. *J. Electrochem. Soc.*, 123(3):315–320, 1976.

[243] M. Stanley Whittingham. Lithium batteries and cathode materials. *Chem. Rev.*, 104(10):4271–4302, Oct 2004.

[244] M. Stanley Whittingham. Ultimate limits to intercalation reactions for lithium batteries. *Chem. Rev.*, 114(23):11414–11443, Dec 2014.

[245] K. Wiesener, W. Schneider, D. Ilić, E. Steger, K.H. Hallmeier, and E. Brackmann. Vanadium oxides in electrodes for rechargeable lithium cells. *J. Power Sources*, 20(1-2):157–164, May 1987.

[246] Abigal R Wizansky, Paul E Rauch, and Francis J Disalvo. Powerful oxidizing agents for the oxidative deintercalation of lithium from transition metal oxides. Technical report, DTIC Document, 1989.

[247] Qi-Hui Wu, Andreas Thiß en, and Wolfram Jaegermann. Photoelectron spectroscopic study of Li intercalation into V2O5 thin films. *Surface Science*, 578(1-3):203–212, March 2005.

[248] Penghao Xiao, Jie Song, Long Wang, John B Goodenough, and Graeme Henkelman. Theoretical study of the structural evolution of a $na_2femn(cn)_6$ cathode upon na intercalation. *Chem. Mater.*, 27(10):3763–3768, may 2015.

[249] Bo Xu and Shirley Meng. Factors affecting li mobility in spinel $limn_2o_4$–a first-principles study by gga and gga+u methods. *J. Power Sources*, 195(15):4971–4976, 2010.

[250] Zhenguo Yang, Jianlu Zhang, Michael C. W. Kintner-Meyer, Xiaochuan Lu, Daiwon Choi, John P. Lemmon, and Jun Liu. Electrochemical energy storage for green grid. *Chem. Rev.*, 111(5):3577–3613, may 2011.

[251] Takeshi Yao, Yoshio Oka, and Naoichi Yamamoto. Layered structures of hydrated vanadium oxides. part 1.−alkali-metal intercalates $a_{0.3}v_2o_5.nh_2o$ (a = na, k, rb, cs and nh_4). *J. Mater. Chem.*, 2(3):331–336, 1992.

[252] Hyun Deog Yoo, Ivgeni Shterenberg, Yosef Gofer, Gregory Gershinsky, Nir Pour, and Doron Aurbach. Mg rechargeable batteries: an on-going challenge. *Energy Environ. Sci.*, 6(8):2265–2279, 2013.

[253] Gabin Yoon, Dong-Hwa Seo, Kyojin Ku, Jungmo Kim, Seokwoo Jeon, and Kisuk Kang. Factors Affecting the Exfoliation of Graphite Intercalation Compounds for Graphene Synthesis. *Chemistry of Materials*, 27:2067–2073, 2015.

[254] Long Yu and Xiaogang Zhang. Electrochemical insertion of magnesium ions into v_2o_5 from aprotic electrolytes with varied water content. *J. Colloid Interf. Sci.*, 278(1):160–165, Oct 2004.

[255] Congli Yuan, Ying Zhang, Yue Pan, Xinwei Liu, Guiling Wang, and Dianxue Cao. Investigation of the intercalation of polyvalent cations (mg^{2+}, zn^{2+}) into λ-mno_2 for rechargeable aqueous battery. *Electrochim. Acta*, 116:404–412, Jan 2014.

[256] Galina S Zakharova and Viktor L Volkov. Intercalation compounds based on vanadium(v) oxide xerogel. *Russ. Chem. Rev.*, 72(4):311–325, 2007.

[257] Ruigang Zhang, Chen Ling, and Fuminori Mizuno. A conceptual magnesium battery with ultrahigh rate capability. *Chem. Commun.*, 51(8):1487–1490, 2015.

[258] Bo Zhou, Hui Shi, Rongfang Cao, Xiaodong Zhang, and Zhenyi Jiang. Theoretical study on the initial stage of a magnesium battery based on a v_2o_5 cathode. *Phys. Chem. Chem. Phys.*, 16(34):18578–18585, 2014.

[259] F. Zhou, M. Cococcioni, C. A. Marianetti, D. Morgan, and G. Ceder. First-principles prediction of redox potentials in transition-metal compounds with lda+u. *Physical Review B*, 70(23):235121–1–8, dec 2004.

[260] Fei Zhou, Thomas Maxisch, and Gerbrand Ceder. Configurational Electronic Entropy and the Phase Diagram of Mixed-Valence Oxides: The Case of Li_xFePO_4. *Physical Review Letters*, 97(15):155704, October 2006.